The Middle Miocene Carbonate Crash: Relationship to Neogene Changes in Ocean Circulation and Global Climate

Dissertation zur Erlangung

des Doktorgrades am

Fachbereich Geowissenschaften

der Universität Bremen

vorgelegt von

Thomas Westerhold

Bremen, November 2003

Tag des Kolloquiums:

19. Dezember 2003

Gutachter:

1. Prof. Dr. G. Wefer

2. Prof. Dr. R. Henrich

Prüfer:

1. Prof. Dr. H. J. Kuss

2. Priv. Doz. Dr. M. Zabel

dedicated to Uli

Table of contents

Abstract

Drastic and repeated reductions of calcium carbonate contents characterize pelagic sediment sequences at the middle to late Miocene transition. These so-called carbonate crash events first have been identified in the eastern Equatorial Pacific. Similar occurrences of carbonate reductions have been recorded in the western Equatorial Atlantic and the Caribbean Sea suggesting a common cause. The opening and closing of gateways at the middle to late Miocene transition is thought to have changed the global ocean thermohaline circulation and, as a result, triggered the carbonate crash events. Until today, little is known about the global variations in the carbonate sedimentation pattern during the transition from middle to late Miocene. The comparable nature, especially the rapidness of the crash events in the Pacific, Atlantic and Caribbean has been subject to discussion mainly focusing on changes in ocean circulation. None of these models yet explain the observed different timings of the carbonate reduction events in distinct regions and water depths.

The aim of the present PhD project was to document and understand the causal relationships of the fundamental changes in carbonate and terrigenous sedimentation in the eastern South Atlantic in relation to changes in ocean circulation and global climate in the middle to late Miocene. For this purpose ODP Sites 1085 (1713 mbsl) and 1087 (1372 mbsl), drilled on the continental margin off Namibia, and ODP Site 1092 (1974 mbsl), drilled on the northern slope of the Meteor Rise in the sub-Antarctic sector of the Southern Ocean were investigated.

At ODP Site 1085 and 1087 the changing pattern of carbonate and terrigenous deposition from 14 - 6.5 Ma have been reconstructed using high-resolution XRF core-scanning measurements (Ca, Fe). The Fe intensity records of both sites were spliced together and then used to construct an astronomically calibrated chronology based on orbital tuning. In the middle to late Miocene interval at least six carbonate crash events have been identified, characterized each by a dramatic drop in carbonate content, a continuous period of low carbonate accumulation, and a gradual increase towards normal levels of carbonate deposition. Detailed discussion with other proxies at Site 1085 revealed that these carbonate crash events are mainly caused by dilution due to enhanced terrigenous input linked to sea-level lowering, and by dissolution due to increased flux of corrosive Southern Component Water during Miocene glacial events. On a global scale, the comparison with carbonate records from the eastern Equatorial Pacific, western Equatorial Atlantic and Caribbean Sea gave evidence that the carbonate crash events appeared with different intensities and temporal offsets, but clearly demonstrated the geochemical reorganization of the ocean circulation at the middle to late Miocene transition. The observed redistribution in carbonate sedimentation pattern between Pacific and Atlantic at 11.2 Ma is attributed to changes in ocean circulation and the evolving geochemical basin-to-basin fractionation due to the uplift of the Central American Seaway and the intensification of Northern Component Water production.

A high-resolution benthic stable oxygen isotope record obtained from Site 1085 sediments provided a detailed chronology for the middle to late Miocene (13.9 - 7.3 Ma)

climate transition in the eastern South Atlantic. Results showed that the long-term cooling trend in $\delta^{18}O$ record is punctuated by significant increases with maxima at 13.8, 13.2, 11.7 and 10.4 Ma, corresponding to the Miocene glacial events. The ages for the Mi-events derived in this study are consistent with the results of Miller et al. (1998) and therefore support a causal link between sequence boundaries traced from the shelf and glacioeustatic changes due to ice-sheet growth. Based upon $\delta^{18}O$ values the long-term sea-level lowering from 13.8 - 10.4 Ma is estimated to range in the order of ~85 meters, consistent with results from the New Jersey Margin and Marion Plateau. Spectral analysis of oxygen isotope data indicates that the middle to late Miocene climate system was driven by obliquity induced variations of the Antarctic ice-sheet. In addition, eccentricity- and precession-related cyclicity in the $\delta^{18}O$ record suggests strong influence of low latitude processes to the ice-sheet dynamic.

To reconstruct the Pleistocene climate history of South Africa, benthic oxygen isotope data and high-resolution XRF core-scanning data (Ca, Fe) have been obtained from the uppermost section of Site 1085. An astronomically calibrated timescale for the last 1.8 Ma was developed by tuning the benthic $\delta^{18}O$ record to obliquity. This study was conducted to understand the major driving mechanism for the climate in South Africa and to understand the response of the climate system with the change from unipolar to bipolar ice-sheets in the Pleistocene. Results show that Pleistocene sediments at Site 1085 were dominated by high terrigenous input of the nearby Orange River during interglacial periods, and low input during glacial periods. This suggests that precipitation variations rather than sea-level fluctuations cause higher terrigenous input. Time series analysis shows that these variations in precipitation are linked to shifts in the high- (i.e. ice-sheet oscillations) and low-latitude (i.e. tropical SST) climate systems. Prior to the Mid-Pleistocene Transition at ~ 0.9 Ma our results support the hypothesis that South African climate is mainly controlled by shifts of the atmospheric frontal systems due to fluctuations of the Antarctic ice-sheet.

At Site 1092 high-resolution XRF core logging data were used to revise the composite depth record. As a consequence the number of magnetic polarity subchrons within Chron had to be reduced C5n.2n from four to three consistent with the number of “cryptochrons” recognized in marine oceanic anomaly data. The reconstruction of carbonate sedimentation pattern from 13.7 - 5.3 Ma revealed distinct drops accompanied by enhanced iron concentrations between 9.3-9.1 and 6.2-5.3 Ma. These carbonate minima coincide with the nadir of the carbonate crash observed in all major ocean basins and the Messinian Salinity Crisis, respectively. The close association of the events to increased opal content is interpreted to mirror the northward migrations of Antarctic Fronts due to cooling processes on Antarctica. The results of the South Atlantic Sites 1085, 1087 and 1092 suggest that supralysocline carbonate dissolution is the most feasible common cause for the carbonate crash event centered at 9.2 Ma. Moreover, the results from the Meteor Rise compared to those off Namibia lead to the assumption that the first five carbonate crash events observed at Site 1085 are mainly caused by dilution rather than dissolution of carbonate. The middle to late Miocene Fe concentration record of Site 1092 documented increased aridity and desert expansion in Patagonia at 10 Ma. This is synchronous with

substantial drying of Southern Africa documented by changes in terrigenous input, and phase relation between $\delta^{18}O$ and terrigenous sedimentation at Site 1085.

The results of this thesis document fundamental changes in global ocean chemistry and continental climate in conjunction with the evolving modern ocean thermohaline circulation across the middle to late Miocene. The uplift of the Central American Seaway and the expansion of the Antarctic ice-sheet seem to play a key role setting the stage for the observed dramatic and irreversible shifts in ocean and atmospheric circulation. However, the nature of the observed response is highly dependent on the regional settings.

Kurzfassung

Wiederholte, drastische Reduzierungen des Karbonatgehalts charakterisieren pelagische Sedimentabfolgen am Übergang vom mittleren zum späten Miozän. Diese Reduzierungen wurden zuerst in Sedimentabfolgen des äquatorialen Ostpazifiks nachgewiesen und als Karbonat-Zusammenbruch (‚Carbonate Crash') bezeichnet. Da ähnliche Sedimentationsereignisse mittlerweile auch im äquatorialen Atlantik und der Karibik dokumentiert wurden, kann von einer gemeinsamen Ursache ausgegangen werden. Im Zeitraum vom mittleren bis späten Miozän begann sich die thermohaline Zirkulation im Ozean zu ihrer modernen Form hin zu entwickeln. Als entscheidender Faktor wird dabei die Schließung des Panama Isthmus angesehen, die auch als Hauptursache des ‚Carbonate Crash' diskutiert wird. Allerdings liegen für diesen Zeitraum nur spärliche Informationen über globale Variationen in den Ablagerungsmustern von karbonatischen Sedimenten vor. Die Vergleichbarkeit der Karbonateinbrüche in Pazifik, Atlantik und Karibik war Gegenstand von Diskussionen, die sich hauptsächlich auf die Veränderungen der ozeanischen Zirkulation als Ursache dafür konzentrierten. Jedoch kann keines dieser Modelle das zeitlich versetzte Auftreten der Karbonateinbrüche in verschiedenen Regionen und Wassertiefen erklären.

Ziel der vorliegenden Arbeit ist es, die kausalen Zusammenhänge der grundlegenden Veränderungen in der Karbonat- und terrigenen Sedimentation im Südostatlantik in Bezug zu Veränderungen der Ozeanzirkulation und des globalen Klimas im mittleren bis späten Miozän zu verstehen und darzustellen. Zu diesem Zweck wurden die ODP Sites 1085 (1713 mbsl) und 1087 (1372 mbsl), gelegen am Kontinentalrand vor Namibia, und ODP Site 1092 (1974 mbsl), gelegen am nördliche Hang des Meteor Rise im subantarktischen Bereich des Südozeans, untersucht.

Anhand von hochauflösenden Röntgen-Fluoreszenz-Messungen (Ca, Fe) an Kernen aus den ODP Bohrungen 1085 und 1087 wurden Veränderungen der Karbonat- und terrigenen Sedimentation im Zeitraum von 14 - 6.5 Ma rekonstruiert. Die Eisenintensitäten beider Bohrungen wurden kombiniert und für eine hochauflösende zeitliche Einstufung der Sedimentabfolge mittels orbital tuning verwendet. Im mittleren bis späten Miozän konnten wenigstens sechs `carbonate crash´ Ereignisse beobachtet werden. Diese sind jeweils charakterisiert durch eine drastische Abnahme des Karbonatgehalts, eine kontinuierliche Phase niedriger Karbonatakkumulation und einen kontinuierlichen Anstieg hin zu Normalwerten. Ein detaillierter Vergleich mit anderen Proxies aus Bohrung 1085 zeigt, dass die ‚carbonate crash' Ereignisse zum einen bedingt sind durch Verdünnung aufgrund erhöhten Eintrags von terrigenem Materials während Meerespiegelabsenkungen und zum anderen durch vermehrte Lösung von Karbonat durch den Einstrom von korrosivem Südkomponentenwasser (Southern Component Water, SCW) während miozäner Glaziale. Global betrachtet zeigt der Vergleich zwischen Sedimenten aus dem äquatorialen Ostpazifik, dem äquatorialen Westatlantik und der Karibik, dass die ‚carbonate crash' Ereignisse zeitlich versetzt mit unterschiedlichen Intensitäten auftreten. Bei 11.2 Ma kann eine Umverteilung des Karbonatablagerungsmusters zwischen Pazifik und Atlantik beobachtet werden. Dies kann als Indiz für Veränderungen in der ozeanischen Zirkulation

und der beginnenden Becken-zu-Becken-Fraktionierung angesehen werden. Diese weitreichenden Veränderungen sind Folge der Verflachung des Panama Isthmus und der verstärkten Produktion von Nordkomponentenwasser (Northern Component Water, NCW).

An Bohrung 1085 konnte eine detaillierte Chronologie der Klimavariationen im Südostatlantik anhand einer hochauflösenden, benthischen Sauerstoffisotopenkurve erstellt werden (13.9-7.3 Ma). Anhand der $\delta^{18}O$ Daten lässt sich nachweisen, dass der lang anhaltende Abkühlungstrend von Maxima bei 13.8, 13.2, 11.7 und 10.4 Ma unterbrochen wird. Diese $\delta^{18}O$ Exkursionen spiegeln die miozänen Glazialereignisse (‚Mi-events') wieder. Die in der vorliegenden Arbeit ermittelten Alter der ‚Mi-events' stehen im Einklang mit den Ergebnissen von Miller et al. (1998) und bestätigen somit einen kausalen Zusammenhang zwischen nachgewiesenen Sequenzgrenzen im Schelfbereich und glazio-eustatischen Meerespiegelschwankungen infolge der Ausdehnung des antarktischen Eisschildes. Das Ausmaß der langfristigen Meeresspiegelabsenkung von 13.8 bis 10.4 Ma wird anhand von $\delta^{18}O$ Daten auf ca. 85m eingeschätzt, übereinstimmend mit neueren Untersuchungen des New Jersey Kontinentalrandes und des Marion Plateaus. Spektral-Analysen der Sauerstoffisotopendaten weisen darauf hin, dass das Klima im mittleren bis späten Miozän vorwiegend durch obliquitätsinduzierte Fluktuationen des antarktischen Eisschildes gesteuert wurde. Ferner deuten Zyklizitäten in den $\delta^{18}O$ Daten, die auf Exzentrizität und Präzession zurückzuführen sind, darauf hin, dass die Fluktuationen im antarktischen Eisschild auch von klimatischen Prozessen niederer Breiten beeinflusst worden sind.

Zur Rekonstruktion der Klimageschichte des pleistozänen Südafrika wurden benthische Sauerstoffisotopen-Messungen und hochauflösende Röntgen-Fluoreszenz-Messungen am obersten Abschnitt von Bohrung 1085 vorgenommen. Mittels orbital tuning benthischer $\delta^{18}O$ Daten wurde eine Zeitskala für die letzten 1.8 Ma Jahre erstellt. Ziel dieser Studie war es, die klimasteuernden Faktoren und die Auswirkungen des Übergangs von uni- zu bipolaren Eisschilden auf das südafrikanische Klimasystem zu ergründen. Die Ergebnisse zeigen, dass die pleistozänen Sedimente im Bereich der Bohrung 1085 während der Interglaziale von terrigenem Eintrag aus dem nahen Oranje River dominiert worden sind, während in Glazialzeiten deutlich weniger terrigenes Material abgelagert wurde. Dies deutet darauf hin, dass Variationen der Niederschlags-mengen im Bereich des Oranje River einen größeren Einfluss auf den terrigenen Eintrag haben, als die Remobilisierung von Schelfablagerungen aufgrund von Meerespiegel-absenkungen. Anhand von Zeitreihenanalyse kann gezeigt werden, dass Änderungen der Nierderschlagsmenge an Variationen der Klimasysteme in hohen (z.B. Fluktuationen der Eisschilde) und niederen (z.B. Schwankungen der tropische Meeresoberflächen-temperaturen) Breiten gekoppelt sind. Desweiteren unterstützen die Daten von Bohrung 1085 die Annahme, dass vor der ‚Mid-Pleistocene Transition' (~0.9 Ma) das süd-afrikanische Klima durch Verschiebungen der Windsysteme, die wiederum von Fluktuationen im Antarktischen Eisschild gesteuert wurden, beeinflusst wurde.

Hochauflösende Röntgen-Fluoreszenz-Messungen an Bohrung 1092 wurden dazu genutzt, die Tiefenskala der Bohrung zu revidieren. Aufgrund der neuen Tiefenskala wurde

die Zahl der magnetischen ‚polarity subchrons' im Chron C5n.2n von vier auf drei reduziert. Die Rekonstruktion der Karbonatsedimentation von 13.7 - 5.3 Ma belegt zwei deutliche Erniedrigungen bei 9.3 - 9.1 Ma und 6.2 - 5.3 Ma, die mit erhöhten Opalgehalten assoziiert sind. Diese verminderten Karbonatgehalte korrespondieren mit dem Nadir des ‚carbonate crash' in allen Ozeanbecken und der ‚Messinischen Salinitätskrise'. Die enge Beziehung dieser Ereignisse mit erhöhten Opalgehalten spiegelt die Verlagerung der antarktischen Fronten nach Norden wieder, die vermutlich auf Abkühlungsprozesse in der Antarktis zurückzuführen ist. Der Vergleich der Ergebnisse der Bohrungen 1085, 1087 und 1092 belegt supralysoklinale Lösung von Karbonaten als Hauptursache des ‚carbonat crash' Ereignisses bei 9.2 Ma. Allerdings zeigt der Vergleich, dass die ersten fünf Karbonatreduktionen der Bohrung 1085 durch Verdünnung aufgrund erhöhten terrigenen Eintrags und nicht durch Lösung verursacht worden sind. Erhöhte Eisenkonzentrationen im Bereich der Bohrung 1092 ab 10 Ma dokumentieren die zunehmende Aridität und Ausbreitung der Wüsten in Patagonien. Dies verläuft parallel zu einer grundlegenden Verschiebung des südafrikanischen Klimas hin zu trockeneren Bedingungen.

Die Ergebnisse dieser Arbeit dokumentieren fundamentale Veränderungen in der Chemie der Ozeane und des kontinentalen Klimas in Südafrika und Patagonien. Diese stehen in enger Verbindung mit der sich entwickelnden modernen thermohalinen Ozeanzirkulation im mittleren bis späten Miozän. Die Verflachung des Panama Isthmus und die Expansion des antarktischen Eisschildes scheinen dabei für die beobachteten, weitreichenden und irreversiblen Veränderungen in der ozeanischen und atmosphärischen Zirkulation eine Schlüsselrolle zu spielen.

Introduction

The Cenozoic is characterized by a long-term global cooling trend from early Paleogene ice-free conditions towards the Neogene ice-house regime, as inferred from globally compiled deep-sea foraminiferal oxygen isotope records (Figure 1.1). This long-term Cenozoic climatic trend is punctuated by three major cooling steps around the Eocene/Oligocene boundary (ca. 33.4 Ma), the middle Miocene (15 - 11 Ma), and the late Pliocene (3.5 - 2.6 Ma) (Miller et al. 1987, Zachos et al. 2001a). Of these three Cenozoic oxygen isotope events, the Eocene/Oligocene and the middle Miocene positive isotope shifts are generally interpreted to indicate the major expansion and permanent establishment of the East Antarctic Ice Sheet accompanied by some effect of deepwater cooling (Woodruff and Savin 1989, Wright et al. 1992, Wright and Miller 1996, Flower and Kennett 1993, 1995). The late Pliocene cooling event is ascribed to the onset of ice growth in the northern hemisphere (Maslin et al. 1998). A combination of changes in atmospheric carbon dioxide concentration (Berner 1994) and oceanic heat transport (D'Hondt and Arthur 1996) in cause of horizontal and vertical tectonic movements like opening or closing of oceanic gateways and mountain building episodes are assumed to be main factors inducing these global climate changes.

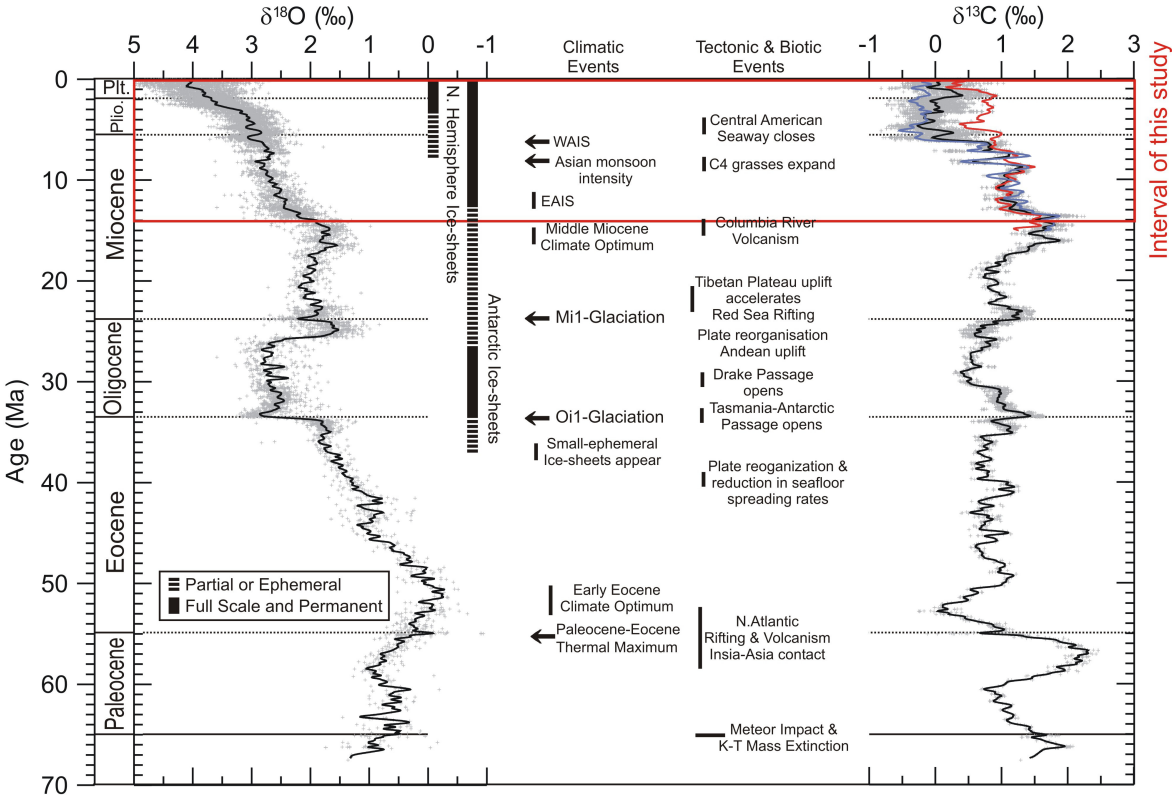

Figure 1.1 Global deep-sea oxygen and carbon isotope record from the Paleocene to Holocene with some key tectonic and biotic events (from Zachos et al. 2001a).With the carbon isotope record, separate curve fits were derived for the Atlantic (red) and Pacific (blue) above the middle Miocene to illustrate the increase in basin-to-basin fractionation. The red box represents the time frame of this study.

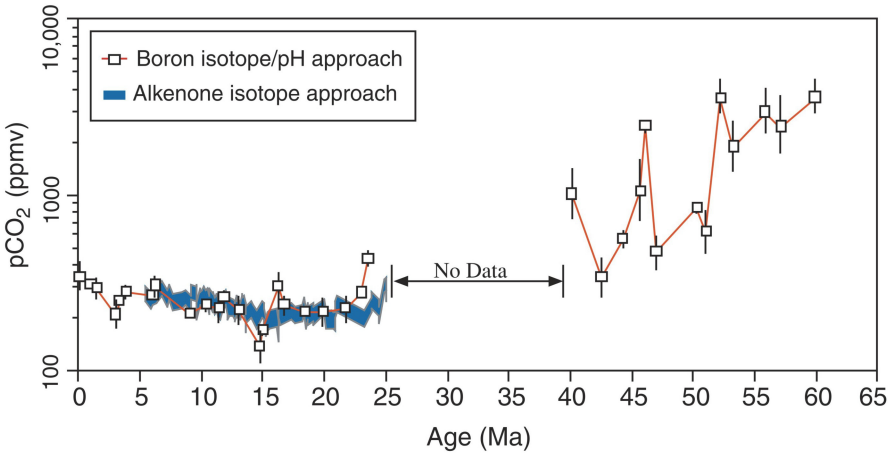

Figure 1.2 Estimates of Cenozoic atmospheric pCO_2 based on two independent proxies as measured in subtropical deep-sea sediment cores from the Pacific. The first curve spanning most of the Cenozoic is estimated from surface ocean pH as derived from the boron isotope ratios of planktonic foraminifers (Pearson and Palmer 2000). The second pCO_2 curve spanning the Miocene is based on the $\delta^{13}C$ values of phytoplankton organic compounds known as alkenones (Pagani et al. 1999) (from Zachos et al. 2001a).

The role of pCO_2 as a cause of the Neogene cooling was challenged by independent geochemical proxy records from deep-sea sediments that do not match with the Miocene benthic foraminiferal $\delta^{18}O$ trend. On the basis of alkenone $\delta^{13}C$ records, Pagani et al. (1999) reconstructed atmospheric CO_2 for the Miocene (Figure 1.2) and found that pCO_2 was lower in the early Miocene, followed by an increasing trend through the middle and late Miocene, suggesting that changing pCO_2 played little or no direct role in long-term climate variability during the Miocene. Paleo-pCO_2 estimates based on boron isotopic ratios of planktonic foraminiferal shells also show low values overall for the Miocene (Figure 1.2). Furthermore, the hypothesis of chemical weathering as a CO_2 sink and cooling in the Neogene (Raymo 1994) may not be valid because the riverine $^{87}Sr/^{86}Sr$ flux is controlled not only by continental weathering rate but also by the strontium isotopic compositions of the minerals that are chemically eroded (Quade et al. 1997, Kashiwagi and Shikazono 2003).

In the absence of pCO_2 control on the Cenozoic global climate variability, changes in oceanic heat and atmospheric water vapor transport driven by oceanic gateway reconfigurations (Figure 1.3) are considered to have played important roles (Pagani et al. 1999, Zachos et al. 2001a). For instance, the opening of the Tasmanian Gateway and the Drake Passage and the resulting intensification of circumpolar currents and thermal isolation of Antarctic waters from the subtropics have been invoked as a primary driving factor for the Cenozoic cooling and accumulation of ice on Antarctica (Barker and Burrell 1977, Kennett 1977). Although the Drake Passage is thought to have opened initially in the

Oligocene (Lawver and Gahagan 1998), Pagani et al. (2000) postulated that the initiation of unrestricted eastward flow across the Passage and strengthening of the Antarctic circumpolar current (ACC) occurred at ~15-14.5 Ma. Furthermore, Lee and Lawver (1995) suggested that the closure of the Indonesian Seaway in the western Equatorial Pacific triggered the intensification of gyral circulation and western boundary currents, resulting in a northward migration of tropical planktonic foraminiferal assemblages into the northwestern Pacific in the middle Miocene. Finally, the closure of the Central American Seaway is considered to trigger the last cooling step in the Cenozoic climate change due to the intensification of the Gulf Stream which introduced warm and saline waters to high northern latitudes favoring early Pliocene glaciation of the northern continents (Jansen and Sjöholm 1991, Haug and Tiedemann 1998). However, the question whether the increase in polar moisture and heat transport promoted or delayed the onset of enhanced Northern Hemisphere glaciation is still a subject of debate (Berger and Wefer 1996, Haug and Tiedemann 1998, Nisancioglu et al. 2003, Lear et al. 2003).

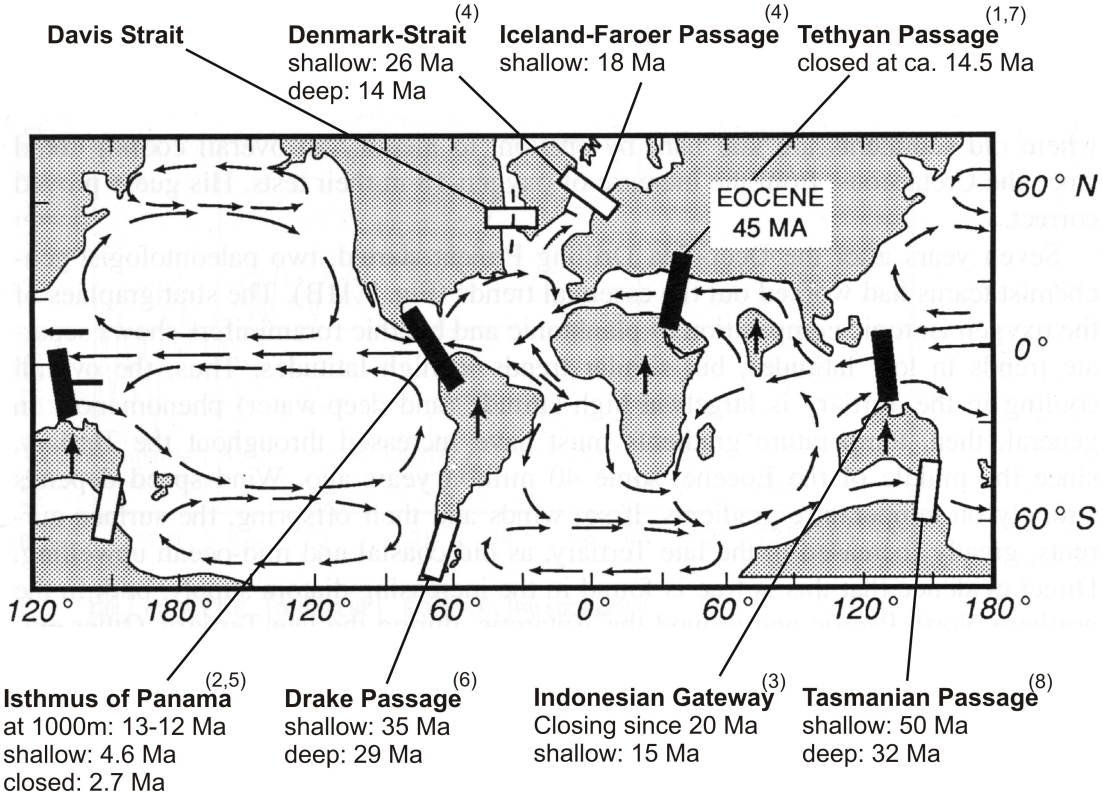

Figure 1.3 Geography of the Middle Eocene (~45 Ma) and major oceanic gateways critical for ocean circulation. Tropical gateways are closing (filled rectangles), high latitude gateways are opening (open rectangles) throughout the Cenozoic. Modified after Seibold and Berger (1996). Important ages for the opening and closing history of gateways are taken from: (1) Woodruff and Savin 1989, (2) Duque-Caro 1990, (3) Lee and Lawver 1995, (4) Hay 1996, (5) Haug and Tiedemann 1998, (6) Lawver and Gahagan 1998, (7) Ramsay et al. 1998, (8) Lawver and Gahagan 2003. Shallow and deep refer to the critical depth to allow overflow of deep- and intermediate waters.

1.1 The middle to late Miocene onset of modern ocean thermohaline circulation

The Miocene was a period of geochemical reorganization of the world ocean. At the end of the middle Miocene cooling step a strong basin-to-basin asymmetry developed between North Atlantic and North Pacific, with the deep Atlantic collecting carbonate, while the accumulation of silica shifted to the North Pacific ('silica switch', Keller and Barron 1983). This large-scale geochemical change points to a major reorganization in the deep circulation of the ocean (Woodruff and Savin 1989) and is thought to assign the beginning of the modern ocean thermohaline circulation (e.g. Berger and Wefer 1996). Additionally, the divergence of Cd/Ca ratios of benthic foraminifers from the South Atlantic and the western Equatorial Pacific demonstrate that the asymmetry becomes noticeable around ~12 Ma ago and is growing since 10 Ma (Delaney 1990). This is consistent with the ocean-wide patterns developed from carbon isotope synthesis of Woodruff and Savin (1989). Their benthic $\delta^{13}C$ records give evidence for modern deep water stratification and age differences between abyssal waters starting around ~10 Ma ago. The establishment of the major asymmetry between Atlantic and Pacific, as reflected by tracer data, has been attributed to enhanced production of Northern Component Water (NCW), a precursor of the North Atlantic Deep Water (NADW), due to the uplift of the Central American Seaway and the resulting northward heat transport in the Atlantic (e.g. Woodruff and Savin 1989, Maier-Reimer et al. 1990, Nisancioglu et al. 2003).

From early to middle Miocene the deep water circulation changed from a one-component-system dominated by Southern Component Water (SCW) to a three-component-system consisting of SCW, NCW and Mediterranean Outflow Water (MOW) (Wright et al. 1992). A significant $\delta^{13}C$ gradient between the Atlantic and Pacific at 20 Ma indicates the initiation of NCW production (Wright et al. 1992, Wright and Miller 1996), whereas the origin and nature of NCW is uncertain between 20 - 13 Ma due to the contribution of Mediterranean Outflow Water (see Ramsay et al. 1998). Between 20 - 13 Ma the North and Central Atlantic Ocean was characterized by two deep, southward flowing water masses: the deep (2 - 4 km), dense, saline MOW and the overlying less dense NCW. The reduction in Atlantic outflow between 15 - 12.5 Ma based on low intrabasinal $\delta^{13}C$ values has been attributed to either enhanced influx of SCW due to extensive glaciation at the middle Miocene cooling step (Wright et al. 1992, Wright and Miller 1996) or to changes in MOW production (Ramsay et al. 1998). By 13 Ma the southward flowing water masses were replaced by the single cold, dense NCW (Ramsay et al. 1998). The presence of two deep-water masses, a more corrosive SCW and a less

corrosive NCW after 12.5 Ma is reflected in the changing shallow-to-deep gradients in carbonate flux between 13.1 and 12.5 Ma at Ceara Rise (King et al. 1997). Increased NCW flux at around 12.5 Ma (Wright et al. 1992, Lear et al. 2003) coincided with the first significant overflow of Norwegian-Greenland Sea Water across the Greenland-Scotland Ridge between 13 - 11 Ma (Bohrmann et al. 1990). In contrast, Larsen et al. (1994) suggested that significant overflow of Norwegian-Greenland Sea Water through the Denmark Strait did not occur before 11.5 Ma, consistent with the suggested age of the NCW intensification by Wei and Peleo-Alampay (1997).

The intensity of NCW flux has been linked to changes in the depth of the Greenland-Scotland Ridge, which varies with the intensity of the mantle plume below Iceland (Wright and Miller 1996). This hypothesis has been questioned because the subsidence history of the ridge is poorly known, and the middle Miocene sea-level drop (Haq et al. 1987) suggests that the Greenland-Scotland Ridge became rather shallower than deeper during the time of NCW intensification (Wei and Peleo-Alampay 1997). Therefore, based on sedimentological and paleontological data from the North Atlantic and the Norwegian-Greenland Sea, another hypothesis was established suggesting that the intensification of NCW may have been triggered by climate cooling. In contrast, modeling studies suggested that shoaling of the Central American Seaway allowed the North Atlantic to become saline enough for the formation of NCW (Maier-Reimer et al. 1990). Furthermore, modeling studies revealed that some level of north Atlantic thermohaline flow can exist with partial opening of the Central American Seaway (Maier-Reimer et al. 1990, Mikolajewicz and Crowley 1997). Results also indicate that the reorganization of ocean circulation due to the uplift of the Central American Seaway could cause changes in the depth of the lysocline as much as 0.5-3.0 km (Figure 1.4) and in opal sediment accumulation as much as 35% in weight (Heinze and Crowley 1997). Thus, the shoaling of the Central American Seaway could explain both the basin-to-basin fractionation and evolving modern circulation with strong NCW flux to the south. NCW outflow into the Pacific is significantly reduced when the Central American Seaway reached a critical depth of 1000 m by 12 - 13 Ma (Duque-Caro 1990), dramatically changing the intermediate and deep circulation in the tropical Pacific, the western boundaries of the South Pacific and South Atlantic (Nisancioglu et al. 2003). The timing is close to the proposed ages for major changes in carbonate sedimentation in the eastern Equatorial Pacific (Lyle et al. 1995), western Equatorial Atlantic (King et al. 1997) and Caribbean Sea (Roth et al. 2000). These events, entitled the Miocene ‘carbonate crash’ (Lyle et al. 1995), have been ascribed to a shoaling of the

lysocline in the eastern Equatorial Pacific. Due to the closure of the Central American Seaway, the deep water exchange was cut off and the Pacific carbonate saturated NCW was replaced with older, carbonate undersaturated deep water from the Southern Ocean (Lyle et al. 1995, Farrell et al. 1995).

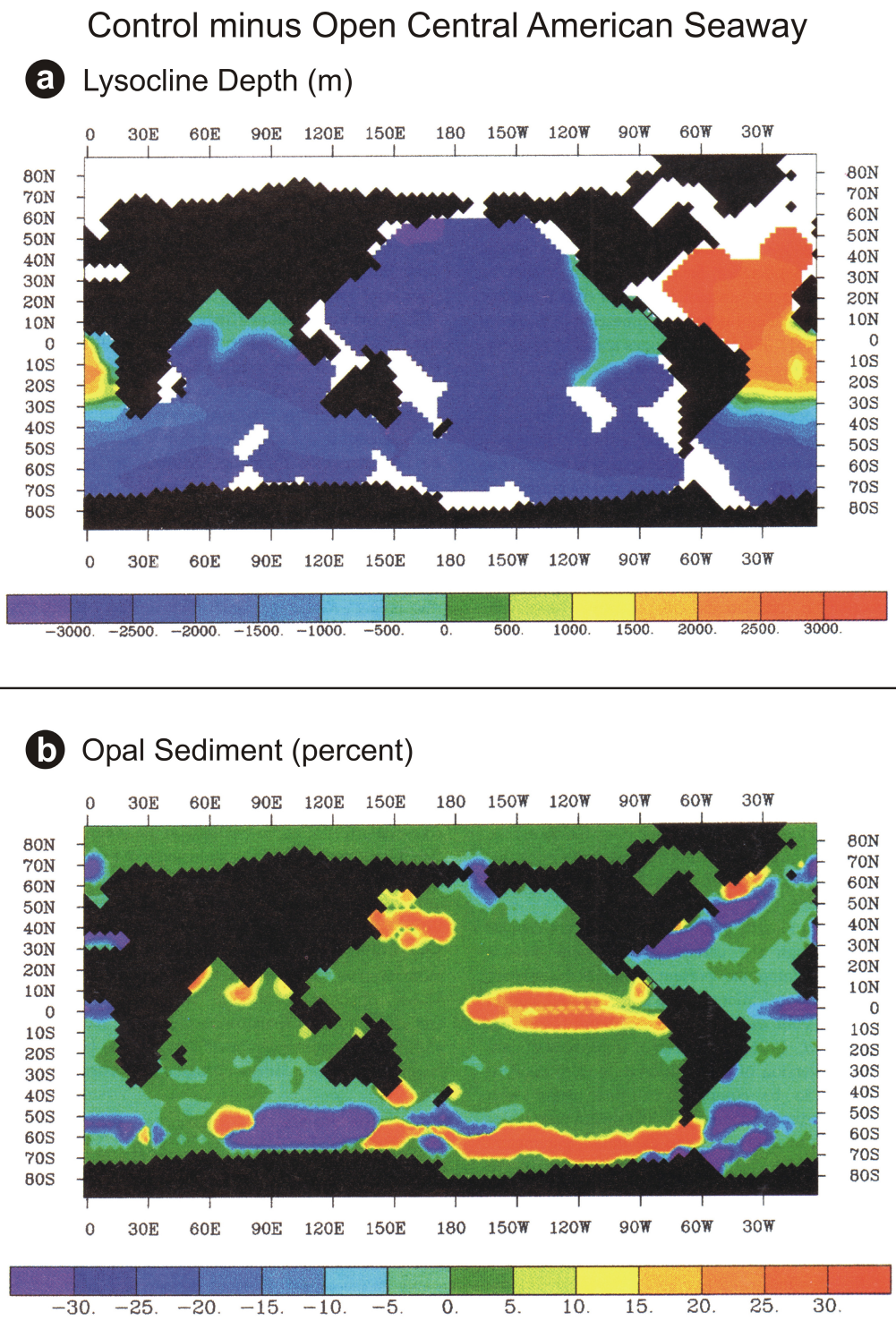

Figure 1.4 Model-calculated sedimentary responses to the closure of the Central American Seaway. Plotted are the differences between the control experiment (closed Central American Seaway) and the one with the Central American Seaway open for (a) lysocline depth (in meters) and (b) opal in the sediment model core top layer. Positive values mean that the lysocline is deeper and opal deposition rates are greater in the control run (from Heinze and Crowley 1997).

However, between 10 - 8.5 Ma the inter-ocean $\delta^{13}C$ gradients document little to no flow of NCW (Wright et al. 1991, Wright and Miller 1996), which might be attributed to the fact that the still strong flow through the Central American Seaway makes the modes with NCW unstable (Mikolajewicz and Crowley 1997). As the opening becomes narrower and shallower, NCW production increases because the advection of low salinity Pacific waters in the Atlantic diminishes (Mikolajewicz and Crowley 1997, Nisancioglu et al. 2003).

On the other hand, carbonate and opal sedimentation are also influenced by ocean productivity. The efficiency of productivity in the ocean is linked to the advection of nutrient-rich water masses, whose distribution in the ocean is controlled by wind intensity and thermohaline circulation. Present-day upwelling systems can be dominated either by carbonate producers (e.g., northwest Africa upwelling) or by organisms with siliceous skeletons (e.g., upwelling off Namibia). For the Neogene, changes in the extent and intensity of productivity, as well as the type of production (changes from opal to carbonate) have been described in high-productivity areas such as the coastal upwelling off California (Lyle et al. 2000). These changes are considered in relation to the development of thermohaline circulation during the Miocene.

The opening of the Drake Passage, first as a shallow, then later as a deep-water throughway, and the resulting formation of the Antarctic Circumpolar Current, are considered to be critical in the formation and spread of a cold, nutrient-rich Antarctic Intermediate Water (AAIW) (Pagani et al. 2000). The presence of AAIW below the warm Atlantic surface water is a prerequisite for the formation of gradients in the upper water column - such as the thermocline - that are necessary for the creation of high-productivity cells on the coasts or at oceanic fronts. From vertical $\delta^{13}C$ gradients similar to the present it is inferred that the ACC was in operation between ~20 - 17 Ma and ~14 - 3 Ma, resulting in relatively strong proto-AAIW production and northward migration of the Polar Front Zone (PFZ) (Pagani et al. 2000). But it is not clear if reduced proto-AAIW production is due to decreased NADW flux and/or tectonically induced reductions of proto-AAIW. The intensification of proto-AAIW production at 16.8 Ma coincides closely with the East Antarctic Ice Sheet (EAIS) expansion, potentially linking renewed strong ACC flow with a major climatic step in the middle Miocene (Pagani et al. 2000).

The closing of the Central American Seaway resulted in salinization of the North Atlantic and caused increased production of NCW (Maier-Reimer et al. 1990). The increase in NCW production in turn increased the production of AAIW and Antarctic Bottom Water (AABW). The increased rate of production of these water masses resulted in

differentiation of nutrients among them, and may have resulted in a shallower pycnocline enhancing the likelihood of upwelling nutrient-rich AAIW (Hay and Brock 1992). The South Atlantic AAIW is the ultimate source of the nutrients upwelled along the Namibian margin (Lange et al. 1999). The begin of upwelling off Namibia between 11 - 10 Ma has been attributed to major influx of cold waters linked to ice-sheet expansion on Antarctica (Siesser 1980, Diester-Haass et al. 1992). The timing is close to the major increase in NCW production, which might have increased AAIW production and therefore fueling upwelling along Namibia. Thus, the middle Miocene cooling trend caused the invigoration of surface ocean circulation systems, the intensification of gyral circulation and increases in the strength of oceanic fronts (Thunell and Belyea 1982, Kennett 1985). Moreover, it has been suggested that the growth of the Antarctic ice-sheet changed the atmospheric circulation pattern driving ocean currents and upwelling (Hay and Brock 1992). Further evidence for major changes in atmospheric circulation linked to ice-sheet expansion is documented by enhanced aridity in the Asian interior and the onset of the Indian and east Asian monsoons, about 9 - 8 Ma ago (Zhisheng et al. 2001). Generally, continental climates underwent major changes in the middle Miocene. Increased aridity is inferred at this time for mid-latitude continental regions including Australia, Africa, North America and South America, and may have fostered the development of grasses and the consequent evolution of grassland adapted biota (Flower and Kennett 1994).

1.2 Objectives and Approach

The main objective of this thesis is to document and understand the causal relationships of the fundamental changes in carbonate and terrigenous sedimentation in the eastern South Atlantic in relation to changes in ocean circulation and global climate in the middle to late Miocene. The role and effect of the evolution of the modern thermohaline circulation on ocean geochemistry, nutrient supply, and ocean productivity will be addressed. Additionally, the chronology of the onset of the modern thermohaline circulation and the effects to continental climate in the eastern South Atlantic will be explored. Therefore, the main questions are:

- Is there a global variation of the carbonate sedimentation during the transition from the middle to late Miocene, from which regional phenomena can be separated?
- To what extend are the closing of the Central American Seaway and the carbonate preservation in the Atlantic and Pacific associated?
- How are temporal variations and changes in carbonate and terrigenous sedimentation linked to the development of the modern ocean circulation and climate events during the Neogene?

To answer these questions three sites located in the South Atlantic (Figure 1.5) have been investigated: ODP Sites 1085 and 1087, drilled in the southern part of the Cape Basin during Leg 175, and ODP Site 1092, drilled on the northern Slope of the Meteor Rise in the sub-Antarctic sector of the Southern Ocean. ODP Sites 1085 (1713 m water depth) and 1087 (1372 m water depth) have been utilized to reconstruct the history of deep ocean chemistry, carbonate sedimentation, and terrigenous fluxes off Southwest Africa in the middle to late Miocene and Pleistocene. Their close position to the continent are most useful in detecting upwelling signals, clues to changes in continental climate and sea-level. ODP Site 1092 (1974 m water depth) has been chosen to study paleoceanographic changes in the sub-Antarctic South Atlantic during the middle to late Miocene and past migrations in the position of the Polar Front Zone. Because Site 1092 has provided one of the rare and more complete Upper Miocene polarity stratigraphies from the South Atlantic, a detailed chronology of paleoclimatic changes has been achieved. All three sites are located well above the regional carbonate lysocline and within the mixing zone between upper NADW and CDW, thus being sensitive to changes in NADW fluctuations over the course of the Neogene.

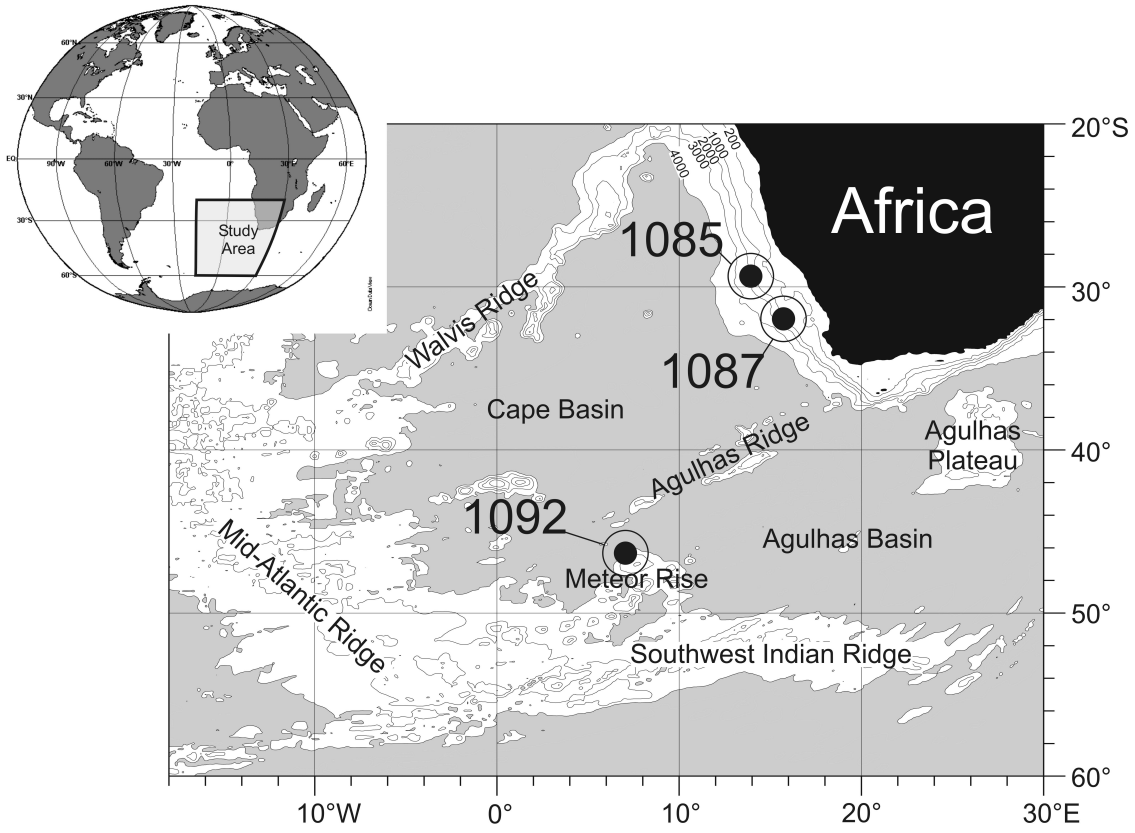

Figure 1.5 Map of study area. Relevant topographic features and locations of studied drill sites are presented. Gray shaded areas mark regions below 4000 m water depth.

In this study, a comprehensive data collection is compiled mainly from continuous, high-resolution and non-destructive analysis of chemical elements (XRF core scanner) for a detailed reconstruction of the Neogene carbonate and terrigenous sedimentation pattern in the South Atlantic. For Site 1085, a high-resolution benthic stable oxygen isotope stratigraphy is compiled. The combination of these various data sets is used to develop a high-resolution time series for the middle to late Miocene sedimentary and climatic development in detail. Furthermore, at Site 1085 the Pleistocene is investigated in order to evaluate and understand the development of the ocean climate system with respect to the changing climate boundary conditions. The comparison between Miocene and Pleistocene climate systems, and hence the change from unipolar to bipolar ice-sheets, will provide information about the change in major driving mechanism for the climate in South Africa, and the prevailing interactions between regional changes and the global climate development.

The results of this thesis are presented in five manuscripts (chapters 2 through 6) of which the first one is already submitted to *Marine Geology* and the fifth one is accepted by *Geophysical Journal International*.

Westerhold, T., Bickert, T., Röhl, U., Miocene evolution of carbonate sedimentation in the eastern South Atlantic: High-resolution XRF-scanning records of ODP Sites 1085 and 1087, Marine Geology, submitted. (*Manuscript #1*)

Westerhold, T., Bickert, T., Middle to Late Miocene Oxygen Isotope Stratigraphy of ODP Site 1085 - SE Atlantic, will be submitted to Palaeogeography, Palaeoclimatology Palaeoecology, (*Manuscript #2*)

Westerhold, T., Vidal, L., Bickert, T., Pleistocene Oxygen Isotope Stratigraphy of ODP Site 1085 - SE Atlantic, will be submitted to Earth and Planetary Science Letters, (*Manuscript #3*)

Westerhold, T., Bickert, T., Middle to Late Miocene History of Carbonate and Terrigenous Sedimentation at South Atlantic ODP Site 1092, in preparation. (*Manuscript #4*)

Evans, H. F., Westerhold, T., Channell, J. E. T., ODP Site 1092: revised composite depth section has implications for Upper Miocene cryptochrons, Geophysical Journal International - Research Note, accepted. (*Manuscript #5*)

1.3 Methods

1.3.1 X-ray fluorescence spectrometry (XRF)

To infer paleoceanographic information from physical and chemical element characteristics of sediments, standard analytical methods for discrete samples are time consuming and expensive. Relatively fast and non-destructive core-logging methods can now be employed to obtain continuous data at much finer scales (down to millimeter range) than are practical for individual sampling methods.

X-ray fluorescence spectrometry (XRF) is an active sensing method that employs X-ray emissions to sense elements of different atomic number. Samples are irradiated with incident X-rays capable of ejecting an electron from the inner shell of an atom. When this void is filled by downward cascade of an outer shell electron, the surplus energy is emitted as a X-ray fluorescent pulse. The energy of the pulse is proportional to the energy difference between two electron shells. Atoms of specific elements thus emit characteristic energy and wavelength spectra due to their distinctive electron configuration. This provides means to differentiate them via XRF.

Standard XRF analysis requires invasive sediment sampling followed by a number of time consuming preparation steps including: oven drying, powdering, and specimen preparation. The advantage of the XRF core scanner is that it can be used to scan the surface of a wet, split core and thus generate elemental data in near real time. For example, scanning a one meter core section at 2 cm resolution requires ~1 hr. Preparation of core surface is relative simple, requiring only a smooth level, split core covered with polyethylene foil to avoid contamination by the measurement prism sitting on the core surface during measurements. The standard measurement area is 10x10 mm.

The XRF core scanner I of the Bremen ODP Core Repository (BCR) - developed and built at the Netherlands Institute for Sea Research (NIOZ, Texel, The Netherlands) - is equipped with a Molybdenum (Mo) X-Ray source (3-50kV), a Peltier-cooled PSI detector (Kevex™) with a 125 µm beryllium window, and a multi channel analyzer with a 20 eV spectral resolution. This system configuration allows the analysis of elements from potassium (K, atomic number 19) through strontium (Sr, atomic number 38; at 20 kV X-ray voltage). The source and the detector are set at a 45 degree angle relative to the core surface. In order to minimize the loss of incident radiation and emitted longwave radiation by air absorption, a hollow prism flushed with Helium is used between the split core surface and the X-ray hardware (Figure 1.6). Data reduction is acquired with the application of the KEVEX^{TM} Toolbox, a commercially available software package. The

data are in counts per second (cps). Conversion to elemental concentration requires calibration against samples analyzed by standard chemical methods such as atomic absorption spectrometry (AAS), inductively coupled plasma mass spectrometry (ICP-MS) or standard XRF on samples (Jansen et al. 1998, Peterson et al. 2000).

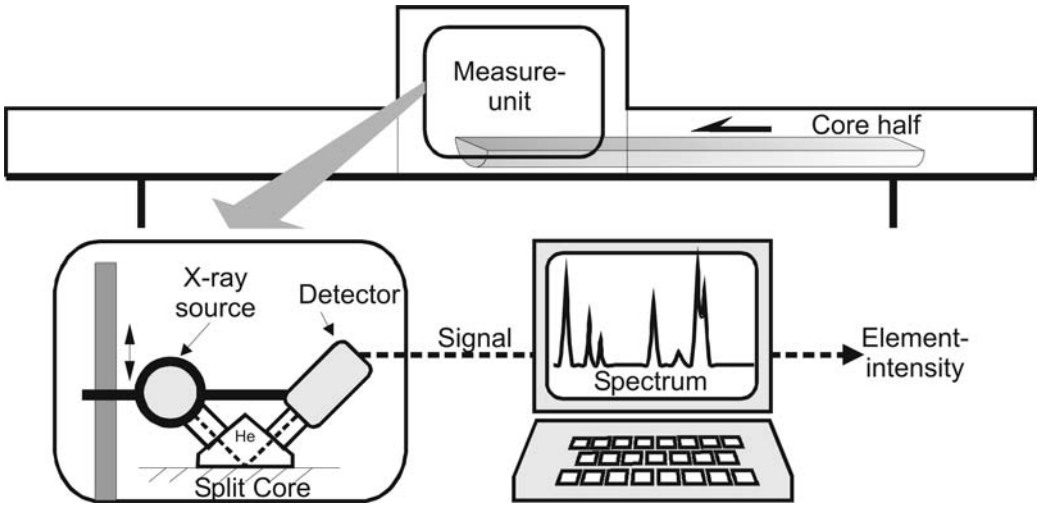

Figure 1.6 Schematic setup of the XRF core scanner I at the Bremen Core Repository (from Arz 1998).

The analyzed element intensities (K, Ca, Ti, Mn, Fe, Cu, Sr) and element ratios obtained by the XRF Core Scanner are used as geochemical proxies for climatic-paleoceanographic cycles, calcium carbonate content and supply of terrestrial material. Iron (Fe) mirrors changes in carbonate/clay ratios, and is in significant abundance throughout the sediments. The response depth of the element in the sample material depends on the chemical composition, the wavelength of the fluorescence radiation and the concentration of the matrix (Jenkins and de Vries 1970). E.g., for calcium (Ca) the response depth is tenths of µm and for Fe a few hundreds of µm. Fe is located in the center of the measurable element range, and therefore provides a stronger and more stable signal than the heavy or light ends of the XRF range.

Another advantage of the XRF scanner data is that the concentration of iron, for example, is less affected by post-burial diagenetic alteration than the often used magnetic susceptibility. Additionally, the XRF data show a significantly higher signal-to-noise ratio and a more consistent hole-to-hole agreement than other proxy data (e.g. GRAPE, color reflectance, magnetic susceptibility). Therefore, the obtained data allow the construction of a more accurate high-resolution composite depth scale (Röhl and Abrams 1998).

Detailed interpretations of XRF scans have substantially improved the knowledge in the areas of high-resolution time series definition, global correlations, important

paleoceanographic events and the detailed reconstruction of the sedimentary and climatic history for various time intervals from the Holocene to the Cretaceous (e.g. Norris and Röhl 1999, Röhl et al. 2000, Peterson et al. 2000, Haug et al. 2001, Pälike et al. 2001, Vidal et al. 2002, Adegbie et al. 2003, Jahn et al. 2003, Röhl et al. 2003).

1.3.1.1 Reproducibility and stability of XRF core-scanner data

In order to evaluate the data quality, the reproducibility and stability of XRF core scanner measurements have been studied. The detection limit of the XRF Core scanner depends on the sediment composition, porosity, grain size, the energy level of the X-ray tube and the count time used (Röhl and Abrams 2000).

To check the quality and reproducibility of XRF scanner data, threefold measurements on sediments from different regions representing a wide spectrum of sediment types have been performed. A set of 90 sampling points from 6 ODP Sites from the Ceara Rise (927, 928, 929), the Cape Basin (1085, 1087) and the Meteor Rise (1092) were measured. Elemental intensities for 7 elements were collected over a 1cm² area using 30 seconds count time, 20 kV X-ray voltage and an X-ray current of 0.087 mA. For every sampling point the arithmetic mean of the threefold measurements were calculated. Then the deviation in percent of the three measurements from the arithmetic mean was determined. The results are plotted against elemental intensity (cps) for the seven elements measured in Figure 1.7 Two general conclusions can be drawn from these plots. First, abundant elements in marine sediments like Ca and Fe can be reproduced within a precision of ±2%. Second, below an intensity level of 200 cps scatter increases dramatically suggesting that the detection limit for Ca and Fe within the above mentioned scanner setting is reached. Each element reveals a different scatter pattern. The Ca data from Site 1087 show a stronger scatter due to the sand-paper effect of abundant foraminiferal tests in these cores (for details see chapter 2). The increase in scatter to ±5% below 3000 cps in the Fe intensity data at Sites 927-929 from the Ceara Rise, is still unknown. The deviation for Titanium (Ti) is below ±5% above 200 cps. If intensities are less than 200 cps the scatter significantly increases both for Ti and Manganese (Mn). As Strontium (Sr) is located at the end of the measurable elemental range, and therefore provides a weaker signal, the scatter below 200 cps is stronger than with the other elements. Potassium (K) shows increased scatter above 200 cps, as the k_α-peak of K (3310 eV) in the intensity spectrum is very close to the k_α-peak of Ca (3690 eV). The processing

of the X-ray spectrum results in artificially higher K counts from sediments containing high amounts of Ca.

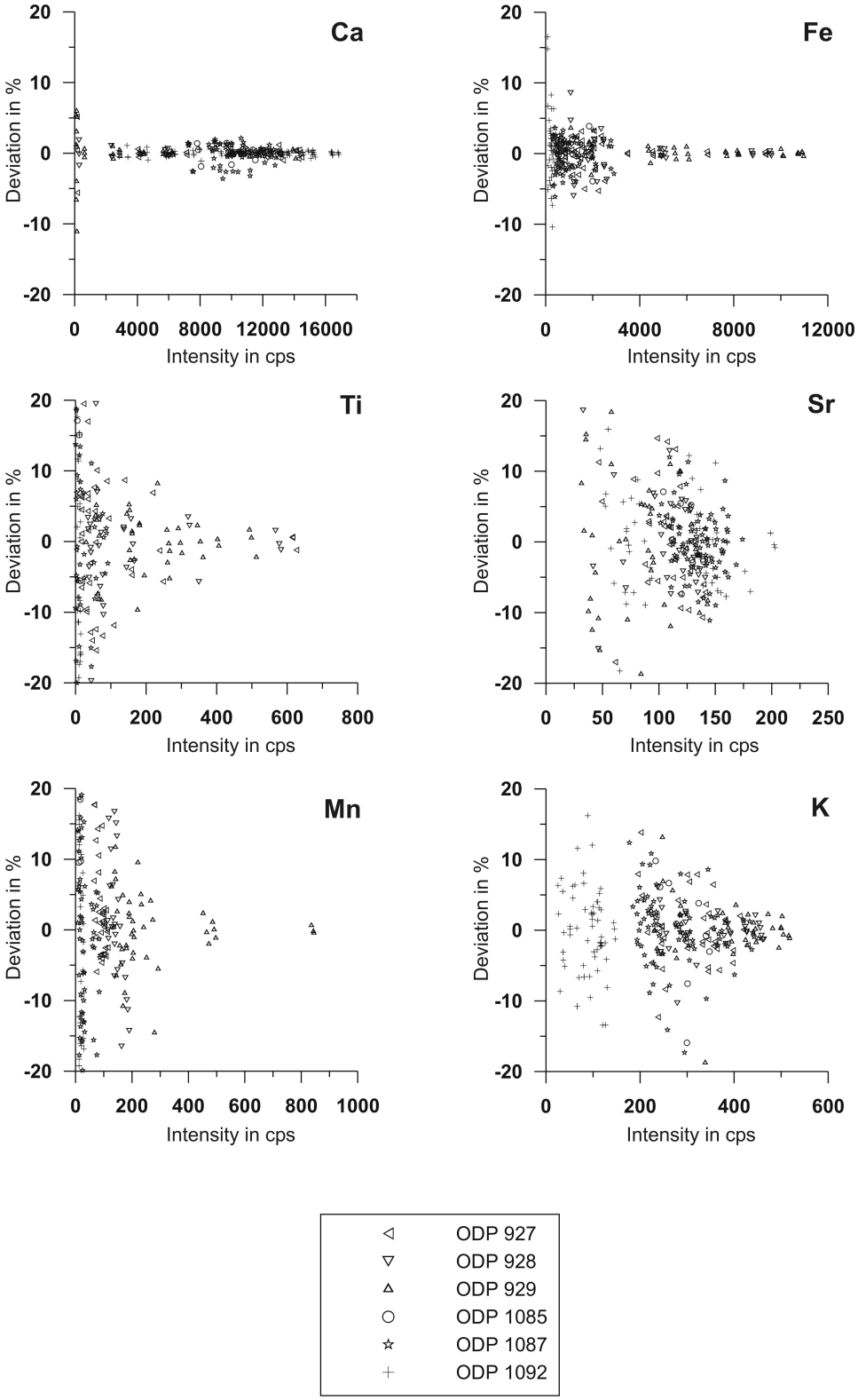

Figure 1.7 Deviation in percent from the mean of threefold XRF core scanner measurements at ODP cores from the Ceara Rise (927, 928, 929), Cape Basin (1085, 1087) and Meteor Rise (1092) plotted against elemental intensity. 90 positions were sampled; n = 270.

In order to evaluate the long-range reproducibility of XRF Core scanner data (i.e. years), core-section 53X-4 of ODP Site 1085 was scanned twice at 1 cm resolution offset by 30 month. The results (Figure 1.8) show that the pattern in Ca and Fe intensity can be reproduced within an error range of ±4% and ±3%, respectively. The absolute elemental intensities for the two runs can not be compared as different detectors have been used. As seen in Figure 1.8 the core section scanned comprises drill biscuits, common when the XCB drilling technique was applied for retrieving ODP cores. Element intensities of both Ca and Fe are elevated in drill mud areas, with stronger amplitudes in the Fe intensities. Drill mud, basically homogenized sediment, features higher density and lower porosity than the sediment biscuits (for discussion see Kuhlmann 2003). Because the XRF core scanner measures a 1 cm² of sediment surface, higher density of sediment provokes higher bulk intensities, and thus higher Ca and Fe intensities. In contrast, Ca and Fe intensities in general are anti-correlated (Figure 1.8). However, strong fluctuations in density will affect the bulk intensity detected by the XRF scanner, but the overall pattern of elemental distribution is reproduced well, even after 30 month offset between the sampling.

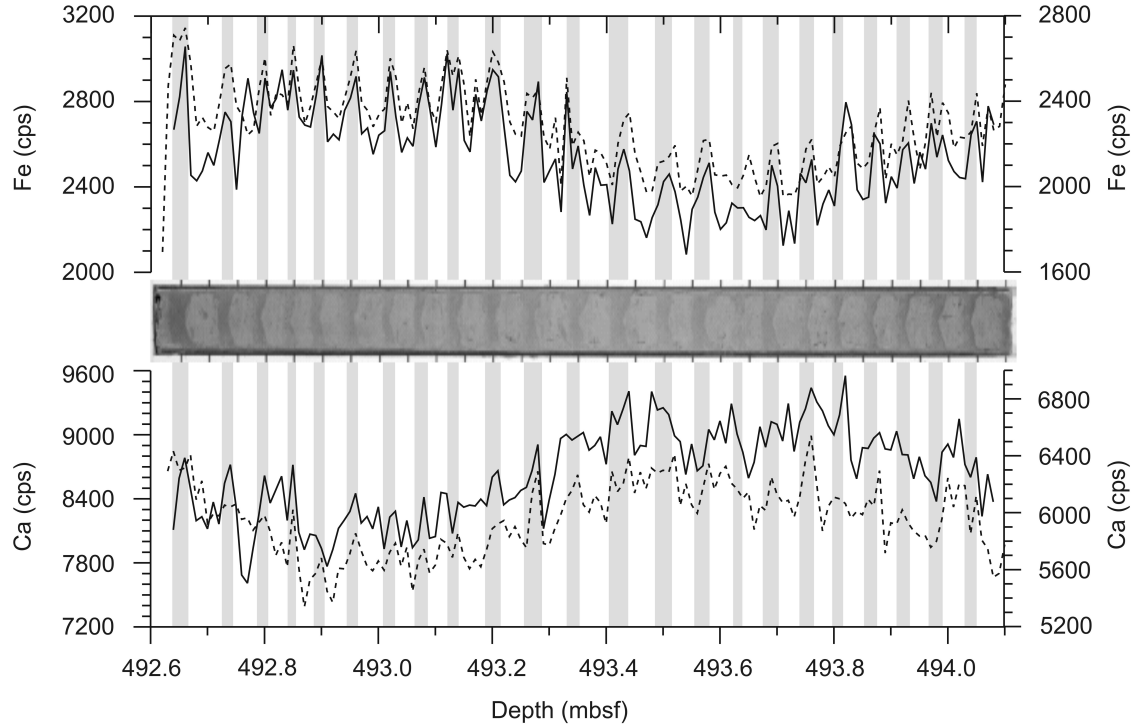

Figure 1.8 Fe (upper panel) and Ca (lower panel) XRF intensity data at 1cm resolution of ODP Site 1085 core-section 53x-4 plotted against msbf. The solid black line represents the first XRF scanning record, the dashed line represents the repeated XRF scanning. Time lag between the logging runs is 30 months. The core image is situated in the middle of the plot; note the drill-biscuits (lighter parts) and the drill-mud (darker parts). The gray bars mark drill-mud apparent in the core section.

To obtain absolute concentrations the XRF elemental intensity data are calibrated with data from standard chemical analyses from discrete samples. Here, Ca intensity data from ODP Site 1085 and 1092 have been calibrated by using ICP-OES and carbonate bomb technique data (see chapter 2 and 5 for details). To test, how close the predicted values match observe $CaCO_3$ values, the residual (observed minus predicted) for ODP Site 1085 and 1092 are displayed in Figure 1.9 as a function of observed carbonate content. These results show that the error for predicted $CaCO_3$ is ±5% at the 95% prediction level at Site 1085. Weaker correlation of XRF core scanner data to geochemical analyzed samples can be attributed to the inhomogeneity of the sample. The scanner detects the sedimentary composition of the 10-100µm of the split core surface, whereby the sample for the ICP-OES analysis is a homogenized fraction of a 10 cm^3 sample. For Site 1092 the $CaCO_3$ (observed vs. predicted) error is larger, about ±11%. As Site 1092 both consists of up to 95% $CaCO_3$ and was also heavily affected by stretching and squeezing during the drilling process, variations in density have affects on the Ca intensity signal. In addition, the relatively high opal content (up to 60%) might have influenced the XRF intensities by the so-called 'matrix-effect', the absorption of both the primary and emitted radiation by the elements present in addition to those actually measured. This effect is strong for elements at the light ends of the XRF range and thus could contribute to the higher error for $CaCO_3$ prediction at Site 1092. An even stronger influence upon the XRF intensities can be ascribed to higher porosity in the sediment due to higher abundance of diatom shells.

These investigations show that no general detection limits for the XRF core scanner are available and difficult to define. Hardware settings, sediment composition and the grain size of sedimentary components strongly influences the signal. Therefore, it is essential to define the data quality and methodical limits for every set of cores from a given area. Threefold measurements are very useful to check for the reliability of XRF data. Nevertheless, the XRF core scanner produces excellent and reliable elemental intensities in almost real time. The most critical aspect of XRF analysis is the core-surface preparation. In future, more investigations that will focus on the effect of grain size and porosity need to be carried out.

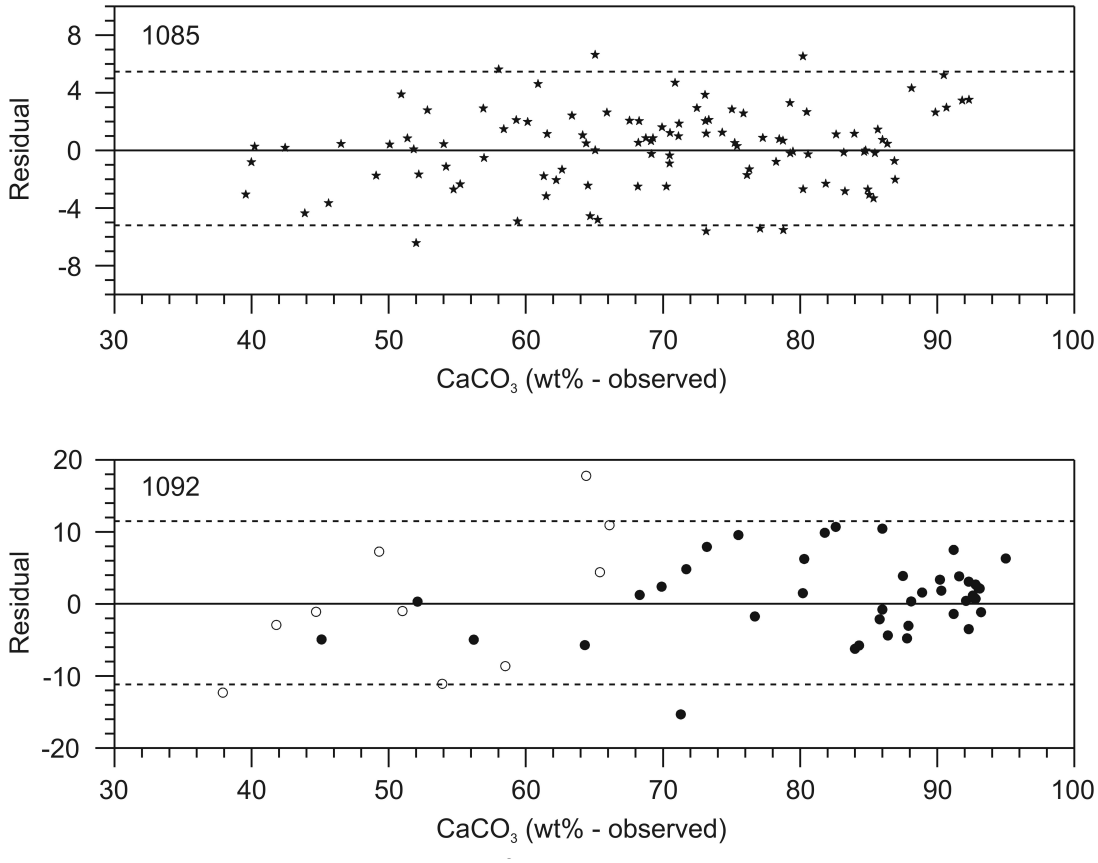

Figure 1.9 Residuals of percent $CaCO_3$ regressions (observed percent $CaCO_3$ minus predicted percent $CaCO_3$) versus observed $CaCO_3$. Dashed lines mark the 95% prediction limit. Site 1085 is represented in the upper plot (stars); observed $CaCO_3$ data are from Twitchell et al. (2002) and predicted data are from Westerhold et al. subm.a. Site 1092 is represented in the lower plot (circles); observed $CaCO_3$ data are from Diekmann et al. (2003) and predicted data are from Westerhold and Bickert in prep. The open circles at the Site 1092 plot represent samples with opal content higher than 5wt%.

1.3.2 Stable oxygen isotopes ($\delta^{18}O$)

About 8-10 cm³ bulk sediments were freez-dried, weighed, washed over a 63-µm mesh sieve and dried in an oven at 50°C. Benthic foraminifers were picked from the >250 µm size fraction. For isotope analysis, the epibenthic species *Cibicidoides wuellerstorfi* and *C. kullenbergii* were picked. Benthic stable oxygen isotope measurements were performed on a Finnigan MAT 252 mass spectrometer equipped with an automated carbonate preparation line at the University Bremen. The carbonate was reacted with orthophosphoric acid at 75°C. All data are reported against the VPDB standard after calibration via the standard NIST 19. Oxygen isotope results are expressed with the standard δ notation (McKinney et al. 1950):

$$\delta^{18}O_{sample} = \frac{(^{18}O/^{16}O)_{Sample} - (^{18}O/^{16}O)_{Standard}}{(^{18}O/^{16}O)_{Standard}} \times 1000$$

1.3.3 ICP-OES analysis

To obtain absolute concentrations the XRF elemental intensity data are calibrated with data from standard chemical analyses from discrete samples as described in Jansen et al. (1998). Total digestion analyses of discrete sediment samples were carried out in a pressure digestion system after filling 50 mg of dried bulk sediment material and a mixture of 3-ml HNO_3 (65%), 2-ml HF (40%), and 2-ml HCl (32%) into PTFE liners. After decomposition under pressure with help of a microwave, the samples were heated to dryness, redissolved in 0.5-ml HNO_3 (65%) and 4.5-ml double-deionized water (MilliQ), and homogenized in a microwave. Thereafter the volume of the solutions was made up to 50 ml. Mg, Al, K, Ca, Ti, Mn, Fe, Sr and Ba analyzed by inductively coupled plasma-optical emission spectrometry (ICP-OES, "Optima 3300 R" PERKIN ELMER). Precision was better than 2%. The accuracy of element determinations was checked using standard reference material USGS MAG-1. For further information about the method see Zabel et al. (2001).

1.3.4 Time Series analysis

The high-resolution stratigraphy at ODP Site 1085 was obtained by orbital tuning. This method is based on the assumption that changes in sedimentary sequences are linked to changes in solar insolation caused by secular variations in earth's orbit. The most important orbital parameters are eccentricity, obliquity and precession. The eccentricity cycle concerns variations in the shape of the earth's orbit around the sun, from nearly circular to distinctly elliptical. The three main periods of eccentricity are 95, 125 and 400 ky. The gradual changes in the angle of the earth's rotational axis relative to the perpendicular plane of the earth's orbit range from 22.5 to 24.5 degrees with a dominant period of 41 ky. The precession cycle refers to the change in the direction in which the earth's rotational axis tilts when it is closest to the sun (perihelion). Its main periods are 23 and 19 ky. For this study, the calculated values of eccentricity, obliquity and precession were taken out of the astronomical solution of Laskar et al. (1993) and Laskar (per. comm. 2003). The data were normalized and summed in an orbital record referred to as ETP (Imbrie et al. 1989). Orbital tuning and spectral analysis were performed with the software package *AnalySeries 1.2* (Paillard et al. 1996). For spectral and cross-spectral analysis the algorithm of Blackman and Tuckey (1958) has been used.

Miocene evolution of carbonate sedimentation in the eastern South Atlantic: High-resolution XRF-scanning records of ODP Sites 1085 and 1087

Thomas Westerhold, Torsten Bickert, Ursula Röhl

Fachbereich Geowissenschaften, Universität Bremen, 28334 Bremen, Germany

submitted to *Marine Geology*

Abstract

In the eastern South Atlantic Ocean the most profound changes in Neogene calcium carbonate deposition occurred in the middle to late Miocene (12 - 9 Ma), when carbonate mass accumulation rates abruptly dropped repeatedly. Similar occurrences of carbonate dissolution have been recorded in the central and eastern Pacific as well as in the Caribbean Sea. This interval has been referred to as the 'carbonate crash' (Lyle et al. 1995) and was interpreted as a dramatic shoaling of the lysocline due to a reorganization of deep-water circulation by the closure of the Central American Seaway.

Here, we document the changing pattern of carbonate and terrigenous deposition from 14 - 6.5 Ma using high-resolution XRF core-scanning measurements (Ca, Fe) performed every 4 cm downcore. We focus on ODP Leg 175 Site 1085 (29°22.47´S, 13°59.41´E, 1713 mbsl) and 1087 (31°27.91´S, 15°18.65´E, 1372 mbsl) sediments retrieved south of the Namibia upwelling area. The composite Fe record was used to construct an astronomically calibrated chronology based on orbital tuning. The derived age model documents high sedimentation rates during intervals of enhanced carbonate sedimentation associated with high terrigenous input from the African continent, delivered by the Orange River.

The high-resolution records demonstrate that the interval across the middle to late Miocene transition is characterized by at least six carbonate crash events. Our findings show that the South Atlantic carbonate crash events I through VI are caused by dilution due to enhanced terrigenous input linked to sea level lowering and by dissolution due to enhanced inflow of corrosive SCW during Miocene glacial events. The most pronounced carbonate crash event VI from 9.6 - 9 Ma seems to be linked to an overall increase in nutrient flux into the world's oceans and therefore the development of poorly ventilated intermediate to deep waters or at least an expansion of the oxygen minimum zone at the continental slope at Sites 1085 and 1087. A distinct 41-ky cyclicity of Fe and Ca within the crash interval is followed by a 100-ky period dominance afterwards. The timing of the carbonate crash events and the periodicity of the sedimentary records are discussed in terms of global sea-level fluctuations, oceanic changes, and paleoproductivity.

2.1 Introduction

Enormous reductions in carbonate content, low carbonate accumulation rates and poor preservation of calcareous microfossils characterize pelagic sediments at the transition from middle to late Miocene. At DSDP-Site 310 on Hess Rise (North-Central Pacific) Vincent (1981) registered abnormal low carbonate content and referred to it as the 'Mid Epoch 10 Event', first discovered in DSDP Site 158 by van Andel (1975). This event is placed between 9.6 and 9.2 Ma after the geomagnetic timescale of Cande and Kent (1995). Similar events have been described by Lyle et al. (1995) in several sediment sequences in the equatorial East-Pacific and referred to as the 'carbonate crash'. Further reduction events have been discovered in other oceanic regions, as in the equatorial Atlantic (King et al. 1997) and in the Caribbean Sea (Roth et al. 2000).

Until today, little is known about the global variations in the carbonate sedimentation pattern during the transition from middle to late Miocene. Lyle et al. (1995) attributed the carbonate crash observed in the eastern Equatorial Pacific sediment sequences to the emergence of the Central American Seaway (CAS). While the CAS was still in a deep position, they calculated that a restriction of 2 Sv of carbonate-rich deep water entering the Pacific from the Atlantic would account for the observed lower carbonate accumulation rates west of the CAS. Ocean circulation experiments by Nisancioglu et al. (2003) reveal that the shoaling of the CAS could have caused dramatic changes to the intermediate and deep-water circulation in the tropical Pacific, the South Pacific and South Atlantic. Sensitivity experiments performed by Heinze and Crowley (1997) using a coupled ocean circulation, carbon cycle and sediment chemistry model revealed a weaker North Atlantic thermohaline cell due to the free exchange of low salinity water between the Atlantic and Pacific. Roth et al. (2000) explained the occurrence of the Caribbean carbonate crash events by a global reorganization of the thermohaline circulation triggered by the opening of seaways along the northern Nicaraguan Rise at the middle to late Miocene transition. Re-establishment of NADW production at this time would have caused an augmented flow of NADW to the circum-Antarctic region, increasing the formation of intermediate water. This corrosive intermediate water entered the Caribbean basins and ultimately resulted in a strong dissolution of calcareous sediments, analogue to the late Quaternary glacial to interglacial perturbations.

King et al. (1997) created synthetic records of the carbonate content for the interval from 14 - 5 Ma of sites recovered from the Ceara Rise in the western tropical Atlantic during ODP Leg 154. Their results show an overall shoaling of the lysocline from 14 - 11.5

Ma, an interval partially predating the Caribbean carbonate crash events, but contemporaneous with the carbonate crash precursor events observed at Sites 999 and 1000, followed by lysocline deepening at 10.5 Ma.

The comparable nature, especially the rapidness of the crash events in the Pacific, Atlantic and Caribbean has been subject to discussion mainly focusing on changes in ocean circulation. None of these models yet explains the different timing of the carbonate reduction events in distinct regions and water depths. Evidently, the most pronounced reductions in the Caribbean Site 998 occur between 12.3 and 10.7 Ma, whereas in the eastern Pacific Site 846 reductions in carbonate content occur between 10.5 and 9.0 Ma, with a late event at 7.5 Ma. A congruent variability of shallow water sites and deep Atlantic sites in the carbonate records might contradict the assumed gradients between intermediate and deepwater masses.

One aim of ODP Leg 175 was to reconstruct the late Neogene history of the Benguela Current and the associated upwelling regimes (Wefer, Berger, Richter, et al. 1998). Sites 1085 and 1087, presented here, are located in the southern part of the Cape Basin (Figure 2.1) and proposed to provide an opportunity to reconstruct the history of deep ocean chemistry, carbonate sedimentation, and terrigenous fluxes from Southwest Africa in the middle to late Miocene. Their close position to the continent should be most useful in detecting upwelling signals, clues to changes in continental climate and sea-level. In this paper we present a detailed chronology for the transition from middle to late Miocene based on high-resolution XRF-core logs (Ca, Fe) for Sites 1085A and 1087C. These high-resolution, non-destructive proxy data were used to reconstruct carbonate and non-carbonate fluxes. We present evidence of carbonate crash events during the middle to late Miocene transition in the South Atlantic in shallow water depths. The very high resolution XRF records give way for addressing critical questions of the middle to late Miocene transition in terms of carbonate sedimentation pattern and abrupt climate changes as well as clues to the climatic conditions on the African continent. We focus on the questions:

- What is the exact timing of carbonate crash events in different oceans?
- What is the relationship to the late Neogene evolution of global ocean circulation and African climate?

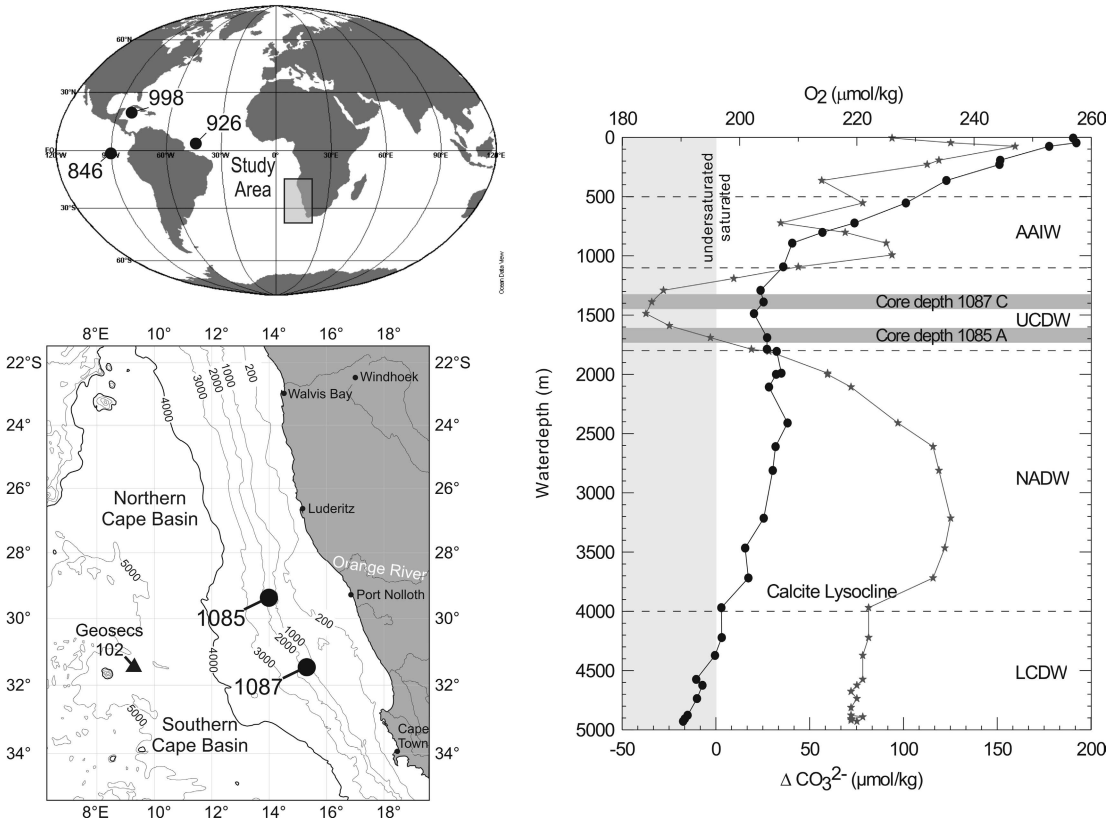

Figure 2.1 Location map showing the position of ODP-Sites 846, 926, 998, 1085, 1087 and Geosecs station 102. On the right ΔCO_3^{2-} and oxygen depth profile of Geosecs station 102, which represent best the water conditions at Sites 1085 and 1087.

2.2 Area description, methods and material studied

2.2.1 Location of Sites

ODP Holes 1085A and 1087C were drilled in the Cape Basin during Leg 175. Site 1085 is located at the southwestern African continental margin (29°22.47´S, 13°59.41´E, 1713 m water depth) off the Orange River, a perennial river discharging into the South Atlantic (Wefer, Berger, Richter, et al. 1998), whose sediment load is moved primarily south by the prevailing bottom currents (Rogers and Bremner 1991). Hole 1085A was drilled down to the middle Miocene. The studied interval (350 - 600 mbsf) spanning from the middle to the late Miocene has no composite section, but shows a mean recovery of over 100% with an average sedimentation rate of 3 - 5 cm/ky (Wefer, Berger, Richter, et al. 1998). Sediments are dominated by nannofossil ooze, dilutes by various amounts of silt and clay.

Site 1087 is located further south at the continental margin (31°27.91´S, 15°18.65´E, 1372 m water depth). Sediments recovered from Site 1087 represent a relatively continuous pelagic section, rich in carbonate and poor in organic carbon (Wefer, Berger, Richter, et al. 1998), down to 430 mbsf spanning the last 10 Ma with sedimentation rates

ranging from 2 - 7 cm/ky. The bottom 70 m contains middle Miocene to early Oligocene sediment layers interrupted by at least two major discontinuities. Due to its close position to Site 1085 the comparison of both sites enables to distinguish and evaluate the driving force of sedimentation with respect to the changing boundary conditions in the middle to late Miocene transition in the Cape Basin. Differentiation between local from global signals give way to a better understanding of the changing ocean circulation.

2.2.2 X-ray fluorescence analysis

Continuous measurements of the elemental composition of sediments at ODP Sites 1085A and 1087C were performed using the X-ray fluorescence (XRF) core scanner (Röhl and Abrams 2000) at the Bremen ODP Core Repository (BCR), which allows high-resolution, nearly continuous, non-destructive analyses of major and minor elements at the surface of split cores (Jansen et al. 1998). The XRF core scanner at the BCR is equipped with a molybdenum X-ray source (3-50kV), a Peltier-cooled PSI detector (Kevex™) with a 125 µm beryllium window and a multi channel analyzer with a 20 eV spectral resolution. This system configuration allows the analysis of elements from potassium (K, atomic number 19) through strontium (Sr, atomic number 38; at 20 kV X-ray voltage).

XRF data were collected every 4 cm downcore over a 1 cm^2 area using 30 seconds count time and an X-ray current of 0.087 mA to obtain the elemental concentration of K, Ca, Ti, Mn, Fe, Cu and Sr. In this paper we present Ca and Fe intensity data, which are highly correlated to the physical and chemical properties measured both downhole and at split cores. More than 240 m of core from Site 1085A (42X through 63X, 382-594 mbsf) were analyzed, representing the time period from about 6.5 - 13.9 Ma, whereas the data from 353.4-392.45 mbsf (39X through 41X) are taken from Vidal et al. (2002). From Site 1087C about 144 m (30X through 44X, 261-405 mbsf) were scanned spanning the time from 6.5-10.2 Ma. Based upon the biostratigraphic age model the step size of 4 cm represents a temporal resolution of 1000 to 2500 years.

2.2.3 Bulk solid phase analysis

Element concentrations were obtained by calibration of the XRF element intensities with data from standard chemical analyses from discrete samples as described in Jansen et al. (1998). Total digestion preparation of 58 discrete sediment samples (Table 2.1) were carried out according to Zabel et al. (2001) and analyzed by inductively coupled plasma-optical emission spectrometry (ICP-OES, “Optima 3300 R” Perkin Elmer). Precision was

better than 2%. The accuracy of element determinations was checked using standard reference material USGS MAG-1. The attained calibration formula, determined by linear regression, gives the concentration of each element in the core in wt%. Assuming that all Ca^{2+} is bound to CO^{3-}, we converted Ca intensities to $CaCO_3$% by multiplying Ca wt% by 2.5.

2.2.4 Mass Accumulation Rate (MAR) determination

For the quantification of the carbonate and iron input, independent of dilution by terrigenous and other biogenic sediment compounds over time, the weight proportion of the individual elements have been converted into accumulation rates (van Andel et al. 1975):

$$MAR_{bulk} = DBD * Sedimentationrate \quad (1)$$

Component MAR is calculated according to the equation:

$$MAR_{component} = MAR * (wt\% \text{ component} / 100) \quad (2)$$

The dry bulk density (DBD) was determined by the equation of Ruddiman and Janecek (1989) with the help of grain density and porosity of the sediment. The porosity was determined via GRAPE data, measured aboard on the closed cores after the formular of Boyce (1976):

$$\phi = \frac{\rho_{gc} - \rho_{bc}}{\rho_{gc} - \rho_{fc}} \quad (3)$$

whereby ϕ is the porosity (volume pore space/ volume wet-saturated sediment), ρ_{gc} is the grain density [2,67 g/cm³], ρ_{bc} is the wet bulk density derived from GRAPE-Data [g/cm³] and ρ_{fc} is the fluid density [1,025 g/cm³].

All data and tables are available at PANGAEA – Network for Geological and Environmental Data (www.pangaea.de).

2.3 Results of XRF core logging and calibration

In Figure 2.2 Ca and Fe intensities derived from the XRF core logs of hole 1085A and 1087C, respectively, are plotted versus depth (mbsf) (Table 2.2 and 2.3). Ca intensities vary between 2000 and 9000 cps. Fe intensities vary between 500 and 6000 cps showing an inverse relationship to Ca intensities. This high resolution records demonstrate that the interval across the middle to late Miocene transition in the eastern South Atlantic is characterized by at least six abrupt events in the Ca and Fe record of ODP Site 1085, characterized each by a dramatic drop in carbonate content, a continuous period of low carbonate accumulation, and a gradual increase towards normal levels of carbonate deposition. In hole 1085A the incidents of minimum Ca intensities occur at 565-570 (I), 556-561 (II), 547-553 (III), 528-537 (IV), 470-481 (V) and 433-453 (VI) mbsf.

At hole 1087C Ca intensities vary between 5000 and 14000 cps, whereas Fe intensities vary between 500 and 2500 cps. One period of low Ca intensities can be observed from 351 - 370 mbsf, matching the carbonate crash event VI of Site 1085 to a large extent. There is no further drop in Ca content, but a pronounced peak in Fe content at 392 - 395 mbsf. The XRF intensity record of Site 1087 reaches down to 405 mbsf below which a hiatus is located.

For both Sites the Ca and Fe record are used as proxies for carbonate and terrigenous sedimentation, respectively. In general the Ca signals in hole 1085A and 1087C are much noisier than the Fe signals due to the increasing scatter in the Ca data with increasing $CaCO_3$ concentrations. Jansen et al. (1998) attribute the scatter, which rises notably at $CaCO_3$ concentrations over 75 - 85%, to the inhomogeneity and the rough, sandpaper-like surface of carbonate oozes. To account for this effect we followed the approach of Jansen et al. (1998) normalizing the Ca intensities to the 7 elements measured by XRF analysis. The results of the bulk solid phase analysis are listed in Table 2.1. Linear regression of these data plotted versus the XRF data (Figure 2.3) resulted in the following formula, which have been used to calculate $CaCO_3$ and Fe wt%:

For Site 1085: $CaCO_3$ wt% = Ca (% of 7 Elements) / 1.07577 (4)

Fe wt% = Fe (cps) / 1199.79344 (5)

For Site 1087 $CaCO_3$ wt% = Ca (% of 7 Elements) / 1.08281 (6)

Fe wt% = Fe (cps) / 1112.46888 (7)

Deduced from the coefficient of determination (r^2) the linear regression for Site 1085 can explain 97.77% and 96.69% of the variance in $CaCO_3$ and Fe content, respectively. For Site 1087 the linear regression can explain 95.33% and 91.70% of the variance in $CaCO_3$

and Fe content, respectively. These high values for the coefficient of determination suggest that the XRF measurements give reliable estimates of $CaCO_3$ and Fe content of the sediment cores.

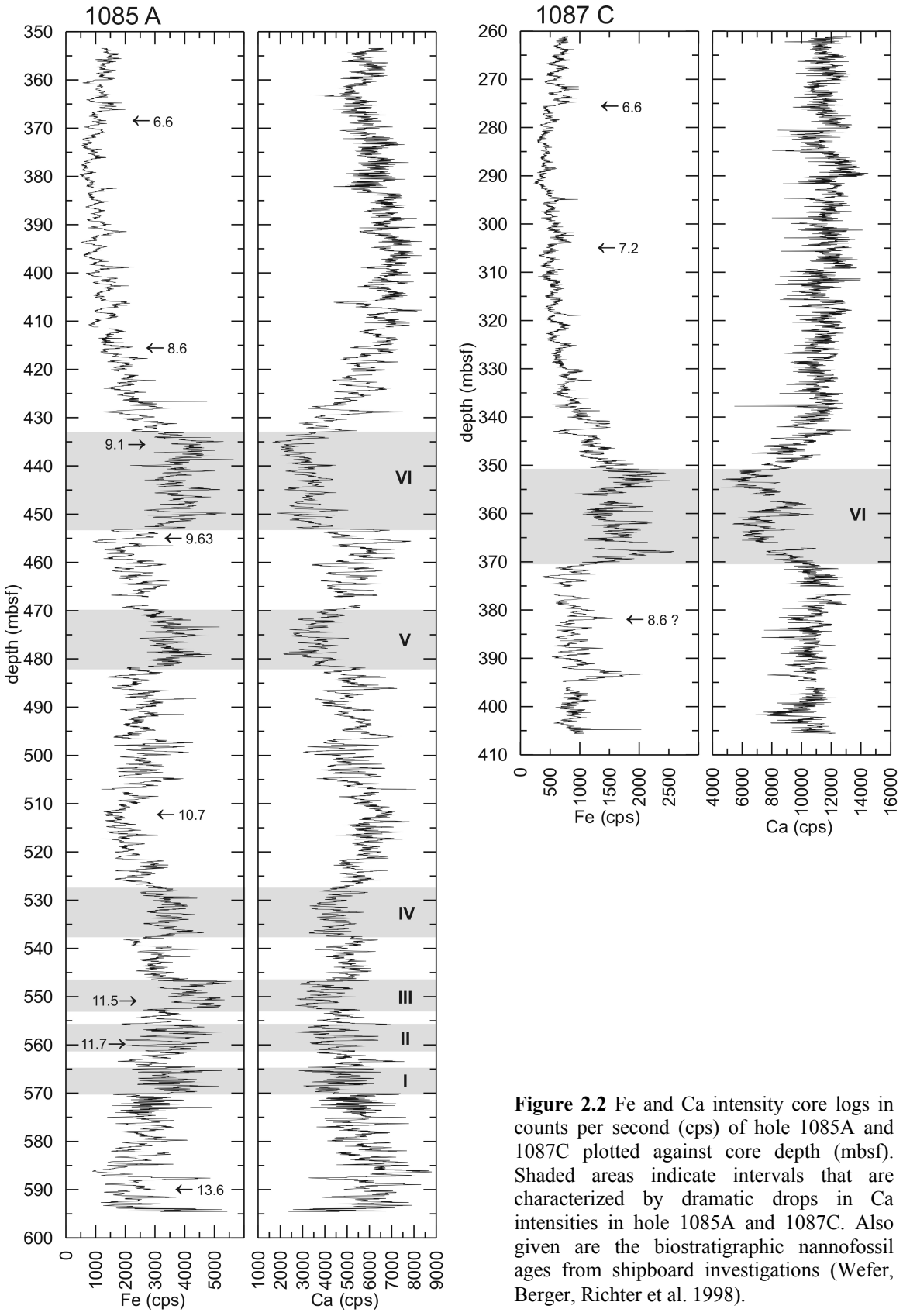

Figure 2.2 Fe and Ca intensity core logs in counts per second (cps) of hole 1085A and 1087C plotted against core depth (mbsf). Shaded areas indicate intervals that are characterized by dramatic drops in Ca intensities in hole 1085A and 1087C. Also given are the biostratigraphic nannofossil ages from shipboard investigations (Wefer, Berger, Richter et al. 1998).

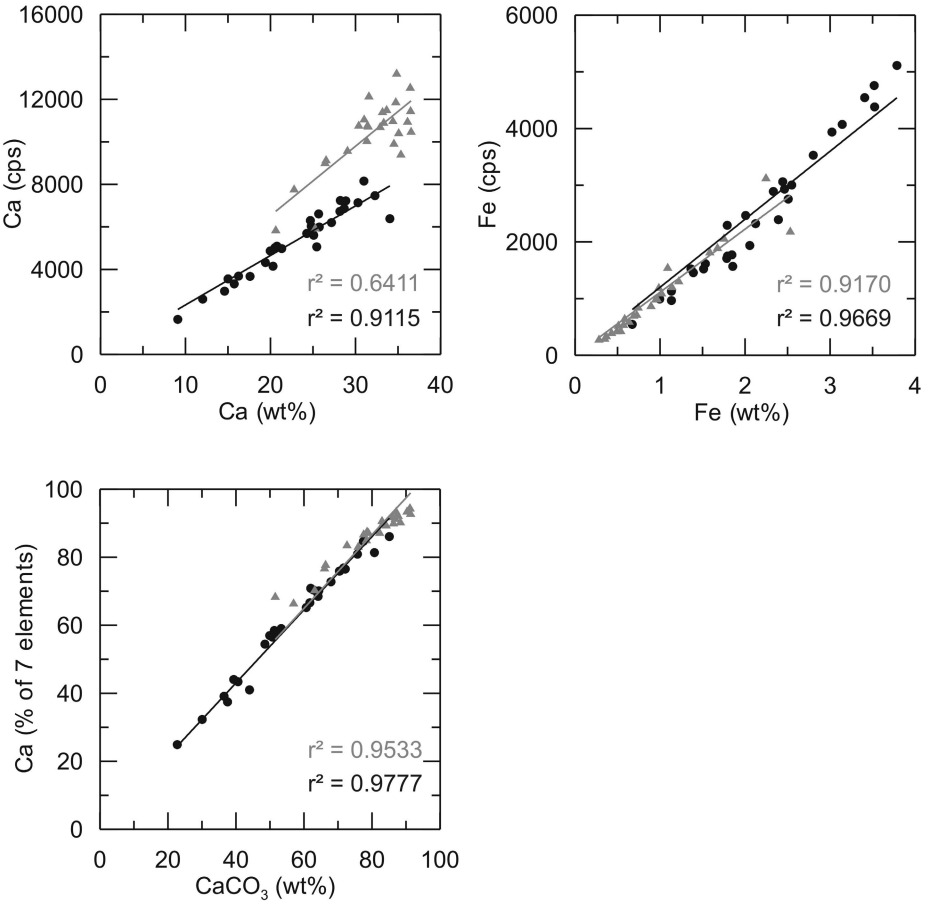

Figure 2.3 Calibration of the XRF-scanner Ca and Fe measurements of hole 1085A (black dots) and 1087C (gray triangles) to ICP-OES analysis of samples taken from the same depth intervals (two upper panels). After removal of outliers, 29 for Site 1085 and 26 ICP-OES samples for Site 1087 were used for calibration. The lower panel on the left shows the linear regression of measured $CaCO_3$ and Ca intensities normalized to the seven elements measured by the XRF-scanner as proposed by Jansen et al. (1998) to account for the grain size effect. In each panel the coefficient of determination is given.

2.4 Chronostratigraphy

2.4.1 Composite section

At Sites 1085 and 1087 a composite depth scale was established only for the upper 300 and 200 m, respectively, based on splicing together the susceptibility records of multiple holes at these sites (Wefer, Berger, Richter, et al. 1998). Below, single hole drilling prevented continuous splicing. Due to the similarity of the Fe-records we established a composite record by correlating holes 1085A and 1087C. Using Fe-intensities of the XRF measurements as the primary hole-to-hole correlation tool, each core at Sites 1085A and 1087C were then individually correlated to the corresponding downhole logging interval of the Total Gamma Ray (SGR) measurements gained by the Natural Gamma Tool (NGT) string in Hole 1085A (Figure 2.4). This procedure provides the opportunity to create a spliced Fe record of 1085A independent from drilling disturbances (e.g., Hagelberg et al. 1992). The NGT measures the spectrum of natural gamma ray

radiation of a formation resolving the spectrum into the three most common compounds of the naturally occurring radiation: potassium, thorium and uranium. Potassium and thorium are the primary radioactive elements present in clays, whereas thorium is frequently found in ash layers. Therefore, it is assumed that higher portion of terrestrial material in the sediment will be reflected by higher SGR values, and thus consequently correlate with high intensities in the Fe record of Sites 1085A and 1087C. Regardless of the absolute depth value, relative thickness and spacing of features displayed on SGR and other downhole measurements should be identical within the limits of varying vertical resolution capabilities. Figure 2.4 shows the correlation with reference to the SGR logging depth of Site 1085A, which is referred to as the revised meters composite depth (rmcd) hereafter.

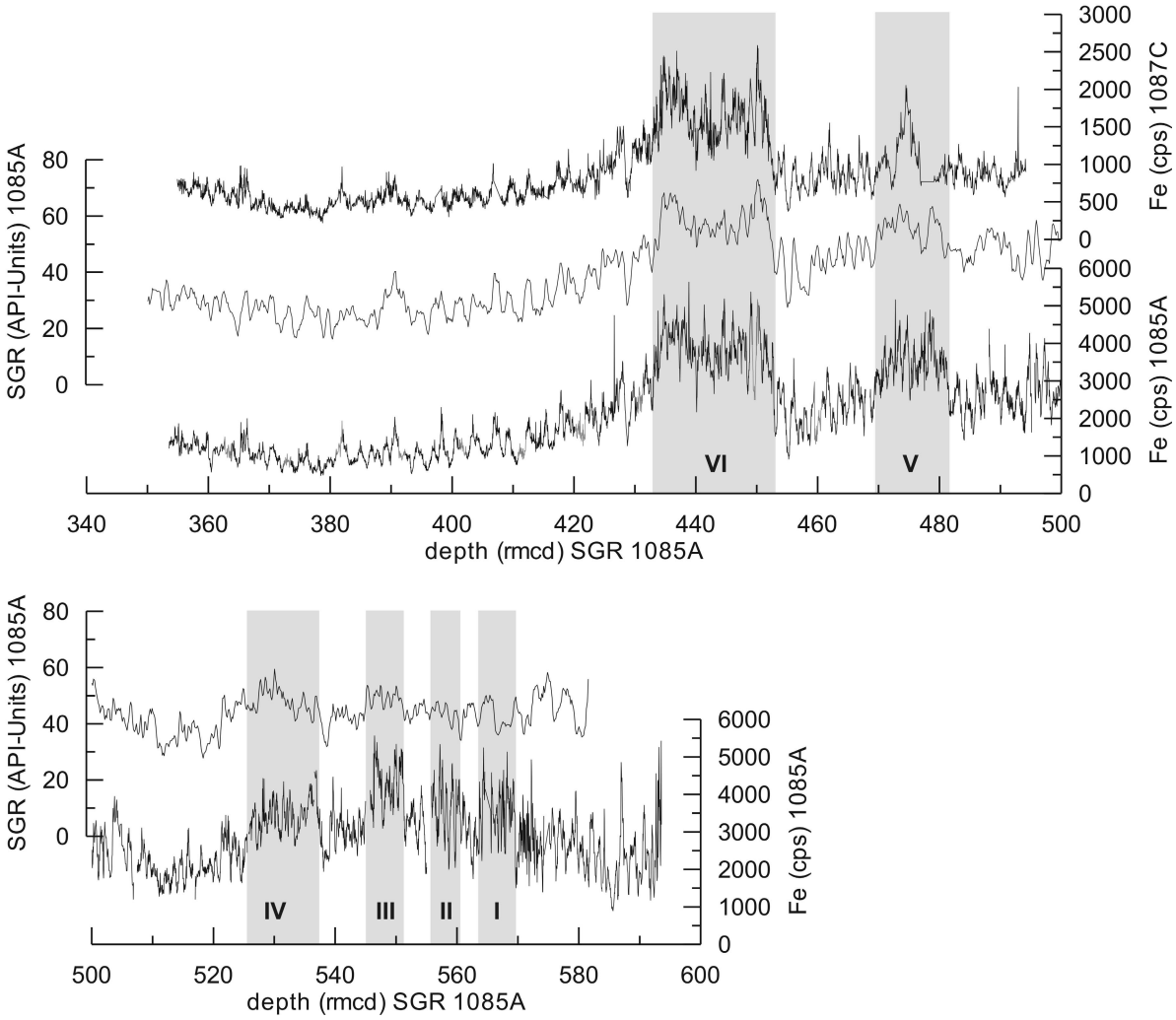

Figure 2.4 Composite section for hole 1085A and 1087C. The Fe intensities are plotted for holes 1085A and 1087C. These two logs are correlated to the SGR-log depth of the Gamma Ray Spectrometry - Dual Induction Tool String (NGT-DIT) of hole 1085A. For the creation of a composite Fe-intensity record the gaps in 1085A are filled with data from the Fe-log of 1087C. Below 555 rmcd the record of 1085A can not be tuned to the SGR-log. For discussion see text.

The tie points to create the new composite depth for the Fe intensity record of Site 1085A and 1087C based on the SGR logging depth of the NGT tool are listed in Table 2.4 and 2.5. Completing the correlation, gaps between each core in Site 1085A were filled with the appropriate Fe intensity data from Site 1087C to create a composite Fe intensity record for Site 1085. The tie points are given in Table 2.6. Due to the lower Fe concentration in 1087C the intensity data have been adjusted to the intensity level of 1085A by multiplying an arbitrary factor taking care not to alter the original variation signal. The spliced Fe intensity data were then used for orbital tuning without smoothing or stacking of data.

The generation of a complete composite record for Site 1085 has been obtained from 353.60 down to 460.83 rmcd. Due to the slump deposition in Site 1087C below 409 mbsf, the composite record for Site 1085 was extended from 460.85 down to 555.04 rmcd by correlation to the SGR log revealing the size of core break gaps. From 555.82 down to 593.57 rmcd sections were adjusted to mcd scale, considering that mcd values exceed mbsf values by about 10% at Site 1085A as observed by Wefer, Berger, Richter, et al. (1998). To account for this extension, each core in this part of the record was compressed by 10 %.

2.4.2 Orbital Tuning

Shipboard data of the biostratigraphic datums and the paleomagnetic events provided the preliminary age model for Site 1085 (Wefer, Berger, Richter, et al. 1998). Because of coring-induced magnetization (CIM) the magnetostratigraphic interpretation at Site 1085A was only possible down to the bottom of Chron C3n.4n at 5.23 Ma in 280 mbsf depth (Wefer, Berger, Richter, et al. 1998) precluding a magnetostratigraphic supported age model for the middle to late Miocene. Therefore, the stratigraphic framework needed for orbital tuning is based on the biostratigraphy established during Leg 175 using the integrated time scale of Berggren et al. (1995a, 1995b). We chose calcareous nannofossil datums only, because they have been shown to give more reliable datums than those derived from foraminifera (e.g., Backman and Raffi 1997). Regarding the fact that the determined ages are based on core-catcher samples a maximum error of at least 200 ky has to be taken into consideration. The visual correlation of Site 1085 with 1087 and the comparison of their biostratigraphic ages (Figure 2.2) result in a discrepancy in the position of the first occurrence of *Discoaster quinqueramus* (8.6 Ma). Additional investigations on smear slide samples confirmed the proposed position for LO *Discoaster hamatus* and FO *Discoaster quinqueramus* at Site 1085A, whereas the biostratigraphy at 1087C appears to be problematic (Cepek, pers. comm.). Thus, the biostratigraphic framework of Site 1085A

is robust and suitable for further investigations. Due to the excellent fit of the Fe intensities between Site 1085 and 1087 we assigned the tuned ages from Site 1085 to Site 1087.

As shown by Christensen and Maslin (2001) and Vidal et al. (2002) eccentricity modulates the signals derived from terrigenous material (magnetic susceptibility, XRF Fe record) in the Cape Basin. Maxima in eccentricity correspond to maxima in the terrigenous signal. Therefore we first examined the cyclic fluctuations of the Fe intensity record by using the preliminary age model from biostratigraphy with the help of the *AnalySeries* software package (Paillard et al. 1996). Frequency spectra of the Fe record revealed that much of the spectral power is concentrated in the low-frequency domain (Figure 2.5). Peaks are observed close to 400-ky and 100-ky. Spectral analysis of the data in the depth domain confirmed, that the main components of the Fe signal are associated with the 400-ky and 100-ky cycles. Comparing the biostratigraphic dated Fe record to the target curve, a 400-ky and a 100-ky peak is apparent, although the power spectrum is shifted according to that of the ETP target. There is little variance at periods <100 ky. Furthermore, the work of Vidal et al. (2002) and Westerhold et al. (subm. b) proof, that light $\delta^{18}O$ values of benthic foraminifers are associated with maxima in the Fe intensities. Consequently high Fe intensities can be contributed to interglacial periods that are characterized by high eccentricity and/or maxima in obliquity.

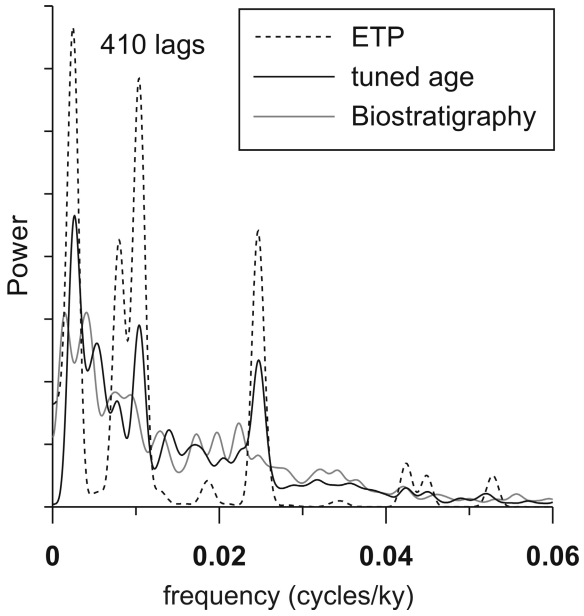

Figure 2.5 Blackman-Tuckey power spectrum of the ETP target curve, biostratigraphic age model and the tuned composite Fe intensity age model computed with the *AnalySeries* software package (Paillard et al. 1996). Prior to spectral analysis Fe intensity data have been high pass filtered at 0.002 Hz to remove variations above 500-ky, low pass filtered at 0.075 Hz to remove noise below 10-ky period, normalized to unite variance and padded with zeros. Spectral estimates are based on a Parzen smoothing window with 410 lags and an interpolated time interval of 2 ky resulting in a bandwidth of 0.002261, whereas the confidence interval at 80% is given by $0.765165 < DP/P < 1.396291$.

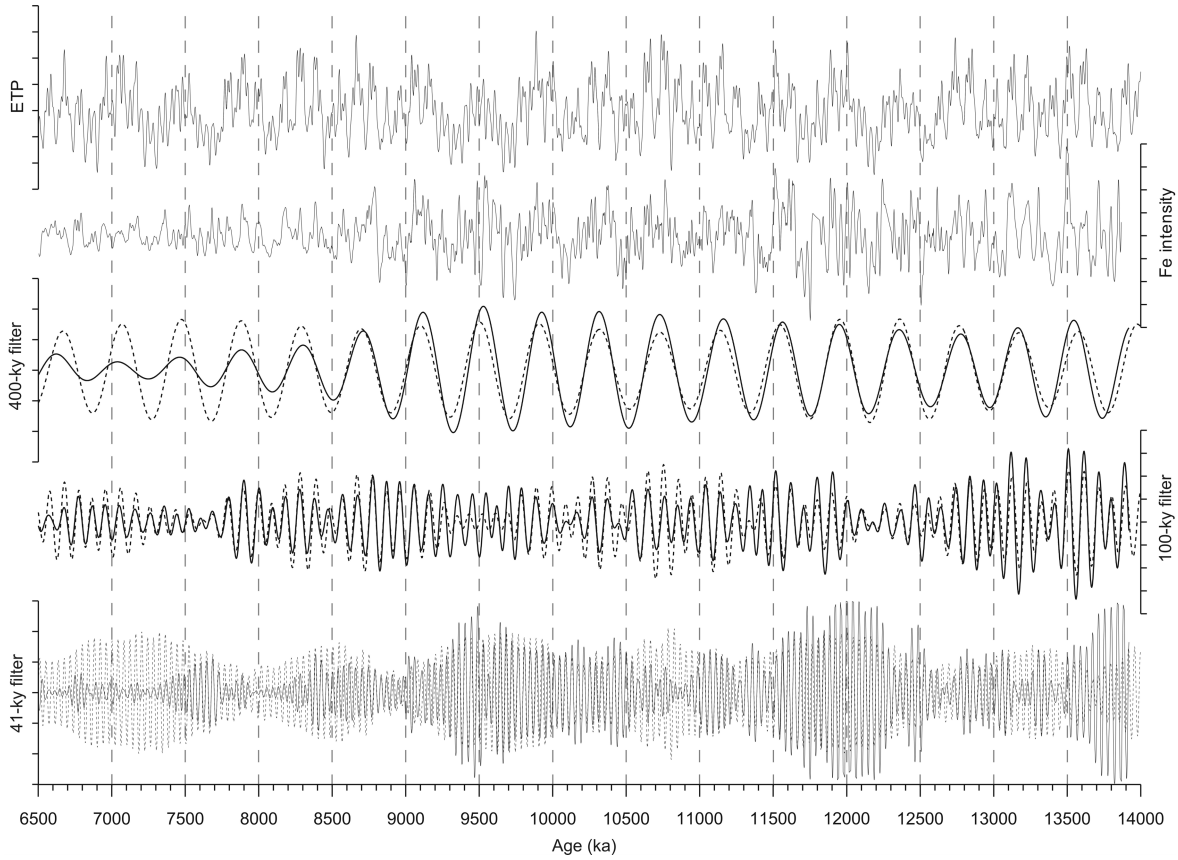

Figure 2.6 In the upper two panels the ETP target curve and the composite Fe intensity signal, which has been smoothed by a 5-point weighted average and variations of 500-ky have been removed, are plotted vs. age. The lower three panels show the filtered Fe intensity (black) vs. ETP (dashed) at the 400-ky-band (upper panel), the 100-ky-band (middle panel) and the 41-ky-band (lower panel). For comparison all data have been normalized to unite variance.

Therefore, an astronomically calibrated age model for the Miocene section of ODP Site 1085 and 1087 was constructed by tuning the composite XRF-Fe intensity record to an Eccentricity-Tilt-Precession (ETP) target curve. We assumed no lag between the tuning target and the lithologic signal. In the absence of an identified mechanism for generating a lag during the Miocene in the region we are dealing with, we consider that our record should be assumed to have responded without delay. The ETP curve was generated by normalizing Eccentricity (Laskar pers, comm. 2003), Obliquity (Tilt) and Precession (Laskar et al. 1993) values and then combining it by the following expression:

$$E + 0.5*T - 0.5P \qquad (8)$$

Tuning was performed by correlating prominent features of the Fe record to the ETP target, whereas the record first was tuned in the 400-ky domain (0.0025 ± 0.0005 cycles/ka) and then in the 100-ky domain (0.01 ± 0.003 cycles/ka). A good match in amplitude variation is found between the astronomical forcing and the filtered outputs (Figure 2.6). The age model derived from orbital tuning is presented in Table 2.7. Spectral

analysis of the tuned Fe intensity signal reveals an excellent match with the spectrum of the target curve (Figure 2.5), including distinct spectral power in the obliquity band. The 400-ky, 100-ky and 41-ky filter of the Fe intensity (Figure 2.6) shows a remarkably similarity in the amplitudes to its orbital counterpart. During times of low amplitudes in the 100-ky filter the Fe record shows high amplitudes in the obliquity component. After 9 Ma the overall amplitude in the filtered outputs decrease and the obliquity component appears to be of minor importance in the Fe record. Generally, high obliquity and low eccentricity response occur during crash events. Crash event VI with a duration of 600 ky features high amplitudes in the obliquity band at the beginning, followed by increasing power of the eccentricity signal.

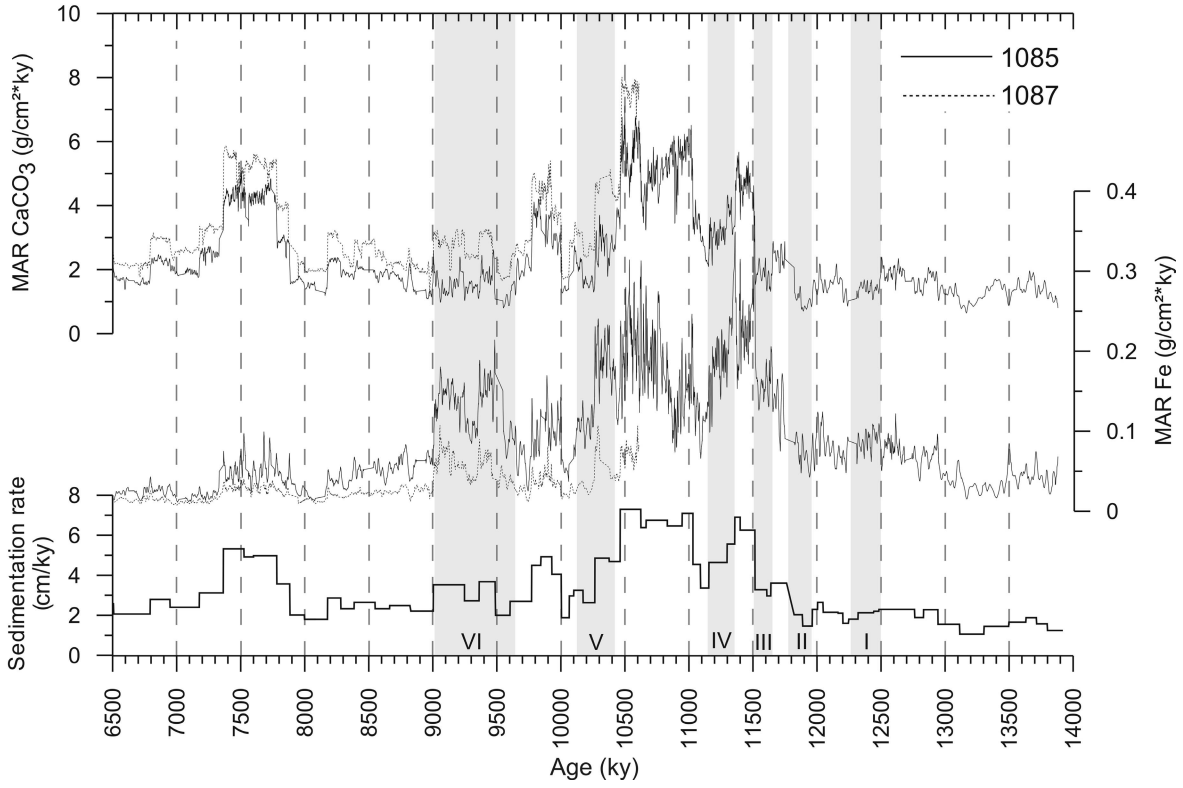

Figure 2.7 Carbonate and Fe mass accumulation rates and sedimentation rate for Site 1085 and 1087 obtained from the tuned Fe intensity record. Numbered gray columns mark the carbonate crash events.

The derived sedimentation rates (Figure 2.7) range between 1 and 7.3 cm/ky. From 14.0 up to 11.7 Ma the sedimentation rates are well below 4 cm/ky. Then they steadily increase to 7 cm/ky remaining at that value from 11.5 - 10.4 Ma, punctuated by a drop in sedimentation rates at 11.1 Ma. Thereafter rates decrease to an average value of 3 cm/ky till 6.5 Ma, interrupted by enhanced sedimentation rates at 9.9 Ma and around 7.6 Ma. Obviously, there is no relationship between sedimentation rate and crash events. The

calculated carbonate MAR (Figure 2.7) for Site 1085 from 14.0 up to 11.5 Ma are slowly increasing from 1 to 2 g/cm²*ky. From 11.7 - 10.4 Ma the carbonate MAR is well above 4 g/cm²*ky. After 10.4 Ma the carbonate MAR abruptly drops down to values below 3 g/cm²*ky and remain until 6.5 Ma at these values. At 9.9 and 7.6 Ma the carbonate MAR increases to values over 4 g/cm²*ky. At Site 1087 the carbonate MAR resembles those of Site 1085, exhibiting on average values 1 g/cm²*ky higher due to the lower input of terrigenous material (Figure 2.7). From 14 - 11.7 Ma the Fe MAR at Site 1085 varies around 0.1 g/cm²*ky. In the period from 11.7 to 10.2 Ma the Fe MAR is on the average at 0.2 g/cm²*ky with prominent lows at 11.1 and 10.9 Ma. After 10.2 Ma the Fe MAR decreases significantly down to 0.05 g/cm²*ky while at carbonate crash event VI the Fe MAR increases to about 0.2 g/cm²*ky.

2.5 Discussion

2.5.1 Global Significance of the Carbonate Crash Events

To answer the question to what extend the Neogene variations in the carbonate sedimentation pattern in the eastern South Atlantic mirror local effects (terrigenous input, productivity due to upwelling activity) or global phenomena (change in ocean circulation, extension of Antarctic ice-sheets, carbon budget), we first compare carbonate contents of Site 1085 with Site 846 from the eastern Equatorial Pacific (Lyle et al. 1995), Site 926 from the western Equatorial Atlantic (King et al. 1997) and Site 998 from the Caribbean Sea (Roth et al. 2000). These sites have been interpreted to show regional response to global changes during the middle to late Miocene transition. Afterwards we will discuss the local mechanisms of the carbonate crash events in the eastern South Atlantic.

In the eastern Equatorial Pacific $CaCO_3$ concentrations decline at 11.2 Ma in a series of steps (Figure 2.8) with minima centered at 10.8, 10.5, 9.7, 8.9 and 7.7 Ma. Stratigraphic correlation of Farrell et al. (1995) demonstrates that these events are evident in records from the central Equatorial Pacific, the western Equatorial Pacific and the northern Central Pacific. The most pronounced carbonate crash event around 9.7 Ma is referred to as the Nadir, dubbed Event 5 by Lyle et al. 1995 (Leg 138), Mid Epoch 10 event by Vincent 1981 (DSDP Site 158 and 310) and event 10e by Barron et al. (1985) (Leg 85). Lyle et al. (1995) assigned the carbonate crash events to an abrupt rise in CCD at 10 Ma due to reduced exchange of deep waters rich in $[CO_3]^{2-}$ between Atlantic and Pacific Ocean as a result of the emerging Central American Seaway (CAS). They proof that neither productivity nor changes in sea level produced the observed carbonate sedimentation patterns, whereas

observed differences in the CCD's found in the eastern Pacific basins are maintained by different levels of deep CO_2 storage from C_{org} degradation (Farrell et al. 1995). Comparison with Site 1085 reveals that only crash event 11 in the eastern Equatorial Pacific at 11.6 Ma coincides with a major low in carbonate concentration (Event III). After 11.6 Ma no Pacific carbonate crash event corresponds to carbonate minima in the eastern South Atlantic, but instead minima in carbonate preservation in the Pacific correspond to maxima in the eastern South Atlantic. As the preservation of carbonate decreases in the eastern Equatorial Pacific from 11.5 - 10 Ma a strong increase at 1085 can be observed. Furthermore between carbonate crash event V and VI $CaCO_3$ values at 1085 are high, coupled with enhanced carbonate MAR's, and correlate with the nadir of the Pacific carbonate crash period at 9.7 Ma. During the strong drawdown of $CaCO_3$ at 1085 from 9.6-9 Ma the preservation of $CaCO_3$ in the Pacific increases, pointing to a lowering of the CCD in the eastern Equatorial Pacific. After 9 Ma, $CaCO_3$ preservation in the eastern Equatorial Pacific sites is generally low due to rise in CCD (Lyle et al. 1995) and high in the eastern South Atlantic, whereas sedimentation rates are low in both oceanic regions. The most astonishing fact is that the opposite sedimentation pattern in the eastern Equatorial Pacific and the eastern South Atlantic began at exactly the same time as the oxygen depletion in eastern South Atlantic starts, at 11.3 Ma. This redistribution in carbonate sedimentation pattern is attributed to changes in ocean circulation and the evolving geochemical basin-to-basin fractionation due to the uplift of the CAS. Thus, the carbonate accumulation records of the eastern Equatorial Pacific and eastern South Atlantic document that the shoaling of the CAS may have caused dramatic changes to the intermediate and deep-water circulation in the tropical Pacific and South Atlantic as proposed by the model of Nisancioglu et al. (2003). Furthermore, Berger et al. (1993) propose that if NCW increase is responsible for simultaneous increase in both production and depth-dependent dissolution in western Pacific sites, than this should lead to a corresponding increase in carbonate saturation in the deep Atlantic to balance the deficit found in the deep Pacific. Increased carbonate content at Sites 1085 and 1087 since 9 Ma and high carbonate deposition rate since 10.5 Ma at the Ceara Rise (King et al. 1997) could be related to this basin-to-basin fractionation. Distinct carbonate dissolution events appear in the Caribbean Site 998 (12.4 - 10.0 Ma) and can be compared to the events I to V in 1085 (Figure 2.8). Admittedly the events in the Caribbean site are much more peculiar, whereas the carbonate content drops to 0% several times. In a similar period as in Site 998 less explicit reductions in carbonate content can be observed in the western Equatorial Atlantic Site 926. Roth et al. (2000)

attribute the simultaneous dissolution events in the deep Atlantic and Caribbean to the repeated re-initiation of a still weakly developed thermohaline circulation in the Atlantic. The observed higher amplitudes of the dissolution events in the Caribbean Site 998 can be attributed to the poor ventilation of the Caribbean basin. Roth et al. (2000) proposed, that with high production of NCW carbonate is dissolved in the Caribbean due to enhanced inflow of AAIW, whereas at times of reduced NCW production well oxygenated NAIW entered the Caribbean, hence preserving carbonate.

Cd/Ca differences measured on benthic foraminifers from the Atlantic and Pacific are reasonable indicators of deep-water circulation patterns as shown by Delaney (1990), with increasing contrast through the middle to late Miocene (Figure 2.8). These differences between the Pacific and Atlantic were virtually non-existent in the early Miocene and increased from middle to late Miocene, indicating the increasing importance of NCW sources (Delaney 1990). This is consistent with the ocean-wide patterns developed from carbon isotope syntheses by Woodruff and Savin (1989). From benthic $\delta^{13}C$ ratios of foraminifers they deduced that in the early Miocene the dominant flow of intermediate and deep water in the Atlantic was from south to north, the opposite of todays. Due to the closure of the Tethys the meridional heat transport to high southern latitudes probably increased in the middle Miocene, leading to growth of the Antarctic ice cap. During early to middle Miocene the deep-water circulation changed from a one-component-system dominated by SCW to a three-component-system consisting of SCW, NCW and Mediterranean Outflow Water (Wright et al. 1992). From 14.4 Ma to 11 Ma NCW formation was weak, and circumpolar and Antarctic water flooded the deep South Atlantic and South Pacific as the Antarctic ice cap grew. NCW formation became more intense at the nick of the middle Miocene, at approximately 11 Ma, (Wright and Miller 1996) and AABW in a form similar to today's began to flow into Atlantic and Pacific. King et al. (1997) proposed that the changing shallow- to deep-gradients in carbonate flux between 13.1 and 12.5 Ma at the Ceara Rise reflect the presence of two deep-water masses, a more corrosive SCW and a less corrosive NCW after 12.5 Ma. Unlike the interpretation of Wright et al. (1992), King et al. (1997) have evidence that more corrosive waters and overall lower $CaCO_3$ fluxes between 11.8 and 10.5 Ma are due to diminished NCW production. With increasing carbonate flux at 10.5 Ma an increased less corrosive NCW supply is proposed, enhancing the preservation of carbonates at the Ceara Rise. If we put these findings in context with our observations in the eastern South Atlantic, it is evident that NCW production rate had deep impact on carbonate preservation at the middle to late

Miocene transition. The onset of NADW is suggested to begin at 11.5 Ma coinciding with oxygen isotope event Mi5 and thus is contributed to climate cooling and/or ice volume increase (Wei and Peleo-Alampay 1997).

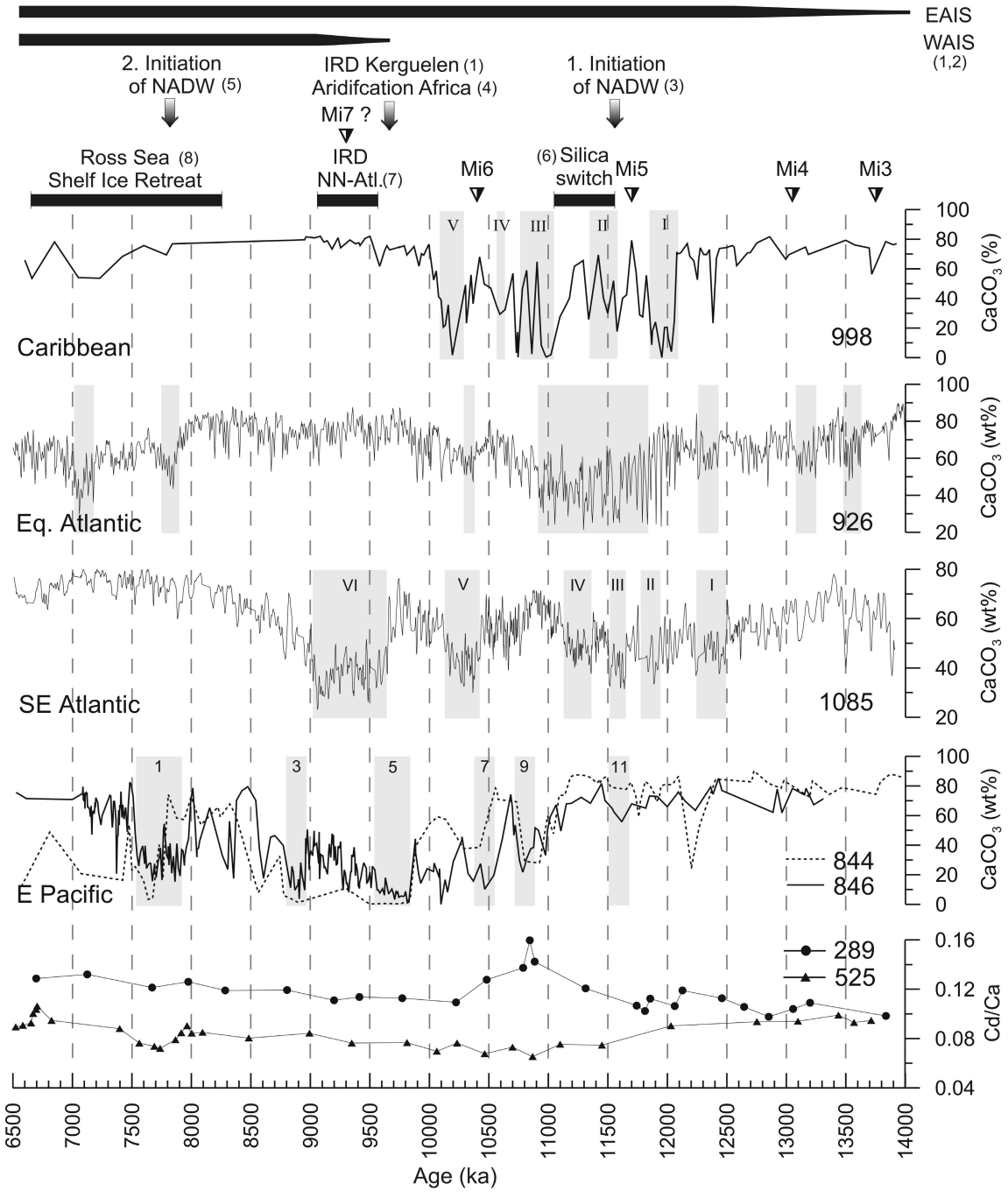

Figure 2.8 Variations of carbonate content values between 14 and 6.5 Ma in the Caribbean Sea (Site 998 - Roth et al. 2000), in the western Equatorial Atlantic (Site 926 - King et al. 1997), in the eastern South Atlantic (Site 1085, this study) and the eastern Equatorial Pacific (Site 846 and 844 - Lyle et al. 1995) with carbonate crash periods assigned by the above mentioned authors. The lower panel shows Cd/Ca data from Delaney (1990), whereas circles correspond to DSDP Site 289 from the western Equatorial Pacific and triangles correspond to DSDP Site 525 from the South Atlantic. Ages for Miocene isotope events Mi3, Mi4, Mi5 and Mi6 are plotted with the assigned ages from Westerhold and Bickert (subm.), Mi7 is after Lourens and Hilgen (1997). (1) Ehrmann (1994), (2) Flower and Kennett (1994), (3) Wei and Peleo-Alampay (1997), (4) Paturel et al. (2000), (5) Billups (2002), (6) Johnson (1990), (7) Winkler et al. (1996) and (8) Harwood et al. (1989).

Evidence for reorganization or intensification of ocean circulation also is reported from the Northern North Atlantic (Site 908 and 909) at about 11.2 Ma (Winkler et al. 2002). A distinct change at 11.2 Ma is indicated by variations within clay mineral distribution and increased bulk accumulation rates as a result of an increase in water mass exchange through the Fram Strait (Winkler et al. 2002). At about 11 Ma a dramatic shift ('silica switch') of silica deposition pattern in the tropical Indian, the North Pacific Ocean and the North Atlantic (Johnson 1990) is ascribed to the formation of NCW (Berger 1970). A global change in ocean circulation pattern is documented at Site 1085 in the eastern South Atlantic at 11.3 Ma, as proofed later, by the decrease in oxygenation due to poor ventilation and the increase in productivity due to upwelling of cold nutrient rich intermediate waters. Decreasing $CaCO_3$ concentrations at the Ceara Rise and the strong input of terrigenous matter at the eastern South Atlantic, caused by sea-level lowering, from 14 - 11.2 suggests strong SCW production during ice sheet expansion in Antarctica, culminating at 11.6 Ma in the pronounced oxygen isotope event Mi5. From 12 - 11.5 Ma Cd/Ca ratios indicate an increase in Atlantic to Pacific geochemical gradient. After the first initiation of NCW production (Figure 2.8) carbonate preservation in the eastern Equatorial Pacific starts to cease and increases at the Ceara Rise at 11.2 Ma, where corrosive SCW is pushed downwards by less corrosive NCW. At that time the emerging CAS prevents influx of less corrosive water from the Caribbean into the eastern Equatorial Pacific and probably enhanced transport of warm, more saline water to the north. At that time carbonate content at the eastern South Atlantic increases despite high terrigenous MAR's. This development could be due an increase in carbonate saturation in the Atlantic to balance the deficit found in the deep Pacific as proposed by Berger et al. (1993). The high carbonate content from 11.2 - 9.5 Ma at the Ceara Rise and Site 1085 is punctuated by a drawdown at 10.4 Ma. The correspondence with the Mi6 event suggests increased flow of corrosive SCW and a sea-level fall induced by a strong glaciation on the Antarctic continent. NCW production probably did not die down because this event is not very pronounced at the Ceara Rise and sparse enhancement in carbonate preservation can be observed in the eastern Equatorial Pacific.

But neither at Site 998 nor in the western Equatorial Atlantic Site 926 one can find an equivalent to carbonate crash event VI observed at Site 1085 and 1087 off Namibia. Despite this, at the Kerguelen Plateau a shift from carbonate dominated to opal dominated sedimentation started around 12 Ma accompanied by a drastic drop in carbonate MAR's centered at 9.5 - 9 Ma (Böhm and Dullo 2000) and in eastern Equatorial Atlantic the

carbonate preservation increases from 9.6 - 9 Ma. At about 9.6 Ma first peaks in IRD appear at the Kerguelen plateau and in the Australian-Antarctic basin (Ehrmann 1994) corresponding to deep-sea hiatus NH5 (Keller and Barron 1983). These observations have been linked to a cooling on Antarctica associated with an intensification of the ACC or bottom currents (Ehrmann 1994). Extended shelf ice built up in the Weddell Sea at 9.3 Ma and first IRD peaks in southwest Atlantic and the Ross Sea at 9.2 Ma (Ehrmann 1994) document the expansion of the Antarctic ice cap far north, which probably enhanced the production of nutrient-rich intermediate water flowing to Southwest Africa. On the Northern Hemisphere between 9.5 and 9 Ma high IRD input in the Northern North Atlantic (Winkler et al. 2002) and first appearance of dropstones in the Baffin Bay (Site 645, Stein 1991) are documented indicating cooler climate conditions. These observations correlate well with the duration of carbonate cash event VI in the eastern South Atlantic. The absence of the carbonate crash event at 9.5 Ma at Site 926 can be explained by the fact that SCW inflow to the north was not strong enough to push the prevailing NCW to depth shallower than 3500 meters. There is evidence for a drawdown of carbonate at the deep Site 928 (4012 mbsl) (Murray and Peterson 1997) supporting stronger inflow of corrosive SCW to the western Equatorial Atlantic. In the Caribbean also the deepest drilled Site 1001 (3259 mbsl) shows a reduction in carbonate content and carbonate MAR (Sigurdsson et al. 1997), whereas the shallower sites do not. Comprising these results the carbonate crash event at 9.6 - 9 Ma is of global significance with different effects at various locations due to different environmental settings (i.e. water depth, etc.).

Thus, the late Miocene expansion of ice-sheets on Antarctica and associated deep water circulation changes gave rise to increased latitudinal climate gradients that also affected low-latitude processes on the southern hemisphere. The supply of cool intermediate waters to mid-latitude surface waters upwelling regions resulted in decreased moisture levels in the atmosphere (Flower and Kennett 1995), which initiated the formation of the Namib Desert (Siesser 1978). Aridification in southern Africa, as documented in Site 1088 at 9.7 Ma (Diekmann et al. 2003) and Site 1085 at 9.6 Ma, also shown later, is consistent with the first establishment of trade-wind-driven Benguela upwelling system around 10 Ma, likely as a consequence of northward movement of the Intertropical Convergence Zone (Hay and Brock, 1992).

From 8.3 - 6.6 Ma, ice retreats from the shelf of the Ross Sea (Harwood et al. 1989), Australian-Antarctic Basin and Prydz Bay (Ehrmann 1994). Better preservation of $CaCO_3$ and ventilation of bottom waters after 9 Ma at Site 1085 and 1087 presume a decrease in

SCW and increase in NCW influx. At around 7.6 Ma a strengthening in deep Atlantic overturning at rates comparable to present day interglacial interval, as inferred from $\delta^{13}C$ gradients between the Equatorial Atlantic and Equatorial Pacific (Bickert et al. in press), marks the second initiation of NADW production. Whereas the late Miocene basin-to-basin difference is still substantially smaller than that estimated from Quaternary data (Delaney 1990), but it helps to explains the asynchrony of carbonate record in middle to late Miocene times. A stronger NCW flux from 8 - 7.5 Ma could explain the decrease in carbonate preservation in the eastern Equatorial Pacific being compensated by increased carbonate MAR's at Site 1085.

2.5.2 The Carbonate Crash Events in the eastern South Atlantic

The carbonate crash events in eastern South Atlantic are characterized by a dramatic drop in the carbonate content, a increase in terrigenous content, a continuous period of low carbonate accumulation, and a gradual increase towards normal levels of carbonate deposition (Figures 2.7 and 2.9). Carbonate content in sediments is governed by the production of biogenic carbonate in the surface water, dissolution during sinking and deposition and/or dilution by other components (Berger and Vincent 1981). Comparison of the short-term variations (<200 ky) in our data to data of Diester-Haass et al. (in press), Twichell et al. (2002) and Westerhold and Bickert (subm.) show that peaks in iron contents are associated with lighter values in $\delta^{18}O$, peaks in the magnetic susceptibility record, peaks in the TOC content, and peaks in the pyrite abundance (Figure 2.9). Throughout Miocene to Quaternary times higher terrigenous input at Site 1085 can be related to higher river discharge during interglacial like conditions, whereas the amplitude of the terrigenous input is modulated by eccentricity (Westerhold et al., subm. b).

To investigate the causes of the carbonate crash events we have to look at the long-term variations in the sedimentary pattern. Sediments deposited prior to 9 Ma have somewhat lower carbonate content and show a much higher variation than subsequent sediments. Both the decrease in iron content and the low amplitude in iron signal after 9 Ma point to changes in climatic conditions on the African continent. Paturel et al. (2000) showed that in the carbonate crash period from 9.6 - 9 Ma the clay mineral composition at Site 1085 changes dramatically. Chlorite, Illite and Kaolinite content decrease due to changes in the weathering pattern and decreasing river runoff, revealing that African climate changes from humid to arid. This is supported by the fact that Kaolinite content, originating from deeply weathered soils and rocks of tropical and subtropical Africa,

decreases in the Period from 9.6 - 9 Ma substantially. Palynologic investigations of Oboh-Ikuenobe (2001) at Site 1085 predict a more humid climate with high continental runoff from 14 to about 9.6 Ma, and drier climate thereafter. The change from humid to dry climatic conditions modified the form of erosion of the exposed rocks on land as well as the amount of river runoff and therefore the amount of iron in the sediment.

Before we discuss the reasons for this development we have to contribute to the fact that the large volumes of terrigenous sediment delivered to shelf can be transported further downslope during times of sea-level fall. Higher frequency shifts in oxygen isotope record are proposed as proxy indicators for glaciations and sea-level fluctuations. Abreu and Haddad (1998) demonstrate a strong stratigraphic relationship between higher frequency shifts in the oxygen isotope record and sequences proposed from the rock record. Oxygen isotope curves provide an independent method for stratigraphic calibration of major eustatic changes (Miller et al. 1987) and demonstrate synchronicity of depositional sequences on different continents. Such link is not unexpected during intervals with large- or even moderate-sized ice-sheets. Large ice-sheets (> 50% of present East Antarctica) have existed in East Antarctica since the Oligocene (Miller et al. 1991; Zachos et al. 1993, 2001a) and therefore should contribute to sea-level changes. But it is important to note that big uncertainties in assigned ages for sequence boundaries still exist complicating an exact correlation of oxygen isotope variations and third order sea-level changes. At Site 1085 variations of $\delta^{18}O$ in benthic foraminifera and iron record at the order of 100-ky show that heavy $\delta^{18}O$ values correspond to low iron content (Westerhold et al. subm. b). As discussed above iron content is higher in interglacial like times. Because of sea-level lowering in glacial times higher values in iron are not triggered by sea-level changes but by climate variations on the African continent. On a larger scale the picture changes. In the period from 14 - 11.5 Ma (Figure 2.9) third-order sequence boundaries of Haq et al. (1987, TB2.5 and TB2.6, age are recalibrated to Berggren et al. 1995b) coincide with times of high iron values. The deepest core of Site 1085A from 594.4-604 mbsf (64X) is interpreted as a major slump block (Wefer, Berger, Richter, et al. 1998) corresponding to TB 2.5 and the Mi3 event. Probably the slump therefore was triggered by a major sea-level lowstand. Overall high values of iron intensity from 12.5 - 11.1 Ma correlate perfectly with the late middle Miocene sea-level fall (calcareous nannofossil zones N12 - N14; 12.5 - 11.4 Ma) at the Marion Plateau and northeast Australia (Isern, Anselmetti, Blum, et al. 2002). Additionally, carbonate crash events I, II, III, IV and V coincide with increased $\delta^{18}O$ values at Site 1085. A very pronounced iron peak from 11.6 - 11.5 Ma coincides with the

Mi5 event, which is interpreted as a major glacial on Antarctica (Miller et al. 1991). Oxygen isotope values at Site 1085 show a major shift from 10.7 - 10.1 Ma, culminating at 10.4 Ma in the Mi6 event. This period of increasing $\delta^{18}O$ values coincides with a substantial low in the sea-level curve of Haq et al. (1987), an increase in iron content and high sedimentation rates indicating major downslope transport of terrigenous matter and, as proposed by Berger et al. (1993), repartitioning of carbonate from the shelf to the deep sea (Figure 2.7). The overall high accumulation rates for terrigenous matter also coincides with a eustatic sea-level lowering reported from the Queensland Plateau and at the Great Bahama Bank at 10.7 Ma (Betzler et al. 2000). Oxygen isotope values at Site 1085 steadily decreased from 14 - 10 Ma due to the expansion of the Antarctic ice-sheet lowering sea level continuously. The overall lowered sea-level reduced the accommodation space on the shelf and probably caused higher terrigenous accumulation rates at Site 1085. Elevated iron values in carbonate crash event VI do not coincide with major sequence boundaries or major shift in $\delta^{18}O$ values. Furthermore, high amplitudes in obliquity in the Ca and Fe record of Sites 1085 and 1087 (Figure 2.6) during carbonate crash events support the idea that the cause is linked to high latitude climate processes. After 9 Ma, no major peaks in iron are observed at sequence boundary TB3.3 (7.5 Ma) and during times of high amplitude variations in the $\delta^{18}O$ record. Thus, no close relationship between sea-level changes and terrigenous sedimentation exists after 9 Ma, because sea-level fall was not strong enough and/or no material was available for downslope transport to Site 1085. The aridification of the catchment area of the Orange River and the associated decrease in terrigenous input at 9 Ma probably weakened the response to sea-level variations. Additionally, evidence exists that the tectonic uplift associated with the East African rift system modified the South African interior climate conditions and water run-off by blocking former river systems (Gurnis et al. 2000). Such processes could have had significant implications for the fluvial discharge of terrigenous matter from the South African continent into the South Atlantic.

The carbonate sedimentation pattern at ODP Site 1085 and 1087 is strongly influenced by dilution. But carbonate sedimentation is also dependent on dissolution and productivity at the surface. During periods of enhanced polar glaciation in the Miocene deep-sea hiatuses are interpreted as an intensification of circulation and increase in bottom water corrosiveness (Barron and Keller 1982). Calcium carbonate dissolution can also be enhanced in upwelling regions during periods of increased productivity (Berger and Winterer 1974, Melguen 1978). Due to the beginning of upwelling at Site 1085 at about 12

Ma changes in primary productivity (Twichell et al. 2002) and global changes in ocean circulation pattern (Wright and Miller 1996) might have caused substantial carbonate dissolution.

Dissolution of carbonate in the deep ocean depends mainly on the PCO_2 of the bottom water and the depth of the CCD. Reconstructions of the CCD depth for the Miocene in the South Atlantic reveal a minimum depth of 3000 m (Berger and Wefer 1996). Bickert and Wefer (1996) show that the lysocline in the South Atlantic for the last glacial is located between 3770 and 4000 m water depth. The water depth of the studied sites is shallower than 2000 m (Figure 2.1), which is substantially shallower than the mean lysocline depth of 3750 m along the SW African margin (Dittert et al. 1999). Thus, carbonate dissolution due to shoaling of the CCD, as proposed for the deep Site 926 by King et al. (1997), is probably not affecting carbonate sedimentation patterns at Site 1085 and 1087 in the middle to late Miocene.

Increased input of CO_2 into the atmosphere by enhanced volcanic activity will raise the PCO_2 in the ocean and therefore cause dissolution of carbonate. Reconstruction of atmospheric carbon dioxide for the early to late Miocene (25 - 9 Ma) by Pagani et al. (1999) revealed that pCO_2 was similar to levels recorded for Pleistocene glacial/interglacial intervals (180-290 ppmv). Therefore, we conclude that the carbonate crash events probably have not been caused by dramatic changes in pCO_2. Additionally, the recent investigations of Pearson and Palmer (2000) show that with low levels in pCO_2 over the last 25 Ma, tectonic events such as mountain building or oceanic gateway reconfiguration altering ocean/atmosphere circulation and heat and vapor transport, may have had a dominant role in triggering large-scale shifts in climate. Short-term (less than 1 Ma) changes in ocean chemistry alter the carbonate preservation. The short-term carbon cycle comprises the exchange between atmosphere, ocean, biosphere and soil influencing the CO_2 content of the atmosphere. The reconstruction of pCO_2 by Pagani et al. (1999) predicts no major changes in the carbon budget contributing to a common cause of the carbonate crash events.

Another dominant factor on regional scale is the primary productivity. Emerson and Bender (1981) estimated that with higher productivity in the surface water the particulate rain ratio of C_{org} to C_{CO_3} increases. Therefore increased productivity in the surface water and lateral supply with organic matter from the shelf induces dissolution of carbonate above the lysocline due to metabolic increased PCO_2 in the pore water. First indications for increased paleoproductivity at Site 1085, which are increased carbonate MAR, TOC MAR

(Twichell et al. 2002) and benthic foraminifera MAR (Diester-Haass et al. in press), have been interpreted as the onset of coastal upwelling off Southwest Africa at 12 Ma (Twichell et al. 2002). Organic matter at 1085 overall is predominantly marine in origin and marine paleoproductivity as represented by mass accumulation rates of $CaCO_3$ and organic matter to the sea floor increased from 12 - 3 Ma (Twichell et al. 2002). Pollen content of sediments from Site 532 on the Walvis Ridge indicates that the Namib Desert has existed since the late Miocene (van Zinderen Bakker 1984). Delivery of much land-derived organic matter is therefore unlikely since the onset of coastal upwelling at about 12 Ma. As seen in Figure 2.9, peaks in TOC content correlate with peaks in iron intensity. During precession extremes enhanced fluvial transport and increased bergwinds would on the one hand cause rapid burial leading to enhanced preservation of biogenic components and on the other hand cause higher nutrient concentrations in the surface water triggering augmented productivity (Christensen et al. 2002). Primary productivity and thus export of organic matter to the sea floor at Site 1085 is not primarily dependent on fertilization by dissolved river load as suggested by Diester-Haass et al. (in press), because the XRF record of iron, representative for terrigenous material and itself a limiting nutrient shows high input throughout the time from 14 - 10.4 Ma while productivity is low. Therefore, we suggest that increased productivity off Southwest Africa depends on upwelling of nutrient-rich intermediate water.

Sea-level changes can contribute to changes in organic carbon content because of mobilization of terrigenous material from the shelf to the deep sea and lead to increased dissolution of carbonate. In times of regression the input of terrigenous matter and therefore C_{org} influx from the shelf is high and in times of transgression it is low, thus altering the corrosiveness of the pore water (Broecker and Peng 1982). But again, the XRF measurements document low C_{org} values in time of proposed high terrigenous input (14 - 11.5 Ma). Carbonate Crash events I - IV in Site 1085 generally do not coincide with significantly higher TOC content, but reveal decreased carbonate content and carbonate MAR. The decrease in carbonate preservation correlates with increased $\delta^{18}O$ values at Site 1085 and therefore is attributed to enhanced bottom water corrosiveness due to enhanced glaciations on Antarctica. This shows that a mixture of dilution and dissolution of carbonate caused the carbonate crash events at Site 1085.

In contrast, carbonate crash events V and VI are associated with higher TOC content. Especially at carbonate crash event VI, low carbonate accumulation rates during times of low sedimentation rate and enhanced productivity suggests enhanced dissolution above the

lysocline due to metabolic increased PCO_2 in pore water. But looking at the record of 1085 after crash event VI contradicts this hypothesis, because very high carbonate content are accompanied by enhanced TOC percentage and low carbonate MAR. Therefore, productivity seems not to be the overall process that affected carbonate preservation at that period. Comprising the record of Site 1087 the picture even changes more. Carbonate crash event V is not observed in 1087, but crash event VI is. If we assume productivity to be the causal link between 1085 and 1087 than the missing carbonate crash event V in 1087 can only be explained in terms of a decreased productivity with respect to 1085 at that time, supported by lower productivity estimates at 1087 (Diester-Haass et al. in press).

Other processes seem to govern the preservation, and these apparently are determined by the characteristics of the surrounding water mass. Comparison with phosphate accumulation rates from the nearby DSDP-Site 526 (Hermoyian and Owen 2001) show that at the nick of carbonate crash event VI in Site 1085 and 1087 coincides with enhanced phosphate accumulation rates in the eastern South Atlantic. This suggests an increase in productivity in the surface waters and an expansion of the oxygen minimum zone at the continental slope off Namibia. Evidence for depletion in oxygenation is the increase in pyrite content at Site 1085 (Diester-Haass et al. in press) from 11.5 - 9 Ma. Pyrite formation is controlled by abundance of TOC, detrital Fe, and dissolved sulfate (Emeis et al. 1991). Diester-Haass et al. (in press) suggest that the onset of high terrigenous matter supply at about 12.5 Ma probably resulted in an increase in detrital Fe supply and enhanced productivity resulted in higher TOC mass accumulation promoting oxygen depletion in the uppermost sediment layers and thus triggering pyrite formation. The XRF intensity record of Site 1085 (Figure 2.9) reveals high Fe values in times of low pyrite content indicating that pyrite formation at Site 1085 is exclusively dependent on C_{org} content and oxygen concentration in the pore water. At 11.3 Ma the magnetic susceptibility record of Site 1085 shows a sharp decrease caused by a higher proportion of magnetic minerals (Wefer, Berger, Richter, et al. 1998) and an increase in pyrite content. Slightly after the increase in pyrite, carbonate MAR as well as total organic carbon MAR firmly increase and iron MAR decreases, suggesting that at about 11.3 Ma a less oxygenated water mass reached Site 1085 preventing magnetite and promoting pyrite formation, thus damping the magnetic susceptibility signal. After 11.3 Ma increased productivity and poor oxygenation of bottom waters accompanied by enhanced burial favor pyrite formation. Oxygen depletion was strongest during the period from 9.6 - 9 Ma when pyrite content is highest (Figure 2.9) and benthic fauna shows a reduced number in individuals (Diester-Haass et al. in press).

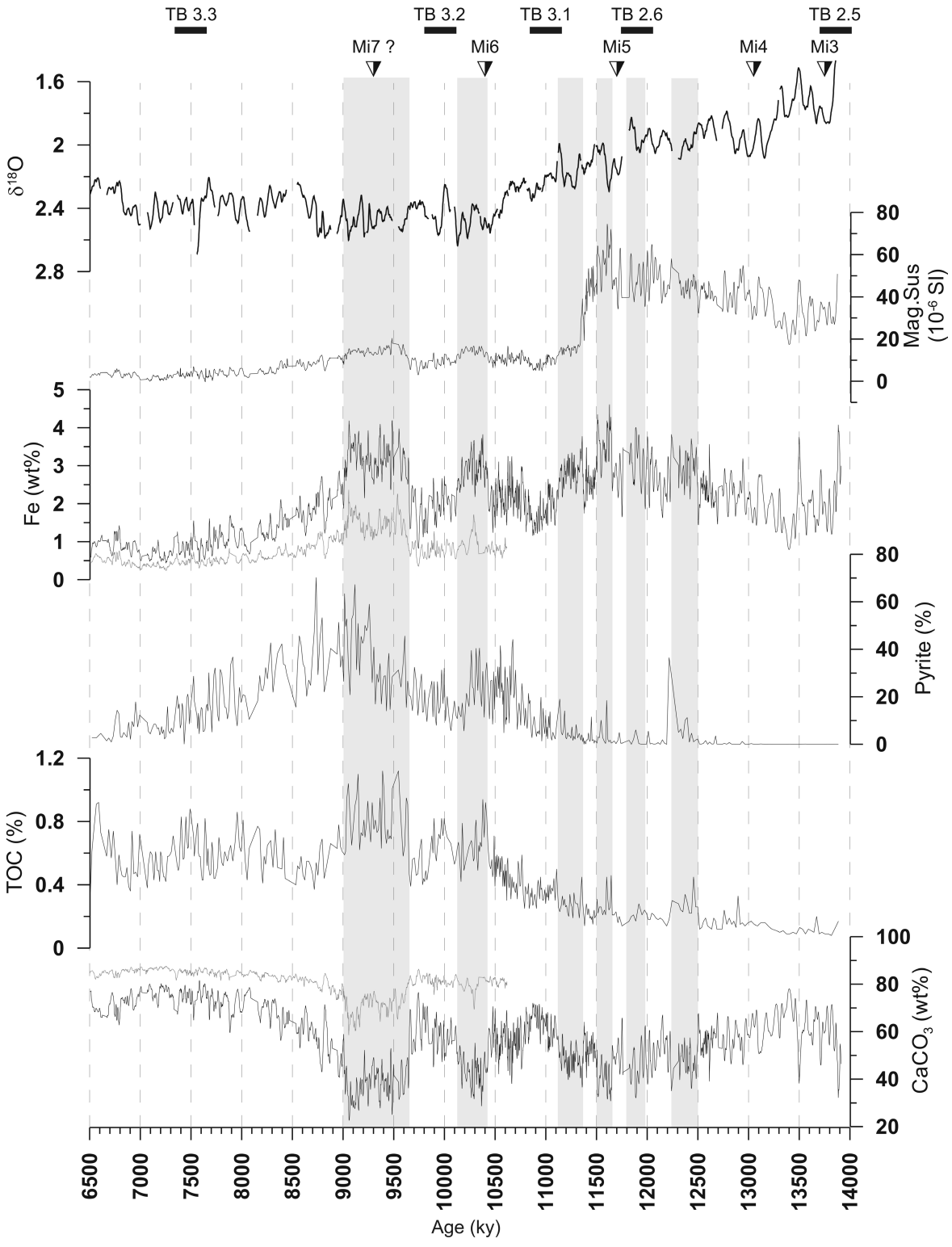

Figure 2.9 Comparison of multiple proxies from Sites 1085 (black line) and 1087 (gray line). TOC and pyrite data from Diester-Haass et al. (in press), magnetic susceptibility from Wefer, Berger, Richter, et al. (1998), $\delta^{18}O$ 50-ky moving average of benthic foraminifera of Site 1085 (Westerhold and Bickert subm.), sequence boundaries after Haq et al. (1987).

At the onset of carbonate crash event VI carbonate MAR decreases and iron MAR increases at low sedimentation rates pointing to dissolution of carbonate rather than dilution. This period is also characterized by an abrupt increase in TOC and a shift in $\delta^{13}C$ values of benthic foraminifera towards light values indicating an increase in productivity (Bickert, pers. comm. 2002). Pyrite content does not increase with the first part of the carbonate crash at 9.6 Ma, but starts to increase at about 9.3 Ma marking the onset of the second part of the crash. From 9.5 - 9 Ma carbonate MAR increased slightly and iron MAR increased significantly documenting higher productivity in the surface waters during times of enhanced input of terrigenous matter. Still the carbonate MAR is lower compared to the period prior to the carbonate crash event VI, which also is reported from the Kerguelen Plateau by Böhm and Dullo (2000). The input of dissolved nutrients by the Orange River thus could have fertilized surface waters. Increased focusing of organic matter below upwelling regions at the ocean margins would have had the effect of decreasing the access of oxygenated water and therefore enhancing burial of organic carbon promoting respiratory dissolution of carbonates. In upwelling areas, the organic carbon content is high, and in many cases is sufficient for sulfate reduction and pyrite formation. We propose that the surrounding water mass is better ventilated at 9.6 Ma preventing extensive pyrite formation during times of enhanced productivity. Higher values in the magnetic susceptibility record marked an increase in oxidized magnetic minerals and point to higher oxygenation as well. From 9.3 - 9 Ma higher pyrite formation was triggered by poor ventilation and elevated productivity. Thus, carbonate crash event VI is dominated by dilution of terrigenous matter and dissolution of carbonates. In contrast to the other carbonate crash events, event VI is accompanied by enhanced carbonate accumulation rates. But enhanced respiration of organic matter causes reduced conditions in the pore water of the continental slope sediments favoring carbonate dissolution as proposed by Emerson and Bender (1981). This paradox can be explained by the fact that sulphate-reducing conditions will produce alkalinity that enhances carbonate preservation (Morse and MacKenzie 1990).

After 9 Ma the sedimentary pattern in 1085 is dominated by carbonate deposition and no obvious correlation between pyrite and organic content exists. Decrease in pyrite content and increase in benthic foraminifera number (Diester-Haass et al. in press) point to well ventilated water partly accounted by the low rate of terrigenous input. Due to lowered productivity and well ventilated bottom water no major carbonate dissolution can be expected. After the drying of the African continent, terrigenous input is minimized

significantly at 9 Ma eliminating the complex interaction between sea-level change, productivity and intermediate water ventilation as seen in the highly variable sedimentation pattern prior to 9 Ma. Decreasing $\delta^{18}O$ values at Site 1085 document a reduction in the Antarctic ice-sheet and thus SCW production from 9 - 8.5 Ma. This promotes with increased NCW a modern-type ocean circulation pattern with well-ventilated intermediate water, moderate productivity and little terrigenous input at Site 1085.

2.6 Conclusion

Using high-resolution XRF core-scanning data (Ca, Fe) of ODP Sites 1085A and 1087C performed every 4 cm downcore we document the changing pattern of carbonate and terrigenous deposition from 14 - 6.5 Ma in the eastern South Atlantic. The Ca and Fe records were spliced together and then used to construct an astronomically calibrated chronology based on orbital tuning.

The interval across the middle to late Miocene transition in the eastern South Atlantic is characterized by six carbonate crash events. Comparison of eastern South Atlantic, eastern Equatorial Pacific, western Equatorial Atlantic and Caribbean Sea reveals that the carbonate crash events appear with different intensities and temporal offsets, but clearly demonstrate the geochemical reorganization of the ocean circulation at the middle to late Miocene transition. The redistribution in carbonate sedimentation pattern between Pacific and Atlantic at 11.2 Ma is attributed to changes in ocean circulation and the evolving geochemical basin-to-basin fractionation due to the uplift of the CAS and the intensification of NCW production.

In the eastern South Atlantic the carbonate crash events are caused by dilution due to enhanced terrigenous input linked to sea-level lowering and dissolution due to increased flux of corrosive SCW during Miocene glacial events. The dominance of terrigenous input prevails from 14 - 9 Ma, whereas the change in terrigenous input around 9 Ma at Site 1085 resembles the drying of South Africa due to the expansion of the Antarctic ice-sheet, which moved the subpolar and subtropical front northward. The pronounced carbonate crash event VI from 9.6 – 9.0 Ma is associated with enhanced burial of organic carbon, probably linked to an overall increase in nutrient flux into the world's oceans at about 9.5 Ma and therefore the development of poorly ventilated intermediate to deep waters or at least an expansion of the oxygen minimum zone at the continental slope. The increase in organic carbon at Site 1085 marks the development of the modern Benguela Current circulation and associated enhanced productivity as early as the late Miocene.

Acknowledgments:

We are indebted to M. Zabel for ICP-OES analysis. We would like to thank F. J. Hilgen, L. J. Lourens, L. Diester-Haass for discussion, and A. Wuelbers and W Hale for help at the Bremen Core Repository. We thank the Ocean Drilling Program for providing samples. This study was funded by the Deutsche Forschungsgemeinschaft (We 992/28).

Middle to Late Miocene Oxygen Isotope Stratigraphy of ODP Site 1085 - SE Atlantic

T. Westerhold, T. Bickert

Fachbereich Geowissenschaften, Universität Bremen, 28334 Bremen, Germany

submitted to *Palaeogeography, Palaeoclimatology, Palaeoecology*

Abstract

The middle Miocene $\delta^{18}O$ increase represents a fundamental change in earth's climate system due to a major expansion and permanent establishment of the East Antarctic Ice Sheet accompanied by some effect of deepwater cooling. The long-term cooling trend in the middle to late Miocene was superimposed by several punctuated period of glaciations (Mi-Events) characterized by oxygen isotopic shifts that have been related to the waxing and waning of the Antarctic ice-sheet and bottom water cooling.

Here, we present a high-resolution benthic stable oxygen isotope record from ODP Site 1085 located at the southwestern African continental margin that provides a detailed chronology for the middle to late Miocene (13.9 - 7.3 Ma) climate transition in the eastern South Atlantic. The oxygen isotope data exhibit four distinct $\delta^{18}O$ excursions, which have astronomical ages of 13.8, 13.2, 11.7 and 10.4 Ma and correspond to the Mi3, Mi4, Mi5 and Mi6 events of Miller et al. (1991). A global climate record was extracted from the oxygen isotopic composition. Both long- and short-term variability in the climate record are discussed in terms of sea-level and deep-water temperature changes. The oxygen isotope data support a causal link between sequence boundaries traced from the shelf and glacioeustatic changes due to ice-sheet growth.

Spectral analysis of the benthic $\delta^{18}O$ record shows strong power in the 400-ky and 100-ky bands documenting a paleoceanographic response to eccentricity-modulated variations in precession. A spectral peak around 180-ky might be related to the asymmetry of the obliquity cycle indicating that the response of the dominantly unipolar Antarctic ice-sheet to obliquity-induced variations probably controlled the middle to late Miocene climate system. Major change in the phase relation between $\delta^{18}O$ and terrigenous sedimentation at ~9 Ma is coeval with aridification of South Africa, intensification of monsoonal circulation, beginning of the Benguela upwelling, and further ice-sheet expansion on Antarctica.

3.1 Introduction

The Neogene period comprises a major change in climate state from relatively global warmth of the early Miocene to colder climates at the end of the Pliocene. As inferred from co-varying $\delta^{18}O$ values of planktonic and benthic foraminifers the general cooling trend in the middle to late Miocene was superimposed by several punctuated period of intensive glaciations (Mi-Events, Miller et al. 1991). These oxygen isotopic shifts primarily reflect the increase in Antarctic ice volume (Miller et al. 1991, Lear et al. 2000, Turco et al. 2001, Billups and Schrag 2002). The middle to late Miocene is characterized by major changes in deep- and surface-water circulation, increases in the strength of oceanic fronts, a redistribution of silica and carbonate deposition in the global ocean, drying of continental climates, a major sea-level fall and plate tectonic developments including the closure of the eastern portal of the Tethys Ocean, the restriction of the Indonesian Pathway and the closure of the Central American Seaway (e.g. Keller and Barron 1983, Kennett et al. 1985, Haq et al. 1987, Woodruff and Savin 1989, Flower and Kennett 1995, Wright and Miller 1996, Zachos et al. 2001a).

In this paper we present a high resolution benthic oxygen isotope record spanning the middle to late Miocene (13.8 - 7.3 Ma) from ODP Site 1085 located at the Southwest African continental margin retrieved during ODP Leg 175. The long-term trends in the climatic record, timing of Mi-Events and linkages to variations in orbital parameters are investigated. Furthermore, we study the middle to late Miocene evolution of the sedimentation pattern at Site 1085 by comparing a high resolution XRF record, as a proxy for biogenic and terrigenous sediment supply, to decipher the response of South African climate to changes in climate boundary conditions (e.g. ocean circulation, ice-sheet expansion).

3.2 Material and methods

ODP Site 1085, drilled during Leg 175, is located at the southwestern African continental margin (Figure 3.1) (29°22.47´S, 13°59.41´E, 1713 m water depth) off the Orange River, a perennial river discharging into the South Atlantic (Wefer, Berger, Richter, et al. 1998). Today, Site 1085 is bathed primarily in the Upper Circumpolar Deep Water (UCDW) near the mixing zone with the North Atlantic Deep Water (NADW). A continuous hemipelagic sedimentary section reaching the middle Miocene (14 Ma) was recovered from Site 1085. The studied interval between 382 and 600 mbsf covers the middle to the late Miocene. A meter composite depth scale at Site 1085 was obtained down

to 300 mcd, only. The middle to late Miocene has no composite section, but a revised composite depth (rmcd) was established by integrating the core log data and bore-hole logs of natural gamma ray (for details see Westerhold et al. subm. a). Sedimentation rates range from 3-5 cm/ky in the middle to late Miocene (Wefer, Berger, Richter, et al. 1998). Sediments are dominated by nannofossil ooze, diluted by various amounts of terrigenous silt and clay.

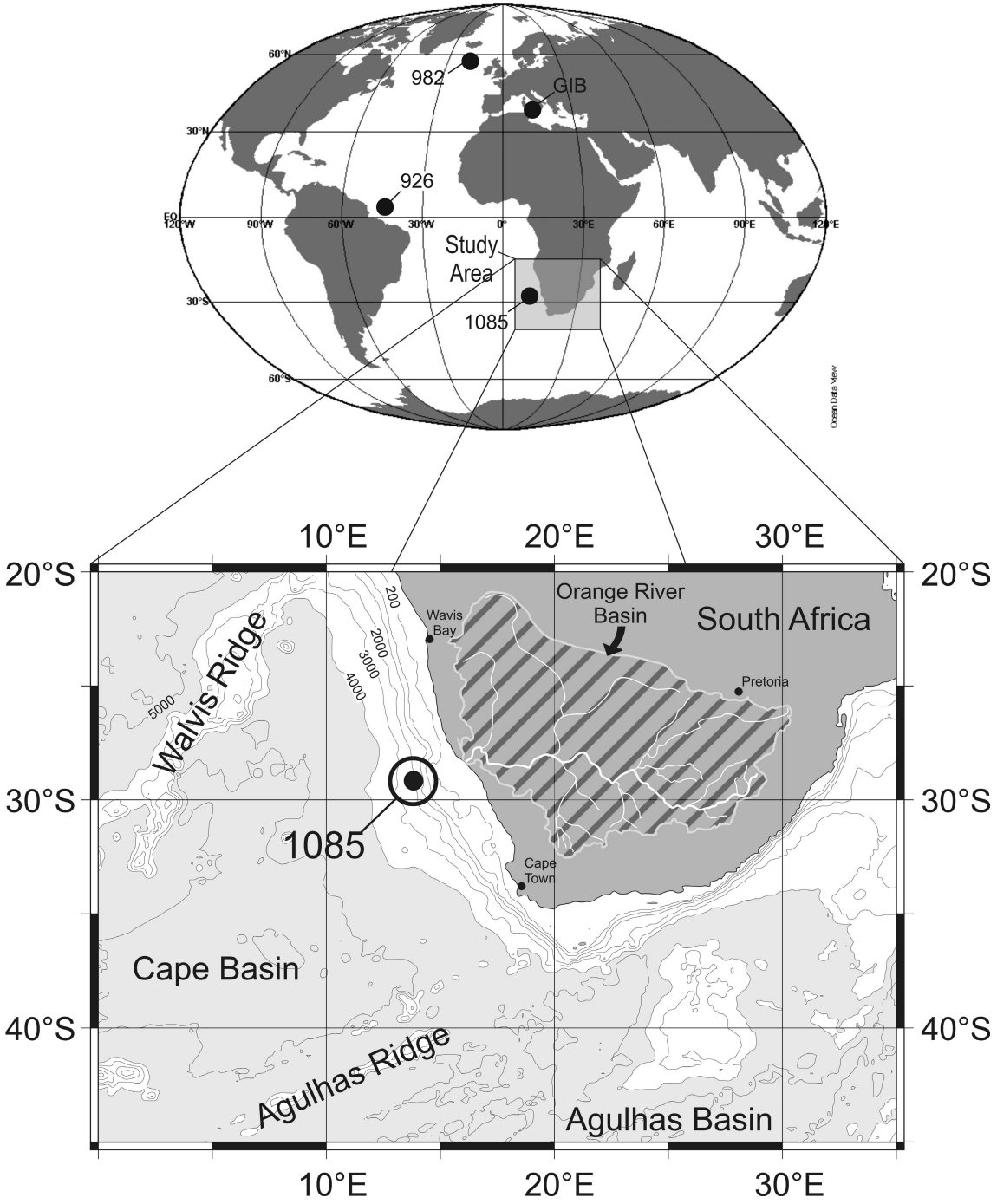

Figure 3.1 Location map showing the position of ODP-Site 1085 off the Orange River. The Orange River and the inflow of minor rivers are displayed. The catchment area of the Orange River in South Africa is hatched (Orange River Basin). Ocean areas deeper than 4000 are shaded in light gray. The global map shows the position of ODP Sites 982, 926, 1085 and the location of the Monte Gibliscemi record (GIB).

Benthic stable oxygen isotope data were generated from analysis of epifaunal benthic foraminifera *Cibicidoides wuellerstorfi* or *Cibicidoides kullenbergi*. Isotope measurements were performed on a Finnigan MAT 252 mass spectrometer equipped with an automated carbonate preparation line at the University Bremen. The carbonate was reacted with orthophosphoric acid at 75°C. Analytical precision is 0.07‰ for $\delta^{18}O$ as referred to an internal carbonate standard. All data are reported against the VPDB standard after calibration with NIST 19. The middle to late Miocene section was sampled every 10 cm along the shipboard mbsf (Cores 1085A-42X through 63X). The total number of samples analyzed was 2622. A number of 714 duplicate analyses of *C. kullenbergi* and *C. wuellerstorfi* prove that no correction between both species is necessary in the middle to late Miocene section (Figure 3.2).

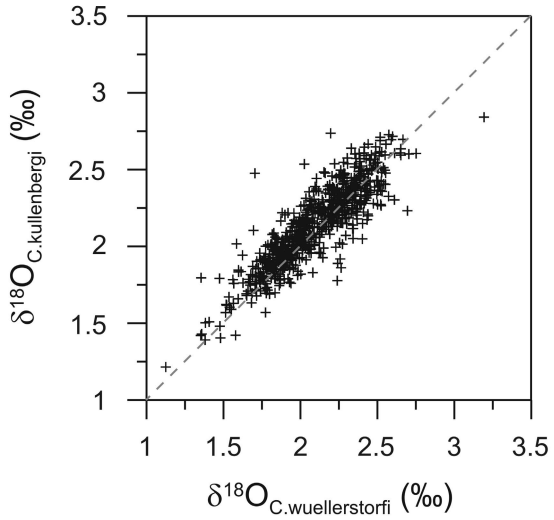

Figure 3.2 Oxygen isotope measurements of specimens of *Cibicidoides wuellerstorfi* and *Cibicidoides kullenbergi* from the same sample (n=714). Note that the trend follows a 1:1 relationship for $\delta^{18}O$.

All data and tables are available at PANGAEA - Network for Geological and Environmental Data (www.pangaea.de). In this paper only Table 3.1 and 3.2 are presented, Table 3.3 is available online.

3.3 Chronology

An astronomically calibrated age model for the Miocene section of ODP Sites 1085 was generated by orbital tuning of a high resolution composite XRF-Fe intensity record of ODP Sites 1085 and 1087 to an Eccentricity-Tilt-Precession (ETP) target curve (Westerhold et al. subm. a). Prior to the tuning procedure, a revised composite depth scale and a spliced composite record was established by integrating core log data of Sites 1085

and 1087 with bore-hole logs of natural gamma ray (SGR-log) of Site 1085A. A complete composite record for Site 1085 has been obtained from 353.60 down to 460.83 rmcd. Due to the slump deposition in Site 1087C below 409 mbsf, the composite record for Site 1085 was extended from 460.85 down to 555.04 rmcd by correlation to the SGR-log of 1085A revealing the size of core-break gaps. From 555.82 down to 593.57 rmcd sections were adjusted to mcd scale, considering that mcd values exceed mbsf values by about 10% at Site 1085A as observed by Wefer, Berger, Richter, et al. (1998). To account for this extension, each core in this part of the record was compressed by 10 %.

Shipboard data of the biostratigraphic datums provided the preliminary age model for Site 1085 (Wefer, Berger, Richter, et al. 1998). The tuning procedure itself was done by correlating prominent features of the Fe record to the ETP target curve, whereby the record first was tuned in the 400-ky domain and then in the 100-ky domain. Because eccentricity modulates the signals derived from terrigenous material (magnetic susceptibility, XRF Fe record) in the Cape Basin, maxima in eccentricity correspond to maxima in the terrigenous signal (Christensen and Maslin 2001, Vidal et al. 2002, Westerhold et al. subm. a). The tuning procedure gave an age control point for at least each eccentricity cycle. No lag between the tuning target and the lithologic signal has been assumed.

The derived sedimentation rates range between 1.0 and 7.3 cm/ky. From 13.8 up to 11.7 Ma the sedimentation rates are well below 4 cm/ka. Then they steadily increase to 7 cm/ky remaining at that value from 11.5 - 10.4 Ma, punctuated by a drop in sedimentation rates at 11.1 Ma. Thereafter rates decrease to an average value of 3 cm/ky till 6.5 Ma, interrupted by enhanced sedimentation rates at 9.9 Ma and around 7.6 Ma.

3.4 Results

Oxygen isotope data (Table 3.3) from the middle to late Miocene section of Site 1085 are presented as raw data vs. age in Figure 3.3. In the investigated period the $\delta^{18}O$ values increase from 1.5‰ to 2.4‰ and vary in amplitude by 0.4‰. The long-term increase from 13.8 - 10.4 Ma approximates the general trend in benthic stable isotopes throughout the Neogene as compiled by Zachos et al. (2001a) from 40 DSDP and ODP Legs. This development resembles the middle Miocene buildup of the East Antarctic Ice Sheet between 15 and 11 Ma. Generally, the $\delta^{18}O$ values at Site 1085 are heavier by 0.3‰ to 0.5‰ compared to the global deep-sea composite of Zachos et al. (2001a) suggesting higher mean salinity of intermediate-waters at this location compared to deep-waters. At Site 1085 the $\delta^{18}O$ values reach Holocene levels at the end of the long-term cooling trend at 10.4 Ma.

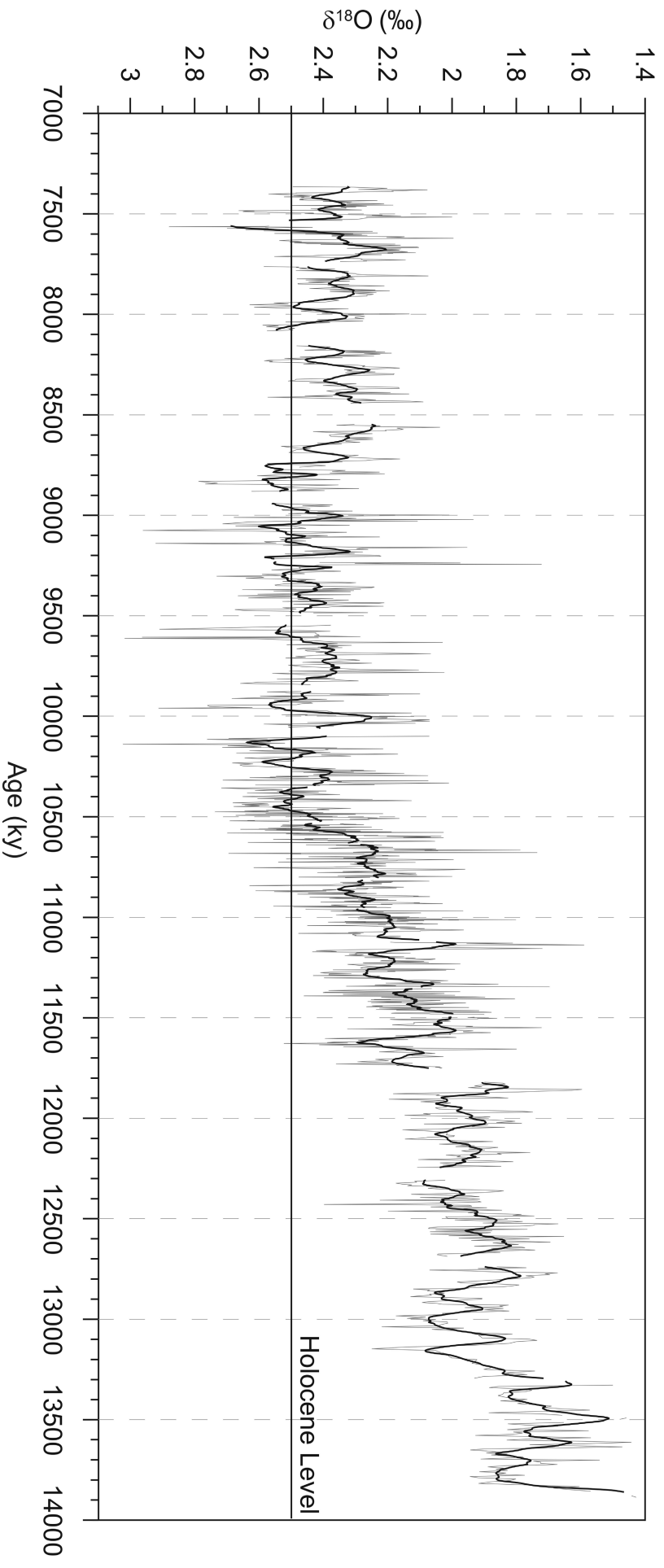

Figure 3.3 Benthic foraminiferal $\delta^{18}O$ data from Site 1085A versus age. Holocene stable oxygen isotope mean value (horizontal black line) for Site 1085 is from Westerhold et al. (subm. b). Black solid curve represents a 51-ky moving average. All $\delta^{18}O$ values are not adjusted for isotopic disequilibrium.

Superimposed on this long-term trend are punctuated episodes with clearly increased values at 13.7, 13.2, 11.7 and 10.4 Ma with amplitudes of 0.4 - 0.7‰. These correspond to the Miocene Glacial Events (Mi-Events) (Miller et al. 1991), although the proposed ages given by Miller et al. (1998) differ slightly from ours. After the long term increase a period (10.4 - 8.7 Ma) of relatively heavy $\delta^{18}O$ values around 2.4‰ with an amplitude of up to 0.6‰ follows. This period ends with a decrease in average $\delta^{18}O$ values of 0.3‰ at 8.7 Ma. From 8.7 - 7.3 Ma $\delta^{18}O$ values reveal low frequency cyclicity (~100 ky). In general, the amplitude of these Miocene changes is small compared to the Pleistocene benthic glacial-interglacial change of up to 1.5‰ documented at Site 1085 (Westerhold et al. subm. a).

3.5 Discussion

3.5.1 Miocene Isotopic Events

The middle to late Miocene open-ocean $\delta^{18}O$ record in the investigated time period is punctuated by five episodes of increased values known as the Mi3 through Mi7 events (Miller and Feigenson 1991, Miller et al. 1991, Wright and Miller 1992, Wright et al. 1992). These oxygen isotopic shifts have been ascribed to a combination of glacioeustatic sea-level lowering and bottom water cooling of 1°-2°C, but are primarily related to the waxing and waning of the Antarctic ice-sheet (Miller et al. 1991).

The Mi3 and Mi4 events constitute the two step middle Miocene $\delta^{18}O$ increase (Savin et al. 1975, Shackleton and Kennett 1975) with increases of between 0.5‰ and 0.8‰ (Miller et al. 1991). The Mi3 event was found within chron C5ABr by Miller et al. (1991) at about 13.6 Ma and the Mi4 event was found across C5AAn/C5An transition (Miller et al. 1991) with peak values at the base of chron C5Ar at 12.85 Ma (Lourens and Hilgen 1997), GPTS ages are after Cande and Kent (1995). The $\delta^{18}O$ record of Site 1085 shows an increase in $\delta^{18}O$ of 0.3‰ at the end of the investigated record (Figure 3.4) interpreted as the Mi3 event. Furthermore, around 13.2 Ma $\delta^{18}O$ values increase by 0.5‰ resembling the Mi4 event which showed a similar increase in benthic $\delta^{18}O$ values at DSDP Sites 563 and 608 (Miller et al. 1991). In our record, the Mi4 event appears first with a 0.5‰ increase in $\delta^{18}O$ values within 200 ky, followed by two saw-tooth like $\delta^{18}O$ variations with a duration of 120 ky each. Mi4 ends with an increase in $\delta^{18}O$ values of 0.3‰ at 12.8 Ma. The timing of the Mi4 event centered at 13.0 Ma in Site 1085 shows an age discrepancy of 200 ky with previous estimates of Lourens and Hilgen (1997). But the $\delta^{18}O$ record of ODP Site 926 from the western Equatorial Atlantic (Shackleton and Hall 1997) with an orbitally tuned timescale (Shackleton and Crowhurst 1997) reveals an

increase by 0.5‰ around 13.2 Ma supporting our age estimate of the onset of Mi4. Furthermore, at Site 926 the $\delta^{18}O$ record shows decreasing values around 12.7 Ma corresponding to the proposed age of the Mi4 event, whereas at Site 1085 the Mi4 event is followed by an increase in $\delta^{18}O$ values of 0.3‰ around 12.8 Ma.

The Mi5 event is positioned at the base of chron C5r by Miller et al. (1991) at about 11.7 Ma and biostratigraphically within the range of *D. kugleri* (Turco et al. 2001) between 11.868 and 11.573 Ma (Turco et al. 2002). At Site 1085, the *D. kugleri* zone is located within a two-fold $\delta^{18}O$ increase of overall 0.5‰ between 11.9 and 11.5 Ma, indicating that this increase corresponds to the Mi5 event (Figure 3.4). Recent results from an astronomically dated deep marine succession in the Mediterranean indicate that the Mi5 event occurred at 11.4 (Turco et al. 2001), giving an age discrepancy with our estimate of almost 300 ky. Shackleton and Hall (1997) proposed that a brief deep-water cooling event at 11.4 Ma might represent Mi5, but also a shift in benthic $\delta^{18}O$ of about 0.4‰ occurs between 11.8 and 11.7 Ma at Site 926. Additionally, a maximum in $\delta^{18}O$ of the fine fraction at Site 926 at 11.62 Ma matches perfectly with the record of Site 1085. A closer look at the data of Turco et al. (2001) shows that the shift in $\delta^{18}O$ values already starts at 11.85 Ma reaching a maximum at 11.7 Ma. The proposed shift at 11.4 Ma is of lower amplitude and probably an artifact of smoothing. Comparing the $\delta^{18}O$ records, it seems that the Mi5 event consists of 3 to 4 maxima with an average duration of 100 ky from 11.8 to 11.4 Ma.

The Mi6 event is found in the center of chron C5n at Site 608 (Miller and Feigenson 1991) and recorded between the LO *C. miopelagicus* at 10.977 Ma (Hilgen et al. 2000) and the FO *D. hamatus* at 10.41 (Turco et al. 2002). In the $\delta^{18}O$ record of Site 1085 a major increase is documented from 10.7-10.4 Ma (Figure 3.4). At 10.4 Ma the heaviest $\delta^{18}O$ values are reached within the period from 13.8-10.2 Ma likely to resemble the Mi6 event. In the $\delta^{18}O$ record of Site 982 (Andersson and Jansen 2003) Mi5 is poorly constrained because of a sampling gap, but Mi6 was identified between 10.55 and 10.4 Ma corresponding reasonably well the increased $\delta^{18}O$ values at Site 1085 and the Mi6 event in the Gibliscemi record of Turco et al. (2001). After the shift of 0.3‰ at Site 1085, mean $\delta^{18}O$ values remain at an average of 2.5‰ from 10.4 to 8.7 Ma. Thereafter $\delta^{18}O$ values decrease by 0.2‰ towards an average of 2.3‰.

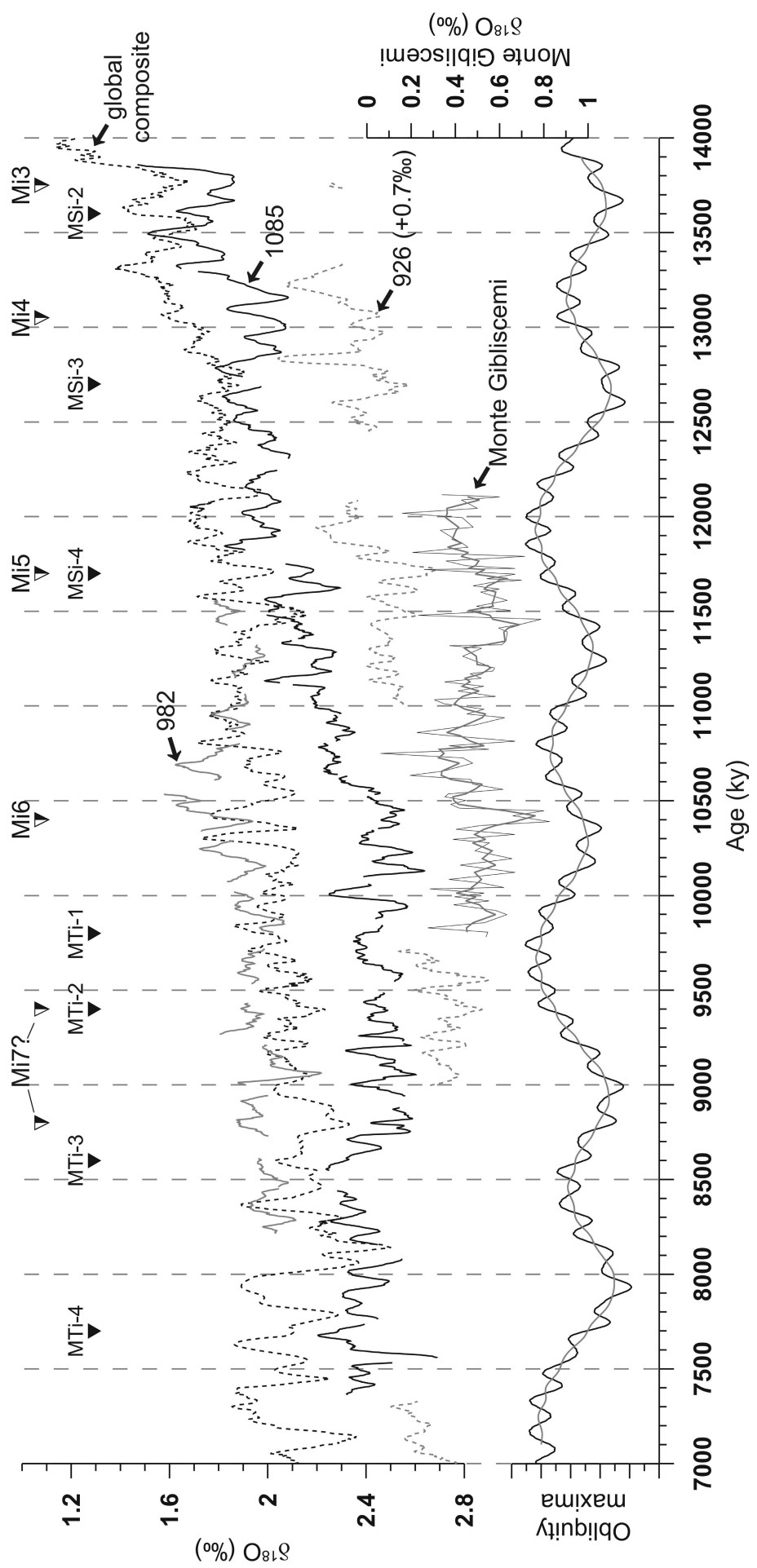

Figure 3.4 For description see next page.

Figure 3.4 Comparison between the long-term trends in the benthic stable oxygen isotope record from ODP Site 1085 (solid black line), ODP Site 926 (dashed gray line, Shackleton and Hall 1997), ODP Site 982 (solid gray line, Andersson and Jansen 2003), the global deep sea composite of Zachos et al. (2001a) (dashed black line) and the Monte Gibliscemi record (thin black line with 51-ky moving average represented by the solid gray line, Turco et al. 2001). All $\delta^{18}O$ records have been smoothed using a 50-ky moving average and are not adjusted for isotopic disequilibrium. To separate the $\delta^{18}O$ data of ODP Site 926 from the global deep sea composite, which contains these data, we shifted the data of Site 926 by +0.7‰. The half filled triangles indicate the ages for Mi3, Mi4, Mi5, Mi6 and Mi7 as suggested in this study. The filled triangles indicate the ages and names of the oxygen isotope events defined by Abreu and Anderson (1998). The lower most panel shows the modulation of the obliquity maxima (black line), the solid gray line represents a 200-ky moving average.

The Mi7 event is positioned in chron C4Ar.1n by Wright and Miller (1992) at 9.45 Ma. The $\delta^{18}O$ record of Site 1085 features no pronounced shift in the vicinity of the assigned age for Mi7 (Figure 3.4). Amplitude variations of $\delta^{18}O$ values are in the order of 0.4 ‰ in this area. In western Equatorial Atlantic Site 926 (Shackleton and Hall 1997) a pronounced maximum in $\delta^{18}O$ values occurs at 9.4 Ma, which corresponds to increased $\delta^{18}O$ values in Site 1085 as well. Generally, there is a good fit between $\delta^{18}O$ values of Site 926 and 1085 in the period from 9.7 to 9.0 Ma. No presence of a marked increase in $\delta^{18}O$ was found in the vicinity of Mi7 at Site 982 which might be ascribed to the uncertainties in the biostratigraphic age model (for discussion see Andersson and Jansen 2003). Comparison of $\delta^{18}O$ variations in the Northern Atlantic (Site 904) and sequence boundaries at the New Jersey margin suggested that the Mi7 event to be located around 8.7 Ma (Miller et al. 1998). At 8.8 Ma $\delta^{18}O$ values show an increase at Site 1085. Comprising, the position of the Mi7 event is uncertain.

As seen from the comparison of different $\delta^{18}O$ records (Figure 3.4), identification of Mi-events during the middle to late Miocene transition is difficult because records in which Mi-events have first been recognized are low in resolution. Thus, undersampling a high frequency $\delta^{18}O$ signal may alias the record and can yield spurious conclusions as shown by Pisias and Mix (1988). Aliasing can obscure the Mi-events making them difficult to recognize because amplitude variations are small (0.5-0.6‰) in the middle to late Miocene. This is also apparent when we compare the Mi-events with the positive oxygen isotope events (Figure 3.4) defined by Abreu and Anderson (1998). Good agreement in terms of timing exists where amplitude shifts in the $\delta^{18}O$ records are in the order of 0.8-1.0‰. In this case MSi-2 corresponds to Mi3 and MSi-4 to Mi5. In the late Miocene there is less agreement in the assigned oxygen isotope events of Miller et al. (1991) and Abreu and Anderson (1998), because the amplitude in $\delta^{18}O$ variations assigned as events is well below 0.5‰. The high frequency variation in the $\delta^{18}O$ record of Site 1085 in late Miocene

varies with an amplitude of about 0.5‰. As pointed out by Shackleton and Hall (1997) as well as Andersson and Jansen (2003) the $\delta^{18}O$ variability observed in late Miocene sediments is probably not appropriate as a correlation tool in the late Miocene. For further evaluation of the characteristics of the Mi-events and their potential for correlation of sedimentary sequences, additional high resolution oxygen isotope records in the middle to late Miocene have to be compiled.

3.5.2 Implications from Site 1085 $\delta^{18}O$ record to global changes in the middle to late Miocene

The long-term trend in $\delta^{18}O$ record exhibits a number of steps and peaks that reflect episodes of global warming and cooling, and ice-sheet growth and decay (Zachos et al. 2001a). The late middle Miocene climate optimum (17 - 15 Ma) was followed by a gradual cooling and reestablishment of a major ice-sheet on Antarctica by 10 Ma (Vincent et al. 1985, Flower and Kennett 1995). Lourens and Hilgen (1997) suggested a possible correlation between third-order eustatic cycles and glacial episodes (Mi-events) during the late Miocene. As documented by Miller et al. (1998), Miocene slope reflections at the New Jersey transect correlate with $\delta^{18}O$ increases suggesting a causal link between sequence boundaries traced from the shelf and glacioeustatic changes. Abreu and Haddad (1998) demonstrated a strong stratigraphic relationship between higher frequency shifts in the oxygen isotope record and sequences proposed from the rock record. Therefore, oxygen isotope curves might provide an independent method for stratigraphic calibration of major eustatic changes and demonstrate synchronicity of depositional sequences on different continents. Such link is not unexpected during intervals with large- or even moderate-sized ice-sheets. Evidence for a causal connection between $\delta^{18}O$ increases and sequence boundaries led to the conclusion that variations in the size of ice-sheets have been the primary control on the formation of sequence boundaries since ~42 Ma (Miller et al. 1998). Recently, Billups and Schrag (2002) have shown that increased $\delta^{18}O$ of sea-water, calculated from paired trace metal and stable isotope measurements are in a very good agreement with the sequence boundaries of Haq et al. (1987) linking $\delta^{18}O$ increases at Mi-events to sea level regression due to ice buildup on Antarctica. Furthermore, Lear et al. (2000) presented evidence that most of the benthic $\delta^{18}O$ increase (~85%) between 15 - 11 Ma can be attributed to an increase in continental ice volume, whereas the remaining shift in $\delta^{18}O$ reflects cooling of bottom waters. At Site 1085, $\delta^{18}O$ increases at Mi-events coincide with enhanced downslope transport of shelf derived terrigenous matter supporting

a causal link to sea-level lowstands (Westerhold et al. subm. a) in periods of increased ice-sheet growth on Antarctica. From 13.8 - 10.4 Ma the overall increase in $\delta^{18}O$ at Site 1085 is 1.1‰. We now assume that 85% of the $\delta^{18}O$ long term increase is due to ice volume increase (Lear et al. 2000) and that the Pleistocene rate of $\delta^{18}O$/sea-level change is applicable for the Miocene. Using the Pleistocene gradient of 0.11‰ for a 10 m change in sea level (Fairbanks and Matthews 1978) and the simple linear equation of Bemis et al. (1998) to convert the $\delta^{18}O$ carbonate values into $\delta^{18}O$ seawater values, the increase in benthic $\delta^{18}O$ values resemble sea-level lowering of ~85 meters from 13.8 - 10.4 Ma. In contrast, if we assume a 3°C cooling of deep waters as proposed by Billups and Schrag (2002), we end up with only 43 meters of sea-level fall. Recent results from the Marion Plateau suggest bottom-water cooling of ~1°C and a sea level fall of 73 meters (John 2003) being consistent with the results from the New Jersey Margin (Miller et al. 1998). Water temperature estimates of deep-water cooling based on Mg/Ca ratios is controversial since the chemical intake of Mg into carbonate and subsequent diagenetic overprint effects are poorly understood (Billups, pers. comm. 2003). The amplitude and timing of the Mi-events (Table 3.1) matches perfectly with the results from Miller et al. (1998) confirming the close relation of sequence boundaries and ice-sheet growth. However, future estimates of deep-sea temperature change have to confirm these findings. The major difference to the Haq et al. (1987) sea-level curve is the absence of the strong middle to late Miocene sea-level fall in the oxygen isotopes. The middle to late Miocene sea-level fall starts at the sequence boundary 3.1 (11.3 Ma) of Haq et al. (1987) after the Mi5 event (Miller et al. 1998). Beginning with the Mi5 event, the $\delta^{18}O$ record of Site 1085 shows a decreasing trend till 10.4 Ma. This increase lasting for 1.2 Ma might represent the major middle to late Miocene sea-level fall.

Table 3.1 Comparison of the Ages of $\delta^{18}O$ maxima and the Haq et al. (1987) sequences.

Oxygen Isotope Event	Age of Maximum (Ma) Miller et al. 1998	Age of Maximum (Ma) this study	Age of Inflection (Ma)	Haq et al. 1987 Sequence
Mi7	~8.7	8.8	~8.8	TB 3.2
Mi6	~10.3	10.4	~10.4	Not resolved
Mi5	11.7	11.7	11.9	TB 3.1
Mi4	12.9	13.1	13.1	TB 2.6
Mi3	13.7	13.8	13.8	TB 2.5

Note: The timing of the Mi7 event is uncertain.

Deep-sea temperature estimates from Mg/Ca ratios at the Kerguelen Plateau (Billups and Schrag 2002) reveal an increase in local deep ocean temperatures similar to those of the Miocene climatic optimum between 12 - 11 Ma and again at ~8.5 Ma. The high-resolution $\delta^{18}O$ record of Site 1085 documents no such overall trend towards lighter isotopic levels between 12 - 11 Ma, as expected during times of deep-sea warming. At Site 1085 a decrease of up to 0.6‰ in $\delta^{18}O$ values occurs prior to the Mi5 event at 11.85 Ma, after the Mi5 event at 11.55 Ma, and at 11.15 Ma. These relatively short decreases in $\delta^{18}O$ values might correspond to the increase in deep-sea temperatures as reported from the Kerguelen Plateau. In the period from 10.4 - 8.7 Ma heavy $\delta^{18}O$ values at Site 1085 indicate an increased influx of Southern Component Water (SCW) due to stronger glacial conditions on Antarctica. $\delta^{13}C$ reconstructions show that between 10 and 8.5 Ma there was little difference between the North Atlantic, Pacific and Southern oceans, indicating little to no flow of proto-NADW (Lear et al. 2003) and increased flow of SCW into the Atlantic. This increased SCW production caused dissolution of carbonates (Westerhold et al. subm. a) at 10.4 and 9.5 Ma in the eastern South Atlantic. Around 9.5 Ma Mg/Ca-temperatures at Site 926 (Ceara Rise, western Equatorial Atlantic) decreased by ~1°C, coincident with the nadir of the 'carbonate crash' in the South Atlantic (Westerhold et al. subm. a) and eastern Equatorial Pacific (Lyle et al. 1995), suggesting strong SCW inflow to the Atlantic. An increase in Mg/Ca temperatures at ~8.5 Ma at the Kerguelen Plateau (Billups and Schrag 2002) is in accordance with a decrease of in $\delta^{18}O$ values at Site 1085 at 8.7 Ma suggesting warming of ~2°C and/or freshening of deep waters. Between 8.5 and 7 Ma, the inter-ocean $\delta^{13}C$ gradients increased, recording the flow of proto-NADW to the south (Wright et al. 1996) reaching the South Atlantic as suggested by Billups and Schrag (2002) due to the intensification of Northern Component Water (NCW) production (Lear et al. 2003).

3.5.3 Control of $\delta^{18}O$ variations in the middle to late Miocene

The Miocene climate system is dominated by orbitally induced oscillations (Zachos et al. 2001a, Paul et al. 2000, Shackleton et al. 1999, Zachos et al. 1997). The primary beat of the glaciated Cenozoic is the obliquity band, regardless of the state of other boundary conditions or the location of ice-sheets (Zachos et al. 2001a). It has been suggested that long-term astronomical variations in earth's orbit and inclination may have controlled the occurrence of the Mi-events (Beaufort 1994, Lourens and Hilgen 1997). Turco et al. (2001) ascribe the Mi5 and Mi6 events to periods of low-amplitude variations in obliquity (Figure 3.4), in contrast to the last 5.3 Ma when major steps in glacial ice buildup are related to

increasing amplitude variations in obliquity (Lourens and Hilgen 1997). Lourens and Hilgen (1997) argue that the average spacing between the Mi3 to Mi7 events closely matches the 1.2 Ma long-periodic variations in obliquity (Figure 3.4), pointing to the sensitivity of ice-sheets to obliquity-generated changes in high-latitude insolation in the Miocene. The high resolution $\delta^{18}O$ record of Site 1085 reveals that the Mi3, 6 and 7 events are associated by low-amplitude variations in obliquity, but Mi4 and 5 are not (Figure 3.4).

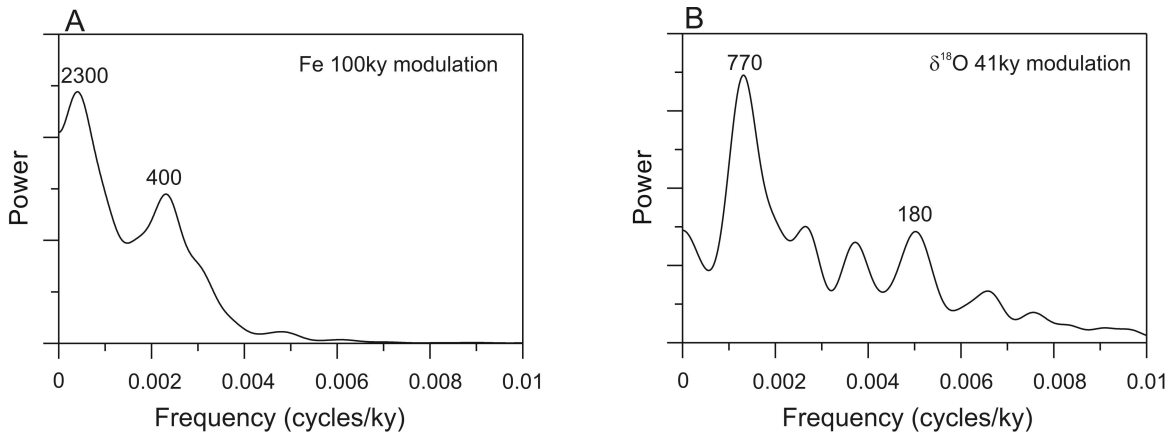

Figure 3.5 Blackman-Tuckey power spectrum of A, the 100-ky modulation of the Fe concentration data from Site 1085A (Westerhold et al. subm. a) and B, the 41-ky modulation of the $\delta^{18}O$ record of Site 1085A (this study). The amplitude variations for Fe in the 100-ky band and $\delta^{18}O$ in the 41-ky band have been calculated with the Program ENVELOPE (Schulz et al. 1999). Prior to the calculation of the amplitude variations, the data have been detrended and normalized to unit variance. Spectral estimates are based on a Bartlett smoothing window with 30% lags with an 80% confidence interval

Spectral analysis of the $\delta^{18}O$ record of Site 1085 reveals variable influence of different orbital frequencies (Figure 3.6). The most interesting feature is a spectral peak around 180-ky, which is close to the 172-ky modulation of the obliquity cycle, ascribed to the asymmetry of the obliquity cycle (Liu 1992), and has been apparent in several paleoclimatic records (e.g. Beaufort et al. 1994). In general, heavier $\delta^{18}O$ values correspond to smaller amplitudes in obliquity resembling less warm summers, a critical episode for ice growth. Spectral analysis of the $\delta^{18}O$ 41-ky modulation reveals significant peaks at 180-ky and 770-ky (Figure 3.5), which are related to modulations of the orbital obliquity (Lourens and Hilgen 1997), pointing to high latitude forcing. Furthermore, the spectrum of the $\delta^{18}O$ record of Site 1085 in the period from 9 - 11.5 Ma indicates the presence of 400-, 100-, 41- and 23-ky cycles (Figure 3.6) matching eccentricity-, obliquity- and precession-related cyclicity. The major difference between the Miocene and Pleistocene is the absence of large ice-sheets on the Northern Hemisphere and the open Central American Seaway. The fluctuations of the Northern Hemisphere ice-sheet are the

driving force of the 100-ky cycles during the Pleistocene (Imbrie et al. 1993). The Southern Hemisphere ice-sheets could have played a similar role with fluctuations large enough to induce 100-ky cycles. The earliest evidence for ice-sheets on the Northern Hemisphere is the appearance of IRD at 11.5 Ma (Fronval and Jansen 1996). Thus, an effect of both Northern and Southern Hemisphere polar ice-sheets can be expected, in which fluctuations of the larger Antarctic ice-sheets will have stronger implications on climate cycles. Clemens and Tiedemann (1997) also found eccentricity-related components in the $\delta^{18}O$ record of Site 659, which they related to an asymmetrical response mechanism that preferentially introduces variance into the climate system from the warmer portion of the eccentricity-modulated precession cycle (Short et al. 1991). Beaufort (1994) showed that the amplitude variations of the 100-ky cycles are enhanced during the Mi-events, but Turco et al. (2001) show a stronger influence of a 100-ky cycle during warmer periods between Mi5 and Mi6, corresponding with a long-term 2.3 Ma eccentricity cycle maximum. At Site 1085, eccentricity maxima correspond to high Fe concentrations in the middle to late Miocene, which are correlated to lower $\delta^{18}O$ values and hence warmer periods. Our data, therefore, support the findings of Turco et al. (2001). The influence of the ~2.3 Ma cycle in eccentricity is at least observed in the Fe intensity data (Figure 3.5) supporting the dominantly precession-controlled precipitation pattern in South Africa in the middle to late Miocene.

From 8.5-7 Ma a very dominant eccentricity cycle with almost no precessional- and obliquity-related components can be seen in Site 1085 (Figure 3.6) marking a change in climate response from obliquity- to eccentricity-dominated sedimentation. After 8.5 Ma the influence of obliquity on global climate during ice-free periods, without an ice-sheet amplifier, is weaker or less apparent likely due to the decoupling of the climate around Antarctica by the intensification of the ACC.

3.5.4 Sedimentation pattern at Site 1085 in the middle to late Miocene

In the early Pleistocene the sedimentation pattern at Site 1085 is controlled by a combination of low- and high-latitude climate forcing. A pronounced 41-ky cyclicity during this time points to a regulation of the low-latitude climate system of the Southern Hemisphere by high latitude glacial climates (Westerhold et al. subm. b). Furthermore, terrigenous input is strongly modulated by the amplitude of the precession signal enhancing the power in the eccentricity band. This has been contributed to the fact that winter and summer climate patterns in South Africa have been reported to reinforce one

another (Christensen et al. 2002, Rogers and Bremner 1990). Higher terrigenous input at Site 1085 in the Pleistocene is related to higher river discharge during interglacial-like conditions (Westerhold et al., subm. b). The prevalence of the 100-ky cyclicity in the terrigenous supply at Site 1085 prior to large fluctuations in the Northern Hemisphere ice volume in the early Pleistocene (Christensen et al. 2002, Vidal et al. 2002, Westerhold et al. subm. b), and the anti-phasing of $\delta^{18}O$ values and Fe intensities have been interpreted to indicate that increased shelf erosion during sea-level lowering in glacial times is not the primary mechanism controlling the terrigenous sedimentation at Site 1085.

In the middle to late Miocene section of Site 1085 decreased $\delta^{18}O$ values correspond to higher Fe concentrations, used as a proxy for terrigenous input, pointing to enhanced river runoff in interglacial like conditions, similar to the Pleistocene sedimentation pattern. In contrast, during the middle to late Miocene 'carbonate crash' events enhanced terrigenous input was triggered by strong sea-level lowering associated with the Mi-events (for discussion see Westerhold et al. subm. a). The major difference between the Miocene and Pleistocene climate system is the presence of large ice-sheets on the Northern Hemisphere since 3.2 Ma (e.g. Raymo et al. 1990, Raymo et al. 1992, Berger and Wefer 1996, Wright and Miller 1996, Haug and Tiedemann 1998). The fluctuations of the Northern Hemisphere ice-sheets are inferred to be the driving force of the 100-ky cycle during the late Pleistocene, although the explanations for the late Pleistocene ice age cycles remain controversial in spite of a strong correlation with the eccentricity (Imbrie et al. 1993). Eccentricity, as the major driver of late Pleistocene ice age cycles, is questioned because, among other things, the spectrum of the $\delta^{18}O$ record does not show the 400-ky component of the eccentricity cycle (for discussion see Muller and MacDonald 2000) and the amplitude of eccentricity is too small (e.g. Imbrie et al. 1992, Liu 1995). Alternatively, orbital inclination (Muller and MacDonald 1997), variations in the frequency of the obliquity cycle (Liu 1992) or a nonlinear internal feedback mechanism in the climate system (e.g. Crowley et al. 1992, Imbrie et al. 1993, Berger 1999) are discussed.

In contrast, Clemens and Tiedemann (1997) found eccentricity-related components in the $\delta^{18}O$ record of Site 659 prior to the onset of the late Pleistocene 100-ky glacial-interglacial cycles. These have been related to an asymmetrical response mechanism that preferentially introduces variance into the climate system from the warmer portion of the eccentricity-modulated precession cycle. Model results indicate a substantial transfer of variance from the precession to the eccentricity bands within the maximum temperature response of the tropics (Short et al. 1991).

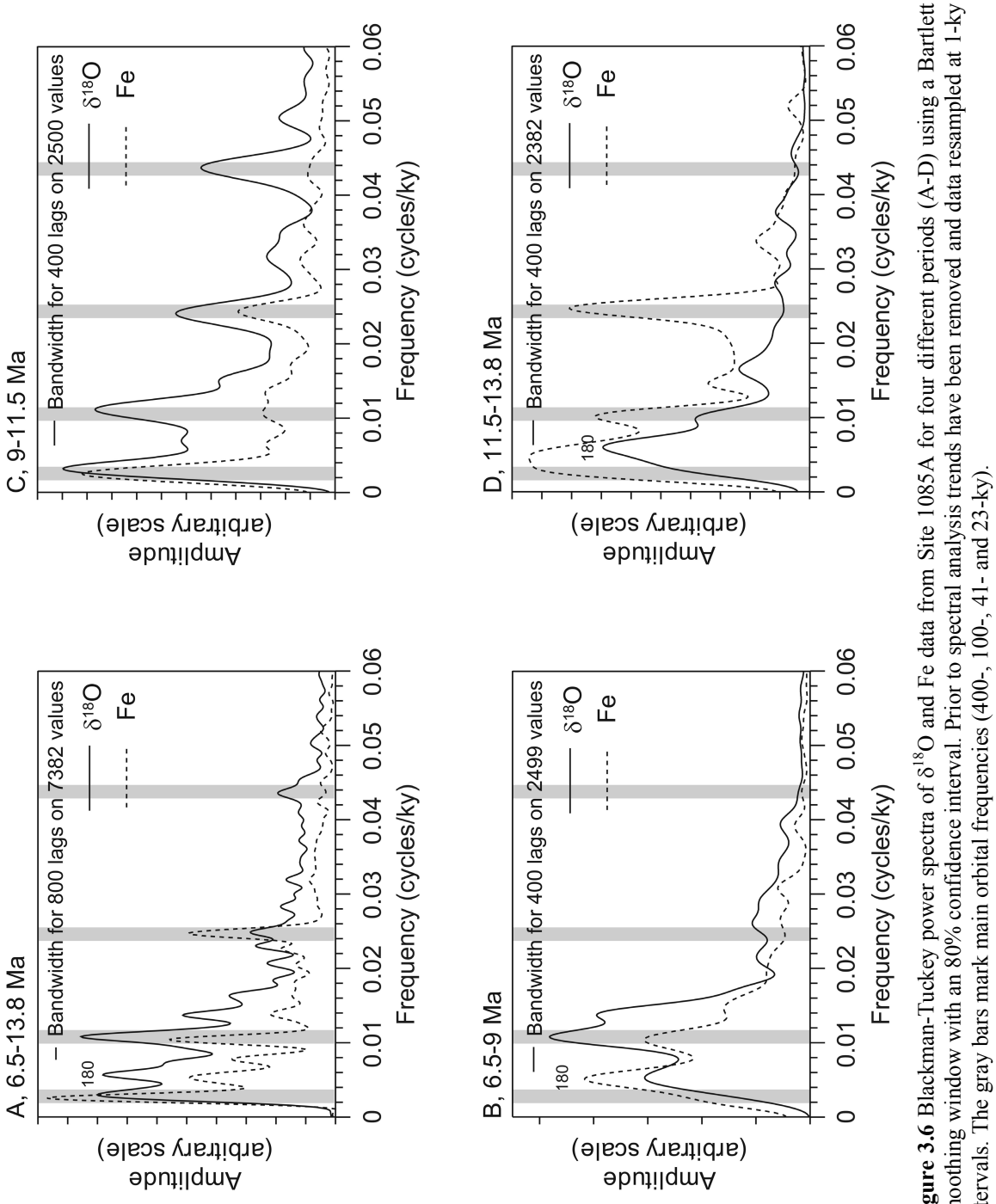

Figure 3.6 Blackman-Tuckey power spectra of $\delta^{18}O$ and Fe data from Site 1085A for four different periods (A-D) using a Bartlett smoothing window with an 80% confidence interval. Prior to spectral analysis trends have been removed and data resampled at 1-ky intervals. The gray bars mark main orbital frequencies (400-, 100-, 41- and 23-ky).

In the middle to late Miocene record of Site 1085 strong eccentricity related peaks at 400- and 100-ky can be observed in the Fe and $\delta^{18}O$ record (Figure 3.6), although no large Northern Hemisphere ice-sheet exists. Furthermore, the spectrum of the $\delta^{18}O$ record of Site 1085 in the period from 9 - 11.5 Ma indicates the presence of 400-, 100-, 41- and 23-ky cycles (Figure 3.6), matching eccentricity-, obliquity- and precession-related cyclicity. Surprisingly, the Fe intensity record lacks power in the 100- and 23-ky band, although the sample resolution is much better. One reason could be that the strong Mi-events and associated 'carbonate crash' events (Westerhold et al. subm. a) deteriorated the anti-phase relationship between $\delta^{18}O$ and terrigenous input. In addition to the riverine input, sea-level lowering might have caused mobilization of shelf derived terrigenous material transported downslope to Site 1085. Because we know from the Plio-Pleistocene that the terrigenous record is responding to the modulation of precession, we would not expect to have much power in the precession band but enhanced power in the 100-ky band. The period from 9 - 11.5 Ma is dominated by major ice-sheet expansion on Antarctica. Thus, the strong obliquity component in the terrigenous sedimentation pattern can be explained by the waxing and waning of the Antarctic ice-sheet, in turn driven by obliquity (e.g. Zachos et al. 2001b). But power in the eccentricity and precession related bands of the $\delta^{18}O$ record suggests strong influence of low latitude processes to the ice-sheet dynamic as suggested by Short et al. (1991). Similar influences at eccentricity frequencies (100-ky, 400-ky) on the Antarctic ice-sheet have been documented in the late Oligocene and early Miocene (Naish et al. 2001, Zachos et al. 2001b). Various mechanisms exist by which the tropical temperature response could be exported to high latitudes influencing ice volume, i.e. moisture and heat transport by ocean currents (Short et al. 1991, Crowley and Kim 1992, Crowley et al. 1992).

Prior to 11.7 Ma (Mi5) the power spectra of the Fe record show a very strong peak in obliquity (Figure 3.6) suggesting high influence of high latitude climate processes on South African precipitation pattern. The $\delta^{18}O$ record does not show a clear peak, but some dispersed power around 180-ky. In this period the $\delta^{18}O$ record of Site 1085 might strongly suffer from the strong cooling trend, the Mi-events and also uncertainties in the timescale. The good match of the $\delta^{18}O$ record to other records, as discussed before corroborated the correctness of the age model for Site 1085. Therefore, we attribute the spectrum of the $\delta^{18}O$ record in the middle Miocene to the effect of the superimposed cooling trend and the Mi-events.

Similarly, the period after 9 Ma also reveals no clear cyclicity (Figure 3.6). The $\delta^{18}O$ and Fe records show peaks at 100- and 180-ky, but no power in the obliquity band. Curiously, no power can be traced in the precession band. The high resolution Fe record reveals eccentricity related cycles with almost no precessional- and obliquity-related component.

In summary, the power spectra (Figure 3.6) reveal a change in climate response from obliquity- to eccentricity-dominated sedimentation with a transition period from 11.5 - 9 Ma. This change in the climate system is also recorded in the phase relationship between insolation, $\delta^{18}O$ and Fe content. Prior to 9 Ma the Fe content lags $\delta^{18}O$ only by two 2 ky (Table 3.2) suggesting a strong influence of high latitude climate to South African precipitation pattern. After 9 Ma the lag between $\delta^{18}O$ and Fe content increases to 6 ky (Table 3.2). If we assume $\delta^{18}O$ to lag ETP by 5 ky, as in the Pleistocene (Imbrie et al. 1984), than the difference between Fe and ETP would be 11 ky. Note that the Fe content shows no lag in the cross spectral analysis to the ETP curve because it has been tuned to it.

Table 3.2 Coherency and phase relationship (in ky) of $\delta^{18}O$, Fe intensities and ETP.

Parameter	100 ky (6.5 - 9 Ma)		41 ky (9 - 11.5 Ma)		100 ky (11.5 - 13.8 Ma)	
	coherency	phase	coherency	phase	coherency	phase
$\delta^{18}O$ vs. ETP	0.49	-6.30	0.47	-0.41	-	-
Fe vs. ETP	0.85	0.08	0.77	1.03	0.92	2.00
Fe vs. $\delta^{18}O$	0.64	6.28	0.67	1.89	-	-

Notes: We analyzed the variability in the frequency domain using the Blackman-Tuckey approach with 30% lags with a Parzen window at the 95%-confidence level (k = 0.41).

This result is close to the relation documented in the Pleistocene period (Westerhold et al. subm. b) and suggests precipitation changes after 9 Ma to be driven by South African monsoon. The timing of the change is coeval with major change in sedimentation pattern at Site 1085 (Westerhold et al. subm. a), major changes in ocean circulation and the aridification of South Africa (Diekmann et al. 2003). The late Miocene expansion of ice-sheets on Antarctica and associated deep water circulation changes gave rise to increased latitudinal climate gradients that also affected low-latitude processes on the Southern Hemisphere. The supply of cool intermediate waters to mid-latitude surface waters upwelling regions resulted in decreased moisture levels in the atmosphere (Flower and Kennett 1995), which initiated the formation of the Namib Desert (Siesser 1978). Aridification in southern Africa, as documented in Site 1088 at 9.7 Ma (Diekmann et al.

2003) and Site 1085 at 9.6 Ma (Westerhold et al. subm. a), is consistent with the first establishment of trade-wind-driven Benguela upwelling system around 10 Ma, likely as a consequence of northward movement of the Intertropical Convergence Zone (Hay and Brock 1992). Enhanced aridity in the Asian interior and onset of the Indian and East Asian monsoon is documented at 9 - 8 Ma (Zhisheng et al. 2001), coincident with the intensification of South African monsoon. Additionally, the northward movement of New Guinea-Australia might have caused the drying of East Africa by switching the source waters of the Indonesian throughflow from the warm south Pacific to the cold north, thereby cooling the Indian Ocean and reducing rainfall in East Africa at that time. Hence, the change in sedimentation pattern at Site 1085 at 9 Ma seems to be the result of global climate change in connection with major changes in ocean and atmospheric circulation. However, the origin of the strong spectral peaks in $\delta^{18}O$ and Fe content at 180- and 100-ky without enhanced response in the obliquity band is unknown and needs to be investigated further in future.

3.6 Conclusion

The high resolution benthic stable oxygen isotope data of ODP Site 1085 provide new insight into the middle to late Miocene paleoclimatic evolution. The long-term cooling trend in $\delta^{18}O$ record of Site 1085 approximates the general trend in the global $\delta^{18}O$ deep-sea composite of Zachos et al. (2001a) resembling the middle to late Miocene buildup of the East Antarctic Ice Sheet. The benthic $\delta^{18}O$ record of Site 1085 shows significant increases with maxima at 13.8, 13.2, 11.7 and 10.4 Ma, corresponding to the Mi-events of Miller et al. (1991). The comparison with other benthic oxygen isotope records shows that the identification of Mi-events is possible from 13.8 to 10 Ma. Afterwards, the identification is difficult because the amplitude of $\delta^{18}O$ variations is rather small and yields aliasing effects in the lower resolution records. The ages for the Mi-events derived in this study are consistent with the results of Miller et al. (1998) and therefore support a causal link between sequence boundaries traced from the shelf and glacioeustatic changes due to ice-sheet growth.

Spectral analysis of oxygen isotope data indicates a change from obliquity- to eccentricity-dominated climate variability. The eccentricity-related components in the $\delta^{18}O$ record (400- and 100-ky) might originate in an asymmetrical response mechanism that preferentially introduces variance from the warmer portion of the eccentricity-modulated precession. A strong spectral peak around 180-ky might be related to the asymmetry of the

obliquity cycle, which also is proposed to be responsible for the 100-ky cyclicity (Liu 1992). This shows that the response of the dominantly unipolar Antarctic ice-sheet to obliquity induced variations probably controlled the middle to late Miocene climate system.

A major change in the phase relation between $\delta^{18}O$ and terrigenous sedimentation at Site 1085 at ~9 Ma is coeval with a global climate change. Major changes in global ocean and atmospheric circulation are documented by the aridification of South Africa and the interior of Asia, the intensification of monsoonal circulation, the beginning of the Benguela upwelling and the ice-sheet expansion on Antarctica.

Acknowledgments

We are indebted to M. Segl and her team for carefully supervising the stable isotope analyses. We thank A. Wuelbers and W Hale for the help at the Bremen Core Repository. This contribution benefits from discussion with C. M. John and K. G. Miller. We thank the Ocean Drilling Program for providing samples. This study was funded by the Deutsche Forschungsgemeinschaft (We 992/28).

Pleistocene Oxygen Isotope Stratigraphy of ODP Site 1085 - SE Atlantic

T. Westerhold[1], L. Vidal[2], T. Bickert[1]

[1]*Fachbereich Geowissenschaften, Universität Bremen, 28334 Bremen, Germany*

[2]*CEREGE, Europôle de l'Arbois, BP 80, 13545 Aix en Provence, Cedex04, France.*

will be submitted to *Earth and Planetary Science Letters*

Abstract

Benthic oxygen isotope data and high-resolution XRF core-scanning data (Ca, Fe) of ODP Site 1085 located at the southwestern African continental margin were used to reconstruct the South African climate history and the changing pattern of carbonate and terrigenous deposition in the eastern South Atlantic during the Pleistocene. An astronomically calibrated timescale for the last 1.8 Ma was developed by tuning the benthic $\delta^{18}O$ record to obliquity.

Pleistocene sediments at Site 1085 document high terrigenous input by the nearby Orange River during interglacial periods and low input during glacial periods. Cross-spectral analysis reveals that the river runoff and thus precipitation in the catchment area of the Orange River is driven by Southern Hemisphere insolation. Aridity in South Africa followed the 41-ky and then 100-ky cyclicity associated with glacial-interglacial cycles of the late Pliocene and Pleistocene. These variations in precipitation are linked to shifts in high- (i.e. ice-sheet oscillations) and low-latitude (i.e. tropical SST) climate change. Distinct shifts in South African climate at 1.70 Ma, 1.00 Ma and 0.64 Ma documented at Site 1085 are coeval to shifts in high latitude climate and correspond to climatic shifts in the Northern Hemisphere. But prior to the Mid-Pleistocene Transition our results support the hypothesis that South African climate is mainly controlled by shifts of the atmospheric frontal systems due to fluctuations of the Antarctic ice-sheet.

4.1 Introduction

Little is known about the evolution of the Southern Hemisphere continental aridity throughout the Pleistocene due to lack of high-resolution records. Only a few Southern Hemisphere continental records, based on sedimentological studies, for South African aridity exist. Stuut et al. (2001) could show that continental aridity in southwestern Africa increased during interglacials as a result of changes in the latitudinal position of the Southern Hemisphere Westerlies. Partridge et al. (1997) showed that on the eastern side of Southern Africa aridity variations are bound to changes in Southern Hemisphere summer insolation. These findings are contrary to aridity records from the Northern Hemisphere, which are reported to co-vary with changes in Northern Hemisphere summer insolation (e.g. Rea 1994, deMenocal et al. 1995, deMenocal et al. 2000). Recently, variations in the middle Pleistocene African aridity have been linked to changes in the strength of the monsoon and changes in the atmospheric moisture balance directly controlled by the tropical SST (Schefuss et al. 2003), whereas wetter conditions prevailed in interglacial periods. Because Equatorial Atlantic SST variations are driven by high-latitude climate variations (McIntyre et al. 1989, Schneider et al. 1995) a complex interaction of high- and low-latitude climate processes can be expected.

In the Pleistocene, a major change in high-latitude climate variability occurred at the Mid-Pleistocene Transition from a 41-ky dominated to a 100-ky dominated climate system at ~0.90 Ma (Ruddiman et al. 1986, Raymo et al. 1990, Berger et al. 1993, Berger and Jansen 1994). The Mid-Pleistocene Transition is characterized by an increase in ice volume due to the growth of shelf-based ice-sheets in high latitudes regions (Berger and Jansen 1994). The associated cooling appears to have moved the global climate system into a mode of high-latitude, bipolar, glacial-interglacial cycles lasting throughout the late Pleistocene (Ruddiman 1989).

In order to investigate the relation of precipitation changes in South Africa to the changes in climate forcing and the remote effects of high-latitude ice volume changes during the Mid-Pleistocene Transition, we conducted a study of sediments deposited off the Orange River mouth from 1.80 - 0 Ma. In this study, we present oxygen isotope and high-resolution X-ray fluorescence data from ODP Site 1085 to investigate the relation between terrigenous sedimentation pattern and climate forcing. Our aim is to examine how precipitation variations in the Orange River catchment area are controlled, and how high- and low-latitude climate changes (i.e. ice volume, monsoon strength) affect South African

climate. Additionally, we want to investigate, how the South African climate system responds to the onset of the 100-ky glacial-interglacial cyclicity.

4.2 Methods and material

ODP Site 1085, drilled in the Cape Basin during Leg 175, is located at the southwestern African continental margin (29°22.47´S, 13°59.41´E, 1713 m water depth) off the Orange River (Figure 4.1), a perennial river discharging into the South Atlantic (Wefer, Berger, Richter, et al. 1998), whose sediment load is moved primarily south by the prevailing bottom currents (Rogers and Bremner 1991). A continuous hemipelagic sedimentary section reaching the middle Miocene (14 Ma) was recovered from Site 1085. A meter composite depth scale at Site 1085 has been constructed down to 300 mcd. The studied interval (0 - 100 mcd) covers the entire Pleistocene. Sedimentation rates range from 3 - 13 cm/ky in the Pleistocene (Wefer, Berger, Richter, et al. 1998). The retrieved sediments are dominated by nannofossil ooze, diluted by various amounts of terrigenous silt and clay.

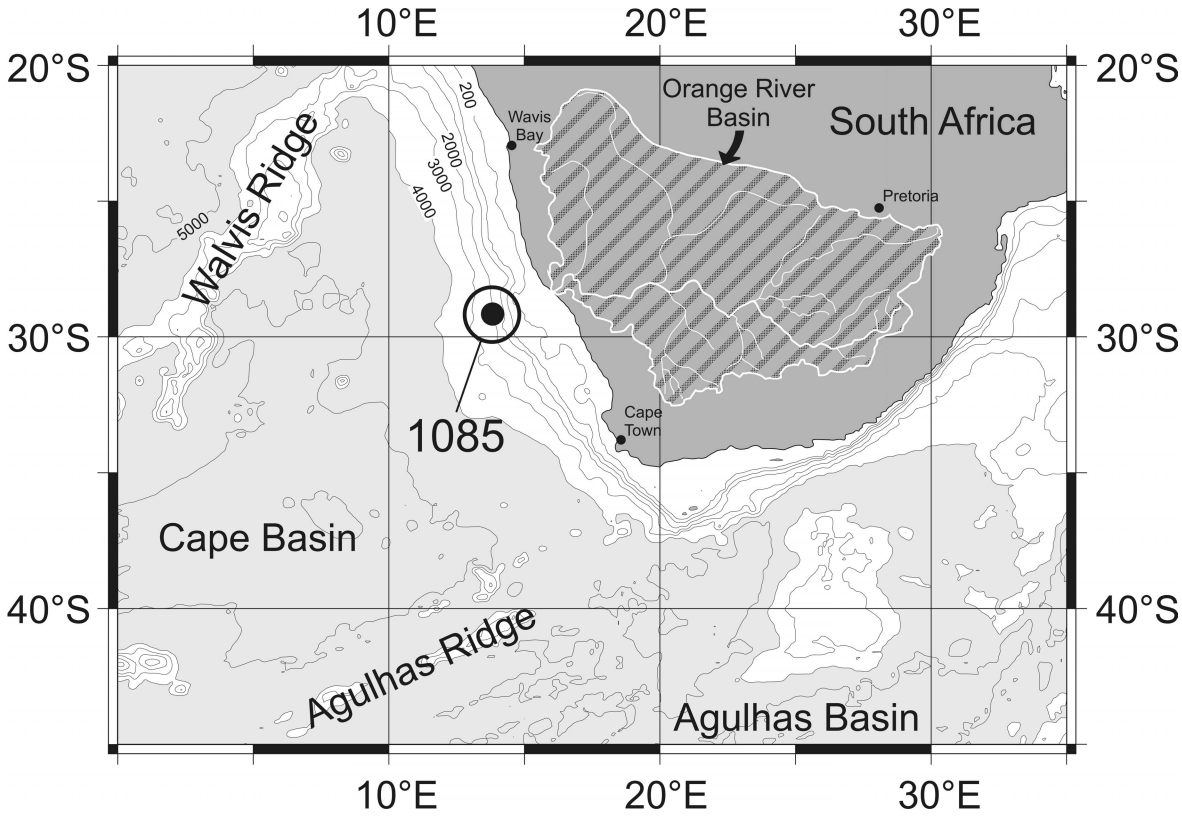

Figure 4.1 Location map showing the position of ODP-Site 1085 off the Orange River. The Orange River and the inflow of minor rivers is displayed. The catchment area of the Orange River in South Africa is hatched (Orange River Basin). Ocean areas deeper than 4000 m are shaded in light gray.

Benthic stable oxygen isotope data were generated from analysis of epifaunal benthic foraminifera *Cibicidoides wuellerstorfi* or *Cibicidoides kullenbergi*. Isotope measurements were performed on a Finnigan MAT 252 mass spectrometer equipped with an automated carbonate preparation line at the University Bremen. The carbonate was reacted with orthophosphoric acid at 75°C. Analytical precision is 0.07‰ for $\delta^{18}O$ as referred to an internal carbonate standard. All data are reported against the VPDB standard after calibration with NIST 19. Site 1085 sediment was sampled along the shipboard composite section every 10 cm from 0 - 19 mcd and every 20 cm from 19 - 75 mcd (Cores 1085A and B). The total number of samples analyzed was 468.

Continuous measurements of the elemental composition of sediments at ODP Site 1085 from 0 - 100.82 mcd were performed using the X-ray fluorescence (XRF) core scanner at the Bremen Core Repository (BCR), which allows for high-resolution, nearly continuous, non-destructive analyses of major and minor elements at the surface of split cores. XRF data were collected every 4 cm downcore over a 1 cm^2 area using 15 seconds count time and an X-ray current of 0.087 mA. For further details concerning this method see Jansen et al. (1998), Röhl & Abrams (2000) and Westerhold et al. (subm.). In this paper we present calcium (Ca) and iron (Fe) intensity data, which are highly correlated to the physical and chemical properties measured both downhole and at split cores.

Element concentrations were obtained by calibration of the XRF element intensities with data from standard chemical analyses from discrete samples as described by Jansen et al. (1998). Total digestion preparation of 22 discrete sediment samples were carried out according to Zabel et al. (2001) and analyzed by inductively coupled plasma-optical emission spectrometry (ICP-OES, “Optima 3300 R” Perkin Elmer). Precision was better than 2%. The accuracy of element determinations was checked using standard reference material USGS MAG-1. The attained calibration formula, determined by linear regression, gives the concentration of each element in the core in wt%. Assuming that all Ca^{2+} is bound to CO^{3-}, we converted Ca intensities to $CaCO_3$% by multiplying Ca wt% by 2.5.

All data and tables are available at PANGAEA - Network for Geological and Environmental Data (www.pangaea.de). In this paper only Table 4.1 and 4.2 are presented, Tables 4.3 through 4.6 are available online.

4.3 **Results**

4.3.1 Oxygen isotopes

The benthic oxygen isotope data for the last 1.80 Ma are presented in Figure 4.2. The $\delta^{18}O$ record exhibits the typical glacial-interglacial changes documenting growth and decay of the Northern Hemisphere ice-sheets. The cyclicity is dominated by an obliquity-related response changing to a 100-ky period dominance at the Mid-Pleistocene Transition (Berger and Jansen 1994, Raymo et al. 1997, Schmieder et al. 2000) (Figure 4.2). Prior and after the Mid-Pleistocene Transition average $\delta^{18}O$ values are at 3.16‰ and 3.25‰, respectively. $\delta^{18}O$ values range between 2.5‰ (Interglacial) and 4.0‰ (Glacial). The amplitudes of Pleistocene glacial-interglacial changes vary between 0.6‰ and 1.5‰. The $\delta^{18}O$ data of Site 1085 are given in Table 4.4.

4.3.2 X-ray fluorescence and ICP analysis

In Figure 4.2 Ca and Fe intensities derived from the XRF core scanning are plotted versus age. Ca intensities vary between 4200 and 12200 counts per second (cps). Fe intensities vary between 400 and 4200 cps showing an inverse relationship to Ca intensities. The Ca and Fe records are used as proxies for carbonate and terrigenous sedimentation, respectively. In general the Ca and Fe signal at Site 1085 show a prominent low- to high-frequency cyclicity. As derived from Figure 4.2 peaks in Fe correspond to low $\delta^{18}O$ values and low Ca intensities. The XRF data of Site 1085 are given in Table 4.5.

Linear regression of these data plotted versus the ICP-OES data (Figure 4.3, Table 4.3) resulted in the following formula, which have been used to calculate $CaCO_3$ and Fe wt%:

$$CaCO_3\ wt\% = Ca\ (cps) / 143.46144 \quad (1)$$

$$Fe\ wt\% = Fe\ (cps) / 1152.29872 \quad (2)$$

Deduced from the coefficient of determination (r^2) the linear regression for Site 1085 can explain 94.05% and 95.94% of the variance in $CaCO_3$ and Fe content, respectively, suggesting reliable estimates of $CaCO_3$ and Fe content of the sediment core (Figure 4.2).

4.3.3 Chronology and Astronomical Tuning of Oxygen Isotopes

The age model for Site 1085 from 0-100 mcd is developed on the basis of the shipboard biostratigraphy and magnetostratigraphy. Oxygen isotope stages were identified by visual correlation with the $\delta^{18}O$ curve of Shackleton et al. (1990, ODP Site 677). This first step was followed by tuning the oxygen isotope record of Site 1085 to an astronomical target curve, which was set by the sum of normalized eccentricity (E), normalized obliquity (T)

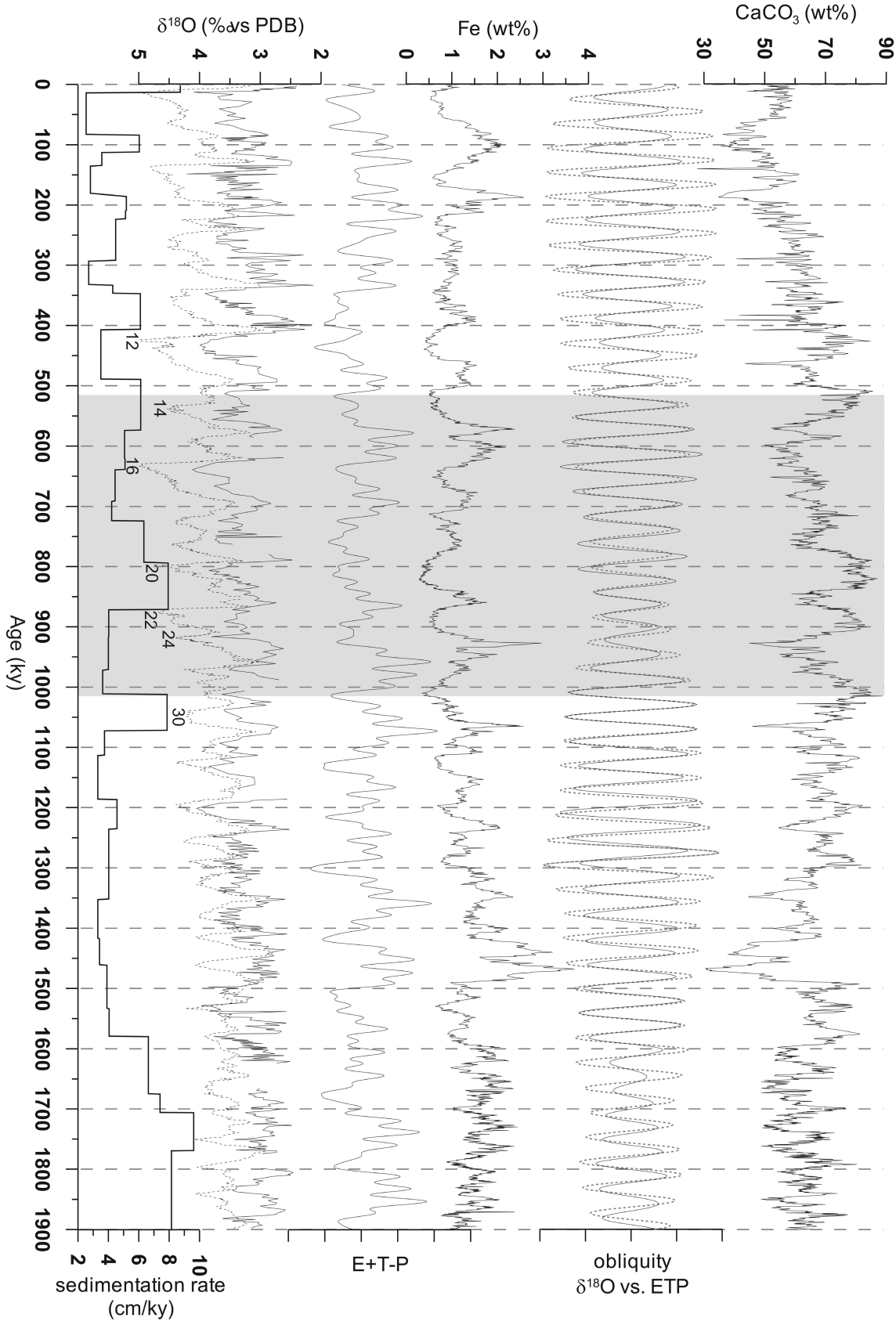

Figure 4.2 For description see following page.

Figure 4.2 Tuned oxygen isotope record of Site 1085 (black line, lower panel) compared to a 5-point moving average of the oxygen isotope Ceara Rise Stack (Lourens et al. in press, stippled line). Nomenclature and position of oxygen marine isotope stages (MIS) are after Shackleton et al. (1990). Below the derived sedimentation rates are plotted. In the middle of the Figure the ETP target curve and the Fe content (in wt%, calibrated Fe intensities) at Site 1085 are shown; note the apparent similarity of both curves. Above the Fe content the obliquity filter (0.02439 ±0.007 cycles/ky) outputs of the tuned oxygen isotope record of Site 1085 and lagged ETP. The upper panel displays the $CaCO_3$ content at Site 1085 derived from the calibrated Ca intensities. The shaded area marks the Mid-Pleistocene Transition.

and negative normalized precession (P) from Laskar et al. (1993) (E+½T-½P). Because the obliquity component of $\delta^{18}O$ is most stable in phase relative to orbital forcing (Clemens 1999), the final age model was obtained by tuning the initial age model to obliquity until the coherency between filtered $\delta^{18}O$ and orbital signal reached a maximum. As a second step, we compared the tuned $\delta^{18}O$ record from Site 1085 with the stacked $\delta^{18}O$ record from the Ceara Rise (Lourens et al. in press). The age model of the latter record is based on orbital tuning of the magnetic susceptibility record to orbital insolation (Bickert et al. 1997). Cross-spectral analysis between both records show a significant coherence over the eccentricity (κ=0.89) and obliquity (κ =0.95) frequency bands at the 95% confidence level. Site 1085 leads the Ceara Rise record by about 5 ky in the obliquity band. This is due to fact that the $\delta^{18}O$ record of 1085 was tuned to insolation and foraminiferal $\delta^{18}O$ is known to lag astronomical forcing in the obliquity band (Imbrie et al. 1984). According to these results, a phase lag of 5 ky between the $\delta^{18}O$ record and the insolation has been subtracted from the tuned ages to obtain the final age model (Table 4.1).

The tuned oxygen isotope record of Site 1085 is presented in Figure 4.2. Comparison of filtered 41-ky component (0.02439 ± 0.007 cycles/ky) of $\delta^{18}O$ with the obliquity component of lagged ETP (Figure 4.2) reveals a good fit. Spectral analysis of $\delta^{18}O$ from 0.90 - 0 Ma shows high spectral power at 100-ky and less power centered at 41-ky and 23-ky. The power spectrum of $\delta^{18}O$ from 1.80 - 0.90 Ma reveals a strong peak only at 41-ky. The $\delta^{18}O$ record gives a good match with the ETP curve (Figure 4.2). Low $\delta^{18}O$ values correspond to maxima in ETP. The Fe intensities show high spectral power at 400-ky and 100-ky from 0.9 - 0 Ma, whereas from 1.80 - 0.90 Ma spectral power is centered at 41-ky. In the latter period the Fe intensity power spectrum lacks a significant peak at 100- and 400-ky. Two results can be drawn from the comparison of calibrated Fe and Ca intensities and the tuned $\delta^{18}O$ record. First, interglacial periods at Site 1085 are characterized by high Fe and low carbonate content, glacial times vice versa. Second, the match between Fe content and ETP curve is remarkably good. Furthermore, $\delta^{18}O$ values and Fe intensities

show similar power spectra with significant periodicities at 100-ky after and at 41-ky before the Mid-Pleistocene Transition.

Cross-spectral analyses indicate that Fe and $\delta^{18}O$ records are coherent in eccentricity from 0.90 - 0 Ma and in obliquity from 1.80 - 0.90 Ma (Table 4.2). In the interval from 0.90 - 0 Ma variations in $\delta^{18}O$ lag ETP by ~6 ky and Fe intensities lag ETP by ~13.6 ky, whereas Fe intensities lag $\delta^{18}O$ by ~9.6 ky. Consistently, prior to the Mid- Pleistocene Transition the $\delta^{18}O$ record lags ETP by ~5.7 ky, Fe intensities lag ETP by ~9.6 ky and Fe intensities lag $\delta^{18}O$ by ~3.8 ky. Thus, our Fe intensity record lags ice volume changes in the obliquity and eccentricity band.

The derived sedimentation rates (Figure 4.2) range between 2.5 and 9.6 cm/ky. From 1.80 Ma up to 1.60 Ma the sedimentation rates are well above 6 cm/ky. Then they decrease to ~4 cm/ky remaining at that value from 1.60 - 0.90 Ma punctuated by a maximum at MIS 30 (1.05 Ma). After the onset of the Mid-Pleistocene Transition sedimentation rates show strong variations between 2.5 and 8 cm/ky superimposed by a long-term decrease.

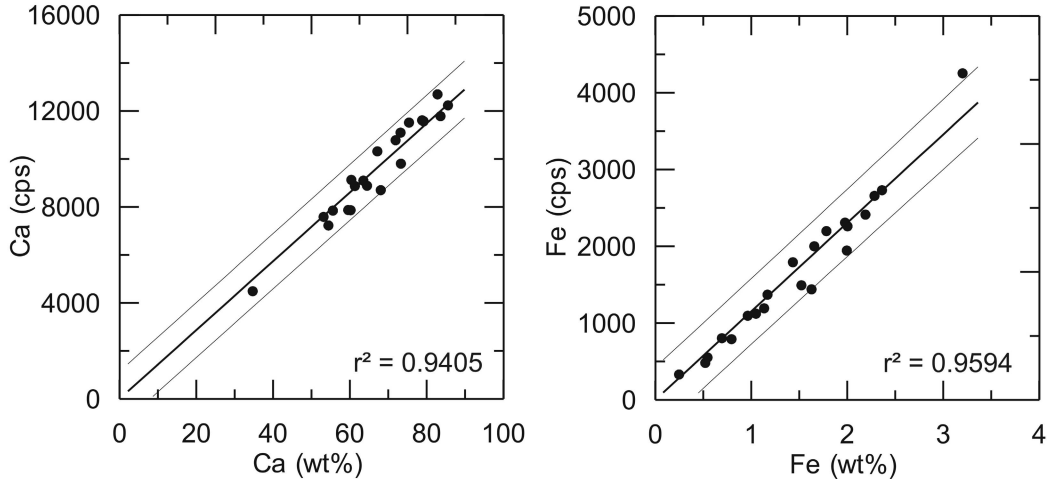

Figure 4.3 Calibration of the XRF core scanner Ca and Fe measurements of Site 1085 to ICP-OES analysis of samples (n=22) taken from the same depth intervals. In each panel the linear regression (bold black line), the upper and lower 95%-prediction limit (light black lines), and the coefficient of determination are given.

Table 4.1 Agemodel for Site 1085 - Pleistocene.

hole depth mcd	age (ka)	phase adjusted age (ka)
1.13	18	13
2.93	89	84
4.62	117	112
5.44	140	135
6.82	189	184
8.14	214	209
8.84	228	223
11.94	297	292
13.04	338	333
13.64	352	347
17.26	411	406
20.16	494	489
25.36	579	574
27.76	626	621
28.66	644	639
30.97	696	691
32.36	729	724
36.79	799	794
42.94	876	871
44.74	921	916
46.94	976	971
48.42	1017	1012
53.12	1077	1072
54.67	1118	1113
57.07	1191	1186
59.34	1241	1236
64.03	1357	1352
66.16	1421	1416
67.68	1466	1461
70.51	1538	1533
72.39	1585	1580
78.69	1680	1675
80.99	1711	1706
87.09	1774	1769
94.57	1866	1861

4.4 Discussion

4.4.1 Age model

Our age model for the $\delta^{18}O$ data of Site 1085 differs slightly from the age model of Anderson et al. (2001) between 1.80 and 1.10 Ma. In the interval prior to 1.72 Ma their ages are up to 40 ky older than ours. After 1.72 Ma the difference between the two age models increased up to ~100 ky at the top of core 1085A-7H. This has several reasons. First, Anderson et al. (2001) only used cores from Hole 1085A instead of the complete composite section. Second, they used spectral analysis to estimate the in-situ sedimentation rate at each single core based on the assumption that 41-ky cycles are present in these early Quaternary sediments. Their basic stratigraphic frame are the shipboard stratigraphic tie points, thus their age assignments do not differ substantially from these tie points. Because Anderson et al. (2001) were only interested in the phase relation between different proxies, there was no need for a complete isotope stratigraphy for this interval, and hence their age model was tentative. However, we feel confident in that time interval to have a consistent tuning supported by the good match between Fe content, $\delta^{18}O$ records and ETP, both in amplitude variation and pattern (Figure 4.5). Prior to 1.60 Ma the tuning procedure was difficult due to the lack of oxygen isotope stage identification, but comparison to the $\delta^{18}O$ record of the Ceara Rise (Lourens et al. in press) (Figure 4.2) corroborates our tuning. These overall problems in tuning could be due to a dramatic change in sedimentation rates at 1.60 Ma, where sedimentation rates step-like increase (Figure 4.2).

The tuned age model is consistent with the shipboard assigned magnetostratigraphic ages, except for the position of the Brunhes-Matuyama boundary. The tuned age model gives an age for the shipboard assigned depth of the Brunhes-Matuyama that is about 160 ky older. This rather large error might suggest that the tuning is not correct around the Brunhes-Matuyama boundary. Nevertheless, the $\delta^{18}O$ record of Site 1085 matches the $\delta^{18}O$ record from the Ceara Rise in this part of the record (Figure 4.2). One reason for the discrepancy could be that eminent coring-induced magnetization (CIM) of the cores (Berger, Wefer, Richter, et al. 1998) could have deteriorated the magnetic signal. Despite this discrepancy, we feel confident to have a consistent tuning in this period, again, supported by the good correlation of the Fe intensity signal to the ETP curve and the good match of $\delta^{18}O$ and obliquity amplitude modulations (Figure 4.2).

4.4.2 Pleistocene sedimentation pattern at Site 1085

In the Pleistocene sedimentation rates at Site 1085 vary from 2.5 to 9.6 cm/ky (Figure 4.2). Significant changes occur prior to 1.60 Ma when average sedimentation rates drop from 10 to 4 cm/ky. This change corresponds to a significant shift in African climate towards more arid conditions (deMenocal 1995) and to the end of the Matuyama Diatom Maximum (Lange et al. 1999) due to a decrease in terrigenous input and in productivity.

The Fe and Ca intensities used as proxies for terrigenous and carbonate sedimentation are negatively correlated over the entire record. Compared to the sedimentation rate, these data indicate that the sedimentation at Site 1085 was mainly influenced by dilution and productivity. In glacial periods carbonate content is high and terrigenous input low, suggesting higher productivity of carbonate, as suggested by Anderson et al. (2001), and less input of terrigenous matter by the Orange River. In interglacial times, the adjacent African continent is more humid therefore the Orange River delivered more terrigenous material.

The transport of continental-derived material in the South Atlantic to the deep sea results from a complex interaction of river and wind input and distribution by ocean currents (Petschick et al. 1996). Today the catchment area of the Orange River receives most of its precipitation in the austral summer, when the ITCZ extends far to the south (Nicholson 2000), and the westerlies are shifted southward. Partridge et al. (1997) show that the amount of precipitation in the eastern part of South Africa is linked to the South African monsoon. The South African monsoon is strong when the North African monsoon is weak due to the anti-phasing in summer insolation between the hemispheres. Cross-spectral analyses of data from Site 1085 reveal coherency between $\delta^{18}O$ and Fe intensity in the obliquity band from 1.80 - 0.90 Ma and in the eccentricity band from 0.90 - 0 Ma (Figure 4.4). Fe intensities lag $\delta^{18}O$ by ~3.8 ky in obliquity and ~9.5 ky in eccentricity (Table 4.2). This result is surprising, because we would expect the terrigenous signal to lead ice volume changes as documented in many other records (e.g. Ceara Rise, Bickert et al. 1997). Pleistocene fluctuations of benthic oxygen isotope record are sensitive to Northern Hemisphere ice sheet variations and changes in deep water temperature (Shackleton et al. 1973, Ruddiman et al. 1989). Imbrie et al. (1992) showed that climate variance at precession and obliquity frequencies appeared to be linearly forced by Northern Hemisphere summer insolation. Thus, interglacial periods characterized by $\delta^{18}O$ minima have been related to Northern Hemisphere insolation maxima. However, Fe concentrations peak at Southern Hemisphere insolation maxima, which is consistent with enhanced

precipitation in the catchment area of the Orange River during stronger South African monsoon. Because precessional variations in the summer insolation are in anti-phase between the hemispheres, maxima in Southern and Northern Hemisphere insolation are offset by half a precessional cycle. This offset is documented in the phase lag between Fe intensities and $\delta^{18}O$ values at Site 1085 in the Pleistocene.

Table 4.2 Coherency and phase relationship (in ky) of $\delta^{18}O$, Fe intensities and ETP.

Parameter	100 ky (0.9 - 0 Ma)		41 ky (1.8 - 0.9 Ma)	
	coherency	phase	coherency	phase
$\delta^{18}O$ vs. ETP	0.74	5.99	0.89	5.76
Fe vs. ETP	0.69	13.63	0.90	9.61
Fe vs. $\delta^{18}O$	0.90	9.57	0.88	3.84

Notes: We analyzed the variability in the frequency domain using the Blackman-Tuckey approach with 30% lags with a Parzen window at the 95%-confidence level (k = 0.56). Parantheses highlight coherencies below the 95%-confidence level.

Moreover, in the Pliocene seasonal climate patterns in South Africa have been reported to reinforce one another. During high amplitudes in precession, eolian input of terrigenous matter in austral winter conditions and fluvial input in austral summer conditions into the Cape Basin have been enhanced (Christensen et al. 2002, Rogers and Bremner 1990). Terrigenous input, therefore, is strongly modulated by the amplitude of the precession signal enhancing the power in the eccentricity band. The effect of eccentricity in modulating the seasonal cycle through the precession cycle is more pronounced over land areas especially in the tropics (Short et al. 1991). The amplification of the eccentricity cycle, as seen in the terrigenous record of Site 1085, could be related to temperature fluctuations in the tropics, which might be exported to higher latitudes by the atmospheric circulation (Short et al. 1991). Amplitude variance analysis of the resulting Fe intensity time series (Figure 4.5) clearly shows strong variance in the 100-ky cycle from 1.80 - 0 Ma suggesting strong linkage between low-latitude African climate and sedimentary pattern at Site 1085 throughout the Pleistocene. At times of high amplitudes in the precession band and maximum solar insolation in the Southern Hemisphere wetter conditions over the catchment area of the Orange River prevail, causing larger volumes of terrigenous sediment supply. On the other hand, in the $\delta^{18}O$ record the variance in the 100-ky band occurs at 0.64 Ma. The dominance of the 100-ky period in the terrigenous supply prior to

large fluctuations in the Northern Hemisphere ice volume (Christensen et al. 2002, Vidal et al. 2002, Westerhold et al. subm. a) and the anti-phasing of $\delta^{18}O$ values and Fe intensities suggest that increased shelf erosion during sea level lowering in glacial times is not the primary mechanism controlling the terrigenous sedimentation at Site 1085. The long-period terrigenous flux cycle could be related to low-latitude continental climate processes acting independently of ice, particularly in the early Pleistocene (Crowley et al. 1992, Mix et al. 1995, Harris et al. 1997).

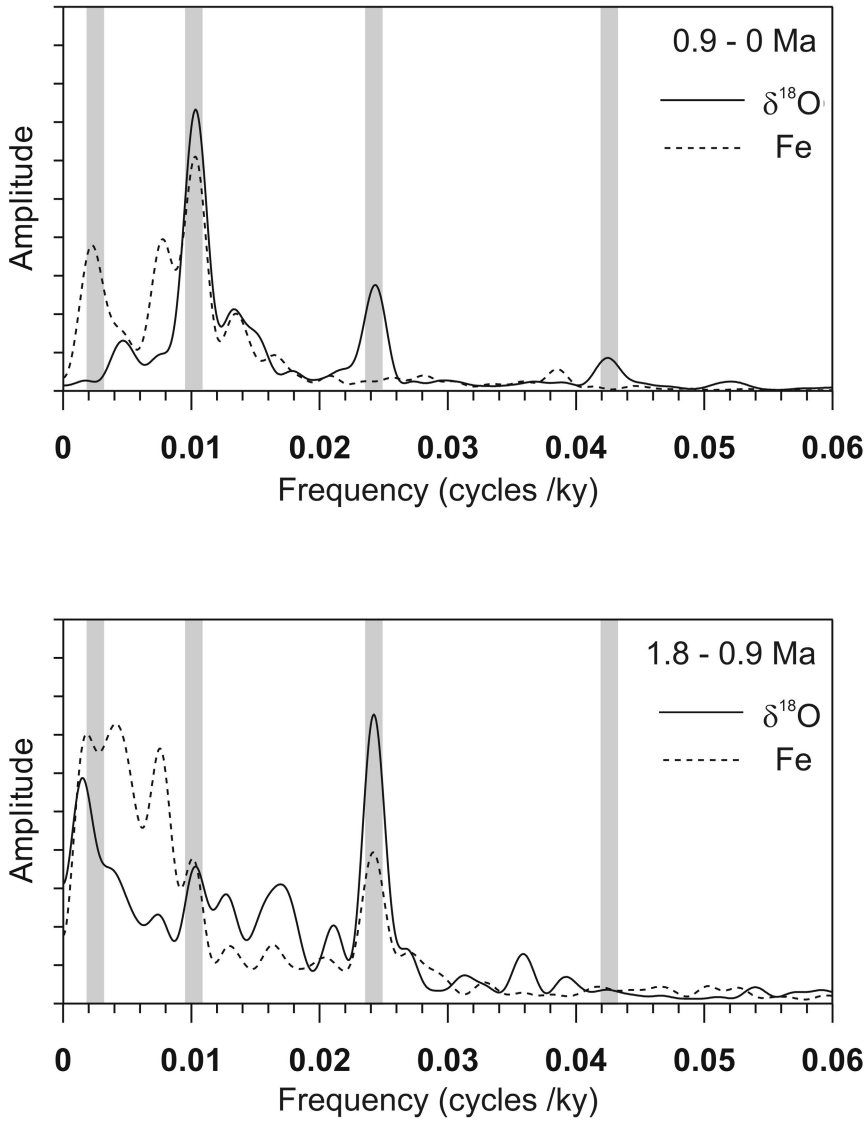

Figure 4.4 Blackman-Tuckey power spectrum of the tuned oxygen isotopes (solid black line) and Fe concentration (strippled back line) of ODP Site 1085 computed with the *AnalySeries* software package (Paillard et al. 1996) for the period from 0.9 - 0 Ma (upper panel) and 1.8-0.9 Ma (lower panel). Prior to spectral analysis trends have been removed. Spectral estimates are based on a Bartlett smoothing window with 512 lags and an interpolated time interval of 1 ky resulting in a bandwidth of 0.002930, whereas the confidence interval at 80% is given by $0.563664 < DP/P < 2.722162$. The gray bars mark main orbital frequencies (400-, 100-, 41- and 23-ky).

However, before the Mid-Pleistocene Transition the terrigenous signal incorporates the strong 41-ky cyclicity of the glacial-interglacial cycles (Figure 4.4). In glacial times overall less terrigenous material is delivered by the Orange River pointing to substantial drying of South African climate. The increase in the 41-ky amplitude variation in the Fe intensity record from 1.60 - 1.40 Ma corresponds to a major phase of Northern Hemisphere ice-sheet growth (Figure 4.5). At 1.0 Ma the 41-ky amplitude variation in the Fe intensity signal is dampened by the onset of the strong 100-ky Northern Hemisphere ice age cycles, causing an aridification in the South African climate system. The simultaneous development of cooler and drier glacial conditions in South Africa has been attributed to the coeval expansion of Northern and Southern Hemisphere polar ice-sheets (Broecker & Denton 1989) and their influence on subtropical African climate (deMenocal 1995). Clemens et al. (1996) have shown that extensive glacial conditions have weakened the summer monsoon circulation giving rise to drier climatic conditions. Thus, a combined low-latitude and high-latitude climate forcing indicated by dominant 100-ky and 41-ky terrigenous flux cycles dominated the South African climate system from 1.80 - 1.00 Ma (Figure 4.5). The pronounced 41-ky cyclicity points to a regulation of the low-latitude climate system of the Southern Hemisphere by high latitude glacial climates as postulated for the Northern Hemisphere by deMenocal (1995).

After the onset of the Mid-Pleistocene Transition at MIS 24 (0.92 Ma), strong glaciations triggered a southward shift of tropical and subtropical circulation systems in the South Atlantic (Bloemendahl et al. 1995) and a reduction in deep water circulation (Schmieder et al. 2000, Raymo et al. 1997). At Site 1085 the onset of the Mid-Pleistocene Transition is characterized by a decrease in response to obliquity in the terrigenous record (Figure 4.4), suggesting that the sensitivity of the Orange River drainage system to trade wind forcing decreased. But still strong influence from the African monsoonal circulation is documented by high amplitude variations in the 100-ky cycle. More interesting are the extremely low Fe values in the strong glacial periods at MIS 22, 20, 16, 14, and 12 (Figure 4.2) pointing to extremely dry periods in the catchment area of the Orange River. In these strong glacial periods the increase in the Antarctic ice-sheet might have caused frontal zones in the ocean and atmosphere to move equatorward. The equatorward shift might inhibit monsoonal circulation and therefore moisture transport to the catchment area of the Orange River. High input of terrigenous material during interglacial periods at 1085 coincides with intensified Asian monsoonal circulation (deMenocal 1995).

With the predominance of 100-ky ice age cyclicity driven by the large ice-sheets in the Northern Hemisphere since 0.64 Ma, the sedimentary pattern at Site 1085 documents strong changes in sedimentation rates. Enhanced terrigenous input occurs in interglacial periods. In contrast to the older part of the record, hardly any response in the obliquity or precession related band appears in the Fe intensities (Figure 4.4). The full establishment of 100-ky ice age cycles has been related to strong changes in the circulation system and shift in frontal systems (Schmieder et al. 2000) which might have perturbed South African climate conditions.

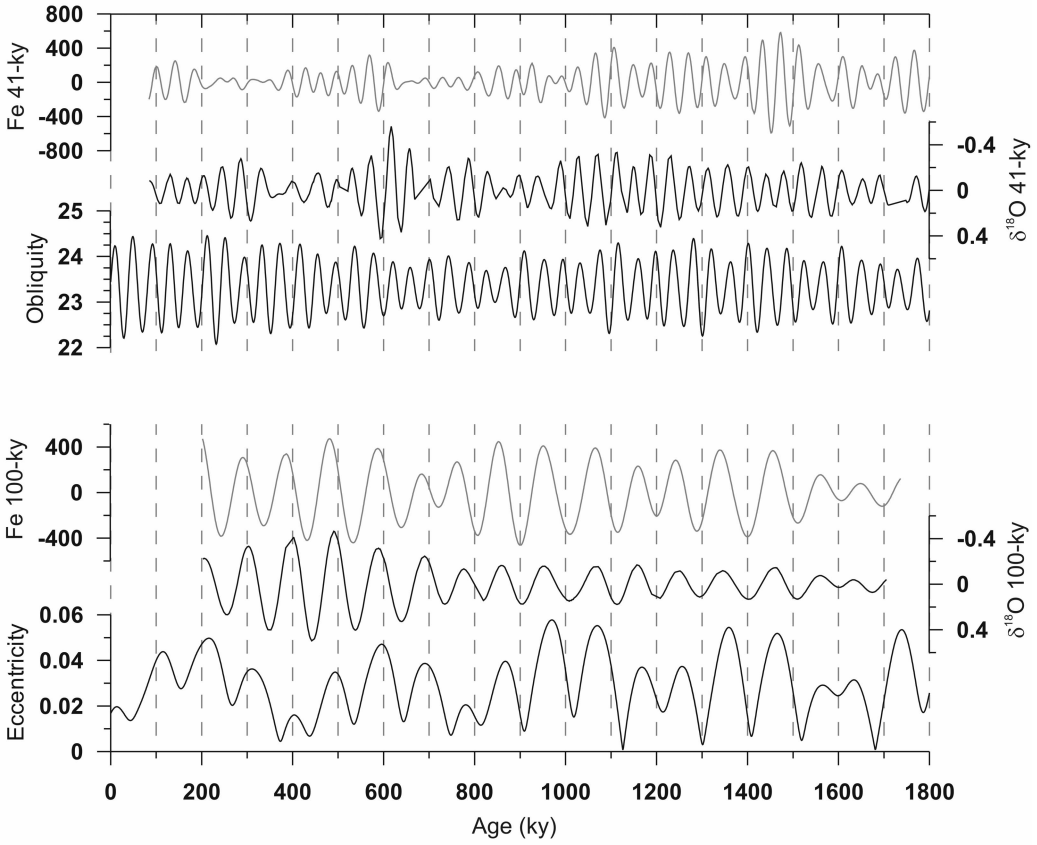

Figure 4.5 Temporal changes in amplitude of oxygen isotopes and Fe content from Site 1085 in the obliquity (upper panel) and eccentricity (lower panel) band. The amplitude variations have been calculated with the Program ENVELOPE (Schulz et al. 1999). The obliquity and eccentricity values are taken from Laskar (1993, $La_{1,1}$).

Distinct shifts in South African climate at 1.70 Ma, 1.00 Ma and 0.64 Ma documented at Site 1085 hence are tied to coeval shifts in high-latitude climate and corresponds to climatic shifts in the Northern Hemisphere as reported by deMenocal (1995) and emphasize the importance of high- and low-latitude climate linkage throughout the Pleistocene. Furthermore, the results from Site 1085 are consistent with the results from Schefuss et al. (2003) who could show that dry conditions in Southern Africa are linked to tropical SST changes, in a way that arid conditions prevail in times of cooler

tropical SST and decreased austral summer insolation in South Africa. As shown by deMenocal (1995) for North Africa and Asia, aridity in South Africa followed the 41-ky and then 100-ky periods associated with glacial-interglacial cycles of the late Pliocene and Pleistocene, documenting regulation of the low-latitude climate system by high-latitude glacial climates.

Our results are in contrast to the findings of Stuut et al. (2001) who state that continental aridity in southwestern Africa for the last 300 ky increased during interglacials. The discrepancy in the precipitation variations between western and eastern part of South Africa can be deduced from the present climate conditions. During austral winter the ITCZ is shifted towards the equator and the moisture-bearing southwesterly winds blow over the southwestern tip of the African continent, causing rain. Due to the eastern circulation around the high-pressure cell in the southwestern Indian Ocean, the eastern part of Africa remains relatively dry. During austral summer the ITCZ moves far south and hence the southwesterly winds do not reach southwestern Africa causing low precipitation. In contrast, the eastern part of Africa now receives more rain from the Indian Ocean. An equatorward shift of the atmospheric frontal zones during glacials related to the expansion of the Antarctic ice-sheet (Brathauer and Abelmann 1999, Kanfoush et al. 2000) would invoke enhanced precipitation over southwestern Africa due to then the northward moved moisture-bearing southwesterly winds, and deliver less moisture to southeastern Africa (i.e. the drainage area of the Orange River) due to the northward driven high-pressure cell in the southwestern Indian Ocean. In this case, the fluctuations of the Antarctic ice-sheet and the associated latitudinal shift of atmospheric frontal zones can explain the contrary response in the sedimentary records. Moreover, Stuut et al. (2001) documented that the southwestern African aridity record shows a phase lag of 3 - 3.5 ky relative to the $\delta^{18}O$ record and Antarctic air temperature in the obliquity frequency. They presume that Southern Hemisphere climate is sensitive to changes in the Antarctic ice volume and sea-ice extend. In turn, this would drive the Southern Westerlies northward during glacials and cause enhanced precipitation at the western boundaries of the continents. Unfortunately, the terrigenous record of Site 1085 does not reveal any response in the obliquity frequency in the last 300 ky. But if we assume that the mechanism for the observed 3 - 4 ky phase lag between $\delta^{18}O$ record and Fe content at Site 1085 prior to the Mid-Pleistocene Transition is the same as proposed by Stuut et al. (2001), than we conclude that South African climate is mainly controlled by Antarctic ice-sheet fluctuation before to the Mid-Pleistocene Transition. The complex climate in South Africa is completed by the influence of South African monsoonal circulation strength driven by Southern Hemisphere insolation.

4.5 Conclusion

Benthic oxygen isotope data and high-resolution XRF core scanning data (Ca, Fe) of ODP Site 1085 were used to reconstruct the South African climate history and the changing pattern of carbonate and terrigenous deposition in the eastern South Atlantic during the Pleistocene. An astronomically calibrated timescale for the last 1.8 Ma was developed by tuning the benthic $\delta^{18}O$ record to obliquity using the $La93_{1,1}$ (Laskar et al. 1993) solution.

Pleistocene sediments off the river mouth of the Orange River consist primarily of biogenic carbonate ooze diluted by varying input of terrigenous matter delivered by the nearby Orange River. Input of terrigenous matter was high during interglacial and low during glacial periods. Additionally, high input of terrigenous material during interglacial periods at Site 1085 coincides with intensified Asian monsoonal circulation. Similar to oxygen isotopic variations, the Fe content reveals strong 41-ky cycles during the early Pleistocene and strong 100-ky cycles after the Mid-Pleistocene Transition. These variations in river runoff are linked to shifts in high- (i.e. ice-sheet oscillations) and low-latitude (i.e. tropical SST) climate change. Cross-spectral analysis reveals that the river runoff and thus precipitation in the catchment area of the Orange River is driven by Southern Hemisphere insolation. In contrast to the oxygen isotope record, the Fe content shows a strong 100-ky cycle component throughout the entire record, which derives from the amplitude-modulation of precession.

Aridity in South Africa followed the 41-ky and then 100-ky cyclicity associated with glacial-interglacial cycles of the late Pliocene and Pleistocene, documenting regulation of the low-latitude climate system by high-latitude glacial climates. South African climate is mainly controlled by the shift of the westerlies due to fluctuations of the Antarctic ice-sheet prior to the Mid-Pleistocene Transition.

Acknowledgments

We are indebted to M. Segl and her team for carefully supervising the stable isotope analyses, to M. Zabel for ICP-OES analyses, and to A. Wuelbers and W Hale for help at the Bremen Core Repository. We would like to thank L. Dupont, F. Hilgen, L. Lourens and J.-B. Stuut for discussion. We thank the Ocean Drilling Program for providing samples. This study was funded by the Deutsche Forschungsgemeinschaft (We 992/28).

Middle to Late Miocene History of Carbonate and Terrigenous Sedimentation at South Atlantic ODP Site 1092

T. Westerhold, T. Bickert

Fachbereich Geowissenschaften, Universität Bremen, 28334 Bremen, Germany

in preparation

Abstract

We present high-resolution X-ray fluorescence (XRF) core logging data performed every 2 to 4 cm downcore on ODP Site 1092 (46°24.70´S, 07°04.79´E, 1974 mbsl, Leg 177), drilled on Meteor Rise in the sub-Antarctic sector of the Southern Ocean, spanning the middle to late Miocene. Based on overlapping multiple hole measurements we present calcium and iron records along the composite depth record of the Shipboard Scientific Party, which has been slightly revised below 115.41 mcd. Site 1092 was drilled to improve and complement the existing record at Site 704 (Leg 114), located only 34 nmi to the southeast, to monitor changes in the flux and chemistry of deep waters, and the movement of the Antarctic Circumpolar fronts.

Carbonate sedimentation prevails in the investigated period (13.7 - 5.3 Ma) at the Meteor Rise with contents of well over 90 wt%. Increases in sedimentation rates, opal deposition and Fe concentrations at 11.2 Ma indicate higher surface productivity and eolian dust input. Distinct drops down to 60 wt% in carbonate content accompanied by enhanced iron concentrations occur between 9.3 - 9.1 and 6.2 - 5.3 Ma. These carbonate minima are associated with an increased opal content, suggesting a northward migration of Antarctic fronts due to cooling processes on Antarctica. The decrease in calcium carbonate at 9.2 Ma corresponds to the nadir of the carbonate crash events in the eastern South Atlantic and Central East Pacific pointing to fundamental changes in global ocean chemistry and nutrient distribution. A pronounced change in iron concentration at ~10 Ma is interpreted as desert expansion in Patagonia and intensification of southern hemisphere westerly winds in conjunction with major ice-sheet expansion on Antarctic. Decreased terrigenous input to Site 1092 at 7.7 Ma documents the expansion of grasslands which reduced influx of wind-blown dust to the South Atlantic. The carbonate and terrigenous sedimentation pattern is discussed in terms of global ocean circulation changes and the evolving geochemical basin-to-basin fractionation.

5.1 Introduction

The Miocene was marked by large changes in deep-ocean circulation due to horizontal and vertical tectonics in combination with the intensification of the Antarctic glaciation (Kennett and Shackleton 1976; Woodruff and Savin 1989, Zachos et al. 2001a). The onset of the Antarctic Circumpolar Current (ACC), ascribed to tectonic and paleoceanographic changes, promoted thermal isolation and glaciation of the Antarctic continent during the late Oligocene and early Miocene (Pagani et al. 2000) influencing intermediate-, deep-, and bottom-water formation in the Southern Ocean. After the middle Miocene climate optimum, an intensification of the ACC is the consequence of the middle Miocene cooling step and ice buildup on Antarctica. Near Antarctica, diatom-rich sediments prevail since 14 Ma and indicate the presence of the Polar Front closer to East Antarctica than at present (Kennett and Barker 1990). It has been proposed that the strengthening of the ACC would act to increase geostrophic flow at depth, intensifying upwelling along Antarctica and increase northward propagation of AAIW (Pagani et al. 2000). Moreover, at the end of the middle Miocene cooling step a strong basin-to-basin asymmetry developed between North Atlantic and North Pacific, with the deep Atlantic collecting carbonate and the North Pacific diatomaceous silica (Keller and Barron 1983). The large-scale transfer of dissolved silicate from the Atlantic into the Pacific points to a major reorganization in the deep circulation of the ocean (Woodruff and Savin 1989) and is thought to assign the beginning of the modern ocean circulation (e.g. Berger and Wefer 1996). The shoaling of the Central American Seaway is proposed to be the main cause for the basin-to-basin fractionation and the evolving modern circulation with strong Northern Component Water (NCW) flux to the south. NCW outflow into the Pacific is significantly reduced when the Central American Seaway reached a critical depth of 1000 m by 12 - 13 Ma (Duque-Caro 1990), dramatically changing the intermediate and deep circulation in the tropical Pacific, the western boundaries of the South Pacific and South Atlantic (Nisancioglu et al. 2003). The timing is close to the proposed ages for increased NCW formation (Keller and Barron 1983, Woodruff and Savin 1989, Delaney 1990, King et al. 1997, Wei and Peleo-Alampay 1995) and major changes in carbonate sedimentation in the eastern Equatorial Pacific (Lyle et al. 1995), western Equatorial Atlantic (King et al. 1995) and Caribbean Sea (Roth et al. 2000). This event, entitled the Miocene ‘carbonate crash’ (Lyle et al. 1995), has been ascribed to a shoaling of the lysocline in the eastern Equatorial Pacific. Due to the closure of the Central American Seaway, the deep water exchange was cut off and the Pacific carbonate saturated NCW was replaced with older, carbonate-

undersaturated deep water from the Southern Ocean (Lyle et al. 1995, Farrell et al. 1995). Information about the carbonate crash in Pacific and Atlantic Ocean are based on records deeper than 3000 m water depth, a level that is highly sensitive to fluctuations in the carbonate compensation depth in these regions (Lyle et al. 1995, King et al. 1997). Recently, carbonate crash events have been reported from intermediate water depth in the eastern South Atlantic well above the regional lysocline (Westerhold et al. subm. a). These reductions in carbonate content have been ascribed to dilution by enhanced terrigenous input linked to sea level lowering and to dissolution due to enhanced inflow of corrosive SCW during Miocene glacial events.

Here, we present high-resolution X-ray fluorescence (XRF) core logging data performed every 2 to 4 cm downcore to reconstruct the long-term history of carbonate and terrigenous sedimentation at South Atlantic ODP Site 1092 for the middle to late Miocene. We revised the composite depth record of the Leg 177 Shipboard Scientific Party (Gersonde, Hodell, Blum, et al. 1999) using overlapping multiple hole measurements. Based on magnetostratigraphy, we study the carbonate and biogenic sedimentation patterns in conjunction with the evolution of the Antarctic ice-sheets, changes in ocean circulation, changes in ocean geochemistry and the development of the Antarctic Circumpolar Current. We focus on the questions:

- How are changes in terrigenous input related to changes in ocean circulation and continental climate conditions?
- Are the carbonate crash events detected in the eastern South Atlantic also apparent in the Atlantic Sector of the Southern Ocean? What are the implications of the carbonate crash events observed in different oceans in different water depth with respect to the global climate change in the middle to late Miocene?
- How does the evolving modern thermohaline circulation change the sedimentation pattern at the Meteor Rise?

5.2 Material and methods

Ocean Drilling Site 1092 (46°24.70´S, 07°04.79´E) was drilled on the northern slope of Meteor Rise in the sub-Antarctic sector of the Southern Ocean (Figure 5.1). The site is located approximately 3° north of the present-day Polar Front in the Polar Front Zone (PFZ) which is bounded by the Sub-Antarctic Front (SAF) to the north and the Polar Front (PF) to the south. The PFZ separates cold, nutrient-rich Antarctic surface water to the south from warmer, less nutrient-rich Sub-Antarctic Surface Water to the north.

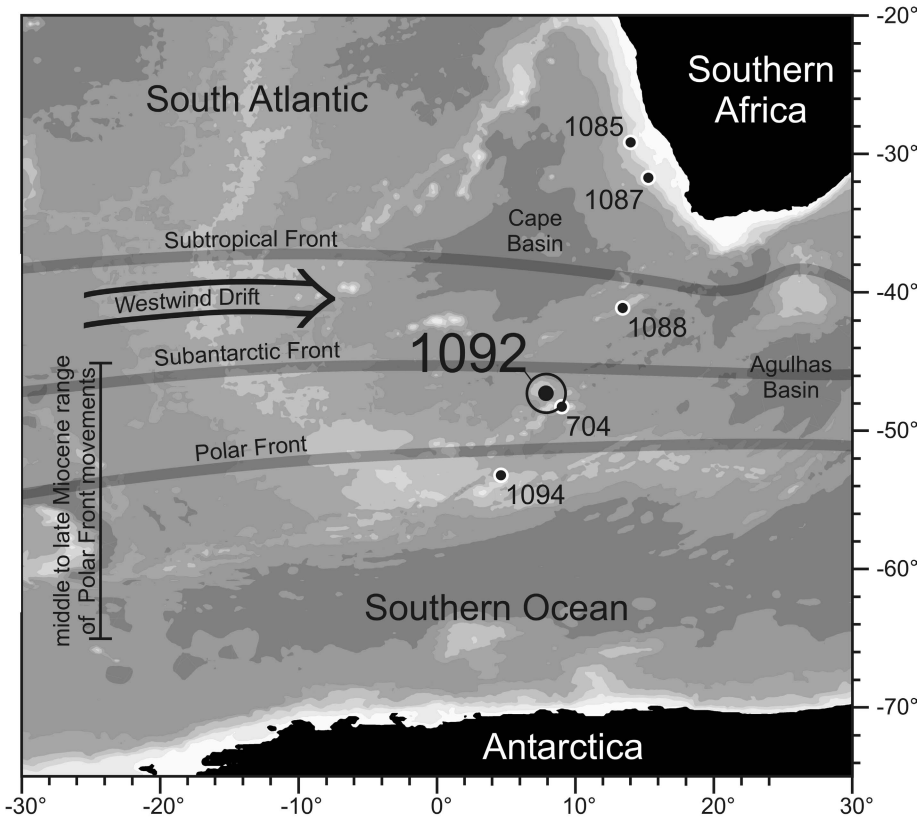

Figure 5.1 Location of ODP Site 1092 in the southeastern Atlantic sector of the Southern Ocean drilled during Leg 177 and the major fronts of the Antarctic Circumpolar Current (from Hodell et al. 2002, modified). Also shown are the positions of ODP Sites 704, 1085, 1087, 1088 and 1094. Range of the Polar Front movements in the middle to late Miocene after Cervato and Burckle (2003). Sea floor below 1000 m is gradually shaded in 1000 m steps.

Today, the PFZ also represents a transition zone in sediment lithology from diatom ooze near the PF to a mixed siliceous-calcareous ooze near the SAF. The sediments drilled (1974 m water depth) are above the regional calcite lysocline and are bathed today by upper Circumpolar Deep Water (CDW) with certain amounts of North Atlantic Deep Water (NADW). The primary objective for drilling at Site 1092 was to recover a carbonate-bearing, Late Neogene sediment sequence to improve and complement the existing record at Site 704 (Leg 114), located only 34 nmi to the southeast. At Site 1092 four (A-D) overlapping holes were drilled by APC technology down to 188 mbsf, yielding a complete spliced section of 211 mcd of Holocene to early Miocene age. The sediments consist of pale brown-green to pure white nannofossil oozes with mixtures of diatom and foraminifer oozes and muds (Gersonde, Hodell, Blum, et al. 1999). The sedimentary section was subdivided into two subunits. In subunit IA (0 - 53.89 mcd) the sedimentary column consists of alternation of nannofossils, foraminifers, diatoms, mud and rarely dropstones. Carbonate content fluctuates between 17 and 95 wt%. In subunit Ib (53.89 - 185 mcd) nannofossils are the predominant lithologic component and are replaced by

diatoms or foraminifers in only a few intervals. Carbonate content is well over 80 wt%. Below 112 mcd nannofossil ooze is the only major lithologic type with minor admixtures of diatoms and foraminifers.

Continuous measurements of calcium (Ca) and iron (Fe) composition of sediments at ODP Site 1092 were performed using the X-ray fluorescence (XRF) core scanner at the Bremen ODP Core Repository, which allows high-resolution, non-destructive analyses of major and minor elements at the surface of split cores. XRF data were collected every 2 - 4 cm down-core along mbsf depth over a 1 cm^2 area using 30 seconds count time and an X-ray current of 0.087 mA (for further details concerning this method see Jansen et al. 1998, Röhl and Abrams 2000). In total, 8656 measurements were taken from Holes 1092 A (cores 3-13, 15-18), B (1, 2, 4, 6, 8, 9, 11-18), C (1-3, 7, 9, 10, 13-18) and D (1, 3), including double measurements of selected sections.

For the conversion of the Fe intensities into elemental contents total digestion preparation of 20 discrete sediment samples were carried out according to Zabel et al. (2001) and analyzed by inductively coupled plasma-optical emission spectrometry ("Optima 3300 R" Perkin Elmer). Precision was better than 2%. The accuracy of element determinations was checked using standard reference material USGS MAG-1. For the calibration of the Ca intensities, published bulk carbonate (wt%) data from Diekmann et al. (2003) have been used.

All data and tables are available in electronic format at PANGAEA - Network for Geological and Environmental Data (www.pangaea.de). In this paper only Table 5.1 is presented, Tables 5.2 through 5.7 are available online.

5.3 Chronology

5.3.1 New revised composite depth (rmcd)

Multisensor track (MST) and color reflectance data collected from holes 1092A-D were used to construct an initial shipboard composite section for Site 1092 down to 188 mcd (base of Core 177-1092A-18H). Aboard the ship it was already noticed that much distortion occurred within individual cores. Alignment of MST and color reflectance features by simply adding a constant to the mbsf core depth turned out to be rather difficult and needed shore-based reevaluation. Moreover, below 110 mcd downhole variations in physical properties appeared with much lower amplitude than above this depth and showed a rather low signal-to-noise ratio due to the high amount of carbonate present (Gersonde, Hodell, Blum, et al. 1999).

Based on both MST and XRF data high resolution cross-hole correlation documents that the shipboard composite section (mcd) is consistent with hole-to-hole correlations above core 1092A-12H. Therefore, the new rmcd is equal to the mcd from 0-115.41 rmcd. Cores outside the shipboard splice have been stretched or squeezed to conform with the overall mcd depth scale. This was done by matching the Fe intensity data to the shipboard magnetic susceptibility or overlapping Fe intensity data from adjacent holes. The resulting mapping pairs are given in Table 5.4. Drilling-related expansion and compression in these poorly consolidated sediments contribute to this lack of precise correlation of depth scales between holes.

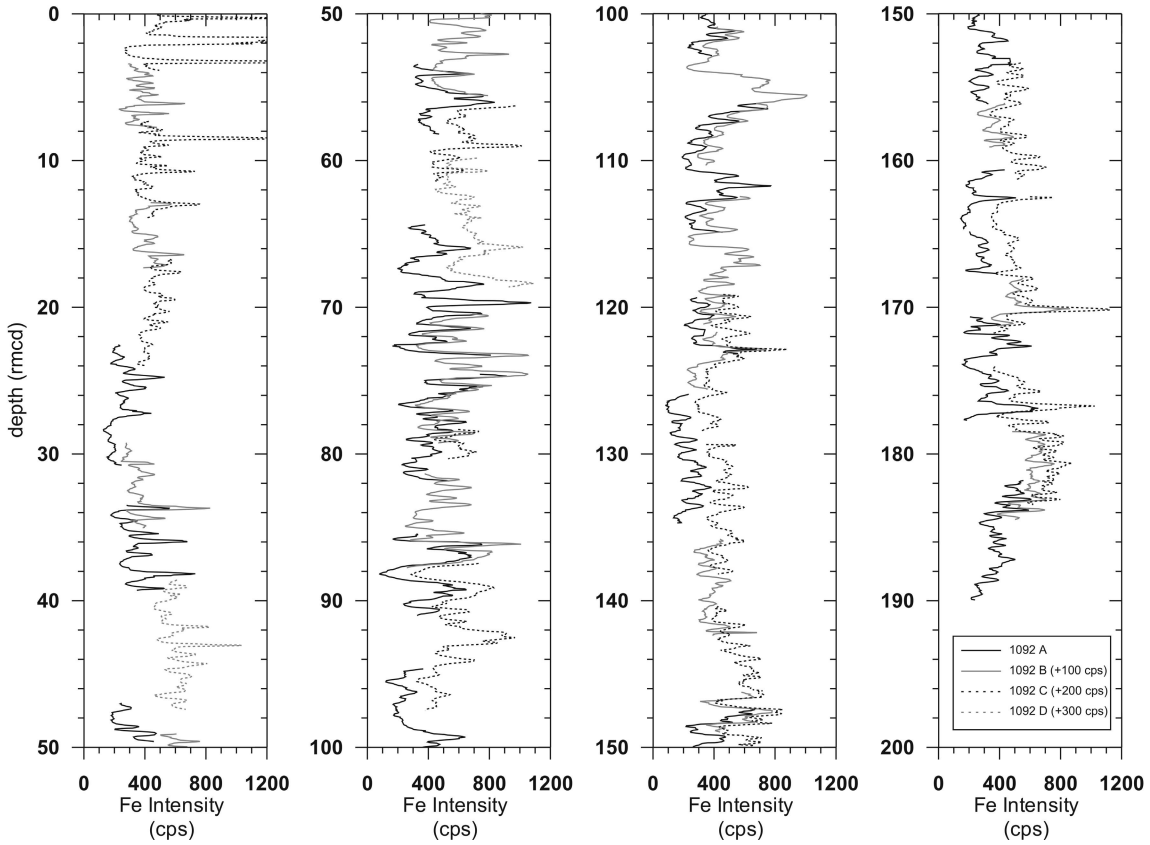

Figure 5.2 Composite section for Site 1092. Smoothed (5-point average) Fe intensity data are plotted for Holes 1092A (black line), 1092B (gray line), 1092C (black dotted line) and 1092D (gray dotted line). The Fe intensity data are shown in revised meters composite depth (rmcd). Offsets have been applied for clarity.

The uppermost modification of the composite section depth occurs around 115.41 mcd at core 1092A-12H. In the shipboard splice core 1092A-11H is followed by 1092C-12H, which could not be scanned due to heavy sampling. Hence, core 1092B-12H was scanned, matching well with core 1092A-11H and 1092C-12H according to XRF data and magnetic susceptibility. Correlation from 1092C-12H to the underlying core in the splice (1092A-12H) is very poor for MST data. Additionally, core 1092B-12H and 1092A-12H

show no good match in the XRF data following the shipboard splice. But core 1092B-12H can be well correlated to 1092A-12H and 1092C-13H when the latter are moved about 92 cm up relative to 1092B-12H. Below this, matching of cores according to the shipboard splice was not possible and therefore we created a new splice by cross-hole correlation of Fe intensity data. The data used to construct the composite section and to determine core overlaps are presented on a revised composite depth scale (rmcd) in Figure 5.2. The depth offsets that comprise the new composite section for Holes 1092A-1092D are given in Table 5.5. Cores which are not in the revised composite section were adjusted to the rmcd composite depth scale by correlation of XRF data (Table 5.3). The new spliced composite section for Site 1092 is given in Table 5.1. A spliced composite section along the correlated XRF data has been constructed down to 190.14 rmcd (1092A-18H, 6).

Table 5.1 List of tie points used to create the revised composite depth sequence (rmcd) for Site 1092

Core, section, interval (cm)	Depth (mbsf)	Revised Composite Depth (rmcd)		Core, section, interval (cm)	Depth (mbsf)	Revised Composite Depth (rmcd)
177-				177-		
1092C-1H-3, 56	3.56	3.56	tie to	1092B-1H-3, 4	3.04	3.59
1092B-1H-5, 94	6.94	7.49	tie to	1092C-2H-1, 86	4.86	7.51
1092C-2H-5, 28	10.28	12.93	tie to	1092B-2H-4, 20	12.10	12.95
1092B-2H-7, 16	16.06	16.91	tie to	1092C-3H-2, 32	15.32	16.92
1092C-3H-6, 60	21.60	23.20	tie to	1092A-3H-1, 100	18.50	23.23
1092A-3H-6, 4	25.04	29.77	tie to	1092B-4H-2, 68	28.58	29.79
1092B-4H-5, 28	32.68	33.89	tie to	1092A-4H-2, 56	29.06	33.93
1092A-4H-5, 116	34.16	39.03	tie to	1092D-1H-1, 60	37.00	39.07
1092D-1H-6, 148	45.38	47.45	tie to	1092A-5H-4, 61.5	41.62	47.49
1092A-5H-5, 57	43.07	48.94	tie to	1092B-6H-1, 4	45.44	48.99
1092B-6H-4, 56	50.46	54.58	tie to	1092A-6H-1, 120	47.20	54.63
1092A-6H-2, 124	48.47	56.53	tie to	1092C-7H-1, 32	51.82	56.54
1092C-7H-3, 68	55.18	60.52	tie to	1092D-3H-1, 84	56.24	60.55
1092D-3H-5, 72	62.12	66.43	tie to	1092A-7H-2, 76	57.76	66.45
1092A-7H-6, 24.5	63.25	71.93	tie to	1092B-8H-2, 8	65.98	71.94
1092B-8H-5, 12	70.52	76.47	tie to	1092A-8H-2, 56	67.06	76.51
1092A-8H-5, 108	72.08	81.53	tie to	1092B-9H-2, 32	75.17	81.58
1092B-9H-6, 62	80.38	86.17	tie to	1092A-9H-2, 85	76.85	86.18
1092A-9H-3, 130	78.80	88.13	tie to	1092C-10H-1, 80	80.80	88.16
1092C-10H-6, 12	87.62	95.52	tie to	1092A-10H-1, 100	85.00	95.54
1092A-10H-5, 72	90.72	101.26	tie to	1092B-11H-1, 48	93.38	101.31
1092B-11H-4, 76	98.16	106.79	tie to	1092A-11H-1, 84	94.34	106.83
1092A-11H-5, 72	100.22	112.71	tie to	1092B-12H-1, 40	102.80	112.73
1092B-12H-6, 100	110.90	120.83	tie to	1092C-13H-2, 36	110.36	120.87
1092C-13H-6, 146	117.46	127.97	tie to	1092A-13H-2, 72	114.72	128.02
1092A-13H-5, 104	119.54	132.84	tie to	1092C-14H-3, 60	121.60	132.88
1092C-14H-6, 20	125.70	136.98	tie to	1092B-14H-3, 133	127.73	137.01
1092B-14H-6, 132	130.22	141.50	tie to	1092C-15H-1, 132	128.82	141.54
1092C-15H-5, 114	134.64	147.36	tie to	1092A-15H-1, 12	131.62	147.38
1092A-15H-6, 108	140.08	155.84	tie to	1092C-16H-3, 116	141.16	155.88
1092C-16H-6, 144	145.94	160.66	tie to	1092A-16H-2, 16	142.66	160.67
1092A-16H-5, 142	148.42	166.29	tie to	1092C-17H-3, 112	150.62	166.46
1092C-17H-6, 144	155.22	171.06	tie to	1092A-17H-1, 94	151.44	171.08
1092A-17H-5, 86	156.79	176.43	tie to	1092C-18H-2, 104	158.54	176.45
1092C-18H-6, 140	160.90	182.81	tie to	1092A-18H-1, 128	161.28	182.85
				end of splice		

5.3.2 Stratigraphy

A first age model for Site 1092 was developed by Censarek and Gersonde (2002) based on diatom biostratigraphy supported by shipboard paleomagnetic data. Recently, Evans and Channell (2003) published a detailed magnetic stratigraphy from ~5.9 to 13.5 Ma based on high-resolution paleomagnetic studies. These two timescales are partly not consistent (for discussion see Evans and Channell 2003). The improved correlation between holes at Site 1092 presented in our study reduced the number of polarity subchrons within C5n.2n from four to three, consistent with the number of 'cryptochrons' recognized in marine oceanic anomaly data (Evans et al. subm.). The revised composite depth has been ratified by normalized remanence (mean NRM/IRM) data (Evans et al. subm.).

In this study we combined the age models of Evans and Channell (Magneto-stratigraphy from 5.9 - 9.8 Ma, 2003) and the revised age model of Evans et al. (Magneto-stratigraphy from 9.8 - 13.5 Ma, subm.). Ages of the Geomagnetic Polarity Time Scale are after Cande and Kent (1995). Based on biostratigraphic investigations a hiatus has been reported at 68.46 rmcd spanning the period from 5.3 - 3.8 Ma (Zielinski and Gersonde 2002). Spectral analysis of the Fe intensity record between 6.137 Ma (Base C3An.1n) and the proposed age of the hiatus basis of 5.3 Ma revealed strong 100-ky cyclicity. Therefore, we tuned the Fe intensity record to eccentricity in this interval to reevaluate the basal age of the early Pliocene hiatus at Site 1092. According to the tuning the basal age of the late Pliocene hiatus at 68.48 rmcd is 5.324 Ma. The combined age model used in this study is presented in Table 5.6.

Linear sedimentation rates (Figure 5.4) in the middle to late Miocene vary around 1 cm/ky increasing across the middle to late Miocene boundary to 3 cm/ky. After 8.7 Ma, linear sedimentation rates decrease towards 1 cm/ky. Despite the hiatus from 5.324 - 3.8 Ma, the sedimentary sequence documents condensed intervals from 12.4 - 12.2, 11.45 - 11.1, 9.25 - 9.0 and 7.1 - 6.3 Ma characterized by sedimentation rates below 0.5 cm/ky.

5.4 Results

5.4.1 Conversion of Fe and Ca intensities into elemental concentrations

The calibration of Fe intensities by linear regression (Figure 5.3) resulted in the following formula, which was used to calculate Fe concentrations in bulk sediment in wt%:

$$\text{Fe wt\%} = ((\text{Fe (cps)} - 51.63431) / 1476.6146) \quad (1)$$

Deduced from the coefficient of determination (r^2) the linear regression can explain 94% of the variance in Fe content in the sediment cores at Site 1092.

For calibration of Ca intensities we used $CaCO_3$ (wt%) data from Diekmann et al. (2003). Ca intensity exhibit an exponential relationship to carbonate content, although we would have expected a linear relation as described by Westerhold et al. (subm. a) for ODP Site 1085 and 1087. The exponential behavior of Ca intensities can be explained by its relation to changes in density. At Site 1092, higher Ca intensities correspond to higher densities in the sediment, suggesting that density changes are driven by carbonate variations. Because the XRF scanner determines the Ca elemental concentration over an area of 1 cm^2, higher densities in the sediment denote higher amounts of Ca in the measured area and thus in the intensity measured. The acquired equation for the calibration of Ca intensities at Site 1092 is a follows:

$$CaCO_3 \text{ wt\%} = (\ln (\text{Ca (cps)}) - 6.214458) / 0.034699 \quad (2)$$

Deduced from the coefficient of determination (r^2) the exponential regression can explain 78% of the variance in carbonate content at Site 1092.

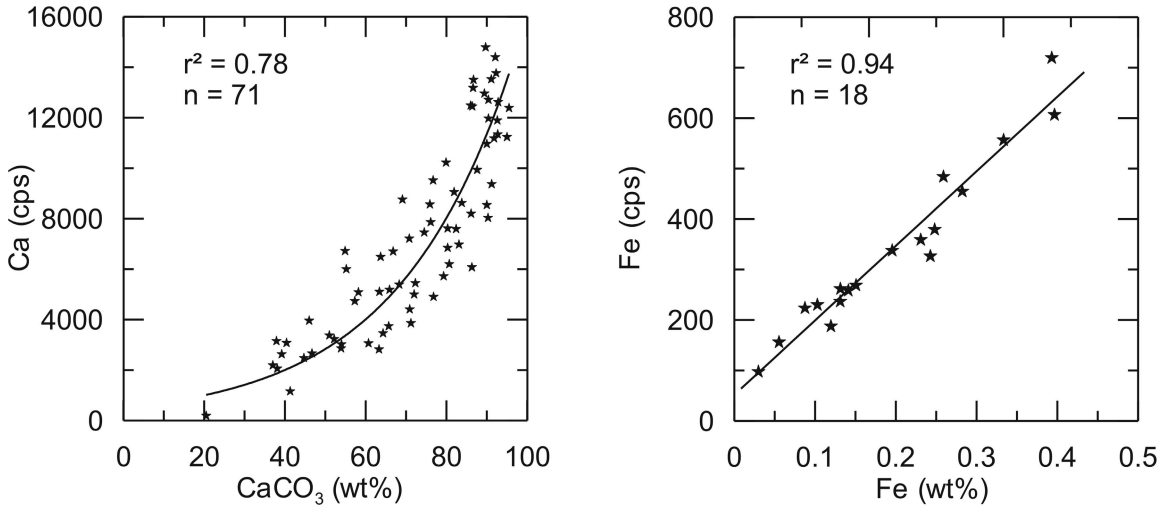

Figure 5.3 Calibration of the XRF core scanner Ca and Fe intensities of Site 1092 to $CaCO_3$ data (Diekmann et al. 2003) and Fe from ICP-OES analysis. After removal of outliers, 71 samples for calcium carbonate and 18 ICP-OES samples for Fe were used for calibration.

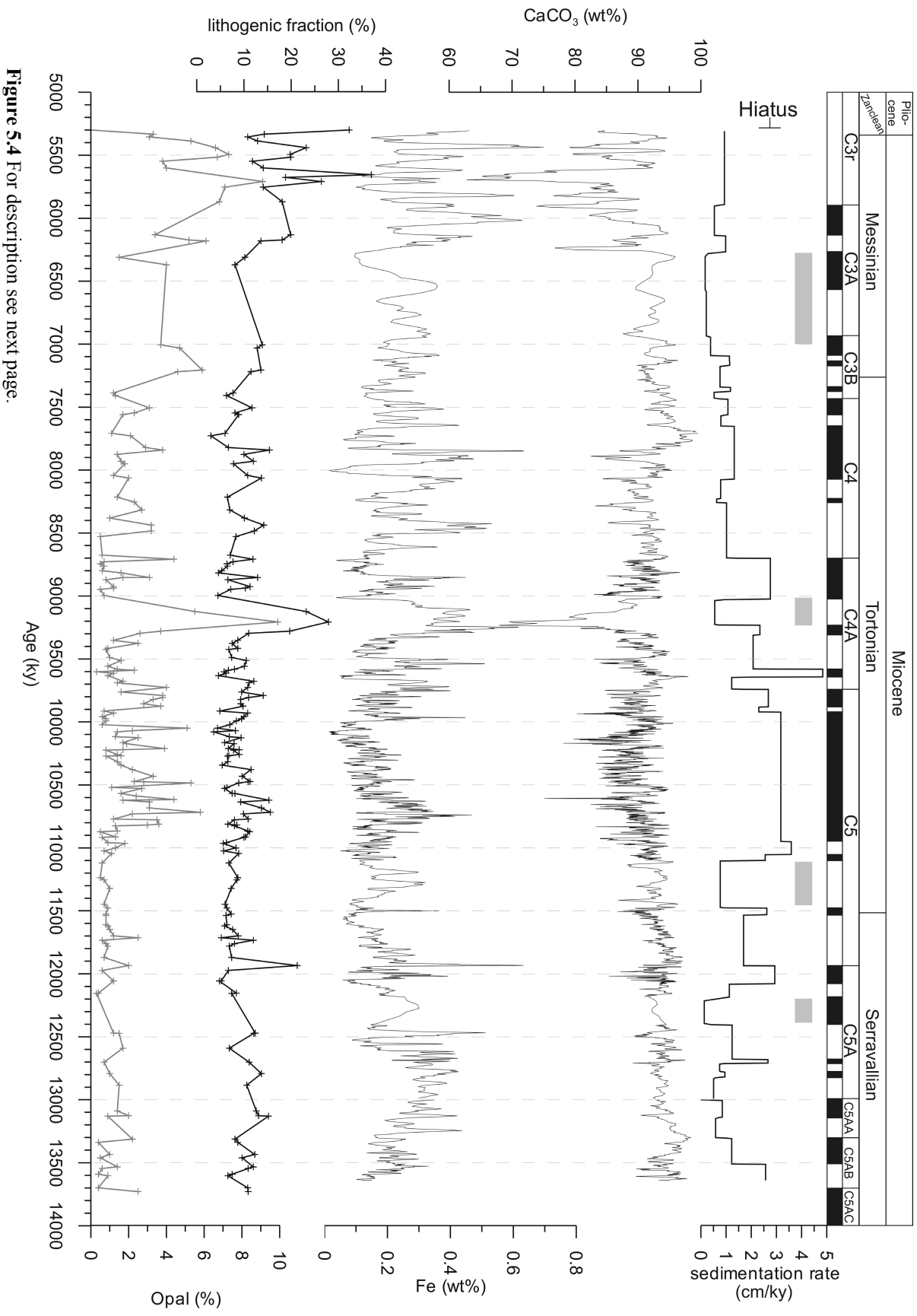

Figure 5.4 For description see next page.

Figure 5.4 Site 1092 time series of $CaCO_3$ (wt%) and Fe concentration (wt%) derived from the calibrated XRF intensities. Lithogenic fraction and opal data are from Diekmann et al. (2003). Paleomagnetic interpretation from Evans and Channell (2003) and Evans et al. (subm.). Sedimentation rates resulting from the age model is plotted at the top. Bars mark the position of condensed sections.

5.4.2 XRF results for the revised composite section

Using the new rmcd scale, we constructed a composite record for Fe and Ca intensities by stacking of all scanned sections after alignment to the rmcd scale excluding those intervals that did not correlate well with other holes. All data were interpolated at 4 cm intervals using a least square smoothing function with a 10 cm window. The composite Fe and Ca intensities stacks for Site 1092 have been converted into elemental concentrations and are plotted versus age in Figure 5.4. The stacked XRF Ca and Fe record is given in Table 5.7. In the middle to late Miocene calcium carbonate concentrations vary between 66 and 99 wt%, equivalent to 5000 - 16000 counts per second (cps) in Ca intensities. Fe concentrations vary between 0.03 and 0.65 wt%, equivalent to 100 - 1000 cps in Fe intensities. Because Ca intensities reflect the $CaCO_3$ content of the sediments, mainly derived from coccoliths and foraminifers, and Fe variations reflect the fine grained terrigenous components, the Ca and Fe records are used as proxies for carbonate and terrigenous sedimentation, respectively. Two periods of drastic variations in carbonate are observed from 9.3 - 9.1 Ma and 6.0 - 5.6 Ma. In these periods carbonate content drops down to 68 and 65 wt%, respectively. In contrast, the Fe content shows much more variability with period of higher values centered at 13.2 - 12.5, 12.0 - 11.9, 10.8 - 10.6, 9.7 -8.8, 8.5 - 7.6 and 6.2 - 5.3 Ma. The drop in carbonate content at 9.3 - 9.1 Ma is associated with higher Fe content. In contrast, the strongest carbonate drawdown centered at 5.65 Ma in the lower-carbonate period from 6.2 - 5.3 Ma is not associated with very high Fe content. Nevertheless, this interval is characterized by the highest Fe content fluctuations observed in the record of Site 1092.

5.5 Discussion

5.5.1 Miocene biogenic and lithogenic sedimentation pattern at Site 1092

In the Southern Ocean the PFZ marks a boundary in the underlying sediments. Calcareous oozes predominate north of the Polar Front, while diatomaceous oozes dominate between the ACC Polar Front and the Antarctic summer sea-ice limit in the ACC Antarctic Zone (Burckle and Cirilli 1987). As already shown in the nearby Site 704 variations between carbonate and opal content are linked to movements in the PFZ, in a way that higher opal contents indicate a more northern position relative to Meteor Rise

(Froelich et al. 1991). Changes in depositional pattern of biogenic sediments at Sites 704 and 1092 have been attributed to shifts and intensification of the ACC frontal system (Froehlich et al. 1991, Diekmann et al. 2003) due to changes in regional and global ocean circulation (Kennett and Barker 1990, Hodell and Venz 1992, Warnke et al. 1992, Hillenbrand and Fütterer 2001).

In the middle to late Miocene sedimentation at Site 1092 is dominated by biogenic sediments consisting of nannofossil ooze with low amounts of planktonic foraminifera and biogenic opal, suggesting prevailing calcareous phytoplankton productivity under oligotrophic conditions (Diekmann et al. 2003). At ODP Site 704, lower carbonate concentrations in glacial period have been partly attributed to dissolution and dilution by biogenic silica and terrestrial material, which are all related to the position of the PFZ (Froelich et al. 1991). Because Site 1092 is located in 1974 m water depth, well above the modern calcite saturation horizon at 3400 m (Howard and Prell 1994), carbonate dissolution due to shoaling of the lysocline is probably not affecting carbonate sedimentation patterns at Site 1092. Throughout the middle to late Miocene the carbonate sedimentation pattern at Meteor Rise is stable, punctuated by two periods of stronger variability from 9.3 - 9.1 and 6.2 - 5.3 Ma. A distinct change at 11.2 Ma in carbonate export production is indicated by a strong increase in sedimentation rates at Site 1092 (Diekmann et al. 2003). At the same time an increase in carbonate saturation in the deep Atlantic is documented at Ceara Rise and in the eastern South Atlantic (King et al. 1997, Westerhold et al. subm. a) caused by the redistribution in carbonate sedimentation pattern between Atlantic and Pacific due to the evolving geochemical basin-to-basin fractionation (Berger et al. 1993).

The most important factor in controlling sedimentation conditions at Site 1092 is lateral sediment transport by the ACC (Diekmann et al. 2003; Gersonde, Hodell, Blum, et al. 1999), which causes winnowing and focusing in this regions as described by Frank et al. (1996). A vigorous ACC was established during the early Miocene which caused the thermal isolation of Antarctica (Kennett 1977, Lawver et al. 1992, Pagani et al. 2000). Increased thermal contrast in the Antarctic induced stronger wind fields, which led to an enlargement of the upwelling system, as indicated by the progressive northward displacement of the Antarctic convergence and also to continued growth of the Antarctic ice sheet (Kennett 1977). In the middle to late Miocene episodic pulses in deep- and bottom-water circulation caused widespread deep-sea hiatuses during periods of increased polar refrigeration (Barron and Keller 1982). Such invigorations of ACC intensity are

apparent at Site 1092 (Figure 5.4) as periods of low sedimentation rates and hiatuses. Condensed sections appear at 12.4 - 12.2, 11.5 - 11.1, 9.2 - 9.0 and 7.1 - 6.3 Ma. The hiatus around the Miocene-Pliocene boundary is also evident in deeper Sites 1090 and 1093 and correlates with a current induced erosion event in the southwestern Atlantic (Censarek and Gersonde 2002, Diekmann et al. 2003). Additionally, synchronous stepwise decreases in illite/(kaolinie+chlorite) ratios at ODP Site 1088 and 1092 represent intensification of the regional ocean circulation at 14 - 12 and 8.0 Ma (Diekmann et al. 2003).

Along with opal sedimentation, lithogenic sediment components can also lead to mutual dilution affecting relative proportion of the diverse sediment components. At Site 1092 variations in lithogenic sediment components correlate well with variations in opal content (Diekmann et al. 2003) suggesting carbonate dilution during periods of enhanced opal production and terrigenous input. In the middle to late Miocene Fe concentrations and lithogenic fraction correlate well at Site 1092 suggesting that higher Fe intensities indicate enhanced terrigenous input.

Lithogenic fluxes have three potential sources: fine-grained material transported by currents, ice-rafted debris (IRD) and wind-blown dust. With increasing distance from source areas, advection of fine-grained particles by deep-water currents becomes the most important mode of terrigenous matter transported to deep-sea sediments (Petschik et al. 1996). In the deep South Atlantic sediment transport and distribution of clay is primarily controlled by the deep-water advection of CDW and NADW in the late Quaternary (Diekmann et al. 1996, Petschik et al. 1996, Gingele and Schmiedl 1999, Walter et al. 2000, Kuhn and Diekmann 2002), such that during glacial periods accumulation rates of terrigenous material increased significantly by sediment focusing due to enhanced concentration of suspended terrigenous material transported by CDW (Frank et al. 1996, Diekmann et al. 1996, Walter et al. 2000, Bayon et al. 2003). In glacial periods the ACC region is mainly bathed by CDW bearing chlorite-rich particles from Patagonia and the Antarctic Peninsula (Petschik et al. 1996, Diekmann et al. 2000, Walter et al. 2000, Chase et al. 2003). Because higher Fe concentrations are associated with maxima in $\delta^{18}O$ values in the middle to late Miocene section of Site 1092 (pers. comm. H. Paulsen 2003), we suggest that like in the Quaternary increased accumulation of terrigenous material is due to an enhanced load of suspended terrigenous material during glacials.

A first identifiable IRD peak above background levels at Site 1092 is present in the late Pliocene at ~3.18 Ma, and IRD peaks become progressively larger thereafter, reaching a maximum at 2.8 Ma (Murphy et al. 2002). Minor amounts of IRD can be expected after

~9.6 Ma when first peaks in IRD in the southwest sub-Antarctic South Atlantic (Ciesielski and Weaver 1983), at the Kerguelen Plateau and in the Australian-Antarctic basin (Ehrmann 1994) show up. Because the procedure and technique of IRD identification uses the fraction larger than 150 µm and the XRF core scanner basically measures the fine bulk fraction, part of the Fe concentration could be due to background rafting of fine grained particles from Antarctica. However, IRD is a minor source for deep-sea sediments (Petschik et al. 1996) and thus contributes negligibly to terrigenous material accumulating at Site 1092 in the middle to late Miocene.

Dust fluxes to the Southern Ocean have been reported to be one of the lowest in the world (Rea 1994) and generally have been very low throughout the Cenozoic (Hovan and Rea 1992). Enhanced input of wind blown particles from the southeastern American continent is considered to be relatively minor compared to increases in terrigenous sediment accumulation rates during glacial periods (Diekmann et al. 2000, Walter et al. 2000). Hence, lithogenic accumulation rates as a proxy for Southern Ocean dust flux have been ascribed to be invalid (Maher and Dennis 2001). Nevertheless, periods of climate cooling give rise to significantly enhanced availability of dust (Ridgwell and Watson 2002). In contrast, enhanced iron flux to the glacial Southern Ocean is reported to be dominantly eolian, largely dust ablated from Patagonia (Kumar et al. 1995). High terrigenous contents were recorded at ODP Site 1094 (Figure 5.1), where glacial peaks in metal (Fe and Ti) concentrations have been observed, probably associated with increased dust inputs due to increased aridity and desert expansion in Patagonia (Filippelli et al. 1999). Synchronous increase in opal accumulation rates and export production north of the Polar Front in the sub-Antarctic Southern Ocean is thought to be fueled by iron fertilization of surface water delivered by eolian input from glacial Patagonian deserts (Martin et al. 1990, Kumar et al. 1995, Ikehara et al. 2000). Long-distance transport of eolian detritus to Site 1092 is mainly achieved by advection within the Antarctic Circumpolar Current and the Circumpolar Deep Water (Petschik et a. 1996). Thus, Fe is not derived from a single source area and transported along a single path. But it can be concluded, that high Fe concentrations, whether delivered by winds or ocean currents, are indicative of arid sources with prevailing physical weathering related to glacial climates.

Figure 5.5 - see next page. Variations of Fe content (wt%) of Site 1092 between 13.8 and 5.3 Ma compared to illite/(kaolinite+chlorite) ratio of Site 1092 (Diekmann et al. 2003), non-carbonate Silt/Clay ratio of Site 1088 with 3-point running average in gray (Diekmann et al. 2003) and 21-ky FFT smooth of Site 1085 $\delta^{18}O$ record (Vidal et al. 2001, Westerhold and Bickert). References: (1) Krijgsman et al. (1999); (2) Bickert et al. (in press), (3) Quade et al. (1989), (4) Lyle et al. (1995), (5) Siesser (1980), (6) Diekmann et al. (2003), (7) Westerhold et al. (subm. a), (8) Wei and Peleo-Alampay (1997), (9) Guo et al. (2002), (10) Ehrmann (1994), (11) Westerhold and Bickert (subm.). For discussion see text.

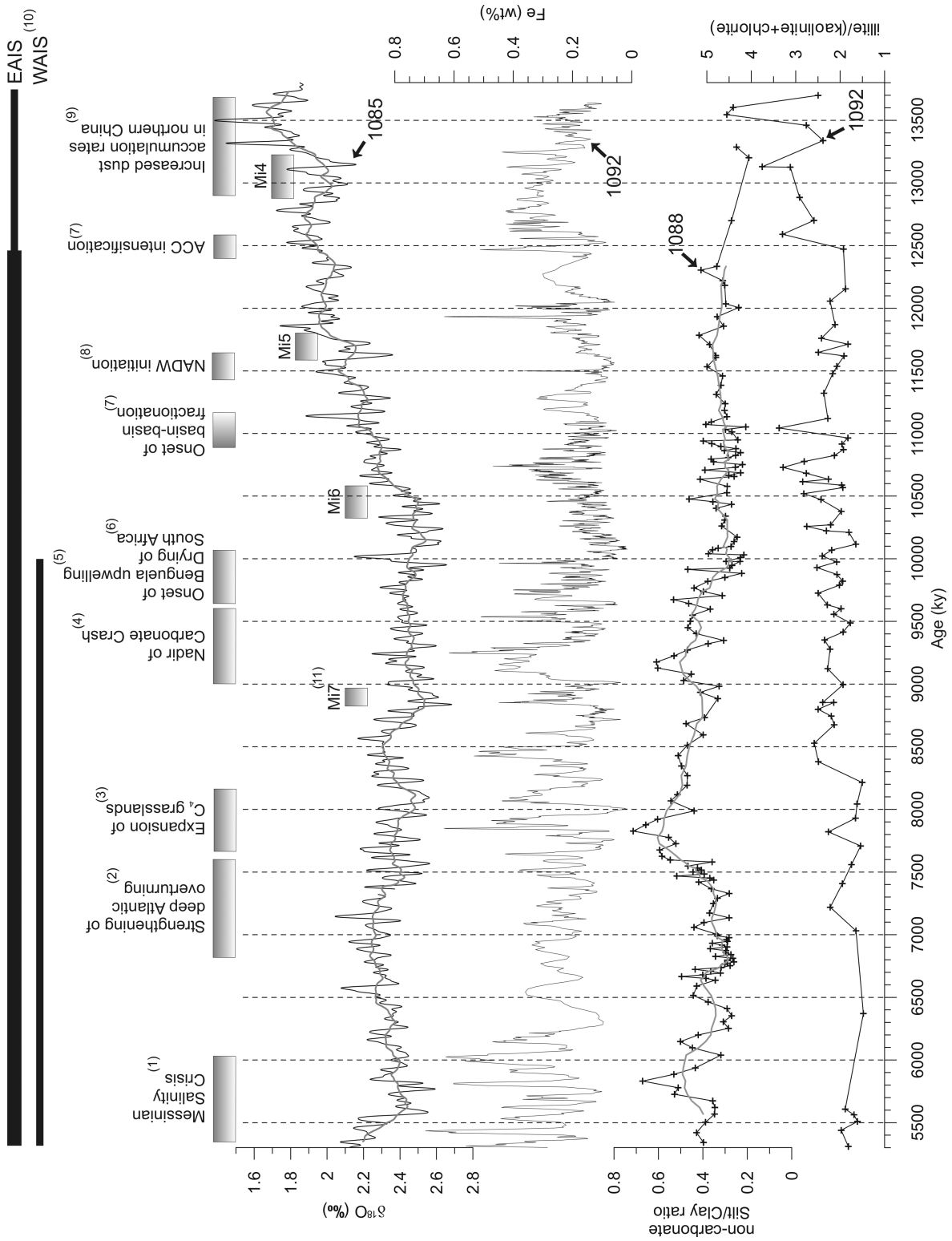
EAIS
WAIS (10)
Messinian Salinity Crisis (1)
Strengthening of deep Atlantic overturning (2)
Expansion of C4 grasslands (3)
Nadir of Carbonate Crash (4)
Onset of Benguela upwelling Drying of South Africa (5) (9)
Onset of basin-basin fractionation (7)
NADW initiation (8)
ACC intensification (7)
Increased dust accumulation rates in northern China (6)
Mi4
Mi5
Mi6
Mi7 (11)
1085
1092
1088
δ18O (‰)
Fe (wt%)
illite/(kaolinite+chlorite)
non-carbonate Silt/Clay ratio
Age (ky)

The occurrence of iron-rich illites, suggesting arid weathering conditions in the source area, and coincident maxima in lithogenic silt/clay ratios at ODP Site 1088 have been interpreted to represent augmented long-distance transport of eolian silt due to stronger wind speed during arid phases (Diekmann et al. 2003). As seen in Figure 5.5, higher Fe concentrations corresponds to periods of enhanced silt/clay ratios from 10.0 - 7.6 and 6.3 - 5.6 Ma suggesting enhanced dust input due to increased aridity. Because Site 1092 is situated in the westwind drift and westward flowing Antarctic Circumpolar Current, we suggest that terrigenous material transported to the Meteor Rise in the middle to late Miocene originated mainly from Patagonia and the Antarctic Peninsula. Therefore, the increase in Fe concentration after 10 Ma points to the intensification of southern-hemisphere westerlies and desert expansion in Patagonia. Synchronously, aridification occurred in southern Africa (Diekmann et al. 2003, Westerhold et al. subm. a, Diester Haass et al. in press) and the Benguela upwelling regime begins, which is attributed to major influx of cold waters linked to ice-sheet expansion on Antarctica (Siesser 1980, Diester-Haass et al. 1992). The reestablishment of a major ice-sheet on Antarctica by 10 Ma (e.g. Miller et al. 1991, Zachos et al. 2001a) gave rise to increased latitudinal climate gradients that changed the atmospheric circulation pattern driving ocean currents and upwelling (Hay and Brock 1992). Further evidence for major changes in atmospheric circulation linked to ice-sheet expansion is documented by enhanced aridity in the Asian interior and the onset of the Indian and east Asian monsoons, about 9 - 8 Ma ago (Zhisheng et al. 2001). Increased aridity is inferred at this time for mid-latitude continental regions including Australia, Africa, North America and South America, and may have fostered the development of grasses and the consequent evolution of grassland adapted biota (Flower and Kennett 1994, Cerling et al. 1997).

In contrast, more humid conditions in southern Africa established at 7.7 Ma inferred from decreased silt/clay ratios and a shift towards iron depleted illites (Diekmann et al. 2003). The decreasing Fe concentrations at Site 1092 also suggest less arid conditions in Patagonia. These results are inconsistent with the drying of tropical South America (Harris and Mix 2002) and prevailing arid conditions in the Orange River drainage area (Westerhold et al. subm. a). Such change towards drier climate during the late Miocene is additionally indicated by palynological evidence as well as the expansion of grassland habitats and C4 plants (Figure 5.5) (e.g. Quade et al. 1989, Cerling et al. 1997). This change in climate coincides with the strengthening of deep Atlantic overturning starting between 7.6 and 6.8 Ma, parallel to the late Miocene carbon shift (Bickert et al. in press),

suggesting stronger influx of NADW to the Southern Ocean. Thus, the expansion of grasslands probably reduced wind erosion and therefore the influx of wind-blown dust to the South Atlantic. Moreover, the strengthening of the thermohaline circulation and associated enhanced NADW flux to the Southern Ocean might have reduced the amount of dust derived particles to reach the Meteor Rise.

After a period of strong Antarctic glaciation from 7 - 6.5 Ma (Hodell et al. 1994) which resulted in winnowing at Site 1092 due to enhanced ACC circulation (Figure 5.4), the portion of wind-blown particles increase at 6.2 Ma indicated by high Fe concentrations and increased silt/clay ratios at Site 1088 (Figure 5.5). Increased sedimentation rates at Site 1092 suggest reduction in ocean circulation intensity. This might be linked to the Messinian Salinity Crisis, because the cessation of MOW, an important source for deep-water formation in the Norwegian-Greenland Sea, caused a strong decrease in NCW production (Woodruff and Savin 1989, Müller et al. 1991). Cold climate conditions due to expansion of the Antarctic ice-sheet (e.g. Hodell et al. 2001, Vidal et al. 2002) induced stronger wind fields driven by increased thermal contrast. Therefore, higher Fe concentrations are related to diminished thermohaline circulation and enhanced dust inputs due to increased aridity in Africa and Patagonia.

5.5.2 The middle to late Miocene carbonate crash at Site 1092

The most intriguing event in the middle to late Miocene at Site 1092 is the dramatic reduction in carbonate content along with increases in opal and iron content from 9.3 to 9.1 Ma. At the adjacent Site 704 a strong decrease in carbonate content accompanied by the first significant occurrence of biogenic opal shows up between 9.2 - 9.0 Ma (Froelich et al. 1991, ages recalibrated to Cande and Kent 1995) and is associated with increased cooling from 9.6 - 8.8 Ma (Müller et al. 1991). Reduced sedimentation rates and the presence of fragmented planktonic foraminifers at Site 1092 give evidence for dissolution as the major cause of the decline in carbonate content (Diekmann et al. 2003).

Similar and coeval occurrences of carbonate dissolution in intermediate water-depth have been recorded in the eastern South Atlantic (ODP Sites 1085 and 1087, Westerhold et al. subm. a) and at the Kerguelen Plateau (ODP Site 1138, Böhm and Dullo 2000). The timing is simultaneous with the nadir of the carbonate crash events in the central and eastern Pacific from 9.5 to 9.0 Ma (Figure 5.6) (Lyle et al. 1995). According to Lyle et al. (1995), the carbonate crash events could not have been caused by an abrupt increase in productivity or by loss of organic carbon from continental shelves.

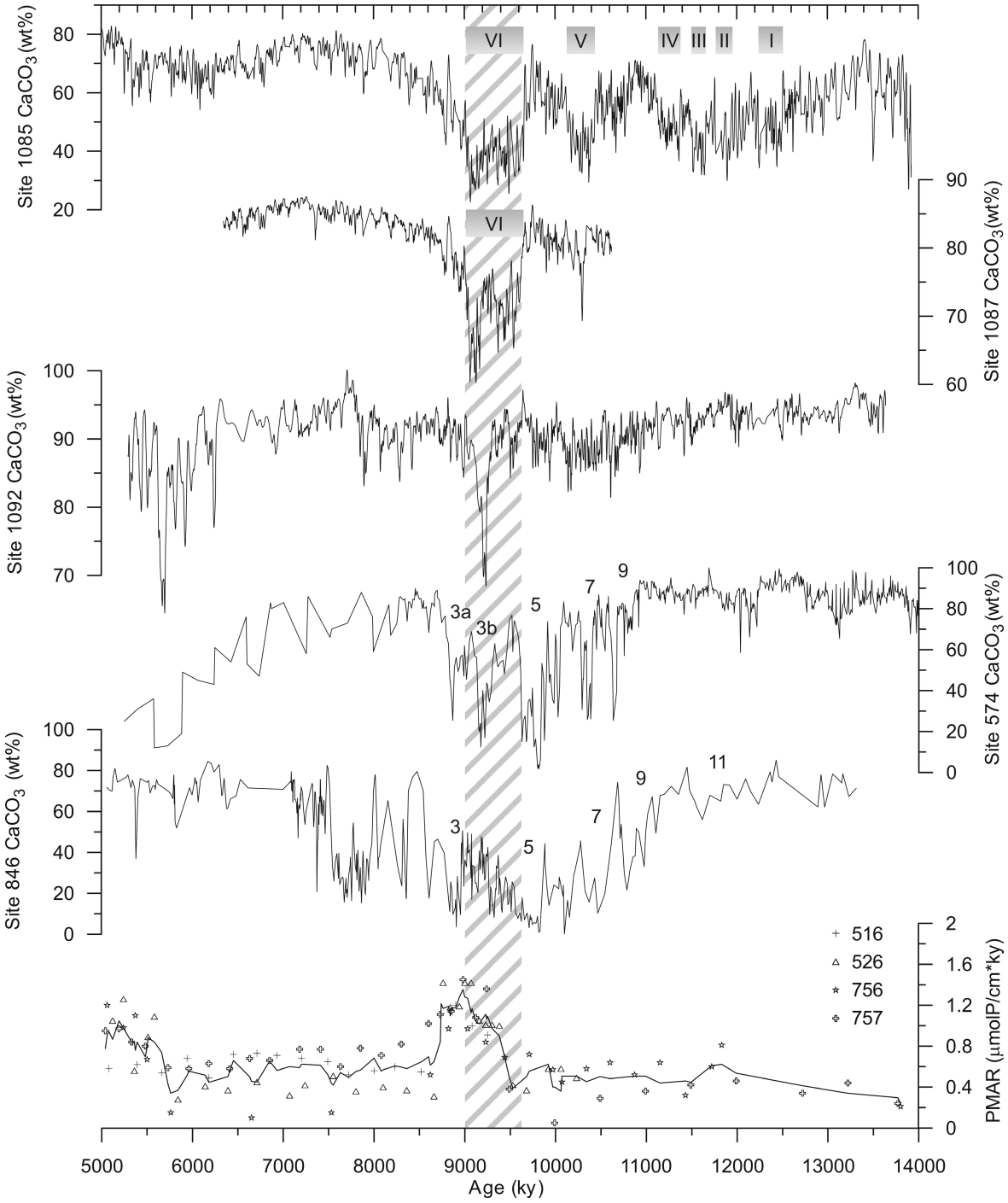

Figure 5.6 Variations of carbonate content between 14 and 5 Ma from the eastern South Atlantic (Site 1085, 1713 mbsl; Site 1087, 1372 mbsl; Westerhold et al. subm. a), Atlantic sector of the Southern Ocean (Meteor Rise, Site 1092, 1974 mbsl; this study), Central Equatorial Pacific (Site 574, 4561 mbsl; Pisias et al. 1985) and eastern Equatorial Pacific (Site 846, 3296 mbsl; Lyle et al. 1995) with carbonate crash periods assigned by the above mentioned authors. The nadir of the carbonate crash is marked by a hatched bar. The lowermost panel shows the phosphate mass accumulation rates (PMAR) from low productivity regions in the eastern Indian Ocean (Sites 757 and 756) and southern Atlantic Ocean (Sites 522 and 526) (Hermoyian and Owen 2001), black line represents a 3-point moving average.

Instead, the carbonate crash was probably caused by a reduction in exchange of deep water rich in $[CO_3]^{2-}$ between the Atlantic and Pacific Oceans as a result of the emerging Central American Seaway (Lyle et al. 1995, Farrell et al. 1995). This interpretation is consistent with modeling results from Nisancioglu et al. (2003). In contrast, the middle to late Miocene carbonate crash events in the eastern South Atlantic are caused by dilution due to enhanced terrigenous input linked to sea-level lowering and by dissolution due to enhanced inflow of corrosive SCW during Miocene glacial events (Westerhold et al. subm. a).

Compared to all the other sites (Figure 5.6) containing carbonate crash events, Site 1092 reveals only a single event which is consistently synchronous with the second part of the carbonate crash event VI at Sites 1085 and 1087, and crash event 3b at Site 574 (Central Equatorial Pacific, Pisias et al. 1985). The proximity and roughly the same water depth of the South Atlantic Sites suggest that dissolution is the most feasible common cause for the event centered at 9.2 Ma. Assuming that Site 1092 is affected by dissolution as Site 1085, carbonate crash events I through V at Site 1085 are mainly caused by dilution with terrigenous material from the Orange River rather than dissolution of carbonate. Additionally, the carbonate record of Site 1087 lacks the strong carbonate crash event V observed at Site 1085 (Figure 5.6). Because Site 1087 is located 150 nm to the South of Site 1085, the carbonate record is less diluted by terrigenous material delivered by the Orange River and thus accounts for a smaller reduction in carbonate content. Despite that, Sites 1085 and 1087 both document the dramatic carbonate crash event VI from 9.6 to 9.0 Ma. The nick of event VI in Sites 1085 and 1087 coincides with enhanced phosphate accumulation rates (Figure 5.6) from low productivity regions in the South Atlantic and Indian Ocean (Hermoyian and Owen 2001), suggesting an overall increase in nutrient flux into the world's oceans and the development of poorly ventilated intermediate to deep waters (Westerhold et al. subm. a). The increased nutrient influx to the Indian and Atlantic Ocean due to the uplift of the Himalayas (Rea 1992) and the Andes (Curry et al. 1995, Dobson et al. 1997) caused an enhanced flux of phosphorus into the world ocean (Hermoyian and Owen 2001). This, in turn, is held responsible for higher opal content in the eastern Indian Ocean and a peak in productivity in the Pacific Ocean around 9 Ma (Filippelli and Delaney 1994, Hermoyian and Owen 2001). The first establishment of trade-wind-driven Benguela upwelling system around 10 Ma (Siesser et al. 1980) indicated by increased productivity in the surface waters and the development of poorly ventilated intermediate waters resulted in the expansion of the oxygen minimum zone at the continental slope off Namibia (Westerhold et al. subm. a). Furthermore, the supply of cool

intermediate waters to mid-latitude surface waters upwelling regions resulted in decreased moisture levels in the atmosphere (Flower and Kennett 1995), which initiated the formation of the Namib Desert (Siesser 1978). Aridification in southern Africa, as documented in Site 1088 at 9.7 Ma (Diekmann et al. 2003) and Site 1085 at 9.6 Ma is consistent with the first establishment of trade-wind-driven Benguela upwelling system and the intensification of the monsoon system (e.g. Gupta and Thomas 1999, Raymo and Ruddiman 1992).

Large scale increases in primary productivity during the late Miocene would have promoted drawdown of atmospheric CO_2 altering the global carbon cycle and potentially leading to atmospheric cooling. At Site 1092, the increase in opal content at 9.2 Ma of up to 10% is associated with weak gradients between surface and mixed layer foraminifera (pers. comm. H. Paulsen) pointing to strong mixing processes. This could be due to intensified upwelling and/or frontal movements. Extended shelf ice built up in the Weddell Sea at 9.3 Ma and first IRD peaks in the southwest Atlantic and the Ross Sea at 9.2 Ma (Ehrmann 1994) document the expansion of the Antarctic ice cap far north, which probably enhanced the production of nutrient rich intermediate water flowing to Southwest Africa (Westerhold et al. subm. a). It has been proposed that the strengthening of the ACC would act to increase geostrophic flow at depth, intensifying upwelling along Antarctica and increase northward propagation of AAIW (Pagani et al. 2000). A proof of an increase of geostrophic flow at depth is the downslope slumping from topographic highs contributing to repletion and lengthening of sedimentary sections at Site 704 during C4An (~9 Ma, Hailwood and Clement 1991) and a decrease in sedimentation rates at Site 1092. Furthermore, around 9.5 Ma Mg/Ca-temperatures at Site 926 (Ceara Rise, western Equatorial Atlantic) decreased by ~1°C and carbonate content declines in the deeper Site 928 (Ceara Rise, Murray and Peterson 1997) suggesting strong SCW inflow to the Atlantic. Thus, dissolution of carbonate in the South and deep Equatorial Atlantic at the nadir of the carbonate crash is likely caused by intensification and northward expansion of corrosive Southern Component Water. This is consistent with low NCW fluxes estimations of Wright and Miller (1996) during this period, which they associate with cold climates.

5.5.3 The late Miocene biogenic bloom at Site 1092

From 6.2 to 5.3 Ma strong fluctuations in carbonate content along with increase in terrigenous and opal supply at Site 1092 (Figure 5.4) are in coherence with results from Site 704, in a way that opal and $\delta^{18}O$ values have been interpreted to indicate a short period

with stronger upwelling, cooler climate conditions and a northward migration of the PFZ (Müller et al. 1991, Froelich et al. 1991). At Site 1092 in the interval from 6.18 - 5.40 Ma eight peaks in Fe concentration with an average spacing of ~100 ky are observed accompanied by lowered carbonate content. Increase of Fe concentrations in times of decreased carbonate content suggests dilution by terrigenous influx. However, the strongest minimum in carbonate content appears from 5.7 - 5.6 Ma (Figure 5.6), coeval with the strong glacial event TG20 (Hodell et al. 2001) and exceptionally high opal content suggesting that the carbonate minima are due to dilution. The increase in opal points to higher productivity that is not associated with an increase in dissolution, a phenomenon also reported from the Ceara Rise at this period (Murray and Petersen 1997). At Central Equatorial Pacific Site 574 carbonate content decreases comparably to Site 1092 due to an increase in opal deposition (Farrell et al. 1995). In the period from 6.7 to 5 Ma augmented productivity is reported from all major ocean basins and referred to as the late Miocene 'biogenic bloom'.

Reconstruction of relative paleo-temperatures using diatom assemblages in the Atlantic sector of the Southern Ocean indicated long-range cooling in the Southern Ocean from 6.3 - 5.9 Ma and northward movement of the frontal system during the Messinian cold period (Censarek and Gersonde subm.). Müller et al. (1991) suggest that this interval of carbonate dissolution events at Site 704 corresponds to the latter stages of the Messinian evaporite deposition in the Mediterranean, which abruptly ended at about 5.3 Ma (Krijgsman et al. 1999). The onset of the early Pliocene hiatus at Site 1092 is coincident with end of the Messinian Salinity Crisis at 5.33 Ma (Krijgsman et al. 1999, Vidal et al. 2002) and related strengthening of ocean circulation (Billups et al. 2002). Hillenbrand and Fütterer (2001) suggest an early onset of Pliocene warming in the Antarctic realm, which might have enabled an intensification of thermohaline deep-water circulation in the Atlantic Ocean at ~5 Ma. With the increase in ocean circulation the more vigorous ACC caused an erosional phase on the Meteor Rise at Site 1092, whereas at the deeper Site 704 no hiatus is apparent. The late Miocene 'biogenic bloom' period is characterized by hiatuses at most locations from southern high latitudes (Barker et al. 1990, Barron et al. 1991, Exon et al. 2001). Increased biogenic production and sedimentation at low latitudes point to a redistribution of nutrients within ocean basins as indicated by enhanced phosphorous accumulation rates (Figure 5.6) (Hermoyian and Owen 2001).

5.6 Conclusion

At Site 1092 increases in sedimentation rates at 11.2 Ma marks the reorganization of ocean circulation and evolving geochemical basin-to-basin fractionation due to the onset of NCW production and uplift of the Central American Seaway. Enhanced opal and Fe deposition after 11.2 Ma indicates a higher surface productivity due to a northward movement of the PFZ over Site 1092 and enhanced southern-hemisphere westerly winds due to stronger latitudinal temperature gradients. The middle to late Miocene Fe concentration record of Site 1092 documents increased aridity and desert expansion in Patagonia at 10 Ma synchronous with substantial drying of Southern Africa and expansion of ice-sheets on Antarctica.

The prominent decrease in calcium carbonate at 9.2 Ma corresponds to the nadir of the late Miocene carbonate crash event observed in the Atlantic and Pacific and confirms supralysoclinal carbonate dissolution in intermediate water depth observed in the eastern South Atlantic. The carbonate crash event documents fundamental changes in global ocean chemistry and nutrient distribution probably caused by major changes in ocean circulation. Additionally, the strengthening of the ACC promoted surface productivity and increase northward propagation of AAIW, a prerequisite for upwelling along Southwest Africa. Decrease in terrigenous input to Site 1092 at 7.7 Ma is believed to be related to stronger influx of NADW to the Southern Ocean due to the strengthening of deep Atlantic overturning and the coeval expansion of grasslands which reduced the influx of wind-blown dust to the South Atlantic. From 6.2 - 5.3 Ma, during the Messinian Salinity Crisis, higher productivity is not associated with an increase in dissolution at Site 1092. Moreover, increased sedimentation rates and higher Fe concentrations suggest reduction in ocean circulation intensity and stronger wind fields driven by increased thermal contrast due to Antarctic ice-sheet expansion.

Acknowledgments

The authors are indebted to A. Wuelbers and W. Hale for the help at the Bremen Core Repository, and to M. Zabel for ICP-OES analyses. We would like to thank B. Censarek, J. Channell, B. Diekmann, H. Evans, R. Gersonde, J. Grützner, F. Hilgen, C. John, H. Paulsen, U. Röhl, O. Romero, J.-B. Stuut and K. Virkus for discussion. We thank the Ocean Drilling Program for providing samples. This study was funded by the Deutsche Forschungsgemeinschaft (Bi 657-3).

ODP Site 1092: revised composite depth section has implications for Upper Miocene "cryptochrons"

Helen F. Evans [1], Thomas Westerhold [2], James E.T. Channell [1]

[1] *Department of Geological Sciences, University of Florida, PO Box 112120, Gainesville, FL 32611, USA*

[2] *Fachbereich Geowissenschaften, Universität Bremen, Postfach 330440, 28334, Bremen, Germany*

Accepted by *Geophysical Journal International* – Research Note

Abstract

An Upper Miocene magnetic polarity stratigraphy has been developed for the C3r-C5ABn interval of ODP Site 1092 from the sub-Antarctic South Atlantic (Evans and Channell 2003). New data from X-ray fluorescence (XRF) scanning of half cores has led to development of a revised composite depth section for the site. This has implications for the magnetostratigraphic interpretation. Using the shipboard-derived composite section, four subchrons were identified within the normal polarity zone correlative to C5n.2n. The revised composite section results in subchrons C5n.2n-2 and C5n.2n-3 of Evans and Channell (2003) becoming a single subchron recorded in two overlapping cores. The revised number of polarity subchrons within C5n.2n is now three, rather than four, which is consistent with the number of "cryptochrons" recognized in marine oceanic anomaly data.

6.1 Introduction

ODP Site 1092 is located in the sub-Antarctic South Atlantic (46°24.7'S, 7°4.8'E, water depth 1974m). A magnetic polarity stratigraphy was presented for two time intervals (1.95 to ~3.6 Ma and ~5.9 to ~13.5 Ma) by Evans and Channell (2003). As is routine aboard the R/V *Joides Resolution*, composite stratigraphic depths (mcd) for site 1092 were constructed from multi-sensor track (MST) data. Magnetic susceptibility, gamma ray attenuation porosity (GRAPE) and light reflectance data were used to correlate among holes at the site and to derive an optimal record (splice) of the sedimentary section (Gersonde, Hodell, Blum, et al. 1999). The composite depths for ODP site 1092 have now been revised using X-ray fluorescence (XRF) scans of half-cores. These new data have allowed improved correlation among the holes at the site. The revised meters composite depth (rmcd) scheme has resulted in significant changes in hole-to-hole correlation, particularly within the interval correlative to subchron C5n.2n.

Using the shipboard composite section, Evans and Channell (2003) identified four reverse polarity subzones within the polarity zone correlative to C5n.2n. The four polarity subzones were considered to be correlative to "cryptochrons" in the polarity timescale of Cande and Kent (1992) and were labeled as C5n.2n-1 to C5n.2n-4. The results imply that "cryptochrons" originally identified within marine magnetic anomaly 5 by Blakely (1974) signify polarity reversals rather than solely geomagnetic intensity minima. On the revised composite depth scale, the reverse polarity subchrons labeled as C5n.2n-2 and C5n.2n-3 by Evans and Channell (2003) become a single subchron recorded in two different holes. The result supports the revised composite depth scale and indicates three, not four, subchrons within C5n.2n.

6.2 Revised composite depth (rmcd)

Shipboard MST data (magnetic susceptibility, GRAPE) and light reflectance data from site 1092 are often too uniform, particularly in the Upper Miocene section (120 - 185 mcd), for precise hole-to-hole correlation. As part of a project to assess carbonate sedimentation in the southern oceans, Westerhold and Bickert (in prep.) have measured most of the archive halves of cores from Site 1092 using the XRF core scanner at the Universität Bremen (Röhl and Abrams 2000). Fe and Ca intensity data, measured every 2 cm, are often more variable than shipboard MST data and generally provide an efficient means of hole-to-hole correlation.

Some core sections within the shipboard composite splice were not scanned for XRF because the working and archive halves had been too heavily sampled (partly for u-channels to generate the magnetic data). For core sections without XRF data, shipboard magnetic susceptibility could be adequately matched to core sections with Fe intensity data from XRF scans. Some cores from outside the splice had to be stretched or squeezed to conform with the overall depth scale of the shipboard composite section. Drilling related expansion and contraction in these poorly consolidated sediments contributes to the lack of precise correlation of depth scales between holes (Gersonde, Hodell, Blum et al. 1999). The depth scale of the shipboard composite section (with no stretching or squeezing of cores within the splice) was adhered to in the construction of the revised composite section (rmcd).

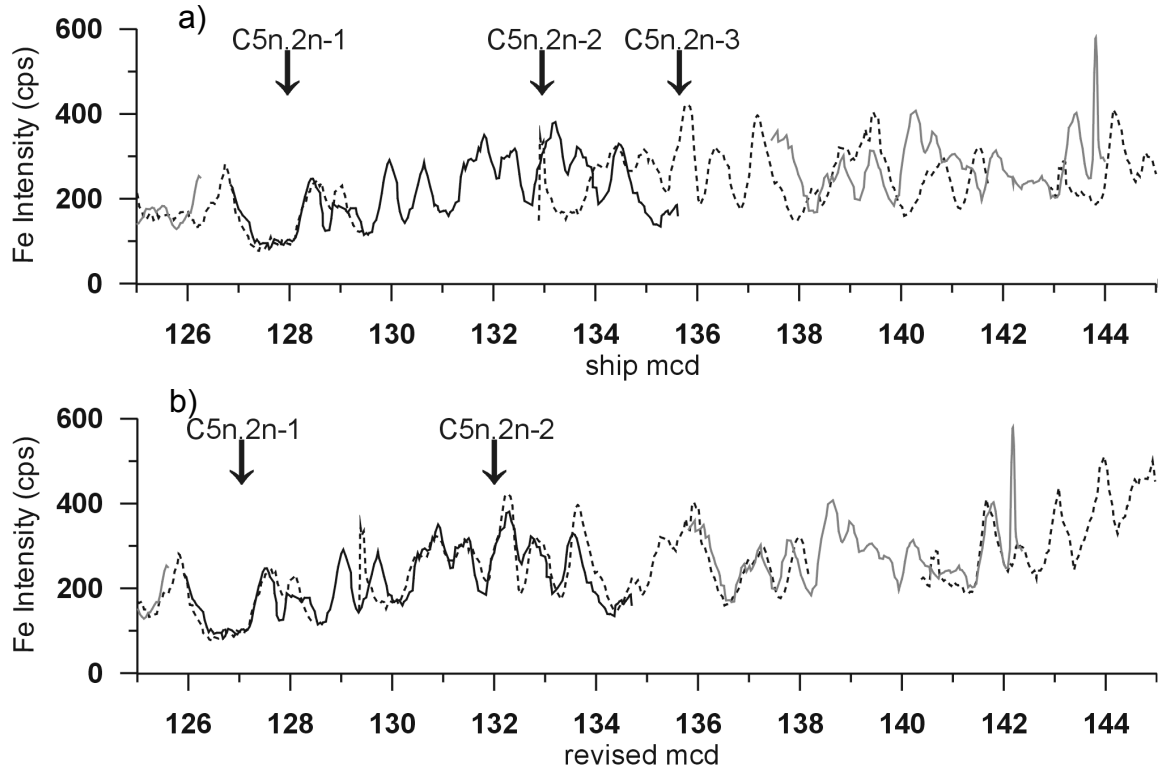

Figure 6.1 (a) Fe intensity (XRF) data plotted as a five-point moving average on the shipboard composite depth (mcd) scheme, with the position of the three subchrons identified in core sections 1092C-13H-6, 1092A-13H-4 and 1092C-14H-2 (C5n.2n-1 to 3) by Evans and Channell (2003). The thick line indicates data from hole 1092A, the thin line from hole 1092B and the dashed line from hole 1092C. (b) Fe intensity (XRF) data plotted as a five-point moving average on the revised composite depth (rmcd) scheme. Line notation as for Fig. 1a. On the revised composite depth (rmcd) scheme, C5n.2n-2 and C5n.2n-3 merge into a single subchron (C5n.2n-2).

Above core 1092A-12H, the shipboard composite section (mcd) is consistent with hole-to-hole correlations based on both MST and XRF data. In the shipboard splice, core 1092C-12H overlies 1092A-12H. Core 1092C-12H can be well correlated to 1092B-12H using XRF and magnetic susceptibility, and this correlation is consistent with shipboard composite depths. Correlation from 1092C-12H to the underlying core in the splice (1092A-12H) is poor for both MST and XRF data. However, 1092B-12H can be well correlated to 1092C-13H, but only when the latter is moved 90 cm up relative to 1092B-12H. This shift is the uppermost modification of the composite section depths. Below this, 1092A-13H can be well correlated to its neighbouring cores in the splice (1092C-13H and 1092C-14H), however, the correlation to 1092C-14H requires that this core should be moved up 2.58 m into 1092A-13H. The rationale for this adjustment, based on Fe intensity (XRF) data, is illustrated in Figure 6.1.

6.3 Implications for magnetic stratigraphy

Augmentation of the MST data by XRF data leads to offsets between the shipboard composite depths (mcd) and the revised composite depths (rmcd) that reach a maximum of 3.54 m in 1092C-14H (Table 6.1). The resulting modification of the composite section provides new composite depths for polarity zone boundaries at site 1092 (Table 6.2 and Figure 6.2), with new age estimates for subchrons not included in the standard geomagnetic polarity timescale (GPTS). The magnetostratigraphic interpretation (the correlation of polarity zones to polarity chrons) is the same as in Evans and Channell (2003) apart from the interval within C5n.2n. When utilizing the shipboard composite section, this normal polarity chronozone appeared to contain four thin polarity subzones that Evans and Channell (2003) associated with “cryptochrons” in marine oceanic magnetic anomaly data. The revision of the composite section indicates that there is duplication of polarity subzones that is an artifact of miscalculations in shipboard composite depths. Polarity subchrons, that were originally labeled C5n.2n-2 (recorded in core 1092A-13H) and C5n.2n-3 (recorded in core 1092C-14H), become a single subchron (relabeled as C5n.2n-2). The realignment of cores 1092A-13H and 1092C-14H within the composite section (Figure 6.1b) results in coincidence of the records of C5n.2n-2 and C5n.2n-3 (Figure 6.3a,b).

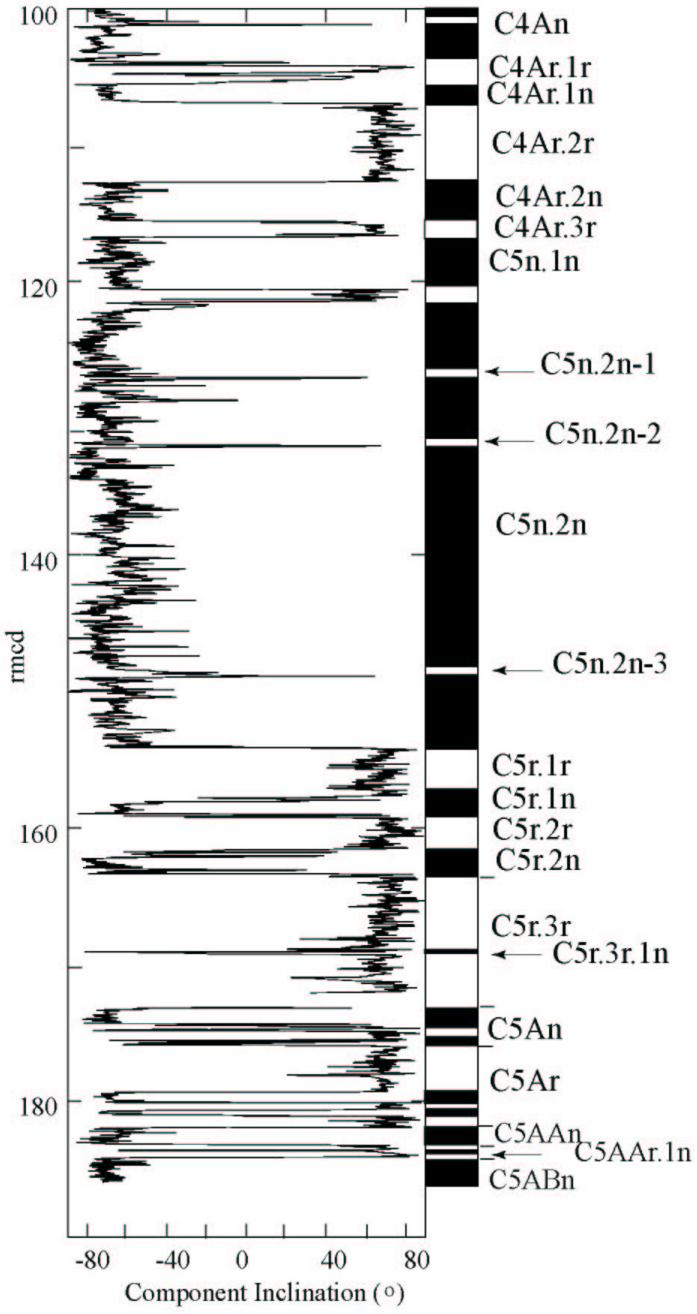

Figure 6.2 Inclination of the characteristic magnetization component plotted against revised composite depth (rmcd) for Site 1092. Polarity chrons are labeled according to Cande and Kent (1992). Arrows indicate subchrons within C5n.2n, C5r.3r and C5AAr.1n. Polarity interpretation: black indicates normal polarity, white reverse polarity.

This not only ratifies the adjustment of the composite section but also reduces the number of subchrons within C5n.2n from four to three (Figure 6.3), consistent with the number of "cryptochrons" in the GPTS of Cande and Kent (1992). Normalized remanence (mean NRM/IRM), used as a proxy for geomagnetic paleointensity in Evans and Channell (2003), can also be well correlated between cores 1092A-13H and 1092C-14H after revision of the composite depths (Figure 3c,d). The revised composite depths also alter the estimated duration of C5n.2n-2 and C5n.2n-3. C5n.2n-2 now has an estimated duration of 5 ky, while the duration of C5n.2n-3 increases to 11 ky, assuming a uniform sedimentation rate within C5n.2n.

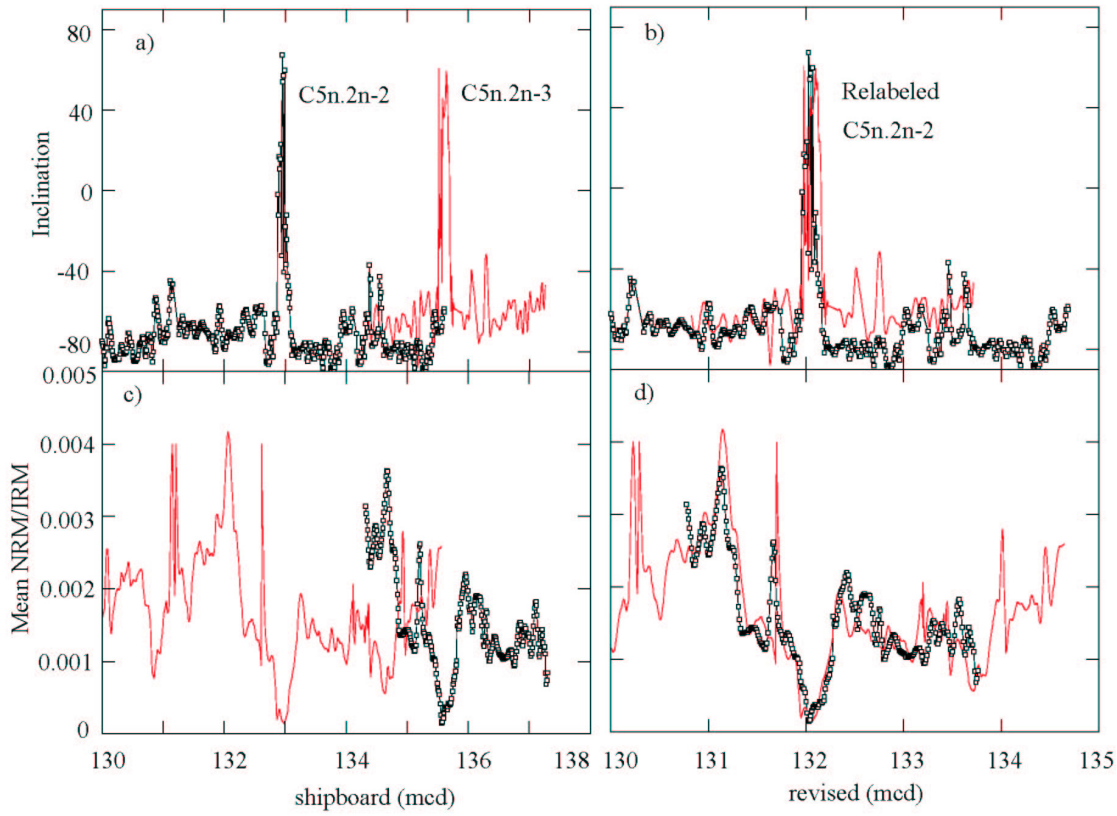

Figure 6.3 Site 1092: (a) Inclination of the characteristic magnetization component plotted against shipboard composite depth (mcd) showing C5n.2n-2 and C5n.2n-3 according to Evans and Channell (2003). (b) Inclination of the characteristic magnetization component plotted against revised composite depth (rmcd) showing that subchrons C5n.2n-2 and C5n.2n-3 of Evans and Channell (2003) become a single subchron (now labeled C5n.2n-2). (c) Mean of the ratio of natural remanent magnetization (NRM) to isothermal remanent magnetization (IRM), calculated for nine demagnetization steps in the 20-60 mT demagnetization range, plotted against shipboard composite depth (mcd). (d) Mean of the ratio of natural remanent magnetization (NRM) to isothermal remanent magnetization (IRM), calculated for nine demagnetization steps in the 20-60 mT demagnetization range, plotted against revised composite depth (rmcd).

In the Orera section (Spain), Abdul Aziz et al. (2003) found three normal polarity subzones within C5r (two within C5r.2r and one within C5r.3r) that are not represented in the GPTS of Cande and Kent (1992, 1995). This augmented C5r could be correlated with the polarity zones at site 1092 by moving the onset of C5r.3r to 179.41 rmcd (Krijgsman, pers comm. 2003). The polarity zones at site 1092 correlative to these three features have thicknesses of 1.75m (C5r.2r-1n), 0.23m (C5r.2r-2n) and 0.38m (C5r.3r-1n). This interpretation appears consistent with a hiatus at 180.48 rmcd advocated by Censarek and Gersonde (2002) from the diatom biostratigraphy. The hiatus was placed at 180.48 rmcd on the basis of the coincidence of the first occurrences of *Denticulopsis praedimorpha* and *Nitzschia denticuloides*, and the last occurrence of *Actinocyclus ingens* var. *nodus*, although the ages of these diatom events are poorly constrained.

In a recent study of chron C5 at ODP Site 887, Bowles et al. (2003) found no evidence for reverse polarity subzones within C5n.2n and concluded that “cryptochrons” of this age recognized in marine magnetic anomaly data represent fluctuations in geomagnetic field intensity. The mean sedimentation rate in C5n.2n at Site 887 is 1cm/ky, or ~ 30% of that at Site 1092, and it is therefore less likely that polarity intervals of the duration seen at ODP Site 1092 would have been recorded at Site 887.

The short duration of the reverse polarity intervals within C5n.2n at Site 1092 may indicate that they are “excursions” rather than polarity subchrons. Various criteria have been suggested to distinguish “excursions” from polarity subchrons (Cande and Kent 1992, Gubbins 1999, Roberts and Lewin-Harris 2000). Roberts and Lewin-Harris (2000) suggested that for a polarity excursion to qualify as a polarity subchron it should be bounded by two field reversals, and that decreases in paleointensity should be apparent at both bounding reversals. Of the three subchrons within C5n.2n at Site 1092, only C5n.2n-3 exhibits a clear recovery in paleointensity between the reversals.

The fundamental conclusion of Evans and Channell (2003) that short duration (5 -11 ky) polarity subchrons exist within C5n.2n, that are probably correlative to “cryptochrons” interpreted from oceanic magnetic anomaly data, has not changed. However, the number of polarity subchrons within C5n.2n has been reduced from four to three by revision of composite depths at site 1092.

Acknowledgements:

We thank Andrew Roberts for suggestions that improved the manuscript, and Torsten Bickert and Ursula Röhl for assistance with XRF core scanning.

Table 6.1 Adjusted depths of core tops from ODP Site 1092.

Core	mbsf	ship mcd*	offset mcd to mbsf (m)	offset mbsf to rmcd (m)	revised mcd (rmcd)	offset mcd to rmcd (m)
177-1092A-						
12H	103.0	115.41	12.41	11.48	114.48	-0.93
13H	112.5	126.72	14.22	13.30	125.80	-0.92
14H	122.0	138.12	16.12	14.51	136.51	-1.61
15H	131.5	149.74	18.24	15.76	147.26	-2.48
16H	141.0	160.18	19.18	18.01	159.01	-1.17
17H	150.5	168.72	18.22	19.64	170.14	1.42
18H	160.0	179.85	19.85	21.57	181.57	1.72
19H	169.5	191.84	22.34	21.57	191.07	-0.77
20H	179.0	201.34	22.34	21.57	200.57	-0.77
177-1092B-						
13H	111.4	122.22	10.82	10.17	121.57	-0.65
14H	121.4	134.32	12.92	11.28	132.68	-1.64
15H	130.9	146.62	15.72	13.24	144.14	-2.48
16H	140.4	155.72	15.32	14.34	154.74	-0.98
17H	149.9	166.76	16.86	15.33	165.23	-1.53
18H	159.4	175.31	15.91	17.56	176.96	1.65
177-1092C-						
13H	108.5	119.93	11.43	10.51	119.01	-0.92
14H	118.0	132.82	14.82	11.28	129.28	-3.54
15H	127.5	142.70	15.20	12.72	140.22	-2.48
16H	137.0	155.70	18.70	14.72	151.72	-3.98
17H	146.5	166.38	19.88	15.84	162.34	-4.04
18H	156.0	175.79	19.79	17.91	173.91	-1.88

*Shipboard Scientific Party, 1999

Table 6.2 Position of the polarity zone boundaries at Site 1092 in shipboard mcd and rmcd. Ages of polarity chrons are from the geomagnetic polarity timescale (GPTS) of Cande and Kent (1992, 1995). Ages of polarity subchrons not featured in the GPTS are marked by an asterisk and estimated assuming constant sedimentation rates within polarity chrons.

Depth (mcd)	Depth (rmcd)	Chron	Age (Ma; CK92_95)
121.48	120.55	Base C5n.1n	9.880
122.40	121.47	Top C5n.2n	9.920
127.92	127.00	Top C5n.2n.1	10.098*
128.01	127.09	Base C5n.2n.1	10.101*
132.88	131.95	Top C5n.2n.2	10.258*
133.02	132.16	Base C5n.2n.2	10.263*
151.31	148.83	Top C5n.2n.3	10.803*
151.43	148.95	Base C5n.2n.3	10.809*
156.60	154.12	Base C5n.2n	10.949
158.80	157.82	Top C5r.1n	11.052
160.00	159.02	Base C5r.1n	11.099
163.10	161.93	Top C5r.2n	11.476
164.54	163.37	Base C5r.2n	11.531
170.60	169.07	Top C5r.3r.1n	11.866*
170.79	169.26	Base C5r.3r.1n	11.877*
171.75	170.22	Top C5An.1n	11.935
173.00	174.42	Base C5An.1n	12.078
174.20	175.62	Top C5An.2n	12.184
174.49	175.91	Base C5An.2n	12.401
177.70	179.35	Top C5Ar.1n	12.678
178.50	180.15	Base C5Ar.1n	12.708
179.00	180.65	Top C5Ar.2n	12.775
179.42	181.07	Base C5Ar.2n	12.819
180.29	181.94	Top C5AAn	12.991
181.55	183.20	Base C5AAn	13.139
181.95	183.60	Top C5AAr.1n	13.208*
182.02	183.67	Base C5AAr.1n	13.220*
182.50	184.15	Top C5ABn	13.302
187.47	186.70	Base C5ABn	13.510
192.43	191.66	Top C5ACn	13.703
194.01	193.24	Base C5ACn	14.076
197.32	196.55	Top C5ADn	14.178
208.17	207.04	Base C5ADn	14.612
209.61	208.84	Top C5Bn.1n	14.800

7. Conclusions and perspectives

In this thesis a comprehensive data collection mainly from non-destructive XRF core scanner measurements and oxygen isotope data have been applied for reconstructing and interpreting paleoenvironmental changes in Neogene sediments of South Atlantic. The obtained data document the geochemical reorganization in the world oceans across the middle to late Miocene transition (basin-to-basin fractionation) which mainly is contributed to the uplift of the Central American Seaway and expansion of the Antarctic ice-sheet. Detailed comparison of carbonate sedimentation patterns from different regions and different water depth clearly show that the carbonate crash events differ substantially in timing and magnitude. In addition, the congruent variability of shallow and deep water carbonate records contradict the assumed gradients between intermediate and deep-water masses as predicted by modeling studies. Furthermore, the present study suggests that interactions exist between the geochemical reorganization of the world oceans and climate events during the Neogene. For example, the close timing of aridification in South Africa and Patagonia, strengthening of the Antarctic Circumpolar Current, begin of Benguela upwelling, intensification of Southern Hemisphere winds and expansion of the Antarctic ice-sheet point to a common driving mechanism. The configuration of ocean gateways and sills (i.e. Central American Seaway, Greenland-Scotland Ridge) seem to play a key role in the observed changes in ocean chemistry. Other factors like the uplift of major orogenes (Andes, Himalayas) might have significant influence on the ocean geochemistry and therefore carbonate sedimentation pattern.

Future research should focus on the identification of the driving mechanisms for the drastic changes in the late Neogene carbonate deposition. Potential thresholds and feedback mechanisms responsible for climate and ocean circulation transitions during that time should be studied using numerical models and compared to changes in sedimentary pattern documented in high-resolution data sets of selected areas. Investigations should focus on key areas that are sensitive to changes in the basin-to-basin fractionation. As inferred from modeling results of Heinze and Crowley (1997), the western Equatorial Atlantic (i.e. Ceara Rise Leg 154, Demeara Rise Leg 207) and western Equatorial Pacific (i.e. Ontong Java Plateau Leg 130, Shatsky Rise Leg 198) might be promising locations. In addition, high resolution carbonate record should be obtained over depth transects in order to reconstruct vertical gradients in calcite dissolution and to obtain information about gradients between the intermediate and deep ocean. Focus of modeling studies should be the potential of ocean gateway changes to cause changes in thermohaline circulation and its effects on ocean geochemistry. Especially the effect of the closing of the Central American Seaway, Gibraltar Passage and Indonesian Seaway combined with the subsidence history of the Greenland-Scotland Ridge should be studied.

8. References

Abdul Aziz, H., Krijgsman, W., Hilgen, F., Wilson, D.S. and Calvo, J.P., 2003. An astronomical polarity timescale for the late middle Miocene based on cyclic continental sequences. Journal of Geophysical Research, 108(B3): 2159, doi:10.1029/2002JB001818.

Abreu, V.S. and Anderson, J.B., 1998. Glacial Eustasy during the Cenozoic: Sequence Startigraphic Implications. AAPG Bulletin, 82(7): 1385-1400.

Abreu, V.S. and Haddad, G.A., 1998. Glacioeustatic Fluctuations: The Mechanism linking Stable Isotope Events and Sequence Stratigraphy from the Early Oligocene to Middle Miocene. In: P.-C. De Graciansky, J. Hardenbol, T. Jacquin, P.R. Vail and M.B. Farley (Editors), Sequence stratigraphy of European basins. Tulsa, SEPM Special Publication, pp. 245-259.

Adegbie, A.T., Schneider, R.R., Röhl, U. and Wefer, G., 2003. Glacial millennial-scale fluctuations in central African precipitation record in terrigenous sediment supply and freshwater signals offshore Cameroon. Palaeogeography, Palaeoclimatology, Palaeoecology, 197: 323-333.

Anderson, P.A., Charles, C.D. and Berger, W.H., 2001. Walvis Paradox confirmed for the early Quaternary at the southern end of the Namibia upwelling system, ODP Site 1085. In: G. Wefer, W.H. Berger, C. Richter, et al. (Editors), Proc. ODP, Sci. Res., 175: College Station, TX (Ocean Drilling Program), pp. 1-31.

Andersson, C. and Jansen, E., 2003. A Miocene (8-12 Ma) intermediate water benthic stable isotope record from the northeastern Atlantic, ODP Site 982. Paleoceanography, 18(1).

Arz, H.W., 1998. Dokumentation von kurzfristigen Klimaschwankungen des Spätquartärs in Sedimenten des westlichen äquatorialen Atlantiks. Berichte, Fachbereich Geowissenschaften, 124. Universität Bremen, Bremen, 96 pp.

Backman, J. and Raffi, I., 1997. Calibration of Miocene Nannofossil Events to Orbitally Tuned Cyclostratigraphies from Ceara Rise. In: N.J. Shackleton, W.B. Curry, C. Richter and T.J. Bralower (Editors), Proc. ODP, Sci. Res., 154: College Station, TX (Ocean Drilling Program), pp. 83-99.

Barker, P.F. and Burrell, J., 1977. The opening of the Drake Passage. Marine Geology, 25: 15-34.

Barker, P.F., Kennett, J.P., et al., 1990. Proc. Ocean. Drill. Program Init. Reports, 113.

Barron, J., Larsen, B., et al., 1991. Proc. Ocean. Drill. Program Init. Reports, 119.

Barron, J.A., 1985. Diatom Paleoceanography and Paleoclimatology of the Central and Eastern Equatorial Pacific between 18 and 6.2 Ma. In: L. Mayer, F. Theyer, et al. (Editors), Init. Repts. DSDP, 85: Washington (U.S. Govt. Printing Office). pp. 935-944.

Barron, J.A. and Keller, G., 1982. Widespread Miocene deep-sea hiatuses: Coincidence with periods of global cooling. Geology, 10: 577-581.

Bayon, G., German, C.R., Nesbitt, R.W., Bertrand, P. and Schneider, R.R., 2003. Increased input of circumpolar deep water-borne detritus to the glacial SE Atlantic Ocean. Geochemistry, Geophysics, Geosystems, 4(3): 10.1029/2002GC000371.

Beaufort, L., 1994. Climatic importance of the modulation of the 100 kyr cycle inferred from 16 m.y. long Miocene records. Paleoceanography, 9(6): 821-834.

Bemis, B.E., Spero, H.J., Bijma, J. and Lea, D.W., 1998. Reevaluation of the oxygen isotopic composition of planktonic foraminifera: Experimental results and revised paleotemperature equations. Paleoceanography, 13(2): 150-160.

Berger, W.H., 1970. Biogenous deep-sea sediments: Fractionation by deep-sea circulation. Geological Society of America Bulletin, 81: 1385-1402.

Berger, W.H., 1999. The 100-kyr ice-age cycle: internal oscillation or inclinational forcing? International Journal of Earth Sciences, 88: 305-316.

Berger, W.H. and Jansen, E., 1994. Mid-Pleistocene climate shift - The Nansen connection. Geophysical Monographs, 84: 295-311.

Berger, W.H., Leckie, R.M., Janecek, T.R., Stax, R. and Takayama, T., 1993. Neogene Carbonate Sedimentation on Ontong Java Plateau: Highlights and Open Questions. In: W.H. Berger, L.W. Kroenke, L.A. Mayer, et al. (Editors), Proc. ODP, Sci. Re., 130: College Station, TX (Ocean Drilling Program).

Berger, W.H. and Vincent, E., 1981. Chemostratigraphy and biostratigraphic correlation: exercises in systemic stratigraphy. Oceanologica Acta, 4: 115-127.

Berger, W.H. and Wefer, G., 1996. Expeditions into the past: Paleoceanographic studies in the South Atlantic. In: G. Wefer, W.H. Berger, G. Siedler and D.J. Webb (Editors), The South Atlantic: Present and Past Circulation. Springer-Verlag Berlin Heidelberg, pp. 363-410.

Berger, W.H. and Winterer, E.L., 1974. Plate stratigraphy and the fluctuating carbonate line. In: K.J. Hsü and H. Jenkyns (Editors), Pelagic Sediments on Land and Under the Sea. Spec. Publ. Intl. Assoc. Sediment, pp. 11-48.

Berggren, W.A. et al., 1995a. Late Neogene chronology: new perspectives in high-resolution stratigraphy. Geological Society of America Bulletin, 107: 1272-1287.

Berggren, W.A., Kent, D.V., Swisher III, C.C. and Aubury, M.P., 1995b. A revised Cenozoic geochronology and chronostratigraphy. In: W.A. Berggren, D.V. Kent, M.P. Aubury and J. Hardenbol (Editors), Geochronology, Time Scales and Global Stratigraphic Correlation. SEPM, Spec. Publ., pp. 129-212.

Berner, R.A., 1994. GEOCARB II: a revised model of atmospheric CO_2 over Phanerozoic time. American Journal of Science, 294: 56-91.

Betzler, C., Kroon, D. and Reijmer, J.J.G., 2000. Synchroneity of major late Neogene sea level fluctuations and paleoceanographically controlled changes as recorded by two carbonate platforms. Paleoceanography, 15(6): 722-730.

Bickert, T., Curry, W.B. and Wefer, G., 1997. Late Pliocene to Holocene (2.6-0 Ma) Western Equatorial Atlantic Deep-Water Circulation: Inferences from Benthic Stable Isotopes. In: N.J. Shackelton, W.B. Curry, C. Richter and T.J. Bralower (Editors), Proc. ODP, Sci. Res., 154: College Station, TX (Ocean Drilling Program), pp. 239-254.

Bickert, T., Haug, G. and Tiedemann, R., in press. Late Neogene benthic stable isotope record of ODP Site 999: Implications for Caribbean paleoceanography, organic carbon burial and the Messinian Salinity Crisis. Paleoceanography.

Bickert, T. and Wefer, G., 1996. Late Quaternary Deep Water Circulation in the South Atlantic: Reconstruction from Carbonate Dissolution and Benthic Stable Isotopes. In: G. Wefer, W.H. Berger, G. Siedler and D.J. Webb (Editors), The South Atlantic: Present and Past Circulation. Springer-Verlag Berlin Heidelberg, pp. 599-620.

Billups, K., 2002. Late Miocene through early Pliocene deep water circulation and climate change viewed from the sub-Antarctic South Atlantic. Palaeogeography, Palaeoclimatology, Palaeoecology, 185: 287-307.

Billups, K. and Schrag, D.P., 2002. Paleotemperatures and ice volume of the past 27 Myr revisited with paired Mg/Ca and $^{18}O/^{16}O$ measurements on benthic foraminifera. Paleoceanography, 17(1): doi:10.1029/2000PA000567.

Blackman, R.B. and Tukey, J.W., 1958. The measurment of power spectra from the point of view of communication engeneering, Dover, New York.

Blakely, R.J., 1974. Geomagnetic Reversals and Crustal Spreading Rates during the Miocene. Journal of geophysical Research, 79: 2979-2985.

Bloemendal, J., Liu, X.M. and Rolph, T.C., 1995. Correlation of the magnetic susceptibility stratigraphy of Chinese loess and the marine oxygen isotope record: chronological and palaeoclimatic implications. Earth and Planetary Science Letters, 131: 371-380.

Böhm, F. and Dullo, W.C., 2000. Neogene Sedimentation at the Central Kerguelen Plateau: Coccoliths, Diatoms, Pumice and a 'Carbonate Crash'. Eos Trans. AGU, 81, Spring Meet. Suppl., Abstract.

Bohrmann, G., Henrich, R. and Thiede, J., 1990. Miocene to Quaternary Paleoceanography in the Northern North Atlantic: Variability in Carbonate and Biogenic Opal Accumulation. In: U. Bleil and J. Thiede (Editors), Proceedings of the 1988 NATO advanced research workshop on Geological history of the polar oceans; Arctic versus Antarctic. NATO ASI Series. Series C: Mathematical and Physical Sciences, pp. 647-675.

Bowles, J., Tauxe, L., Gee, J., McMillan, D. and Cande, S.C., 2003. Source of tiny wiggles in Chron C5: A comparison of sedimentary relative intensity and marine magnetic anomalies. Geochemistry, Geophysics, Geosystems, 4(6): doi:10.1029/2002GC000489.

Boyce, R.E., 1976. Definitions and laboratory techniques of compressional sound velocity parameters and wet-water content, wet-bulk density, and porosity parameters by gravimetric and gamma-ray attenuation techniques. In: S.O. Schlanger, E.D. Jackson,et al. (Editors), Init. Repts. DSDP, 33, Washington (U.S. Govt. Printing Office), pp. 931-958.

Brathauer, U. and Abelmann, A., 1999. Late Quaternary variations in sea surface temperatures and their relationship to orbital forcing recorded in the Southern Ocean (Atlantic sector). Paleoceanography, 14(2): 135-148.

Broecker, W.S. and Denton, G.H., 1989. The role of ocean-atmosphere reorganizations in glacial cycles. Geochemica et Cosmochemica Acta, 53: 2465-2501.

Broecker, W.S. and Peng, T.H., 1982. Tracers in the Sea. Lamont Doherty Geol. Obs. Publications, New York, 689 pp.

Burckle, L.H. and Cirilli, J., 1987. Origin of diatom ooze belt in the Southern Ocean : Implications for late Quaternary paleoceanography. Marine Micropaleontology, 33: 82-86.

Cande, S.C. and Kent, D.V., 1992. A New Geomagnetic Polarity Time Scale for the late Cretaceous and Cenozoic. Journal of Geophysical Research, 97(B10): 13,917-13,951.

Cande, S.C. and Kent, D.V., 1995. Revised calibration of the geomagnetic polarity timescale for the Late Cretaceous and Cenozoic. Journal of Geophysical Research, 100(B4): 6093-6095.

Censarek, B. and Gersonde, R., 2002. Miocene diatom biostratigraphy at ODP Sites 689, 690, 1088, 1092 (Atlantic sector of the Southern Ocean). Marine Micropaleontology, 45: 309-356.

Censarek, B. and Gersonde, R., subm. Late Miocene Southern Ocean Thermal Development and its Connection to Mediterranean Climate History - Diatom Evidence from ODP Sites 701 and 704. Marine Geology: 309-356.

Cerling, T.E. et al., 1997. Global vegetation change through the Miocene/Pliocene boundary. Nature, 389: 153.

Cervato, C. and Burckle, L., 2003. Pattern of first and last appearance in diatoms: Oceanic circulation and the position of polar fronts during the Cenozoic. Paleoceanography, 18(2): doi:10.1029/2002PA000805.

Chase, Z., Anderson, R.F., Fleisher, M.Q. and Kubik, P.W., 2003. Accumulation of biogenic and lithogenic material in the Pacific sector of the Southern Ocean during the past 40,000 years. Deep-Sea Research II, 50: 799-832.

Christensen, B.A., Kalbas, J.L., Maslin, M. and Murray, R.W., 2002. Paleoclimatic changes in southern Africa during the intensification of Northern Hemisphere glaciation: evidence from ODP Leg 175 Site 1085. Marine Geolology, 180: 117-131.

Christensen, B.A. and Maslin, M., 2001. An Astronomically Calibrated Age Model for Pliocene Site 1085, ODP Leg 175. In: G. Wefer, W.H. Berger, C. Richter, et al. (Editors), Proc. ODP, Sci. Res., 175: College Station, TX (Ocean Drilling Program).

Ciesielski, P.F. and Weaver, F.M., 1983. Neogene and Quaternary paleoenvironmental history of Deep Sea Drilling Project Leg 71 sediments, southwest Atlantic Ocean. In: W.J. Ludwig, V.A. Krasheninnikov, et al. (Editors), Init. Repts. DSDP, 71 (Pt. 1): Washington (U.S. Govt. Printing Office), pp. 461-477.

Clemens, S.C., 1999. An astronomical tuning stratigraphy for Pliocene sections: implications for global-scale correlation and phase relationship. In: N.J. Shackleton, M.I.N. and G.P. Weedon (Editors), Phil. Trans. R. Soc. Lond. A, pp. 1949-1973.

Clemens, S.C., Murray, D.W. and Prell, W.L., 1996. Nonstationary phase of the Plio-Pleistocene Asian Monsoon. Science, 274: 943-948.

Clemens, S.C. and Tiedemann, R., 1997. Eccentricity forcing of Pliocene-Early Pleistocene climate revealed in a marine oxygen-isotope record. Nature, 385: 801-804.

Crowley, T.J., Kim, K.-Y., Mengel, J.G. and Short, D.A., 1992. Modeling 100,000 year climate fluctuations in pre-Pleistocene time series. Science, 255: 705-707.

Crowley, T.J. and Kim, K.-Y., 1992. Complementary roles of orbital insolation and North Atlantic Deep Water during late Pleistocene interglacials. Paleoceanography, 7: 521-528.

Curry, W.B., Shackelton, N.J., Richter, C., et al. 1995. Leg 154 Synthesis. Proc. ODP, Init. Repts., 154: College Station, TX (Ocean Drilling Program). 421-442.

Delaney, M.L., 1990. Miocene Benthic Foraminiferal Cd/Ca Records: South Atlantic and Western Equatorial Pacific. Paleoceanography, 5(5): 743-760.

deMenocal, P.B., 1995. Plio-Pleistocene African Climate. Science, 270: 53-59.

deMenocal, P.B. et al., 2000. Abrupt onset and termination of the African Humid Period: rapid climate responses to gradual insolation forcing. Quaternary Science Reviews, 19: 347-361.

D'Hondt, S. and Arthur, M.A., 1996. Late Cretaceous oceans and the cool tropics paradox. Science, 271: 1838-1840.

Diekmann, B., Fälker, M. and Kuhn, G., 2003. Environmental history of the southeastern South Atlantic since the middle Miocene: Evidence from the sedimentological records of ODP Sites 1088 and 1092. Sedimentology, 50: 511-529.

Diekmann, B., Kuhn, G., Rachold, V., Abelmann, A., Brathauer, U., Fütterer, D. K., Gersonde, R., Grobe, H., 2000. Terrigenous sediment supply in the Scotia Sea (Southern Ocean): response to Late Quaternary ice dynamics in Patagonia and on the Antarctic Peninsula. Palaeogeography, Palaeoclimatology, Palaeoecology, 162: 357-387.

Diekmann, B., Petschik, R., Gingele, F. X., Fütterer, D. K., Abelmann, A., Brathauer, U., Gersonde, R., Mackensen, A., 1996. Clay Mineral Fluctuations in Late Quaternary Sediments of the Southeastern South Atlantic: Implications for Past Changes of Deep Water Advection. In: G. Wefer, W.H. Berger, G. Siedler and D.J. Webb (Editors), The South Atlantic: Present and Past Circulation. Springer-Verlag Berlin Heidelberg, pp. 621-644.

Diester-Haass, L., Meyers, P.A. and Bickert, T., in press. The middle to late Miocene "carbonate crash" and "biogenic bloom" in the southeast Atlantic Ocean: Evidence from ODP Sites 1085, 1086 and 1087 in the Cape Basin. Paleoceanography.

Diester-Haass, L., Meyers, P.A. and Rothe, P., 1992. The Benguela Current and associated upwelling on the southwest African Margin: a synthesis of the Neogene-Quaternary sedimentary record at DSDP sites 362 and 532. In: C.P. Prell and K.C. Emeis (Editors), Upwelling Systems: Evolution Since the Early Miocene. Geological Society Special Publication, pp. 331-342.

Dittert, N. et al., 1999. Carbonate Dissolution in the Deep-Sea: Methods, Quantification and Paleoceanographic Application. In: G. Fischer and G. Wefer (Editors), Use of proxies in Paleoceanography: Examples from the South Atlantic. Springer, Berlin Heidelberg, pp. 255-284.

Dobson, D.M., Dickens, G.R. and Rea, D.K., 1997. Terrigenous Sedimentation at Ceara Rise. In: N.J. Shackelton, W.B. Curry, C. Richter and T.J. Bralower (Editors), Proc. ODP, Sci. Res., 154: College Station, TX (Ocean Drilling Program), pp. 465-473.

Duque-Caro, H., 1990. Neogene stratigraphy, paleoceanography and paleobiogeography in northwest South America and the evolution of the Panama Seaway. Palaeogeography, Palaeoclimatology, Palaeoecology, 77: 203-234.

Ehrmann, W.U., 1994. Känozoische Vereisungsgeschichte der Antarktis. Berichte zur Polarforschung, 137: 1-152.

Emeis, K.C., Morse, J.W. and Mays, L.L., 1991. Organic carbon, reduced sulfur, and iron in Miocene to Holocene upwelling sediments from the Oman and Benguela upwelling systems. In: W.L. Prell, N. Niitsuma, et al. (Editors), Proc. ODP, Sci. Res., 117: College Station, TX (Ocean Drilling Program).

Emerson, S. and Bender, M.L., 1981. Carbon fluxes at the sediment-water interface of the deep-sea: calcium carbonate preservation. Journal of Marine Research, 39:139-162.

Evans, H.F. and Channell, J.E.T., 2003. Upper Miocene magnetic stratigraphy at ODP site 1092 (sub-Antarctic South Atlantic): recognition of 'cryptochrons' in C5n.2n. Geophysical Journal International, 153: 483-496.

Evans, H.F., Westerhold, T. and Channell, J.E.T., subm. ODP Site 1092: revised composite depth section has implications for Upper Miocene magnetostratigraphy Geophysical Journal International.

Exon, N.F., Kennett, J.P., Malone, M.J., et al., 2001. Proc. ODP, Init. Repts., 189.

Fairbanks, R.G. and Matthews, R.K., 1978. The Marine Oxygen Isotope Record in Pleistocene Corals, Barbados, West Indies. Quaternary Research, 10: 181-196.

Farrell, J.W. et al., 1995. Late Neogene Sedimentation Patterns in the Eastern Equatorial Pacific Ocean. In: N.G. Pisias, L.A. Mayer, T.R. Janecek, T.R. Palmer-Julson and T.H. van-Andel (Editors), Proc. ODP, Sci. Res., 138: College Station, TX (Ocean Drilling Program).

Filippelli, G.M. and Delaney, M.L., 1994. The oceanic phosphorus cycle and continental weathering during the Neogene. Paleoceanography, 9(5): 643-652.

Filippelli, G.M., Latimer, J.C., King, S., Froelich, P.N. and Party, S.S., 1999. Geochemistry of opal-rich sediments from the Southern Ocean: ODP Leg 177, Site 1094 (abstract). EOS Trans. AGU, 80, Spring Meet. Suppl., S198.

Flower, B.P. and Kennett, J.P., 1993. Relations between Monterey Formation deposition and middle Miocene global cooling: Naples Beach section, California. Geology, 21: 877-880.

Flower, B.P. and Kennett, J.P., 1994. The middle Miocene climatic transition: East Antarctic ice sheet development, deep ocean circulation and global carbon cycling. Palaeogeography, Palaeoclimatology, Palaeoecology, 108: 537-555.

Flower, B.P. and Kennett, J.P., 1995. Middle Miocene deepwater paleoceanography in the southwest Pacific: Relations with East Antarctic Ice Sheet development. Paleoceanography, 10(6): 1095-1112.

Frank, M., Gersonde, R., Rutgers van der Loeft, M., Kuhn, G. and Mangini, A., 1996. Later Quaternary sediment dating and quantification of lateral sediment redistribution applying $^{230}Th_{ex}$: a study from the eastern Atlantic sector of the Southern Ocean. Geologische Rundschau, 85: 554-566.

Froelich, P.N. et al., 1991. Biogenic Opal and Carbonate Accumulation Rates in the Subantarctic South Atlantic: The Late Neogene of Meteor Rise Site 704. In: P.F. Ciesielski, Y. Kristoffersen, et al., (Editors), Proc. ODP, Sci. Res., 114: College Station, TX (Ocean Drilling Program), pp. 515-550.

Fronval, T. and Jansen, E., 1996. Late Neogene Paleoclimates and Paleoceanography in the Iceland-Norwegian Sea: Evidence from the Iceland and Vøring Plateaus. In: J. Thiede, A.M. Myhre, J.V. Firth, G.L. Johnson and W.F. Ruddiman (Editors), Proc. ODP, Sci. Res.., 151: College Station, TX (Ocean Drilling Program), pp. 455-468.

Gersonde, R.E., Hodell, D.A., Blum, P., et al., 1999. Proc. ODP, Init. Repts., 177 [Online]. Available from World Wide Web: <http://www-odp.tamu.edu/publications/177_IR/177TOC.HTM>.

Gingele, F.X. and Schmiedl, G., 1999. Comparison of independent proxies in the reconstruction of deep-water circulation in the South-east Atlantic off Namibia. South African Journal of Marine Sciences, 21: 181-190.

Gubbins, D., 1999. The distinction between geomagnetic excursions and reversals. Geophysical Journal International, 137(F1-F3).

Guo, Z.T. et al., 2002. Onset of Asian desertification by 22 Myr ago inferred from loess deposits in China. Nature, 416: 159-163.

Gupta, A.K. and Thomas, E., 1999. Latest Miocene-Pleistocene productivity and deep-sea ventilation in the northwestern Indian Ocean (Deep Sea Drilling Project Site 219). Paleoceanography, 14(1): 62-73.

Gurnis, M., Mitrovica, J.X., Ritsema, J. and van Heijst, H.-J., 2000. Constraining mantle density structure using geological evidence of surface uplift rates: The case of the African Superplume. Geochemistry, Geophysics, Geosystems, 1.

Hagelberg, T.K., Shackleton, N.J., Pisias, N.G., et al., 1992. Development of Composite Depth Sections for Sites 844 Through 854. In: L.A. Mayer, N.G. Pisias, T.R. Janecek, et al. (Editors), Proc. ODP, Init. Repts., 138: College Station, TX (Ocean Drilling Program), pp. 79-85.

Hailwood, E.A. and Clement, B.M., 1991. Magnetostratigraphy of Site 703 and 704, Meteor Rise, Southeastern South Atlantic. In: P.F. Ciesielski, Y. Kristoffersen, et al., (Editors), Proc. ODP, Sci. Res., 114: College Station, TX (Ocean Drilling Program), pp. 367-386.

Haq, B.U., Hardenbol, J. and Vail, P.R., 1987. Chronology of Fluctuating Sea Levels since the Triassic. Science, 235: 1156-1166.

Harris, S.E. and Mix, A.C., 2002. Climate and tectonic influences on continental erosion of tropical South America, 0-13 Ma. Geology, 30(5): 447-450.

Harris, S.E., Mix, A.C. and King, T., 1997. Biogenic and Terrigenous Sedimentation at the Ceará Rise, Western Tropical Atlantic, Supports Pliocene-Pleistocene Deep-Water Linkage between Hemispheres. In: N.J. Shackelton, W.B. Curry, C. Richter and T.J. Bralower (Editors), Proc. ODP, Sci. Res., 154: College Station, TX (Ocean Drilling Program), pp. 331-345.

Harwood, D.M., Scherer, R.P. and Webb, P.-N., 1989. Multiple Miocene productivity events in West Antarctica as recorded in Upper Miocene sediments beneath the Ross Ice Shelf (Site J-9). Marine Micropaleontology, 15: 91-115.

Haug, G. and Tiedemann, R., 1998. Effect of the formation of the Isthmus of Panama on Atlantic Ocean thermohaline circulation. Nature, 393(18): 673-676.

Haug, G.H., Hughen, K.A., Sigman, D.M., Peterson, L.C. and Röhl, U., 2001. Southward Migration of the Intertropical Convergence Zone through the Holocene. Science, 293: 1304-1308.

Hay, W.W., 1996. Tectonics and climate. Geologische Rundschau, 85: 409-437.

Hay, W.W. and Brock, J.C., 1992. Temporal variations in intensity of upwelling off southwest Africa. In: C.P. Summerhayes, W.L. Prell and K.C. Emeis (Editors), Upwelling Systems: Evolution since the Early Miocene. Geological Society Special Publication, pp. 463-497.

Heinze, C. and Crowley, T.J., 1997. Sedimentary response to ocean gateway circulation changes. Paleoceanography, 12(6): 742-754.

Hermoyian, C.S. and Owen, R.M., 2001. Late Miocene-early Pliocene biogenic bloom: Evidence from low-productivity regions of the Indian and Atlantic Oceans. Paleoceanography, 16(1): 95-100.

Hilgen, F.J., Krijgsman, W., Raffi, I., Turco, E. and Zachariasse, W.J., 2000. Integrated stratigraphy and astronomical calibration of the Serravillian/Tortonian boundary section at Monte Gibliscemi (Sicily, Italy). Marine Micropaleontology, 38: 181-211.

Hillenbrand, C.-D. and Fütterer, D.K., 2001. Neogene to Quaternary Deposition of Opal on the Continental Rise West of the Antarctic Peninsula, ODP Leg 178, Sites 1095, 1096 and 1101. In: P.F. Barker, A. Camerlenghi, G.D. Acton and R.A.T.S. (Editors), Proc. ODP, Init. Res., 178: College Station, TX (Ocean Drilling Program), pp. 1-33.

Hodell, D.A., Benson, R.H., Kent, D.V., Boersma, A. and Rakic-El Bied, K., 1994. Magnetostratigraphic, biostratigraphic, and stable isotope stratigraphy of an Upper Miocene drill core from the Salé Briqueterie (northwestern Morocco): high-resolution chronology for the Messinian stage. Paleoceanography, 9(6): 835-855.

Hodell, D.A., Curtis, J.H., Sierro, F.J. and Raymo, M.A., 2001. Correlation of late Miocene to early Pliocene sequences between the Mediterranean and North Atlantic. Paleoceanography, 16(2): 164-178.

Hodell, D.A., Gersonde, R. and Blum, P., 2002. Leg 177 Synthesis: Insights into Southern Ocean Paleoceanography on Tectonic to Millenial Timescales. In: R. Gersonde, D.A. Hodell and P. Blum (Editors), Proc. ODP, Sci. Res., 177, pp. 1–54.

Hodell, D.A. and Venz, K., 1992. Toward a high-resolution stable isotope record of the Southern Ocean during the Pliocene-Pleistocene (4.8 to 0.8 Ma). In: J.P. Kennett and D.A. Warnke (Editors), The Antarctic Paleoenvironment: A Perspective on Global Change. Antarctic Research Series. AGU, Washington, D. C., pp. 265-310.

Hovan, S.A. and Rea, D.K., 1992. The Cenozoic record of continental mineral deposition on Broken and Ninetyeast ridges, Indian Ocean: Southern African aridity and sediment delivery from the Himalayas. Paleoceanography, 7: 833-860.

Howard, W.R. and Prell, W.L., 1994. Late Quaternary $CaCO_3$ production and preservation in the Southern Ocean: Implications for oceanic and atmospheric carbon cycling. Paleoceanography, 9(3): 453-482.

Ikehara, M., Kawamura, K., Ohkouchi, N., Murayama, M., Nakamura, T., Taira, A., 2000. Variations of terrestrial input and marine productivity in the Southern Ocean (48°S) during the last two deglaciations. Paleoceanography, 15(2): 170-180.

Imbrie, J., A. Berger, E.A. Boyle, S.C, Clemens, A. Duffy, W.R. Howard, G. Kukla, J. Kutzbach, D.G. Martinson, A. McIntyre, A.C. Mix, B. Molfino, J.J. Morley, L.C. Peterson, N.G, Pisias, W.L. Prell, M.E. Raymo, N.J. Shackleton, and J.R. Toggweiler, 1993. On the structure and origin of major glaciation cycles 2. The 100,000-year cycle. Paleoceanography, 8(6): 699-735.

Imbrie, J. et al., 1992. On the Structure and Origin of Major Glaciation Cycles: 1. Linear Responses to Milankovitch Forcing. Paleoceanography, 7(6): 701-738.

Imbrie, J., Hays, J. D., Martinson, D. G., McIntyre, A., Mix, A. C., Morley, J. J., Pisias, N. G., Prell, W. L., Shackleton, N. J., 1984. The Orbital Theory of Pleistocene Climate: Support from a Revised Chronology of the Marine $\delta^{18}O$ Record. In: A. Berger, J. Imbrie, J.D. Hays, G. Kukla and B. Saltzman (Editors), Milankovitch and Climate (Part 1). NATO ASI Series - Series C: Mathematical and Physical Sciences, Vol. 126. Reidel Publ. Comp., pp. 269-305.

Imbrie, J., McIntyre, A. and Mix, A.C., 1989. Oceanic Response to Orbital Forcing in the Late Quaternary: Observational and Experimental Strategies. In: A. Berger, S. Schneider and J.C. Duplessy (Editors), Climate and Geo-Sciences, A Challenge for Science and Society in the 21st Century. Kluwer Academic Publishers, pp. 121-164.

Isern, A.R., Anselmetti, F.S., Blum, P., et al, 2002. Leg 194 summary. Proc. ODP, Init. Repts., 194: College Station TX (Ocean Drilling Program), 1-88 pp.

Jahn, B., Donner, B., Müller, P. J., Röhl, U., Schneider, R. R., Wefer, G., 2003. Pleistocene variations in dust input and marine productivity in the northern Benguela Current: evidence of the evolution of global glacial-interglacial cycles. Palaeogeography, Palaeoclimatology, Palaeoecology, 193q: 515-533.

Jansen, E. and Sjöholm, J., 1991. Reconstruction of glaciation over the past 6 Myr from ice-born deposits in the Norwegian Sea. Nature, 349: 600-603.

Jansen, J.H.F., Van der Gaast, S.J., Koster, B. and Vaars, A.J., 1998. CORTEX, a shipboard XRF-scanner for element analyses in split sediment cores. Marine Geology, 151(1-4): 143-153.

Jenkins, R. and De Vries, J.L., 1970. Practical X-ray Spectrometry. Macmillan, London.

John, C.M., 2003. Miocene Climate as recorded on Slope Carbonates: Examples from Malta (Central Mediterranean) and Northeastern Australia (Marion Plateau, ODP Leg 194). Dissertation Thesis, Potsdam, 90 pp.

Johnson, D.A., 1990. Radiolarian Biostratigraphy in the Central Indian Ocean, Leg 115. In: R.A. Ducan, J. Backman, L.C. Peterson, et al., (Editors), Proceedings of the Ocean Drilling Program, Sci. Res., 115. College Station (TX), Ocean Drilling Program, pp. 395-409.

Kanfoush, S.L. et al., 2000. Millennial-scale instability of the Antarctic ice sheet during the last glaciation. Science, 288: 1815-1818.

Kashiwagi, H. and Shikazono, N., 2003. Climate change during Cenozoic inferred from global carbon cycle model including igneous and hydrothermal activities. Palaeogeography, Palaeoclimatology, Palaeoecology, 199: 167-185.

Keller, G. and Barron, J.A., 1983. Paleoceanographic implications of Miocene deep-sea hiatuses. Geological Society of America Bulletin, 94: 590-613.

Kennett, J.P., 1977. Cenozoic Evolution of Antarctic Glaciation, the Circum-Antarctic Ocean, and their Impact on Global Paleoceanography. Journal of Geophysical Research, 82(27): 3843-3860.

Kennett, J.P. and Barker, P.F., 1990. Latest Cretaceous to Cenozoic Climate and Oceanographic Development in the Weddell Sea, Antarctica: An Ocean-Drilling Perspective. In: P.F. Barker and J.P. Kennett (Editors), Proc. ODP, Sci. Res., 113: College Station, TX (Ocean Drilling Program), pp. 937-960.

Kennett, J.P., Keller, G. and Srinivasan, M.S., 1985. Miocene Planktonic Foraminiferal Biogeography and Paleoceanography Development of the Indo-Pacific Region. In: J.P. Kennett (Editor), The Miocene Ocean: Paleoceanography and Biogeography. Geological Society of America Memoir, 163, pp. 197-263.

Kennett, J.P. and Shackleton, N.J., 1976. Oxygen isotopic evidence for the development of the psychrosphere 38 Myr ago. Nature, 260: 513-515.

King, T.A., Ellis, J., Murray, W.G., Shackleton, N.J. and Harris, S., 1997. Miocene evolution of carbonate sedimentation at the Ceara Rise: a multivariate data/proxy approach. In: N.J. Shackleton, W.B. Curry, C. Richter and T.J. Bralower (Editors), Proc. ODP, Sci. Res., 154: College Station, TX (Ocean Drilling Program), pp. 349-364.

Krijgsman, W., Hilgen, F.J., Raffi, I., Sierro, F.J. and Wilson, D.S., 1999. Chronology, causes and progression of the Messinian salinity crisis. Nature, 400: 652-655.

Kuhlmann, H., 2003. Reconstruction of paleoceanography and terrigenous sedimentation in the Canary Islands Region during the late-Quaternary: Application of core-logging tools. PhD.-Thesis, Universität Bremen, Bremen.

Kuhn, G. and Diekmann, B., 2002. Late Quaternary variability of ocean circulation in the southeastern South Atlantic inferred from the terrigenous sediment record of a drift deposit in the southern Cape Basin. Palaeogeography, Palaeoclimatology, Palaeoecology., 182: 287-303.

Kumar, N., Anderson, R. F., Mortlock, R.A., Frielich, P.N., Kubik, P., Dittrich-Hannen, B., Suter, M., 1995. Increased biological productivity and export production in the glacial Southern Ocean. Nature, 378: 675-680.

Lange, C.B., Berger, W.H., Lin, H.-L., Wefer, G. and 175, S.S.P.L., 1999. The early Matuyama Diatom Maximum off SW Africa, Benguela Current System (ODP Leg 175). Marine Geology, 161: 93-114.

Larsen, H.C. et al., 1994. Seven Million Years of Glaciation in Greenland. Science, 264: 952-955.

Laskar, J., Joutel, F. and Boudin, F., 1993. Orbital, precessional, and insolation quantities for the earth from -20 Myr to + 10 Myr. Astronomy and Astrophysics, 270: 522-533.

Lawver, L.A. and Gahagan, L.M., 1998. Opening of Drake Passage and its impact on Cenozoic ocean circulation. In: T.J. Crowley and K.C. Burke (Editors), Tectonic boundary conditions for climate reconstructions. Oxford Monographs on Geology and Geophysics, pp. 212-223.

Lawver, L.A. and Gahagan, L.M., 2003. Evolution of Cenozoic seaways in the circum-Antarctic region. Palaeogeography, Palaeoclimatology, Palaeoecology, 198: 11-37.

Lawver, L.A., Gahagan, L.M. and Coffin, M.F., 1992. The Development of Paleoseaways around Antarctica. The Antarctic Paleoenvironment: A Perspective On Global Change, 56: 7-30.

Lear, C.H., Elderfield, H. and Wilson, P.A., 2000. Cenozoic Deep-Sea Temperatures and Global Ice Volumes from Mg/Ca in Benthic Foraminiferal Calcite. Science, 287: 269-272.

Lear, C.H., Rosenthal, Y. and Wright, J.D., 2003. The closing of a seaway: ocean water masses and global climate change. Earth and Planetary Science Letters, 210: 425-436.

Lee, T.-Y. and Lawver, L.A., 1995. Cenozoic plate reconstruction of Southeast Asia. In: T.W.C. Hilde and M.F.J. Flower (Editors), Southeast Asia Structure and Tectonics, Tectonophysics, pp. 85-138.

Liu, H.-S., 1992. Frequency variations of the Earth's obliquity and the 100-kyr ice-age cycles. Nature, 358: 397-399.

Liu, H.-S., 1995. A new view on the driving mechanism of Milankovitch glaciation cycles. EPSL, 131: 17-26.

Lourens, L.J. and Hilgen, F.J., 1997. Long-Periodic Variations in the Earth's Obliquity and their Relation to Third-Order Eustatic Cycles and Late Neogene Glaciations. Quaternary International, 40: 43-52.

Lourens, L.J., Hilgen, F.J., Laskar, J., Shackleton, N.J. and Wilson, D., in press. The Neogene Period. In: F. Gradstein, J. Ogg and A. Smith. (Editors), A Geological Timescale 2004.

Lyle, M., Dadey, K. and Farrell, J.W., 1995. The late Miocene (11-8 Ma) eastern Pacific carbonate crash: evidence for reorganization of deep-water circulation by the closure of the Panama gateway. In: N.G. Pisias, L.A. Mayer, T.R. Janecek, J. Palmer-Julson and T.H. van Andel (Editors), Proc. ODP, Sci. Res., 138: College Station TX (Ocean Drilling Program), pp. 821-838.

Lyle, M., Koizumi, I., Delaney, M.L. and Barron, J.A., 2000. Sedimentary Record of the California Current System, Middle Miocene to Holocene: A Synthesis pf Leg 167 Results. In: M. Lyle, I. Koizumi, C. Richter and T.C. Moore, Jr. (Editors), Proc. ODP, Sci. Res., 167 [Online]. Available from World Wide Web:http://www-odp.tamu.edu/publications/167_SR/167sr.htm.

Maher, B.A. and Dennis, P.F., 2001. Evidence agianst dust-mediated control of glacial-interglacial changes in atmospheric CO2. Nature, 411: 176-180.

Maier-Reimer, E., Mikolajewicz, U. and Crowley, T., 1990. Ocean General Circulation Model Sensitivity Experiment with an Open Central American Isthmus. Paleoceanography, 5(3): 349-366.

Martin, J.H., 1990. Glacial-Interglacial CO2 change: The iron hypothesis. Paleoceanography, 5: 1-13.

Maslin, M.A., Li, X.S., Loutre, M.-F. and Berger, A., 1998. The Contribution of Orbital forcing to the Progressive Intensification of Northern Hemisphere Glaciation. Quaternary Science Reviews, 17: 411-426.

McIntyre, A., Ruddiman, W.F., Karlin, K. and Mix, A.C., 1989. Surface water response of the equatorial Atlantic Ocean to orbital forcing. Paleoceanography, 4(1): 19-55.

McKinney, C.R., McCrea, J.M., Epstein, S., Allen, H.A. and Urey, H.C., 1950. Improvements in mass spectrometers for the measurement of small differences in isotope abundance ratios. Review of Scientific Instruments, 21: 724-730.

Melguen, M., 1978. Facies evolution, carbonate dissolution cycles in sediments from the eastern South Atlantic (DSDP Leg 40) since the early Cretaceous, Init. Repts. DSDP, pp. 981-1023.

Mikolajewicz, U. and Crowley, T.J., 1997. Response of a coupled ocean/energy balance model to restricted flow through the Central American Isthmus. Paleoceanography, 12(3): 429-441.

Miller, K.G., Fairbanks, R.G. and Mountain, G.S., 1987. Tertiary oxygen isotope synthesis, sea level history, and continental margin erosion. Paleoceanography, 2: 1-19.

Miller, K.G. and Feigenson, M.D., 1991. Miocene Isotope Reference Section, Deep Sea Drilling Project Site 608: An Evaluation of Isotope and Biostratigraphic Resolution. Paleoceanography, 6(1): 33-52.

Miller, K.G. et al., 1998. Cenozoic Global Sea Level, Sequences, and the New Jersey Transect: Results from Coastal Plain and Continental Slope Drilling. Reviews of Geophysics, 36(4): 569-601.

Miller, K.G., Wright, J.D. and Fairbanks, R.G., 1991. Unlocking the icehouse: Oligocene-miocene oxygen isotope, eustacy, and margin erosion. Journal of Geophysical Research, 96: 6829-6848.

Mix, A.C. et al., 1995. Benthic foraminifer stable isotope record from Site 849 (0-5 Ma): local and global climate changes. In: N.G. Pisias, L.A. Mayer, T.R. Janecek, T.R. Palmer-Julson and T.H. van-Andel (Editors), Proc. ODP, Sci. Res., 138: College Station, TX (Ocean Drilling Program), pp. 371-392.

Morse, J.W. and MacKenzie, F.T., 1990. Geochemistry of Sedimentary Carbonates. Developments in Sedimentology, 48, New York.

Müller, D.W., Hodell, D.A. and Ciesielski, P.F., 1991. Late Miocene to Earliest Pliocene (9.8-4.5 Ma) Paleoceanography of the Subantarctic Southeast Atlantic: Stable Isotopic, Sedimentologic, and Microfossil Evidence. In: P.F. Ciesielski, Y. Kristoffersen, et al., (Editors), Proc. ODP, Sci. Res., 114: College Station, TX (Ocean Drilling Program), pp. 459-474.

Muller, R.A. and MacDonald, G.J., 1997. Glacial Cycles and Astronomical Forcing. Science, 277: 215-218.

Muller, R.A. and MacDonald, G.J., 2000. Ice Ages and Astronomical Causes: Data, spectral Analysis and Mechanisms. Springer Praxis books in environmental sciences. Springer, London, 318 pp.

Murphy, L., Warnke, D.A., Andersson, C., Channell, J. and Stoner, J., 2002. History of ice rafting at South Atlantic ODP Site 177-1092 during the Gauss and Late Gilbert Chrons. Palaeogeography, Palaeoclimatology, Palaeoecology, 182: 183-196.

Murray, D.W. and Peterson, L.C., 1997. Biogenic Carbonate Production and Preservation Changes between 5 and 10 ma from the Ceara Rise, Western Equatorial Atlantic. In: N.J. Shackleton, W.B. Curry, C. Richter and T.J. Bralower (Editors), Proc. ODP, Sci. Res., 154: College Station, TX (Ocean Drilling Program), pp. 375-388.

Naish, T.R., Woolfe, K.J., Barrett, P.J., et al., 2001. Orbitally induced oscillations in the East Antarctic ice sheet at the Oligocene/Miocene boundary. Nature, 413: 719-723.

Nicholson, S.E., 2000. The natural variability over Africa on time scales of decades to millennia. Global and Planetary Change, 26: 137-158.

Nisancioglu, K.H., Raymo, M.E. and Stone, P.H., 2003. Reorganization of Miocene deep water circulation in response to the shoaling of the Central American Seaway. Paleoceanography, 18(1): 1006, doi:10.1029/2002PA000767.

Norris, R.D. and Röhl, U., 1999. Carbon cycling and chronology of climate warming during the Palaeocene/Eocene transition. Nature, 401: 775-778.

Oboh-Ikuenobe, F.E., 2001. A Palynological Record of Middle Miocene to Lower Pliocene Sedimentary Rocks, ODP Hole 1085A (Cape Basin, southwestern Africa) - (Abstract). EOS, 82/20: 228.

Pagani, M., Arthur, M.A. and Freeman, K.H., 1999. Miocene evolution of atmospheric carbon dioxide. Paleoceanography, 14(3): 273-292.

Pagani, M., Arthur, M.A. and Freeman, K.H., 2000. Variations in Miocene phytoplankton growth rates in the southwest Atlantic: Evidence for changes in ocean circulation. Paleoceanography, 15(5): 486-496.

Paillard, D., Labeyrie, L. and Yiou, P., 1996. Macintosh program performs time-series analysis. Eos Trans. AGU, 77(379): (http://www.agu.org/eos_elec/96097e.html).

Pälike, H., Shackleton, N.J. and Röhl, U., 2001. Astronomical forcing in Late Eocene marine sediments. Earth and Planetary Science Letters, 193: 589-602.

Partridge, T.C., deMenocal, P.B., Lorentz, S.A., Paiker, M.J. and Vogel, J.C., 1997. Orbital Forcing of Climate over South Africa: A 200,000 Year Rainfall Record from the Pretoria Saltpan. Quaternary Research Reviews, 16: 1125-113.

Paturel, J., 2000. Evolution des flux terrigenes dans le basin du Cap au Miocene superieur- Pliocene inferieur. Roles du systeme courantologique de Benguela et du climat africain. Mem.DEA, Univ. de la Mediterranee, Aix-Marseille II: 45.

Paul, H.A., Zachos, J.C., Flower, B.P. and Tripati, A., 2000. Orbitally induced climate and geochemical variability across the Oligocene/Miocene boundary. Paleoceanography, 15(5): 471-485.

Pearson, P.N. and Palmer, M.R., 2000. Atmospheric carbon dioxide concentration over the past 60 million years. Nature, 406: 695-699.

Peterson, L.C., Haug, G.H., Hughen, K.A. and Röhl, U., 2000. Rapid Changes in the Hydrologic Cycle of the Tropical Atlantic during the Last Glacial. Science, 290: 1947-1951.

Petschik, R., Kuhn, G. and Gingele, F.X., 1996. Clay mineral distribution in surface sediments of the South Atlantic: sources, transport, and relation to oceanography. Mar. Geol., 130: 203-229.

Pisias, N.G. and Mix, A.C., 1988. Aliasing of the Geological Record and the Search for Long-Period Milankovitch Cycles. Paleoceanography, 3(5): 613-619.

Pisias, N.G., Shackleton, N.J. and Hall, M.A., 1985. Stable Isotope and Calcium Carbonate Records from Hydraulic Piston Cored Hole 574A: High-Resolution Records from the Middle Miocene. In: l. Mayer, F. Theyer, et al., (Editors), Init. Repts. DSDP, 85: Washington (U.S. Printing Office), pp. 753-748.

Quade, J., Cerling, T.E. and Bowman, J.R., 1989. Development of Asian monsoon revealed by marked ecological shift during the latest Miocene in northern Pakistan. Nature, 342: 163-166.

Quade, J., Roe, L., DeCelles, P.G. and Ojha, T., 1997. The late Neogene 87Sr/86Sr record of lowland Himalayan rivers. Science, 276: 1828-1831.

Ramsay, A.T.S., Smart, C.W. and Zachos, J.C., 1998. A model of early to middle Miocene deep ocean circulation for the Atlantic and Indian Oceans. In: A. Cramp, C.J. MacLeod, S.V. Lee and E.J.W. Jones (Editors), Geological Evolution of Ocean Basins: Results from the Ocean Drilling Program. Geological Society, London, Special Publications, pp. 55-70.

Raymo, M.E., 1994. The Himalayas, organic carbon burial, and climate in the Miocene. Paleoceanography, 9: 399-404.

Raymo, M.E., Hodell, D. and Jansen, E., 1992. Response of Deep Ocean Circulation to Initiation of Northern Hemisphere Glaciation (3-2Ma). Paleoceanography, 7(5): 645-672.

Raymo, M.E., Oppo, D.W. and Curry, W.B., 1997. The mid-Pleistocene climate transition: A deep sea carbon isotopic perspective. Paleoceanography, 12(4): 546-559.

Raymo, M.E. and Ruddiman, W.F., 1992. Tectonic forcing of late Cenozoic climate. Nature, 359: 117-122.

Raymo, M.E., Ruddiman, W.F., Shackleton, N.J. and Oppo, D.W., 1990. Evolution of Atlantic-Pacific $\delta^{13}C$ gradients over the last 2.5 m.y. EPSL, 97: 353-368.

Rea, D.K., 1992. Delivery of Himalayan sediment to the Northern Indian Ocean and its relation to global climate, sea level, uplift, and seawater strontium. In: R.A. Duncan, D.K. Rea, R.B. Kidd, U. von Rad and J.K. Weissel (Editors), Synthesis of Results from Scientific Drilling in the Indian Ocean. Geophysical Monograph Series, Washington, D.C., pp. 387-402.

Rea, D.K., 1994. The paleoclimatic record provided by eolian deposition in the deep sea: The geological history of wind. Reviews of Geophysics, 32: 159-195.

Ridgwell, A.J. and Watson, A.J., 2002. Feedback between aeolian dust, climate, and atmospheric CO2 in glacial time. Paleoceanography, 17(4): 1059, doi:10.1029/2001PA000729.

Roberts, A.P. and Lewin-Harris, J.C., 2000. Marine magnetic anomalies: evidence that 'tiny wiggles' represent short-period geomagnetic polarity intervals. Earth and Planetary Science Letters, 183: 375-388.

Rogers, J. and Bremner, J.M., 1991. The Benguela Ecosystem. Part VII. Marine Geological Aspects. In: M. Barnes (Editor), Oceanography Marine Biology Annual Review, pp. 1-85.

Röhl, U. and Abrams, L.J., 2000. High-Resolution, Downhole and Non-Destructive Core Measurements From Sites 999 and 1001 in the Caribbean Sea: Application to the Late Paleocene Thermal Maximum. In: R.M. Leckie, H. Sigurdsson, G.D. Acton and G. Draper (Editors), Proc. ODP, Sci.Res., 165, pp. 191-203.

Röhl, U., Bralower, T.J., Norris, R.D. and Wefer, G., 2000. New chronology for the late Paleocene thermal maximum and its environmental implications. Geology, 28(10): 927-930.

Röhl, U., Norris, R.D. and Ogg, J.G., 2003. Cyclostratigraphy of upper Paleocene and late Eocene sediments at Blake Nose Site 1051 (western North Atlantic). In: P. Gingerich, B. Schmitz, E. Thomas and S. Wing (Editors), Causes and Consequences of Globally Warm Climates in the Early Paleogene. Geological Society of America Special Paper Series, pp. 567-588.

Roth, M.J., Droxler, A.W. and Kameo, K., 2000. The Caribbean Carbonate Crash at the Middle to Late Miocene Transition: Linkage to the Establishment of the Modern Global Ocean Conveyor. In: R.M. Leckie, H. Sigurdsson, G.D. Acton and G. Draper (Editors), Proc. ODP, Sci. Res., 165: College Station, TX (Ocean Drilling Program), pp. 249-273.

Ruddiman, W.F. and Janecek, T.R., 1989. Pliocene-Pleistocene Biogenic and terrigenous Fluxes at Equatorial Atlantic Sites 662, 663 and 664. In: W. Ruddiman, M. Sarnthein, et al., (Editors), Proc. ODP, Sci. Res., 108: College Station, TX (Ocean Drilling Program), pp. 211-240.

Ruddiman, W.F., Raymo, M. and McIntyre, A., 1986. Matuyama 41,000-year cycles: North Atlantic Ocean and northern hemisphere ice sheets. EPSL, 80: 117-129.

Savin, S.M., Douglas, R.G. and Stehli, F.G., 1975. Tertiary marine paleotemperatures. Geological Society of America Bulletin, 86: 1499-1510.

Schefuss, E., Schouten, S., Jansen, J.H.F. and Sinninghe Damsté, J.S., 2003. African vegetation controlled by tropical sea surface temperatures in the mid-Pleistocene period. Nature, 422: 418-421.

Schmieder, F., von Dobeneck, T. and Bleil, U., 2000. The Mid-Pleistocene climate transition as documented in the deep South Atlantic Ocean: Initiation, interim state and terminal event. Earth and Planetary Science Letters, 179: 539-549.

Schneider, R.R., Müller, P.J. and Ruhland, G., 1995. Late Quaternary surface circulation in the east equatorial South Atlantic. Paleoceanography, 10: 197-219.

Schulz, M., Berger, W.H., Sarnthein, M. and Grootes, P.M., 1999. Amplitude variations of 1470-year climate oscillations during the last 100,000 years linked to fluctuations of continental ice mass. Geophysical Research Letters, 26(22): 3385-3388.

Seibold, E. and Berger, W.H., 1996. The Sea Floor - An Introduction to Marine Geology. Springer, 356 pp.

Shackleton, N.J., Berger, A. and Peltier, W.R., 1990. An alternative astronomical calibration of the lower Pleistocene timescale based on ODP Site 677. Transactions of the Royal Society of Edinburgh: Earth Sciences, 81: 251-261.

Shackleton, N.J. and Crowhurst, S., 1997. Sediment Fluxes based on an Orbitally Tuned Time Scale 5 to 14 Ma, Site 926. In: N.J. Shackleton, W.B. Curry, C. Richter and T.J. Bralower (Editors), Proc. ODP, Sci. Res., 154: College Station, TX (Ocean Drilling Program), pp. 69-82.

Shackleton, N.J., Crowhurst, S.J., Weedon, G.P. and Laskar, J., 1999. Astronomical calibration of Oligocene-Miocene time. In: N.J. Shackleton, M.I. N. and G.P. Weedon (Editors), Phil. Trans. R. Soc. Lond. A, pp. 1907-1929.

Shackleton, N.J. and Hall, M.A., 1997. The Late Miocene Stable Isotope Record, Site 926. In: N.J. Shackleton, W.B. Curry, C. Richter and T.J. Bralower (Editors), Proc. ODP, Sci. Res., 154: College Station, TX (Ocean Drilling Program), pp. 367-373.

Shackleton, N.J. and Kennett, J.P., 1975. Paleotemperature History Of The Cenozoic and The Initiation of Antarctic Glaciation: Oxygen and Carbon Isotope analyses in DSDP Sites 277, 279, and 281. In: J.P. Kennett, R.E. Houtz, et al., (Editors), Init. Repts. DSDP , 29: Washington (U.S. Govt. Printing Office), pp. 743-755.

Shackleton, N.J. and Opdyke, N.D., 1973. Oxygen isotope and palaeomagnetic stratigraphy of equatorial Pacific core V28-238: oxygen isotope temperatures and ice volumes on a 10^5 and 10^6 year scale. Quaternary Research, 3: 39-55.

Short, D.A., Mengel, J.G., Crowley, T.J., Hyde, W.T. and North, G.R., 1991. Filtering of Milankovitch Cycles by Earth's Geography. Quaternary Research, 35: 157-173.

Siesser, W.G., 1978. Aridification of the Namib Desert: evidence from oceanic cores. In: van Zinderen-Bakker (Editor), Antarctic glacial history and world paleoenvironment. Balkema, Rotterdam, pp. 105-112.

Siesser, W.G., 1980. Late Miocene origin of the Benguela upwelling system off northern Namibia. Science, 208: 283-285.

Sigurdsson, H., Leckie, R.M., Acton, G.D., et al., 1997. Proc. ODP, Init. Repts., 165: College Station, TX (Ocean Drilling Program).

Stein, R., 1991. Organic carbon accumulation in Baffin Bay and paleoenvironment high northern latitudes during the past 20 m.y. Geology, 19: 356-359.

Stuut, J.-B., 2001. Late Quaternary southwestern African terrestrial-climate signals in the marine record of Walvis Ridge, SE Atlantic Ocean, Utrecht, 128 pp.

Thunell, R. and Belyea, P., 1982. Neogene Planktonic Foraminiferal Biogeography of the Atlantic Ocean. Micropaleontology, 28: 381-398.

Turco, E. et al., 2002. Middle Miocene high-resolution calcareous plankton biostratigraphy at Site 926 (Leg 154, equatorial Atlantic Ocean): palaeoecological and palaeobiological implications. Geobios, 35(Mémoire spécial n° 24): 257-276.

Turco, E., Hilgen, F.J., Lourens, L.J., Shackleton, N.J. and Zachariasse, W.J., 2001. Punctuated evolution of global climate cooling during the late Middle to early Late Miocene: High-resolution planktonic foraminiferal and oxygen isotope records from the Mediterranean. Paleoceanography, 16(4): 405-423.

Twichell, S.C., Meyers, P.A. and Diester-Haass, L., 2002. Significance of high C/N ratios in organic-carbon-rich Neogene sediments under the Benguela Current upwelling system. Organic Geochemistry, 33: 715-722.

Van Andel, T.H., Heath, G.R. and Moore, T.C., 1975. Cenozoic history and paleoceanography of the central equatorial Pacific Ocean. Geological Society of America Memoir, 143: 134 pp.

van Zinderen Bakker, E.M., 1984. Palynological Evidence for late Cenozoic Arid Conditions along the Namibia Coast from Holes 532 and 530A, Leg 75, Deep Sea Drilling Project. In: W.W. Hay and J.-C. Sibuet (Editors), Init. Repts. DSDP, 75: Washington (U.S. Government Printing Office), pp. 763-766.

Vidal, L., Bickert, T., Wefer, G. and Röhl, U., 2002. Late Miocene stable isotope stratigraphy of Site 1085: Relation to Messinian events. Marine Geology, 180: 71-85.

Vincent, E., 1981. Neogene Carbonate stratigraphy of Hess Rise (Central North Pacific) and Paleoceanographic Implications. In: L.N. Stout (Editor), Init. Repts. DSDP 62: Washington (U.S. Govt. Printing Office). pp. 571-606.

Vincent, E. and Berger, W.H., 1985. Carbon dioxide and polar cooling in the Miocene: The Monterey Hypothesis. In: E.T. Sundquist and W.S. Broecker (Editors), The carbon cycle and atmospheric CO2: Natural variations Archean to Present. AGU, Washington D. C., pp. 455-468.

Walter, H.J., Hegner, E., Diekmann, B., Kuhn, G. and Rutgers Van der Loeff, M.M., 2000. Provenance and transport of terrigenous sediment in the South Atlantic Ocean and their relations to glacial and interglacial cycles: Nd and Sr isotopic evidence. Geochemica et Cosmochemica Acta, 64(22): 3813-3827.

Warnke, D.A., Allen, C.P., Müller, D.W., Hodell, D.A. and Brunner, C.A., 1992. Miocene-Pliocene Antarctic Glacial Evolution: A Synthesis of Ice-Rafted Debris, Stable Isotope, and Planktonic Foraminiferal Indicators, ODP Leg 114. In: J.P. Kennett and D.A. Warnke (Editors), The Antarctic Paleoenvironment: A Perspective on Global Change. Antarctic Research Series. AGU, Washington, D. C., pp. 311-325.

Wefer, G., Berger, W.H., Richter, C., et al., 1998. Proc. ODP, Init. Repts., 175: College Station, TX (Ocean Drilling Program).

Wei, W. and Peleo-Alampay, A., 1997. Onset of North Atlantic Deep Water 11.5 million years ago triggered by climate cooling. In: P. Wang and W.A. Berggren (Editors), Proc. 30th Int'l. Geol. Congr, pp. 57-64.

Westerhold, T. and Bickert, T., in preperation. Middle to Late Miocene History of Carbonate and Terrigenous Sedimentation at South Atlantic ODP Site 1092.

Westerhold, T. and Bickert, T., subm. Middle to Late Miocene Oxygen Isotope Stratigraphy of ODP Site 1085 - SE Atlantic. Palaeogeography, Palaeoclimatology, Palaeoecology.

Westerhold, T., Bickert, T. and Röhl, U., subm. a. Miocene evolution of carbonate sedimentation in the eastern South Atlantic: High-resolution XRF-scanning records of ODP-Sites 1085 and 1087. Marine Geology.

Westerhold, T., Vidal, L. and Bickert, T., subm. b. Pleistocene Oxygen Isotope Stratigraphy of ODP Site 1085 - SE Atlantic. Earth and Planetary Science Letters.

Winkler, A., Wolf-Welling, T.C.W., Stattegger, K. and Thiede, J., 2002. Clay mineral sedimentation in high northern latitude deep-sea basins since the Middle Miocene (ODP Leg 151, NAAG). Int. J. Earth Sciences (Geologische Rundschau), 91: 133-148.

Woodruff, F. and Savin, S.M., 1989. Miocene deep-water oceanography. Paleoceanography, 7: 87-140.

Wright, J.D. and Miller, K.G., 1992. Miocene Stable Isotope Stratigraphy, Site 747, Kerguelen Plateau. In: S.W. Wise, Jr., R. Schlich, et al. (Editors), Proc. ODP, Sci. Res., 120: College Station, TX (Ocean Drilling Program), pp. 855-866.

Wright, J.D. and Miller, K.G., 1996. Control of North Atlantic Deep Water circulation by the Greenland-Scotland Ridge. Paleoceanography, 11: 157-169.

Wright, J.D., Miller, K.G. and Fairbanks, R.G., 1991. Evolution of Modern Deepwater Circulation: Evidence from the Late Miocene Southern Ocean. Paleoceanography, 6(2): 275-290.

Wright, J.D., Miller, K.G. and Fairbanks, R.G., 1992. Early and Middle Miocene Stable Isotopes: Implications for Deepwater Circulation and Climate. Paleoceanography, 7(3): 357-389.

Zabel, M. et al., 2001. Late Quaternary Climate Changes in Central Africa as Inferred from Terrigenous Input to the Niger Fan. Quaternary Research, 56: 207-217.

Zachos, J., Pagani, M., Sloan, L., Thomas, E. and Billups, K., 2001a. Trends, Rhythms, and Aberrations in Global Climate 65 Ma to Present. Science, 292: 686-693.

Zachos, J., Shackleton, N.J., Revenaugh, J.S., Pälike, H. and Flower, B.P., 2001b. Climate Response to Orbital Forcing Across the Oligocene-Miocene Boundary. Science, 292: 274-278.

Zachos, J.C., Flower, B.P. and Paul, H., 1997. Orbitally paced climate oscillations across the Oligocene/Miocene boundary. Nature, 388: 567-570.

Zachos, J.C., Lohmann, K.C., Walker, J.C.G. and Sherwood, W.W., 1993. Abrupt Climate Change and Transient Climates During the Paleogene: A Marine Perspective. Journal of Geology, 101: 191-213.

Zhisheng, A., Kutzbach, J.E., Prell, W.L. and Porters, S.C., 2001. Evolution of Asian monsoon and the phased uplift of the Himalaya-Tibetan plateau since Late Miocene times. Nature, 411: 62-66.

Zielinski, U. and Gersonde, R., 2002. Plio-Pleistocene diatom biostratigraphy from ODP Leg 177, Atlantic sector of the Southern Ocean. Marine Micropaleontology, 45: 225-268.

Danksagung

Mein besonderer Dank gilt Prof. Dr. Gerold Wefer für die Vergabe der vorliegenden Dissertation und die vielfältige Unterstützung bei der Durchführung der Arbeit. Für die freundliche Übernahme des Zweitgutachtens bedanke ich mich recht herzlich bei Prof. Dr. Rüdiger Henrich.

Ganz besonders herzlich möchte ich mich bei Dr. Torsten Bickert bedanken für die hervorragende Betreuung, anregenden Diskussionen und die schöne Zeit. In diesem Sinne möchte ich auch Dr. Ulla Röhl ganz herzlich danken. Beide haben mich mit ihrem wissenschaftlichen Rat im Verlauf der Arbeit sehr unterstützt und waren immer hilfreich zur Stelle.

Vielen Kolleginnen und Kollegen aus dem Fachbereich Geowissenschaften der Universität Bremen haben mit Rat und Tat, anregenden Diskussionen und durch den freundschaftlich Umgang sehr zum Gelingen dieser Arbeit beigetragen. Für die vielfältige Hilfe im ODP-Kernlager möchte ich mich bei Alex Wülbers, Walter Hale und Edith bedanken; desweiteren sei allen MitarbeiterInnen der Geochemie gedankt. Im Besonderen sei Dr. Mattias Zabel für die Durchführung der ICP-OES Analysen herzlichst gedankt. Einen herzlichen Dank an das Team vom Isotopenlabor, Dr. M. Segl und B. Meyer-Schack. Einen besonderen Dank an Torsten Klein für die schnelle und unkomplizierte Hilfe bei dem Eine-Woche-vor-Abgabe-Computer-Absturz. Vielen Dank. Besonders möchte ich mich bei folgenden KollegInnen für die schöne Zeit und die fruchtbaren Diskussionen bedanken: Jens Funk, Martin Cepek, Barbara Donner, Laurence Vidal, Holger Kuhlmann, Martin Kölling, Sabine Kasten, Lydie Dypont, Jan-Berent Stuut, Jens Grützner, Harald Paulsen, Oscar Romero, Felix Schewe, Lieselotte Diester-Haass, Bernhard Diekmann, Bernd Censarek, Rainer Gersonde, und viele, viele mehr. Danke.

Für den Aufenthalt in Utrecht möchte ich Frits Hilgen und ganz besonders Luc Lourens danken, die sich viel Zeit für mich genommen haben. Dank auch an Anja Reitz und Julia Becker für die Unterkunft.

Am allermeisten danke ich meinen MitbewohnerInnen und liebsten FreundInnen, die mich gerade am Ende der Arbeit selten zu Gesicht bekamen.

Zu guter Letzt, den liebsten Dank an Uli.

tho